DETERMINATION OF DEPTH OF PLACEMENT OF TUNNELS AND CAVITIES BY THE BOUNDARY ELEMENT METHOD

Dr. Omar Al-Farouk Al-Damluji
Assistant Professor and Head,
Department of Civil Engineering,
University of Baghdad.

Dr. Mohammed Yousif Fattah
Lecturer,
Department of Building and Construction, University of Technology

Rana A. J. Al-Adhamii
Formerly Graduate student,
Department of Civil Engineering,
University of Baghdad.

ABSTRACT

A boundary element numerical algorithm has been developed for the determination of stresses and deformations around cavities and tunnels. A study of the influence of depth below the ground surface on the distribution of stresses and deformations around cavities and tunnels is presented in this paper. The soil is assumed to behave linearly elastic.

A computer program has been built to perform the numerical computations. The results show that with increasing the depth of placement of tunnel or opening below the ground surface, the settlements decrease. The maximum stresses occur at the haunches of the tunnel rather than at the crown.

For the circular cavity that is considered in this paper, it was found that with increasing the depth below the ground surface (depth/tunnel diameter > 3), the surface settlements do not exceed 6 % from those obtained for the case of no-cavity condition.

الخلاصة

لقد طورت طريقة العناصر الحدودية كخوارزمية عددية لايجاد الاجهادات و الازاحات حول الانفاق و الفتحات الارضية. في هذا البحث أجريت دراسة حول تاثير عمق الفتحة أو النفق تحت سطح الارض على توزيع الاجهادات و الازاحات حول الانفاق أو الفتحات الارضية. و قد أعتبر تصرف التربة مرنا خطيا.

و قد بني برنامج حاسبة الكترونية لاجراء الحسابات العدديه. وبينت النتائج أنه مع زيادة عمق الفتحه أو النفق تحت سطح الارض تقل الاجهادات و الهبوطات و أن الاجهادات القصوى تحدث عند الحافات الجانبية للنفق بدلا من قمته.

و في حالة الفتحة الدائرية التي تم تحليلها في هذا البحث، وجد أنه مع زيادة العمق تحت سطح الأرض، (العمق \ قطر النفق > 3)، لا تتجاوز الازاحات السطحية 6% من تلك التي تحصل في حالة عدم وجود فتحة.

KEY WORDS

Tunnels, Cavities and Boundary Element Method.

INTRODUCTION

Rapid growth in urban development has resulted an increased demand for the construction of water supply, sewage disposal and transportation systems. Tunnels are an essential component of these systems and constitute a major portion of project expenditure.

Recent advances in tunnelling technology reduce construction time with consequent decrease in cost. However, even with modern equipment, experience has shown that designing of tunnels must include dealing with three important problems:

1- Maintaining stability of face and wall of the tunnel before supported by lining.
2- Predicting displacements caused by excavation of the tunnel on the surface and throughout the adjacent ground mass.
3- Predicting the magnitude and distribution of earth pressure acting on the tunnel.
   So, there is an urgent need for reliable means to estimate the extent and nature of the movements and disturbance occuring in areas above and adjacent to tunnels. These deformations may significantly affect nearby structures and need to be considered during design.

The object of this paper is to provide, as far as possible, a picture of the stress distribution around cavities and tunnels in an isotropic medium. Also, provide at least a temporary expedient for estimating the settlements to be expected at varying distances laterally from the centre line of a cavity or a tunnel.

PREVIOUS STUDIES

Although the finite element techniques have been used in so many practical problems, the boundary formulations appear as an alternative technique that, in many cases, can provide more reliable or economical analysis. Even with automatic mesh generation techniques, the finite element method has not found widespread application to tunneling problems because of the data preparation problems and considerable computer time requirements.

The input data requirements of the boundary element method (BEM) are considerably less than these of the finite element method (FEM) since only the boundary needs to be discretized. Unlike the FEM, the BEM can model the boundaries at infinity without truncating the outer boundary at some arbitrary distance from the region of interest.

In the boundary element method, the unknowns appear only on the boundaries of a domain, so the number of the unknowns may be reduced compared to the three-dimensional finite element method. This condition is well suited to tunnels, where the most significant unknown, the surface subsidence appears on the boundary.

The research already conducted on tunneling problems or soil-structure interaction using the BEM can be summarized as follows:

1- Brady and Bray (1978a and b) have described a boundary element method for determining the distribution of stress and induced displacements around long, narrow, parallel - sided openings in an elastic medium. A good agreement was found between the results of the boundary element analyses and those obtained from analytical solutions. A BEM of stress analysis was also developed for the solution of complete plane strain problems and applied to determine the stress distribution around openings with irregular cross sections having any arbitrary orientation in a triaxial stress field. The displacements induced by the excavation are also included.
2- Venturini and Brebbia (1981) have described for the first time, the extension of the BEM to no tension materials such as those present in underground and surface excavations.
3- Ito and Histake (1982)* treated generally, a three-dimensional problem of an advancing shallow tunnel in an elastic and non-elastic ground by the boundary element method. The tunnel advance velocity and the position of the face were taken into consideration. The method has been illustrated and verified on two sites where subsidence measurements were taken simultaneously.

The disadvantage of this method is that it does not deal with displacements inside the ground nor with the corresponding changes in stresses.

4- Gioda, Carini and Cividini (1984)** discussed a boundary integral equation technique for the visco-elastic stress analysis of underground openings. The results of a test problem were presented concerning a shallow circular tunnel. These results show that an acceptable accuracy of the numerical solution is obtained even when adopting a relatively small number of free variables
5- Again, Venturini and Brebbia in (1984)** have proposed a boundary element formulation to analyze plane strain problems with possible displacements at the third direction. An algorithm to model nonlinear behavior is presented including an initial stress process. The study of an unlined opening was carried out illustrating that tunnels whose axes do not coincide with the original principal stress direction can not be analyzed assuming plane strain conditions only.

THE BOUNDARY ELEMENT METHOD

There are many engineering problems for which it is possible to represent the governing equations by a system of boundary integral equations (BIEs); that is , the integrated unknown parameters, in such equations, appear only in integrals over the boundary of the problem domain. There are many numerical approaches for the solution of such equations, and each approach gives the solution of such equations, and each one of them may be called a boundary integral equation method (BIEM).

Characteristics of the Boundary Element Method

The boundary element method (BEM) is considered nowadays the most popular numerical technique for the direct solution of BIEM. It is based upon piecewise discretization of the problem boundary in terms of sub–boundaries, known as boundary elements, in a way similar to that employed for the finite element method. The main advantages of the BEM compared with domain numerical techniques can be summarized in the following statements: -

1- For many applications, the dimensionality of the problem is reduced by one, resulting in a considerable reduction in the data and computer CPU time required for the analysis.
2- The BEM is ideal for problems with infinite domains, such as problems of soil mechanics, fluid mechanics and acoustics.
3- No interpolation errors inside the domain.
4- Boundaries at infinity can be modeled conveniently without truncating the outer at some arbitrary distance from the region of interest.
5- Surface problem, such as those of elastic fracture mechanics, or elastic contact, is dealt with more efficiently and economically with the BEM.
6- Valuable representation for stress concentration problems.
7- The BEM offers a fully continuous solution inside the domain, and the problem parameters can be evaluated directly at any point.

The boundary element method has also disadvantages and they can be outlined as follows, (EL-Zafrany 1992):

1- The derivation of the governing BIEs may require a level of mathematics higher than that with other methods, but the procedure of the BEM itself is not different from that of the FEM.
2- It leads to fully populated matrices for the equations to be solved, thus it is not possible to employ the elegant FEM solvers such as the banded or frontal solvers with the BEM.
3- The BIEs of nonlinear problems may have domain integrals which require the use of domain elements for their evaluation, thus losing the main advantage of the dimensionality reduction mentioned above.
4- The method is not accurate for problems within narrow strips or curved shell structures.

The Governing Equations

In the elastic stress analysis of a plane-stress, or a plane strain engineering component, there are eight basic independent parameters to be determined, namely: the displacements u and v, strains ε_x, ε_y and γ_{xy} and stresses σ_x, σ_y and τxy. They are governed, at any point inside the component, by eight partial differential equations, which can be deduced for homogeneous isotropic materials from equations given in the last section.

Strain-displacement relationships

$$\varepsilon_x = \frac{\partial u}{\partial x}, \qquad \varepsilon_y = \frac{\partial v}{\partial y}, \qquad \gamma_{xy} = \frac{\partial v}{\partial x} + \frac{\partial u}{\partial y} \tag{1}$$

Stress-strain relationships

$$\left.\begin{aligned} \sigma_x &= d_{11}\varepsilon_x + d_{12}\varepsilon_y \\ \sigma_y &= d_{21}\varepsilon_x + d_{22}\varepsilon_y \\ \tau_{xy} &= d_{33}\,\gamma_{xy} \end{aligned}\right\} \tag{2}$$

where:

$$\left.\begin{aligned} d_{11} &= d_{22} = 2G(1-p)/(1-2p) \\ d_{12} &= d_{21} = 2Gp/(1-2p) \\ d_{33} &= G \end{aligned}\right\} \tag{3}$$

G = shear modulus

P = ν (Poisson's ratio) for plane strain problems

$= \dfrac{\nu}{1+\nu}$ for plane stress problems.

Equations of equilibrium

$$\left.\begin{aligned} \frac{\partial \sigma_x}{\partial x} + \frac{\partial \tau_{xy}}{\partial y} + f_x &= 0 \\ \frac{\partial \tau_{xy}}{\partial x} + \frac{\partial \sigma_y}{\partial y} + f_y &= 0 \end{aligned}\right\} \tag{4}$$

with the following equations, at any point on the boundary:

$$\left.\begin{aligned} T_x &= l\sigma_x + m\tau_{xy} \\ T_y &= l\tau_{xy} + m\sigma_y \end{aligned}\right\} \tag{5}$$

where: T_x and T_y are the traction components in x- and y- directions.
l and m are directional cosines in x- and y-directions, respectively.

Two-dimensional equations in terms of displacement

Substituting Equations (1) into (2), then the stress components may be expressed in terms of displacement components. Substituting the resulting equations into the equations of equilibrium

(Equations 4), then the governing equations are reduced to the following elliptic partial differential equations in terms of displacement components u and v:

$$\left.\begin{aligned} \nabla^2 u + \frac{1}{1-2p}\frac{\partial}{\partial x}(\nabla.\vec{q}) + f_x / G = 0 \\ \nabla^2 v + \frac{1}{1-2p}\frac{\partial}{\partial y}(\nabla.\vec{q}) + f_y / G = 0 \end{aligned}\right\} \quad (6)$$

where $\vec{\mathbf{q}} = \mathbf{u}\hat{\mathbf{i}} + \mathbf{v}\hat{\mathbf{j}}$, which is the displacement vector.

Biharmonic representation

Gelerkin introduced strain functions G_x and G_y which may be expressed in terms of a vector known as the Gelerkin vector, i.e. (EL-Zafrany 1992):

$$\vec{\mathbf{G}} = \mathbf{G_x}\,\hat{\mathbf{i}} + \mathbf{G_y}\,\hat{\mathbf{j}} \quad (7)$$

such that (Little 1973):

$$\vec{\mathbf{q}} = \nabla^2 \vec{\mathbf{G}} - \frac{1}{2(1-\mathbf{p})}\nabla(\nabla.\vec{\mathbf{G}}) \quad (8)$$

Writing the partial differential equations (6) in the following vectorial form:

$$\nabla^2 \vec{\mathbf{q}} + \frac{1}{2(1-\mathbf{p})}\nabla(\nabla.\vec{\mathbf{q}}) + \vec{\mathbf{f}} / \mu = 0 \quad (9)$$

then from the definition of the Gelerkin vector, the previous equation can be modified as follows:

$$\nabla^2(\nabla^2 \vec{\mathbf{G}}) + \vec{\mathbf{f}} / \mu = 0$$

which can be rewritten explicitly in terms of the following Biharmonic equations:

$$\begin{aligned} \nabla^4 \mathbf{G_x} + \mathbf{f_x} / \mu = 0 \\ \nabla^4 \mathbf{G_y} + \mathbf{f_y} / \mu = 0 \end{aligned} \quad (10)$$

FUNDAMENTAL SOLUTION OF SOLID CONTINUUM PROBLEMS

Fundamental Displacement

A two-dimensional solid continuum problem is considered in a semi-infinite domain, with the x-y plane in a state of loading defined by a concentrated force acting at point (x_i,y_i) with a uniform distribution, in the z direction, over a thickness t, which has a constant value for the whole domain. The applied force is represented by the following vector (Fung 1965):

$$\vec{\mathbf{F}} = \mathbf{t}(\mathbf{e_x}\hat{\mathbf{i}} + \mathbf{e_y}\hat{\mathbf{j}}) \quad (11)$$

where e_x and e_y are the x and y- components of the applied force per unit thickness.
From the definition of the two-dimensional Dirac delta function, a domain distribution of the load intensity equivalent to the applied force, may be expressed as follows (Fung 1965):

$$\left.\begin{aligned} f_x^* = e_x \delta(x - x_i, y - y_i) \\ f_y^* = e_y \delta(x - x_i, y - y_i) \end{aligned}\right\} \quad (12)$$

Using Equations (6) and (7), the governing partial diferential equations for the above case may be written in the following displacement form:

$$\left.\begin{aligned} \nabla^2 u^* + \frac{1}{1-2p}\frac{\partial}{\partial x}\left(\frac{\partial u^*}{\partial x}+\frac{\partial v^*}{\partial y}\right)+\frac{f_x^*}{G}=0 \\ \nabla^2 v^* + \frac{1}{1-2p}\frac{\partial}{\partial y}\left(\frac{\partial u^*}{\partial x}+\frac{\partial v^*}{\partial y}\right)+\frac{f_y^*}{G}=0 \end{aligned}\right\} \tag{13}$$

and the solution to such expressions is known as the fundamental solution.
If the displacement components (u*, v*) are expressed in terms of the componants (G_x^*, G_y^*) of Galerkin's vector, such that:

$$\left.\begin{aligned} u^* = \nabla^2 G_x^* - \frac{1}{2(1-p)}\frac{\partial}{\partial x}\left(\frac{\partial G_x^*}{\partial x}+\frac{\partial G_y^*}{\partial y}\right) \\ v^* = \nabla^2 G_y^* - \frac{1}{2(1-p)}\frac{\partial}{\partial y}\left(\frac{\partial G_x^*}{\partial x}+\frac{\partial G_y^*}{\partial y}\right) \end{aligned}\right\} \tag{14}$$

then, equations (13) can be reduced to the following biharmonic equations:

$$\left.\begin{aligned} \nabla^4 G_x^* + e_x \delta(x-x_i, y-y_i)/G = 0 \\ \nabla^4 G_y^* + e_y \delta(x-x_i, y-y_i)/G = 0 \end{aligned}\right\} \tag{15}$$

The previous equations lead to the conclusion that the parameters G_x^*, G_y^* can be defined in terms of one functions: $G_x^* = g^* e_x,\ G_x^* = g^* e_x$ (16)

Hence, Equations(15) may be reduced to the following equation:

$$\nabla^4 g^* + \delta(x-x_i, y-y_i)/G = 0 \tag{17}$$

Defining another function ϖ^* such that: $\nabla^2 g^* = \varpi^*/G$ (18)

Then Equation (17) can be rewritten in terms of the following Poisson's partial differential equation:

$$\nabla^4 \varpi^* + \delta(x-x_i, y-y_i) = 0 \tag{19}$$

which has the following solution:

$$\varpi^* = \frac{1}{2\pi}\left[\log(1/r) + C_1\right] \tag{20}$$

Substituting the above expression into equation (18), and using direct integration, it can be shown that:

$$g^* = \frac{r^2}{8\pi\mu}\left[\log(1/r) + C_1 + 1\right] + C_2 \tag{21}$$

where C_1 and C_2 are arbitrary integration constants.
Then, equations (14) become as:

$$\mathbf{u}_{\alpha}^{*}(x-x_i, y-y_i) = G_{\alpha 1}(x-x_i, y-y_i)e_x + G_{\alpha 2}(x-x_i, y-y_i)e_y \tag{22}$$

where the fundamental solution parameter $G_{\alpha\beta}$ is expressed as follows:

$$G_{\alpha\beta}(x-x_i, y-y_i) = \nabla^2 g^* \delta_{\alpha\beta} - \frac{1}{2(1-p)}\left(\frac{\partial^2 g^*}{\partial x_\alpha \partial x_\beta}\right) \tag{23}$$

All explicit expressions for the fundamental solution parameters given in this paper are found in (al-Adthami, 2003).

Fundamental Strain

The components of Cauchy's strain tensor can be defined for the previous case, as follows (Desai and Siriwardane 1984):

$$\varepsilon_{\alpha\beta}^{*} = \frac{1}{2}\left(\frac{\partial u_\beta^*}{\partial x_\alpha} + \frac{\partial u_\alpha^*}{\partial x_\beta}\right) \tag{24}$$

and using equation (22), the previous equation may be written in the following form:

$$\varepsilon_{\alpha\beta}^{*} = A_{\alpha\beta 1}^{*} e_X + A_{\alpha\beta 2}^{*} e_y \tag{25}$$

where

$$A_{\alpha\beta\gamma}^{*} = \frac{1}{2}\left(\frac{\partial G_{\beta\gamma}}{\partial x_\alpha} + \frac{\partial G_{\alpha\gamma}}{\partial x_\beta}\right) \tag{26}$$

All fundamental solutions given in this paper are functions of $(x\text{-}x_i, y\text{-}y_i)$.

Fundamental Stress

Substituting the fundamental strain tensor defined by equation (25) into the stress-strain relationships, then it can be proved that:

$$\sigma_{\alpha\beta}^{*} = D_{\alpha\beta 1}^{*} e_X + D_{\alpha\beta 2}^{*} e_y \tag{27}$$

Fundamental Traction

If the fundamental stress components defined above are employed in equations (5), then the corresponding components of fundamental tractions can be expressed in the following form:

$$\left.\begin{aligned} T_x^* &= F_{11} e_X + F_{12} e_y \\ T_y^* &= F_{21} e_X + F_{22} e_y \end{aligned}\right\} \tag{28}$$

Boundary Integral Equations

The governing boundary integral equations are usually obtained by employing fundamental solutions as weighting functions in inverse weighted - residual expressions. For linear elastic problems, the Maxwell-Betti reciprocal theorem may also be used for direct derivation of boundary integral equations.

Boundary Integral Equations of Displacement

Substituting the fundamental loading parameters defined by equations (12) into the inverse expression, and using Dirac delta properties, it can be deduced that:

$$\left.\begin{aligned} & C_i u_i e_x + C_i v_i e_y + \oint_\Gamma (T_x^* u + T_y^* v) d\Gamma = \\ & \oint_\Gamma (T_x u^* + T_y v^*) d\Gamma + \iint_\Omega (f_x u^* + f_y v^*) dx dy \end{aligned}\right\} \tag{29}$$

where: $\mathbf{u_i = u(x_i, y_i)}, \quad \mathbf{v_i = v(x_i, y_i)}$

Employing fundamental displacements (equation 22), and fundamental tractions (equation 28), for arbitrary values of e_x, e_y, then equation (19) can be split into the following boundary integral equations which are defined with respect to the source point (x_i, y_i):

$$\mathbf{C_i u_i + \oint_\Gamma (F_{11} u + F_{21} v) d\Gamma = \oint_\Gamma (G_{11} T_x + G_{21} T_y) d\Gamma + U(x_i, y_i)} \tag{30}$$

$$\mathbf{C_i v_i + \oint_\Gamma (F_{12} u + F_{22} v) d\Gamma = \oint_\Gamma (G_{12} T_x + G_{22} T_y) d\Gamma + V(x_i, y_i)} \tag{31}$$

where:

$$\mathbf{U(x_i, y_i) = \iint_\Omega \left(G_{11} f_x + G_{21} fy\right) dx dy} \tag{32}$$

$$\mathbf{V(x_i, y_i) = \iint_\Omega \left(G_{12} f_x + G_{22} fy\right) dx dy} \tag{33}$$

which represent domain loading terms.

If the source point (x_i, y_i) is inside the domain, then C_i=1, and equations (30) and (31) may be modified as follows:

$$\mathbf{u(x_i, y_i) = U(x_i, y_i) + \oint_\Gamma (G_{11} T_x + G_{21} T_y) d\Gamma - \oint_\Gamma (F_{11} u + F_{21} v) d\Gamma} \tag{34}$$

$$\mathbf{v(x_i, y_i) = V(x_i, y_i) + \oint_\Gamma (G_{12} T_x + G_{22} T_y) d\Gamma - \oint_\Gamma (F_{12} u + F_{22} v) d\Gamma} \tag{35}$$

The analysis given in the remaining subsections will be limited to cases with source points being inside the domain.

Boundary Integral Equations of Strain

Equations (34) and (35) can be differentiated partially with respect to x_i and y_i; that is, Cauchy's strain components may be defined at an internal point (x_i,y_i) as follows (Banerjee 1994):

$$\boldsymbol{\varepsilon}_{\mathbf{xx}}\mathbf{(x_i, y_i) = \frac{\partial u_i}{\partial x_i}}, \quad \boldsymbol{\varepsilon}_{\mathbf{yy}}\mathbf{(x_i, y_i) = \frac{\partial v_i}{\partial y_i}}, \quad \boldsymbol{\varepsilon}_{\mathbf{xy}} = \mathbf{\frac{1}{2}\left[\frac{\partial u_i}{\partial y_i} + \frac{\partial v_i}{\partial x_i}\right]} \tag{36}$$

When employing displacement equations (equations 34 and 35) in the previous expressions of strain components, integral terms are to be differentiated with respect to x_i and y_i. Then, the boundary integral equation for Cauchy's strain tensor may be expressed in the following form:

$$\begin{aligned} & \boldsymbol{\varepsilon}_{\alpha\beta}(\mathbf{x_i, y_i}) = \iint_\Omega (\mathbf{A}_{\alpha\beta 1} \mathbf{f_x} + \mathbf{A}_{\alpha\beta 2} \mathbf{f_y}) \mathbf{dxdy} + \oint_\Gamma (\mathbf{A}_{\alpha\beta 1} \mathbf{T_x} + \mathbf{A}_{\alpha\beta 2} \mathbf{T_y}) \mathbf{d}\Gamma - \\ & \oint_\Gamma (\mathbf{B}_{\alpha\beta 1} \mathbf{u} + \mathbf{B}_{\alpha\beta 2} \mathbf{v}) \mathbf{d}\Gamma \end{aligned} \tag{37}$$

where: $\mathbf{A}_{\alpha\beta\gamma} = -\mathbf{A}_{\alpha\beta\gamma}$, and $\quad \mathbf{B}_{\alpha\beta\gamma} = -\frac{1}{2}\left[\frac{\partial \mathbf{F}_{\gamma\beta}}{\partial \mathbf{x}_\alpha} + \frac{\partial \mathbf{F}_{\gamma\alpha}}{\partial \mathbf{x}_\beta}\right]$ (38)

Boundary Integral Equations of Stress

Substituting the strain tensor defined by the boundary integral equation (37) into the stress-strain relationships, then a boundary integral equation for the stress tensor at the internal source point (x_i, y_i) can be described, and expressed in the following form (Banerjee 1994):

$$\sigma_{\alpha\beta}(x_i, y_i) = \iint_{\Omega} (D_{\alpha\beta1} f_x + D_{\alpha\beta2} f_y) dxdy + \oint_{\Gamma} (D_{\alpha\beta1} T_x + D_{\alpha\beta2} T_y) d\Gamma - \oint_{\Gamma} (E_{\alpha\beta1} u + E_{\alpha\beta2} v) d\Gamma \tag{39}$$

where: $D_{\alpha\beta\gamma} = -D_{\alpha\beta\gamma}$ (40)

Numerical Treatment of the Boundary Integral Equations

The boundary element method, as described in the previous sections, is based upon dividing the boundary into a suitable number of boundary elements, and approximating the boundary distributions of field function parameters such as displacements and tractions by interpolating them in terms of their nodal values within each element. Discretizing the boundary Γ of a two-dimensional elasticity problem into n_e boundary elements, the boundary integral equations (equations 30 and 31) with respect to the source point may be rewritten as follows:

$$\left.\begin{aligned} C_i u_i + \sum_{e=1}^{n_e} \left[\oint_{\Gamma_e} \{ F_{11} u(\Gamma_e) + F_{21} v(\Gamma_e) \} d\Gamma \right] &= \\ \sum_{e=1}^{n_e} \left[\oint_{\Gamma_e} \{ G_{11} T_x(\Gamma_e) + G_{21} T_y(\Gamma_e) \} d\Gamma \right] &+ U(x_i, y_i) \end{aligned}\right\} \tag{41}$$

$$\begin{aligned} C_i v_i + \sum_{e=1}^{n_e} \left[\oint_{\Gamma_e} \{ F_{12} u(\Gamma_e) + F_{22} v(\Gamma_e) \} d\Gamma \right] &= \\ \sum_{e=1}^{n_e} \left[\oint_{\Gamma_e} \{ G_{12} T_x(\Gamma_e) + G_{22} T_y(\Gamma_e) \} d\Gamma \right] &+ V(x_i, y_i) \end{aligned} \tag{42}$$

where each parameter in the form of $f(\Gamma_e)$ represents a field function parameter approximated over the boundary Γ_e of the eth element.

A Computer Program for Two-Dimensional Solid Continuum Problems

A computer program based upon the theory of the two-dimensional solid continuum mechanics problems of the boundary element method with constant elements is coded in FORTRAN 77 and introduced herein. The program can deal with plane-stress and plane strain problems with surface and domain loading.

In the design of tunnels to be constructed in urban areas, it is necessary to estimate the magnitude and distribution of the stresses and settlements that are likely to occur due to a particular design and

construction technique. Also, the effect of these stresses and movements upon existing surface and buried structures has to be studied.
The main factors that greatly affect the stresses and deformations around tunnels and underground excavations are the shape, dimensions, depth of opening below the ground surface, distance between the openings and the kind of supports (gap parameters). Therefore, the influence of the depth of the tunnel below the ground surface is conducted herein by considering a cavity of 4 meters diameter under a constant surcharge load of 50 KN/m^2.
The computer program is used for the determination of the stress and deformation fields around one cavity. The soil is assumed to be homogeneous, isotropic and a linearly elastic medium containing one opening representing the cavity dimensions and positions. The chosen discretization boundary element mesh is shown in **Fig. (1).**

INFLUENCE OF DEPTH BELOW THE GROUND SURFACE:

Case of a Single Cavity:

Fig. (2) shows a schematic representation of the problem to be studied for 6 values of depth/diameter ratios (Z_o/D = 1, 1.5, 2, 2.5, 3 and ∞)
Figs (3) and (4) show the vertical and horizontal displacements (U_y and U_x) along the ground surface. It can be noticed from these figures that as ($Z_o/D>3$), the disturbing influence on the ground surface does not exceed 5% from the case of no-cavity condition.
Fig. (5) shows the variation of vertical stresses over a line passing through the centerline of the surface loading and the center of cavities (line I-I) in **Fig. (3).** The stresses are normalized by dividing the values by the applied load. From this figure, it can be seen that the vertical stress distributions increase with the increase of Z_o/D ratio, reaching to maximum values as $Z_o/D \rightarrow \infty$ (case of no cavity).
Fig. (6) shows the variation of horizontal stresses over a line passing through the centerline of the surface loading and the center of cavities ((line I-I) in **Fig. (3)**). The stresses are normalized by dividing the values upon the applied load, P. From this figure, it can be seen that the maximum value of horizontal stress decreases as Z_o/D increases, and the point of maximum compressive horizontal stress lies between the ground surface and 0.5D below it, depending on the position of the cavity.
Fig. (7) shows the variation of vertical stresses along a vertical line (II-II) (in **Fig. (3)**) at a distance of 0.625D from the cavity's centerline (where D is the diameter of the cavity). It is evident from this figure that the maximum values of σ_y occur at the point lying on the horizontal level of the centerline of the cavities.
Fig. (8) shows the variation of the horizontal stresses along the same line (as described above). From this figure, it can be seen that the value of σ_x increases to a maximum compressive value above the centerline of the cavity then reverses back to a maximum tensile value on the spring level. Afterwards, it decreases asymptotically to a minimum value as $Z_o/D \rightarrow \infty$.

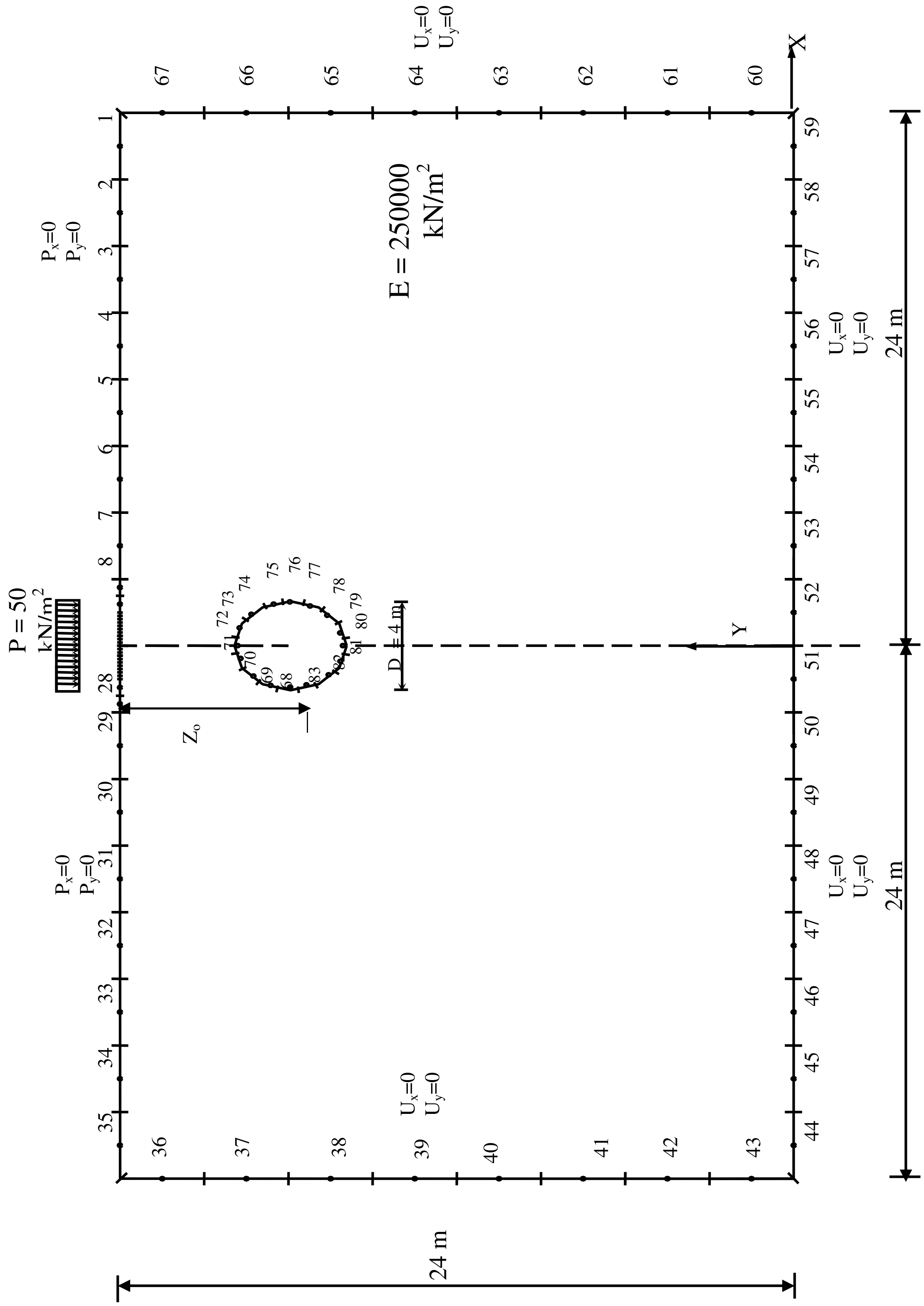

Fig. (1)-Constant boundary element discretization mesh for soil-cavity system.

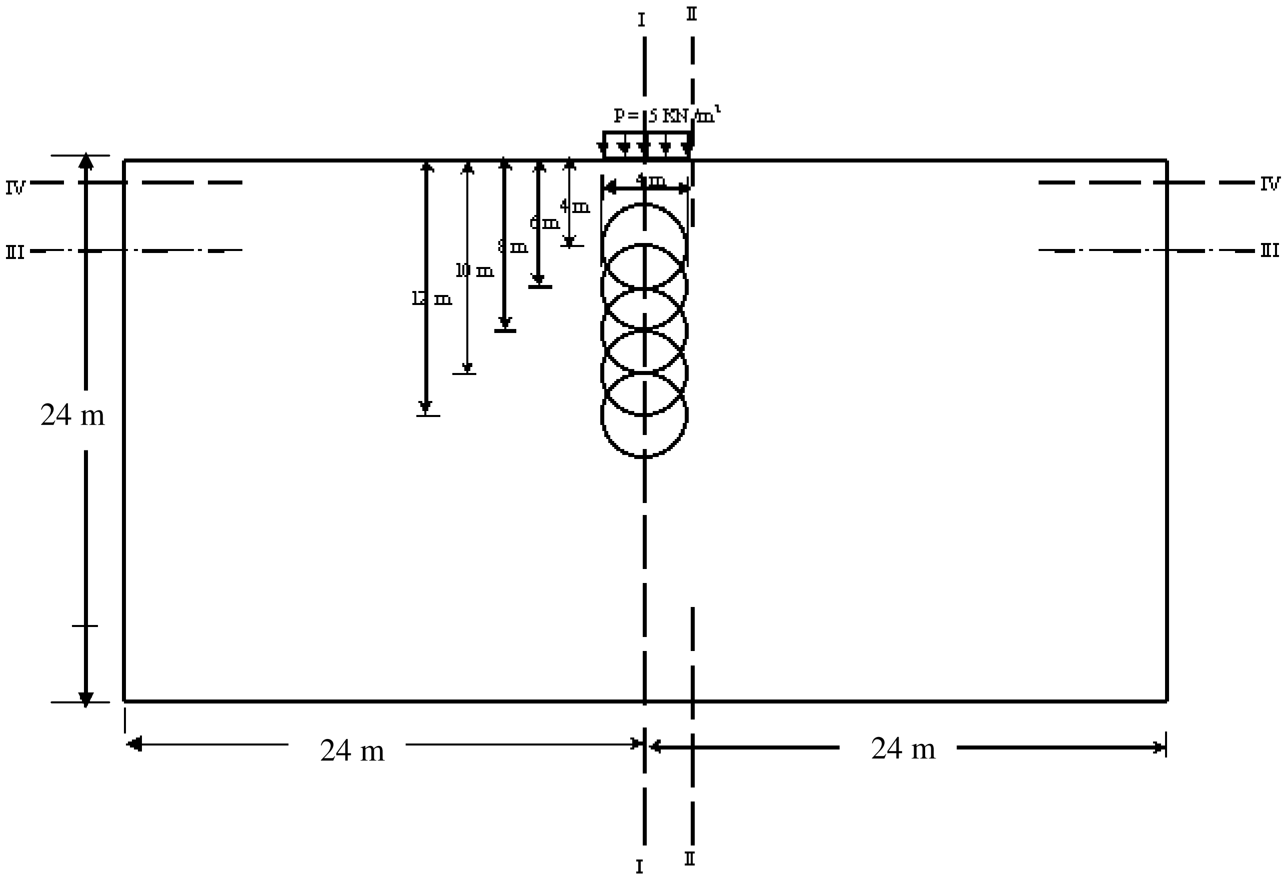

Fig. (2)-Schematic views of surface load-soil-cavities system.

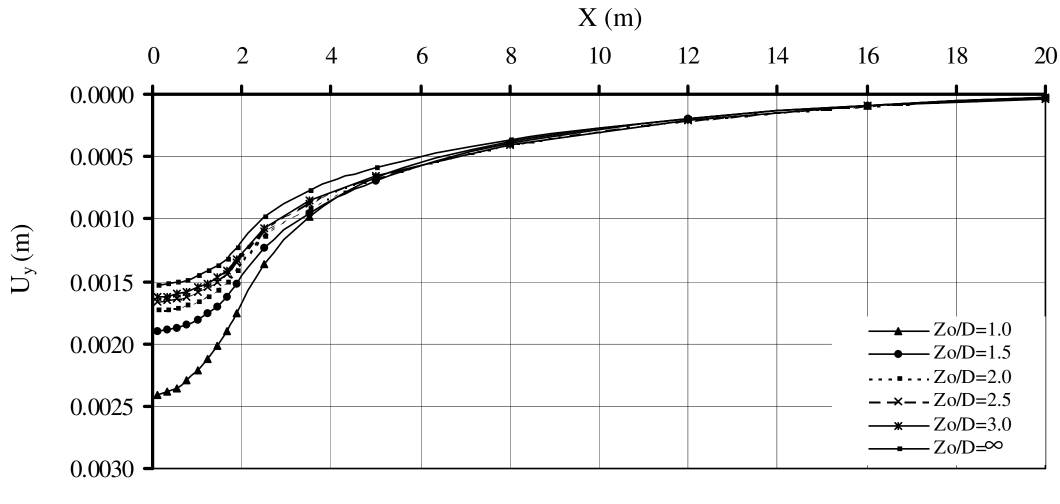

Fig. (3) – Vertical displacements on the surface

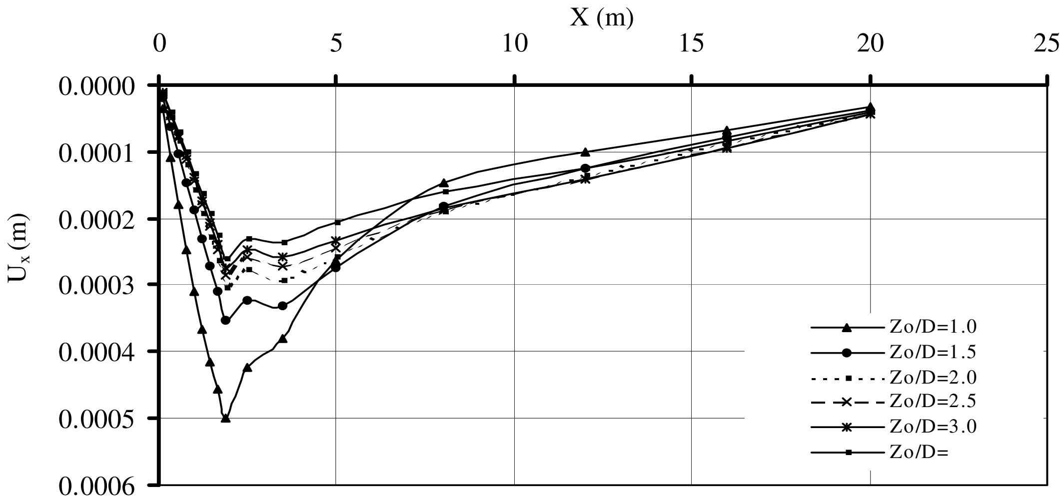

Fig. (4) – Horizontal displacements on the surface

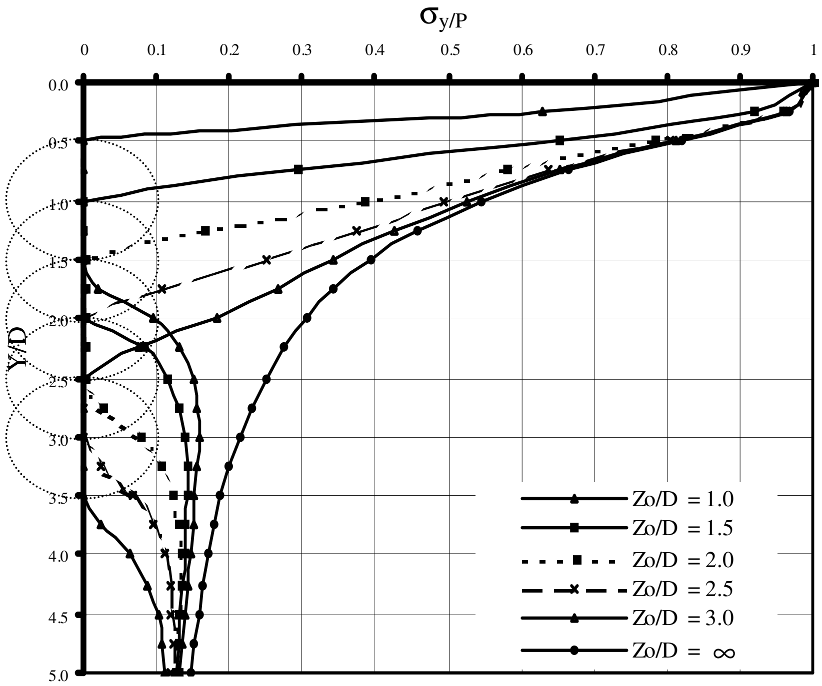

Fig. (5)-Variation of vertical stresses along line I-I.

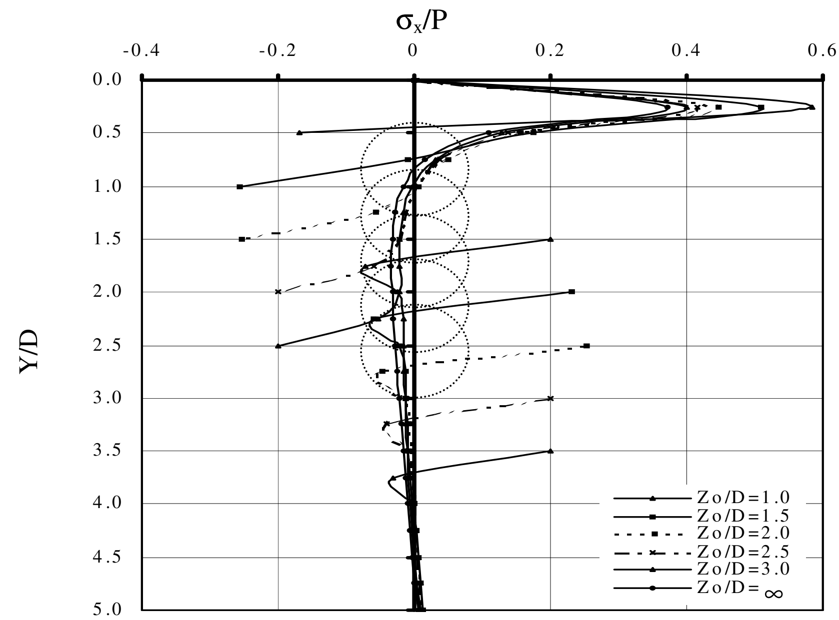

Fig. (6)-Variation of horizontal stresses along line I-I.

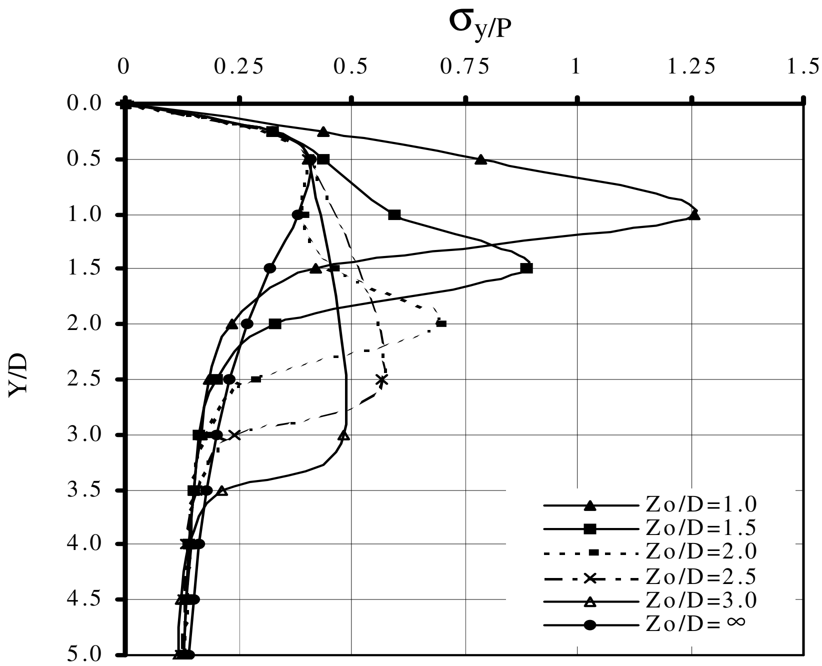

Fig. (7)-Variation of vertical stresses along line II-II.

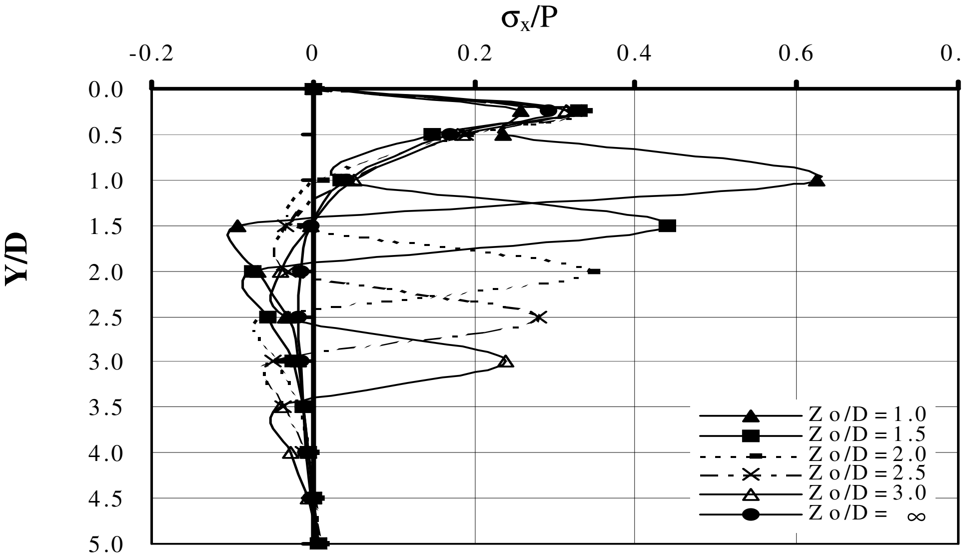

Fig. (8)-Variation of horizontal stresses along line II-II.

Fig. (9) shows the distribution of vertical stresses over a horizontal line 4.0 meters below the ground surface, namely (III-III in **Fig.(3)**), which may represent the raft foundation level of some buildings. It is obvious that by increasing values of Z_o/D, the corresponding σ_y values increase for the region $|X| < D/2$ and then take an opposite trend for $|X| \geq D/2$.

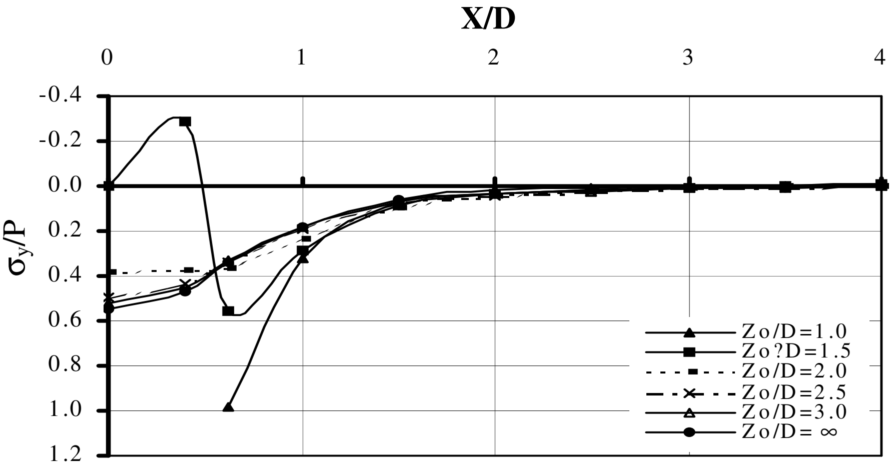

Fig. (9)-Vertical stress distribution on line III-III.

Figs. (10) and (11) show the vertical and horizontal displacements on the same line (III-III). It is noticed that their values increase with the decrease of Z_o/D ratio.

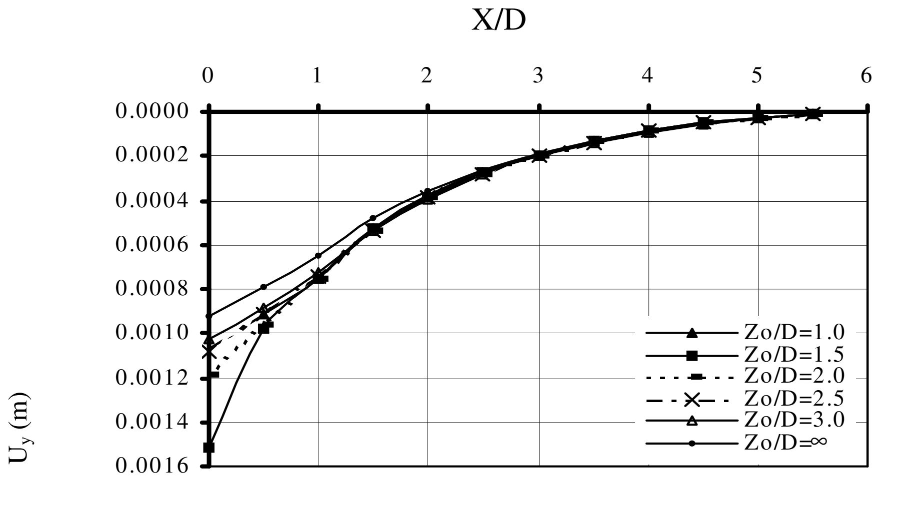

Fig. (10) -Vertical displacements along line III-III.

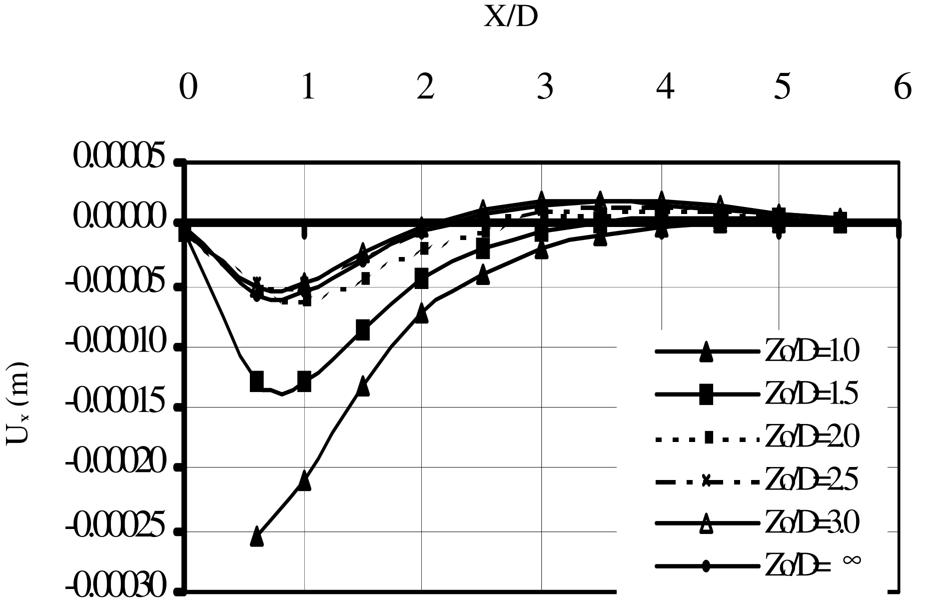

Fig. (11)-Horizontal displacement along line III-III.

Fig. (12) shows the vertical stresses over a horizontal line 1.0 meter below the ground surface (IV-IV) (**Fig. (2)**) which may represent the foundation level of many isolated footings. It is noticed that the heave effect starts to appear at a distance equal to d from the centerline of the surface loading.

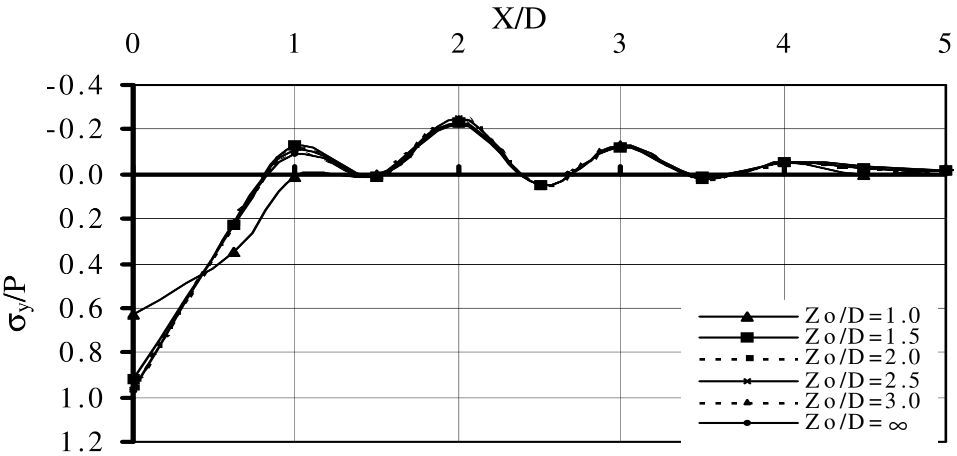

\

Fig. (12)-Vertical stress distribution along line IV-IV.

Fig. (13) shows the vertical displacements along the same line above (IV-IV). It is noticed that for the values of $Z_o/D < 3$, the displacements can be significantly more and the cavity effect has to be considered. For the values of $Z_o/D > 3$, the displacements do not exceed those from the case of no-cavity by more than 6% and then the effect of cavity can be neglected.

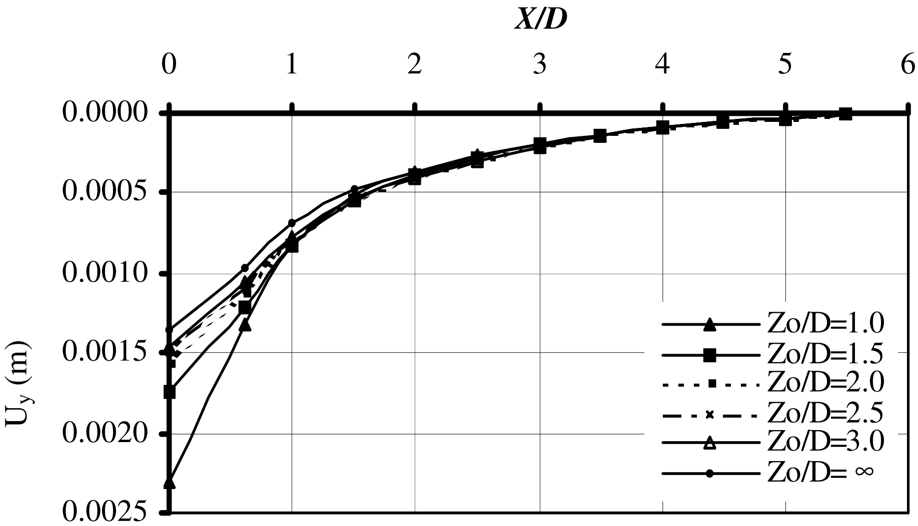

Fig. (13)-Vertical displacements along line IV-IV.

CONCLUSIONS

1- The boundary element method is a practical numerical tool that can be used to obtain solutions to a number of geotechnical problems of considerable complexity.
2- For two-dimensional solid continuum problems, the boundary element method presents the same advantage concerning the discretization of only the boundaries and reduction of the time for preparation of data.
3- A marked increase of stresses is found as the cavity approaches the ground surface and the stress distribution is very sensitive to the depth variation compared with the case of no-cavity conditions.

4- The maximum stresses occur at the haunches of the tunnel rather than at the crown.
5- For the circular cavity that is considered in this paper, it was found that with increasing the depth below the ground surface (depth/tunnel diameter > 3), the surface settlements do not exceed 6 % from those obtained for the case of no-cavity condition.

REFERENCES

Al-Adthami, R. A. J., (2003), Applications of the Boundary Element Method to Soil Media Containing Cavities, M.Sc. thesis, University of Baghdad.

Banerjee, P. K., (1994), The Boundary Element Method in Engineering, McGraw – Hill (UK), London.

Brady, B. H. G. and Bray, J. W., (1978a), The Boundary Element Method for Elastic Analysis of Tabular Orebody Extraction Assuming Complete Plane Strain, International Journal of Rock Mechanics, Mineralogical Science in Geomechanics, Vol. 15, PP. 29 - 37.

Brady, B. H. G. and Bray, J. W., (1978b), The Boundary Element Method for Determining Stresses and Displacements around Long Opening in a Triaxial Stress Field, International Journal of Rock Mechanics, Mineralogical Science in Geomechanics, Vol. 15, PP. 21-28.

Brebbia, C. A., (1984), Boundary Elements VI, Proceedings of the sixth Internation Conference, On Board the Linear, the Queen Elizabeth 2, Springer-Verlag..

Desai, C. S. and Siriwardane, H. J., (1984), Constitutive Laws for Engineering Materials with Emphasis on Geologic Materials, Prentice-Hall, Inc., Englewood Cliffs, N.

El-Zafrany, A., (1992), Techniques of the Boundary Element Method, Ellis Horwood, New York.

Fung, Y. C., (1965), Foundations of Solid Mechanics, Prentice-Hall, Inc., Englewood, Cliffs.

Little, R. W., (1973), Elasticity, Prentice Hall, Englewood Cliffs, New Jersey.

Venturini, W. S. and Brebbia, C. A., (1981), The Boundary Element Method for the Solution of No – Tension Materials, Boundary Element Method, Proceeding of the 3rd International Seminar Irvine, California, edited by Brebbia C. A., pp. 371-390, Springer, Verlage, Berlin.

Note: The superscript (**) refers to a reference cited by Brebbia (1984).

EFFECT OF HARMONICS ON A SOLID-ROTOR INDUCTION MOTOR

Asst. Prof. Dr. Ali M. Saleh **Ahmed Th. Radhi**
College of Engineering University of Baghdad

ABSTRACT
The paper records a study of an investigating the performance of a solid-rotor induction motor with a rectilinear inverter excitation to identify the effects of the associated time harmonics. The performance is determined experimentally by using a stator of a three-phase laboratory induction motor that is fitted with a solid-steel rotor and compared with the theoretical model developed which uses the Fourier components of the supply voltage waveform. Final conclusions are drawn from comparing motor performances with sinusoidal and inverter excitations. An equivalent circuit model is developed to determine the harmonic currents. The development of the theoretical model make use of the results of existing field analyses. Harmonic currents and other performance details including the possible interactions between the co-existing harmonics are determined and discussed. The measured values of torque, input current and power over full speed range with the two types of excitation are presented, and compared with the theoretical values. The waveforms of current, phase and line voltages are analyzed experimentally and compared with simulation results. The theoretical results correlate well with measured results and the significant harmonic effects are identified.

الخلاصة
: تسجل هذه الأطروحة دراسة لبحث أداء المحرك الحثي من النوع ذو الدوار الصلب (Solid-Rotor) بتغذيته من خلال فولتية العاكس للتعرف على التأثير المرافق للتوافقيات الموجودة ضمن فولتية العاكس. لقد تم استنتاج الأداء عمليا باستخدام محرك حثي الجزء الثابت له يعمل مع دوار من نوع الصلب وقورن مع النموذج النظري الذي تم باستخدام مركبات فورير (Fourier Components) لموجة فولتية العاكس. الاستنتاجات النهائية قد تمت بمقارنة أداء المحرك باستخدام فولتية جيبيه وفولتية العاكس. لقد تم تطوير نموذج للدائرة المكافئة لإيجاد تيارات التوافقيات. أن تطوير هذا النموذج النظري تم باستخدام نتائج تحليل المجالات في الدوار الصلب. تيارات التوافقيات وتفاصيل أداء المحرك بما يشمل التداخلات المحتملة بين التوافقيات المتولدة سوية تم استنتاجها ومناقشتها. القراءات المقاسة لكل من التيار والعزم والقدرة على كل مدى السرعة ولكلا النوعين من التغذية، قد تم عرضها وقورنت مع النتائج والقيم النظرية. موجة التيار وموجة فولتية الطور والخط تم تحليلها مختبريا وقورنت مع النتائج النظرية. النتائج النظرية اتفقت بشكل جيد مع القيم العملية وتم تحديد التأثيرات الأكثر أهمية لهذه التوافقيات.

KEY WORDS
Harmonics, induction motor

INTRODUCTION

The most elementary type of rotor used in induction motors is the solid-steel rotor, which offers advantages in ease of manufacture, mechanically rigid and having good thermal properties. These features have made them attractive proposals to replace conventional rotors of induction motors, at least in some particular design and applications, and particularly for high-speed applications such as (20000-200000) rpm. The solid-rotor motor have high starting torque with low starting current, high rotor mass to absorb heat during repetitive starts, and a wide range of speed control for a narrow range of voltage variation. Many attempts have been made at improving their performance. Early attempts rely on using a soft-iron rotor with copper end plates [I. Woolley, 1973], to reduce the effective rotor resistance and achieve the desired torque. New attempts use different approaches of using composite rotor constructions [J. Saari, 1998, D. Gerling, 2000].

The development of static switching devices with high power ratings is leading to their continuously increasing application in the control of electrical machines. The static Inverters started replacing the old rotary converters. Inverters operation is based on the switching techniques. Therefore, their output is a nonsinusoidal voltage waveform. Fourier analysis show that inverter waveform contains many harmonics, when compared with old rotary converters. The solid-rotor motor has a significant advantage over conventional cage-rotor motors, when used in conjunction with solid-state drives [Leo A. Finzi, 1968]. Its rotor impedance have a numerical value which depends strongly on the magnitude of the voltage applied to the stator terminals for any given frequency [Leo A. Finzi, 1968]. The output voltage and current waveforms of the inverter are rich in harmonics, and these harmonics may have adverse effects on the motor performance. Harmonics can be a source of trouble in induction motors, producing extra losses and noise. The orders and magnitudes of the current harmonics which are present in the converter output depend on the design of the static converter and on the type of load, and are usually amenable to analysis by Fourier series.

The performance of induction motors operating on a nonsinusoidal voltage can be analyzed using different approaches. Among these are the equivalent circuit approach [G. C. Jain, 1964, B. J. Chalmers, 1968, A. M, 2001], the generalized machine theory approach and the multi-reference frame approach. The last two approaches yield time domain results making them convenient for analyzing the dynamic performance of induction motors [A. M, 2001]. Since the work presented in this paper deals with the steady-state performance, the equivalent circuit approach is adopted through out the presented work to comply with the Fourier analysis approach.

THEORY AND MODELING OF A SOLID-ROTOR INDUCTION MOTOR

A solid-rotor induction motor operates according to the same principles of operation as a conventional induction motor. The performance of such a motor is characterized by the nature of the interaction between the air-gap revolving field and the eddy currents induced in the solid-rotor, which develop the electromagnetic torque.

It is necessary to evaluate the impedance of the solid- rotor, both in phase and magnitude, to predict the behaviour of the motor under load conditions. The main difficulty in deriving an expression for this impedance arises from the extremely nonlinear magnetisation characteristic of the steel material. Many different approaches have been adopted to the calculation of eddy current loss in unlaminated magnetic materials aiming to develop an equivalent rotor impedance to be included in the parameters of motor equivalent circuit.

Early attempts are based on the assumption of material constant permeability, i.e. they considered the rotor as a linear medium. More realistic attempts used non-linear approximations to fit the magnetising curve, such as a limiting non-linear rectangular approximation. The limiting non-linear method is well established and its result agrees well with practical measurements. It is simple to use, and widely-accepted since the magnetising force at the surface of the solid-rotor is usually high enough to drive the rotor material well into saturation. Both the non-linear and linear models has found application in the modeling of a solid-rotor machines.

SOLID-ROTOR MOTOR WITH SINE-WAVE SUPPLY

In the solid-rotor motor, the mechanism of flux penetration into the magnetic material depends greatly on the magnetic nonlinearity of the iron. Hence it is desirable to think in terms of equivalent circuit, it is recognized that the rotor circuit parameters have a peculiar property that for any given frequency, their numerical values depend strongly on the magnitude of the voltage applied to the stator terminals. To determine the rotor losses and torque of an induction machine with a solid-steel rotor, results of the approximate theory based on an rectangular B-H characteristic for steel material (which has been successfully used for a very wide range of applications which is called the limiting non-linear theory) is used in dealing with the fundamental voltage component as well as sine-wave supply.

The flux penetration into solid steel considers that the flux density within the steel may exist only at a magnitude equal to a saturation level $\pm B_s$. Thus for a given ϕ, as approximately occurs with a constant applied voltage, δ is constant and is independent on rotor frequency [B. J. Chalmers, 1984]. Using the limiting non-linear representation in the analysis of solid-rotor yield an expression for the equivalent rotor impedance referred to the stator [B. J. Chalmers, 1984, -1972- 1980-1982], the rotor phase angle is given by this analysis as 26.6°. Impedance expression is found upon analysis of the eddy-current losses at slip frequency in the solid rotor. The general form of the expression of rotor impedance is given in eq. (1)

$$Z_{2f}=\left(\frac{AmL^2N^2\rho B_s}{K_e D\phi s}\right)\angle\theta_2 \qquad (1)$$

Where

L: Rotor length

m: Number of stator phases.

N: Effective number of stator turn per phase.

ρ: Rotor resistivity.

B_s: Saturation flux density of the rotor material.

K_e: End effect factor [1].

D: Rotor diameter.

s: Slip

A and the phase angle θ_2 are constants.

The value of A is ($\frac{1280}{9\pi^3}$) and θ_2 is 26.6°. In practice the empirical adjustment of θ_2 to 30°, slightly above the value of 26.6°, gives consistently good correlation with practical results for a wide range of design [B. J. Chalmers, 1984, A. M. Saleh, 1985]. The variable quantities in eq. (1) are the slip s and the flux per pole ϕ, which is dependent on the air-gap voltage and this, in turn, varies with stator current owing to the presence of series stator impedance [B. J. Chalmers, 1972]. It is seen that Z_{2f} is inversely proportional to the product of flux and slip and this arises from the effect of the magnetic non-linearity of the rotor material. For an induction machine with uniform air-gap flux the rotor impedance at the fundamental supply frequency can be expressed in terms of the air-gap voltage, E, [A. M. Saleh, 1985] as below

$$Z_{2f}=\left(\frac{AmL^2N^3\rho B_s f}{K_e DEs}\right)\angle\theta_2 \tag{2}$$

Equivalent Circuit

The equivalent circuit of the polyphase induction motor with a solid-rotor, resulting from the treatment mentioned above, is shown in **Fig.(1)**, where r_1 and x_1 represent the stator winding resistance and leakage reactance, x_m represent the magnetizng reactance and Z_{2f} is the rotor equivalent impedance referred to the stator at the fundamental supply frequency eq. (2), the core losses is neglected. So far the circuit appears to have the same configuration as the familiar equivalent circuit of conventional polyphase induction motors.

The equivalent impedance per phase is given by

$$Z=Z_1+Z_m Z_{2f}/(Z_m+Z_{2f}) \tag{3}$$

Where $Z_1=r_1+jx_1$,
$Z_m=jx_m$

The input power to the rotor per phase is given by

$$P_2=I_2^2 R_{2f} \tag{4}$$

Where R_{2f} is the rotor resistance referred to stator (i.e. is the real part of Z_{2f}).
The rotor loss is (s P_2), then the developed gross output power per phase is

$$P=(1-s) P_2 \tag{5}$$

The developed total torque is

$$T_1=3P/w_r \tag{6}$$

But, $w_r=(1-s)\, w_s$, then

$$T_1=3P_2 / w_s = 3I_2^2 R_{2f} / w_s \tag{7}$$

Where w_s is the synchronous speed of the stator field in rad/sec.

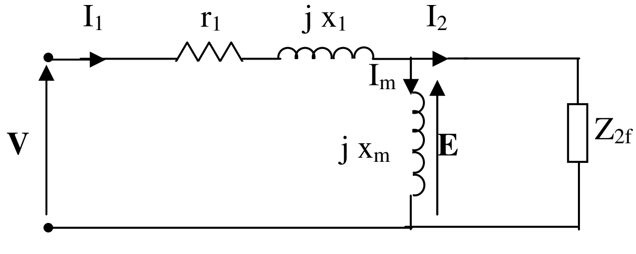

Fig. 1 Equivalent Circuit Per Phase

HARMONIC ANALYSIS OF 3-PHASE INVERTER

The application of symmetrical, nonsinusoidal three-phase voltages of constant periodicity to the motor terminals results in symmetrical nonsinusoidal three-phase motor currents. These currents may be thought to consist of a fundamental component plus higher time harmonics [Muhammad H. , 1993].
The waveform of inverter voltage depends upon the type of converter and the period of conduction of thyristors. It is rectangular or stepped waveform for 180° thyristor conduction angle. For a pulse width modulated inverter, output voltage waveform is a pulsed wave depending upon the method of modulation. The nonsinusoidal input wave is resolved into Fourier series. The behaviour of the machine is obtained by superposing the effects of fundamental and harmonics. This method provides informations about individual harmonic behaviour which reflect a guide to the inverter design.

Fourier Steady-State Analysis

The output voltage waveform of a three-phase inverter feeding a three-phase induction motor depends on the conduction period of the switching elements. The output waveform of the inverter is, however, periodic and can be analyzed using Fourier series. For symmetrical waveforms (the positive half cycle is the same as the negative half cycle) there will be no even order harmonics (i.e. 2,4,6,..etc.). Hence, by using Fourier series and according to the waveform shown in Appendix [A], the only orders of harmonics that can be affect machine performance are

$$n=6k \pm 1 \qquad (8)$$

Where k=1,2,3,…etc.
According to the Appendix [A], the expression for the phase voltage, first phase, say v_a can be written as

$$v_a= \sum_{n=1,5,7,..}^{\infty} V_n \sin(nwt) \qquad (9)$$

Where the constant V_n is determined as shown in appendix [A] depending on the shape of the waveform under consideration.
The harmonic of order n=6k-1 (such as n=5,11,17,…etc.) travels in a direction opposite to that of the fundamental field with the same number of poles as the fundamental field, i.e., it rotates at a speed equal to ((6k-1) N_s) [6]. The harmonics of order n=6k+1 (such as n=7,13,19,…etc.) travels in the same direction as the fundamental at a speed equal to ((6k+1) N_s).
The eq. (8) can be written in a more convenient form to indicate the sequence of the harmonic, too, as:

$$n=1 \pm 6k \qquad (10)$$

Thus, the harmonic orders are -5,7,-11,13,…etc. The negative sign associated with the n^{th} harmonic represents a negative sequence harmonic order. Third harmonic voltages are in time phase, they form a zero-sequence voltages. They can not push a current in a star-connected stator windings with no neutral connection. All harmonics of order triple n will be zero-sequence, and therefore their effect will be negligible.
A time harmonic of order "n" results in a harmonic synchronous speed nN_s and if the machine is rotating at a speed N_r the n^{th} harmonic slip is given by

$$s_n= (nN_s \pm N_r) / nN_s \qquad (11)$$

The negative sign in eq. (11) refers to forward rotating fields, obtained with harmonic order 1,7,13,…etc., while the positive sign refers to backward rotating fields, obtained with harmonic order 5,11,17,…etc. In terms of fundamental frequency slip, the time harmonic slip is found to be

$s_n=(n \pm (1\text{-}s))/ n$ (12)

Hence the frequency of the n^{th} harmonic rotor current is

$f_{2n}=s_n\,(nf_1)=[n-(1-s)]\,f_1$ (13)

For normal operation of an induction machine, s is usually very small and s is much less than n-1 and therefore

$s_n=(n-1) / n$ (14)

and,

$f_{2n} =(n-1)\,f_1$ (15)

Assuming that the saturation effect is negligible, that may arise due to superimposing voltages of different frequencies [1988], the principle of superposition can be applied to determine the overall performance of the 3-phase induction motor. Superposition principle rely on the assumption of linear systems. Therefore, this method is subject to the limitation imposed by the superposition principle. However, for nonsinusoidal voltage waveform, the motor behaviour for the fundamental is, as well as for individual harmonics are, determined independently and the net performance is assumed to be the sum of the contributions of each harmonic of the voltage waveform. The equivalent circuit of the induction motor is used in the analysis and the behaviour of the motor for each harmonic voltage is obtained by modifying the equivalent circuit for the harmonic under consideration. Thus a series of independent equivalent circuits (one for each harmonic) are used to calculate the complete steady state behaviour of the motor. The lack in the superposition principles is overcome by considering the possible interaction between field components which are present in the machine.

INVERTER FED SOLID-ROTOR MOTOR

An alternating magnetic field induces eddy currents in the material of iron cores. The eddy currents oppose the change of the flux, thus the magnetic field and flux can only penetrate to a certain depth within the magnetic material. The inner part of the material is left without flux. The depth of flux penetration is defined as the distance from a surface of a conductive material plane where an amplitude of an electromagnetic incident wave penetrating into the magnetic material [J. Lahteenmaki, 2002]. As the harmonic flux penetration into the rotor material is relatively small, the rotor is therefore assumed to have a constant permeability equal to the computed value at the rotor surface, and the surface impedance may be evaluated for each harmonic [D. O'Kelly, 1976]. The small harmonic flux component (of high frequency) is considered superimposed upon the larger fundamental component of flux. Results of the linear electromagnetic representation of the B-H curve is used in the analysis of a solid-rotor motor with nonsinusoidal supply. This method yields the classical depth of penetration which is dependent upon rotor angular frequency. The linear representation of the B-H characteristic of rotor steel, obviously, assumes a constant permeability, μ (i.e., B= μ H).

The assumption of linear magnetic material is non-realistic and this analysis is rarely used. However, it is widely used to treat cases of superimposed flux components rotating at different frequencies [B. J. Chalmers, A. M. Saleh, 1980-1982-1985]. The rotor impedance referred to the stator according to this method of analysis may be presented for each harmonic order under consideration as given below

$$Z_{2n} = \left(\frac{4\sqrt{2}mN^2L}{\sqrt{\pi}DK_e}\right)\left(\frac{\mu_\circ\mu_r\rho f_n}{s_n}\right)^{1/2}\angle 45^\circ \qquad (16)$$

Where $f_n =nf_1$,

and,
$s_n = n \pm (1-s)/n$

This expression with a value of a phase angle of 45^o and with a value of constant incremental permeability μ_r of 43 is used in the analysis of this study. Reference [10] gave a table with values of μ_r for different sizes of machines and ranges of electromotive forces, derived from tests carried out on rotor materials. The use of a constant value of μ_r of 43 was found acceptable during the experimental test over a wide range of positive and negative sequence field intensities [B. J. Chalmers, 1984, A.M. Saleh, 1985].

Harmonic Equivalent Circuit

The fundamental frequency equivalent circuit shown in **Fig. (1)** must be modified to take into account the harmonic frequencies. This can be achieved by introducing the following changes [B. J. Chalmers, 1977, A.M. Saleh, 2001]:

i- all reactances have a value of "n" times their value at the fundamental frequency f_1,
ii- the operating slip is the harmonic slip s_n.

The equivalent circuit of a solid-rotor induction motor with nonsinusoidal voltage supply appears to have the same configuration as the familiar equivalent circuit of a conventional induction motor under the same supply voltage as shown in **Fig. (2)**. The only difference is in the expression of the rotor impedance referred to the stator for harmonic orders under consideration as given in eq. (16) above.

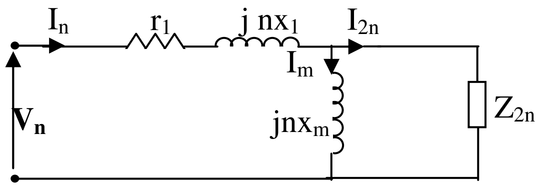

Fig. 2 Harmonic Equivalent Circuit Per Phase.

PRINCIPAL EFFECTS OF HARMONICS

The additional losses due to the presence of harmonic may be high if the supply waveform have large harmonic contents. These losses result from the increase in magnetic and ohmic losses. Magnetic losses are caused by harmonic main flux and harmonic leakage flux. Since rotor slip, s_n, is almost unity, stator harmonic current is reflected in the rotor and the resultant main harmonic flux is low. Magnetic loss in metallic parts caused by harmonic leakage flux is difficult to estimate [A.M. Saleh, 1985]. It is believed that ignoring these losses can introduce negligible error, due to the low level harmonic fluxes. Therefore the magnetic loss increase is considered negligible and loss increase is attributed, mainly, to the copper loss.

Stator Copper Losses

The total rms value of harmonic currents is given by

$$I_h = \sqrt{\sum_{n=5,7,..}^{\infty} I_n^{\,2}} \qquad (17)$$

Where I_h=harmonic currents.

The rms value of the total current is

$$I = \sqrt{I_1^{\,2} + I_h^{\,2}} \qquad (18)$$

The additional stator copper losses are determined by adding the losses due to each harmonic. Therefore, the increase in the stator copper losses is ($I_h^2 r_1$) and the total copper losses per phase can be written as [G. C. Jain, 1964, B. J. Chalmers, 1977]

$$P_s=I_1^2 r_1+I_h^2 r_1=I^2 r_1 \tag{19}$$

The above equation describes the loss increase if the supply waveform have large harmonic contents. The additional losses owing to time-harmonic currents will increase the conductor heating due to higher current flow. In large machines and due to the skin effect the resistance of windings is subject to further increase, too. Higher the frequency, higher the resistance, so when harmonic current flows, the resistance associated with a given harmonic will get increased amplifying the copper loses and increasing the heating of the machine. This is not considered in the present work.

Rotor Losses

For a conventional cage-rotor induction motor, the rotor resistance variation due to skin effect must be taken into consideration and particularly for deep-bar rotor construction. The rotor loss for every harmonic can be determined. The losses due to each harmonic are added to get the total losses. Usually, these additional rotor losses form a large portion of additional losses in the induction motor operating on a nonsinusoidal voltage [B. J. Chalmers, 1977].

For a solid-rotor induction motor, the rotor resistance for each harmonic order can be determined and the losses due to each harmonic order are determined and added to get the total rotor losses as given by

$$P_r=I_2^2 s R_{2f} + \sum_{n=5,7,..}^{\infty} I_{2n}^2 s_n R_{2n} \tag{20}$$

Mean Developed Torque

Due to the nonsinusoidal air-gap flux and rotor current, a torque is developed for each harmonic component as happens with the fundamental component. The developed torques can act in the forward or in the backward direction depending on the harmonic order [Subrahmanyam, Vedam., 1988].

A unidirectional harmonic torque is generated by the interaction between an air-gap flux and a rotor current component of the same harmonic frequency. It is noted that the net effect of torque harmonics is usually too small in comparison to motor rated torque [W. Shepherd, 1998], as will be explained hereunder.

Each harmonic produces an air-gap power and this power corresponds to a harmonic torque T_n acting at a speed of nw_s (radians per second). Thus, the air-gap power per phase is

$$T_n nw_s=I_{2n}^2 R_{2n} \tag{21}$$

Where R_{2n} is the resistance of a solid-rotor referred to stator at the frequency of the harmonic under consideration.

This torque can be positive or negative depending on the order of the harmonic under consideration. The equivalent torque in synchronous watts per phase, referred to the fundamental frequency is given by

$$T_n= I_{2n}^2 R_{2n} /n \tag{22}$$

For forward rotating fields of order 1,7,13,….etc., the torque is positive and for reverse rotating fields of order 5,11,17,….etc., the torque is negative. The net developed torque due to fundamental and harmonic currents are

$$T=T_1 \pm \sum_{n=5,7,....}^{\infty} T_n \qquad (23)$$

Where T_1 is the fundamental torque.
The positive sign refers to the torque of a harmonic order in the same direction of fundamental torque (i.e., n=7,13,19,…) and the negative sign refers to the torque of a harmonic order in the reverse direction of fundamental torque (i.e., n=5,11,17,…). Although, the net harmonic torques are acting against the fundamental one, it is clear that T_n is very small and the most significant torque reduction arises from the low order harmonics (i.e., 5^{th} and 7^{th}).

Torque Pulsation

The fundamental useful steady state torque is developed by the interaction between the fundamental stator air-gap flux and the rotor current. This is a steady constant torque i.e., it does not pulsate in magnitude. However, it is superimposed by the parasitic torques which may be either steady or pulsating torques. Steady torques are due to interaction of air-gap flux and rotor current belonging to the same harmonic. As explained in the previous section, a fifth order harmonic produce braking torque as their direction of rotation is opposite to that of the fundamental. A seventh order harmonic produce a motoring torque as their rotation is in the forward direction. In addition to the unidirectional harmonic torques, a pulsating torque is developed due to interaction between air-gap flux and rotor current belonging to different harmonics.

This pulsating torque whose frequency is the difference between the frequencies under consideration [A. M. Saleh, 2001]. For example, the pulsating torque pulsating at $6f_1$ is generated when fundamental flux reacts with either fifth or seventh harmonic rotor currents. The result is a torque pulsation of six times the fundamental frequency superimposed on the steady-state unidirectional torque [W. Shepherd, 1998].

Table (1) summarises the possible interaction of harmonics with each other and the frequency or the direction of the resulting torque. The interaction can be denoted by flux (or magnetizing current) and rotor current [A. M. Saleh, 2001]. All harmonics co-exist and the following torques, up to the seventh harmonic, are generated by the interactions between their fluxes and currents: -

a)I_m I_2 : the fundamental torque.
b)I_{m5} I_{25} and I_{m7} I_{27} : the torque of each harmonic current.
c)I_m I_{25} and I_m I_{27} : torque of harmonic currents and fundamental flux.
d)I_{m5} I_2 and I_{m7} I_2 : torque of fundamental current and harmonic fluxes.
e)I_{m5} I_{27} and I_{m7} I_{25} : torque of harmonic currents and fluxes.

The torques in (a) and (b) are steady torque and non-pulsating and have been covered in previous sections. Since I_{m5} and I_{m7} are very small, and the most significant pulsation of torque is resulting from the interaction between fundamental flux and harmonics currents, that in (c) above, and the torque in (d) and (e) are of negligible importance. For the fundamental component, the air-gap power is equal to the developed mechanical power which can be expressed as torque in (Newton-meters) acting at the synchronous speed. Thus, the torque per phase is given by

$$T_1 = E_1 I_2 \cos\Phi / w_s \qquad (24)$$

Where Φ is the phase angle between the air-gap voltage E_1 and rotor current I_2 and with solid-rotor its value is 30°, and $w_s=2\pi f_1/p=w_1/p$ where p is the number of pole pairs, then $w_s=w_1/p$.
E_1 is given by

$E_1=jI_mx_m=jI_mL_mw_1$ (25)

Where I_m is the magnetizing current and L_m is the magnetizing inductance.
From the phasor diagram shown in **Fig. (3)**, $\theta = 60^\circ$ and one can show that ($I_2 \cos\Phi = I_2 \sin\theta$), therefore,

$T_1=0.866p\, I_mL_mI_2$ (26)

Fig. (4) shows the phasor diagram of a harmonic, and from this phasor diagram the harmonic torque per phase is given by

$T_n=pI_{mn}\, L_mI_{2n} \cos\Phi_n = pI_{mn}\, L_mI_{2n} \sin\theta_n$ (27)

Where $\Phi_n=\theta_n=45^\circ$. Therefore,

$T_n=0.707pI_{mn}\, L_mI_{2n}$ (28)

From the combined phasor diagram shown in **Fig. (5)** the varying torque is

$T_v=I_mL_mp\, (I_{25} \sin(\theta_5 -45^\circ) + I_{27} \sin(\theta_7 +45^\circ))$ (29)

with $\theta_5=\alpha-6wt$

$\theta_7=\gamma+6wt$

Where α and γ are the values of θ_5 and θ_7 at wt=0. For any square symmetrical waveform $\alpha=\gamma=0$ or π [7]. Thus,

$T_v=I_mL_mp\, (I_{27} \sin(6wt+45^\circ) - I_{25} \sin(6wt+45^\circ))$ (30)

Since $I_mL_m=E_1/w_1$, then,

$T_v=(E_1/w_1)p(I_{27} - I_{25}) \sin(6wt+45^\circ)$ (31)

For a conventional induction motor, the torque pulsation can be expressed as [A. M. Saleh, 2001]

$T_v=(E_1/w_1)p(I_{27} - I_{25}) \sin(6wt)$ (32)

This expression is the same as that in solid-rotor induction motor as given by eq. (31). The only difference from solid-rotor is the phase shift of (45°) in torque waveform. Therefore, this torque pulsate at six times the supply frequency. In the absence of 5th and 7th harmonics, the 11th and 13th harmonics give pulsation at twelve times the supply frequency. The motor torque pulsation can be made smaller by increasing the magnetizing inductance, and by reducing the direct-current ripple when the motor is on no-load [G. K. Creightion, 1980]. It might be possible to reduce the torque pulsations by lowering the ripple current with a high-frequency dc link chopper [G. K. Creightion, 1980].
The self-reactance of the induction motor have great influence on the amplitude of torque pulsation. An external reactance can be added to a low reactance machines to reduce the torque pulsation [A. M. Saleh, 2001]. However, this may effect the fundamental torque and it is applicable to small machine of low output torque. The main effect of torque pulsation result from the low order harmonic. Usually the lower pulsating frequency is much higher than the natural frequency of the

mechanical system composed of the rotor and the coupled load. The high inertia of the rotating part can damp out these oscillation at the shaft at normal running speeds. However, for wide range variable speed drives an analysis of the mechanical resonance speeds is necessary to avoid damages due to possible amplification of pulsating torque at resonance.

Table (1) Reaction of Stator and Rotor Harmonics

Stator Harmonic	Rotor Harmonic	Nature of Torque	Direction or Frequency of pulsation
1	1	Steady	Forward
1	5^{th}	Pulsating	$6f_1$
1	7^{th}	Pulsating	$6f_1$
1	11^{th}	Pulsating	$12f_1$
1	13^{th}	Pulsating	$12f_1$
5^{th}	1	Pulsating	$6f_1$
5^{th}	5^{th}	Steady	Backward
5^{th}	7^{th}	Pulsating	$12f_1$
5^{th}	11^{th}	Pulsating	$6f_1$
5^{th}	13^{th}	Pulsating	$18f_1$
7^{th}	1	Pulsating	$6f_1$
7^{th}	5^{th}	Pulsating	$12f_1$
7^{th}	7^{th}	Steady	Forward
7^{th}	11^{th}	Pulsating	$18f_1$
7^{th}	13^{th}	Pulsating	$6f_1$
11^{th}	1	Pulsating	$12f_1$
11^{th}	5^{th}	Pulsating	$6f_1$
11^{th}	7^{th}	Pulsating	$18f_1$
11^{th}	11^{th}	Steady	Backward
11^{th}	13^{th}	Pulsating	$24f_1$

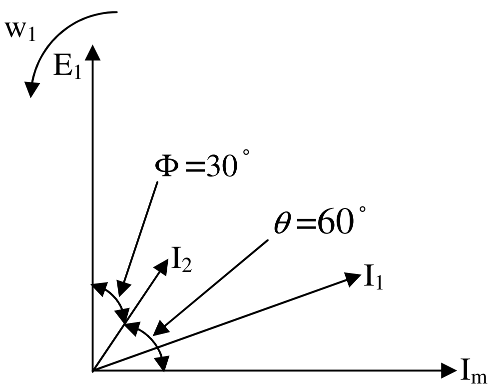

Fig. (3) Fundamental Phasor Diagram

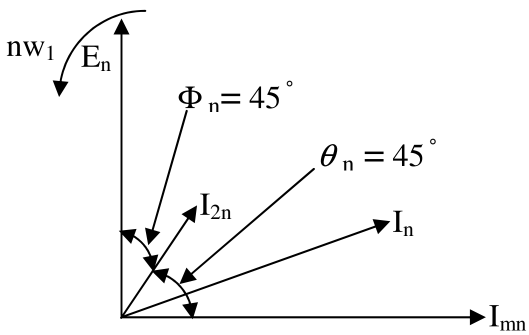

Fig. (4) Harmonic Phasor Diagram

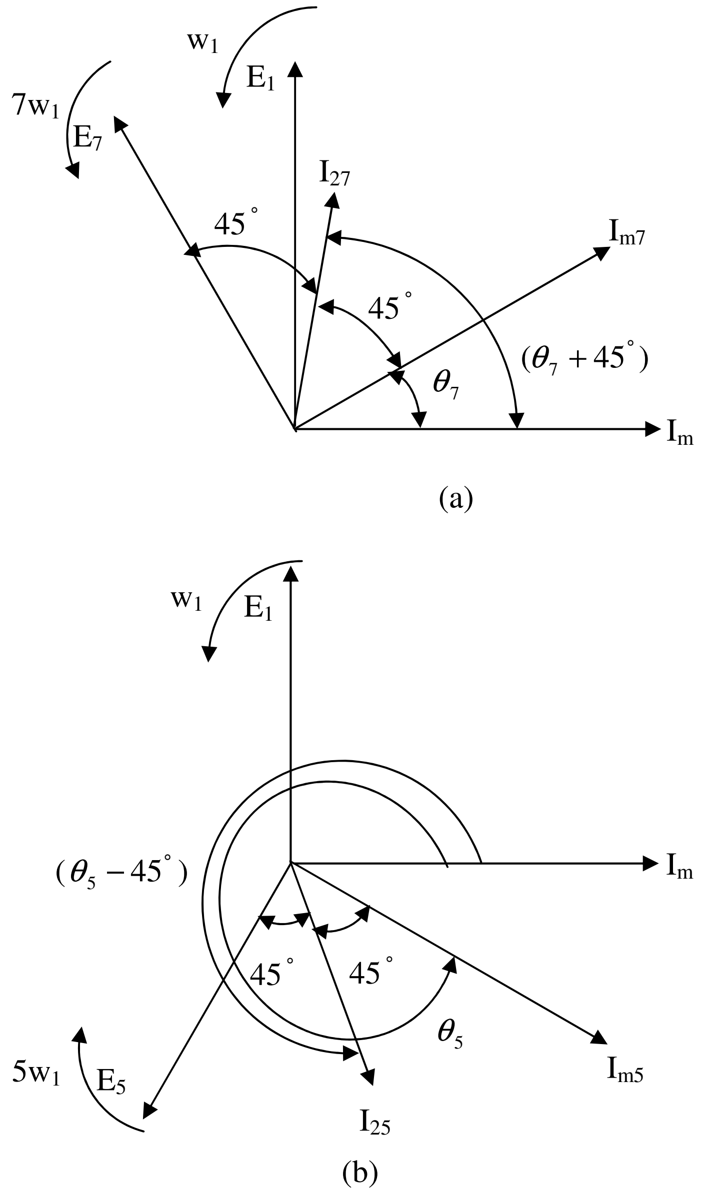

Fig. (5) Combined Phasor Diagram
(a) Fundamental and 7th harmonic
(b) Fundamental and 5th harmonic

SIMULATION AND EXPERIMENTAL RESULTS

The induction motor used in simulation and in the experimental tests has the following characteristics: a three-phase induction motor with a conventional stator wounded with a four-pole three-phase windings. Fitted with a solid-steel rotor. The parameters of this motor were identified through the necessary tests. The parameters are given with operating motor data in appendix [B].

The three-phase induction motor was studied under nominal load for two different source conditions: i) sinusoidal and balanced three-phase supply. ii) Variable frequency inverter at 50Hz. The motor performance was calculated by computer simulation and found experimentally in the laboratory for the two conditions.

The three-phase motor with solid-rotor was tested with a sinusoidal supply at rated voltage and frequency. The calculated and measured stator input current as a function of slip is shown in **Fig. (6)**. It is clear that the calculated and experimental results are in a close agreement.
Torque/slip curve is given in **Fig. (7)** for the motor tested in the motoring condition. Experimental points are also shown in this figure. The measured torque, at a given slip, is in general less than the corresponding calculated values by not more than 4.1%. This is caused by neglecting the friction, windage (i.e. the mechanical losses) and surface losses in the simulation analysis.
The input power / slip curve is shown in **Fig. (8)**. This figure shows that the measured points at small values of slip are higher than the calculated points by an average error percent of 3.87%. This is owing to ignorance of the stator core losses in the simulation program and might be due to an error in wattmeter readings. **Fig. (9)** and **Fig. (10)** show oscillograms of phase and line voltage waveform of laboratory inverter with its wave analyzer result. This laboratory inverter is used to drive the solid-rotor motor in laboratory work with a square wave supply voltage at 50Hz whose fundamental voltage component equal to rated sinusoidal value.

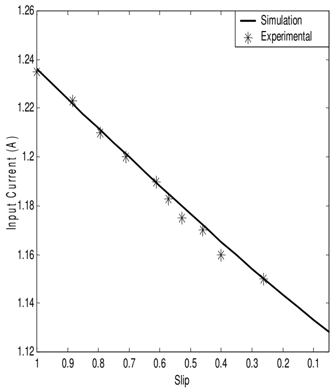

Fig. (6) Input Current versus Slip

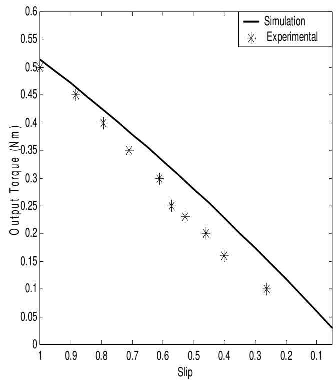

Fig. (7) Output Torque versus Slip

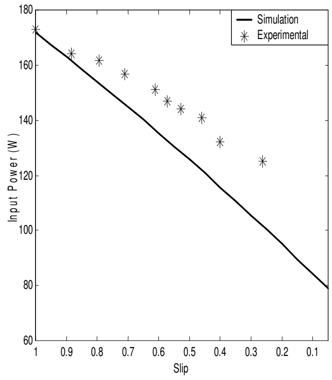

Fig. (8) Input Power versus Slip

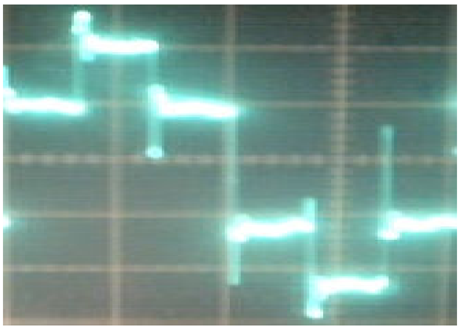
(a)

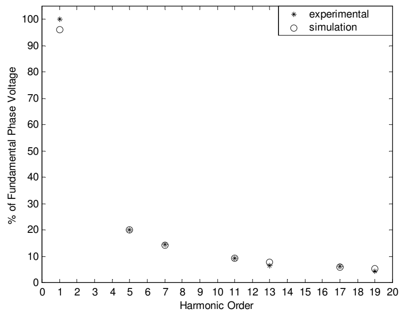

(b)

Fig. (9) Inverter phase voltage a) Experimental Waveform
(50 v/div, 5ms/div) b) Results of Wave analyzer

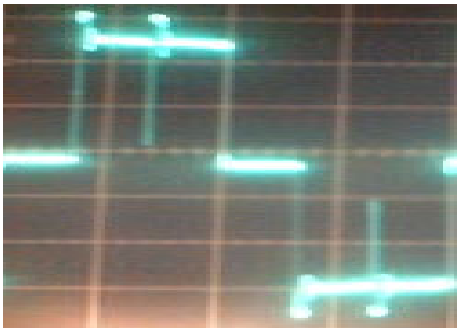

(a)

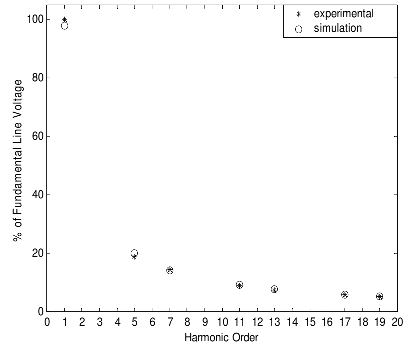

(b)

Fig. (10) Inverter line voltage
a) Experimental Waveform (50 v/div, 5ms/div)
b) Results of Wave analyzer

Fig. (11) show the simulation and measured stator input current as a function of slip of a solid-rotor motor fed by inverter. The Figure shows that the results are in good agreement. Torque /slip and input power curves are given in **Fig. (12)** and **Fig. (13)** respectively. The experimental torque measurement are lower than the calculated points by not more than 6.36%. This is caused by neglecting the friction, windage (i.e. the mechanical losses) and surface losses in the simulation analysis. The input power measured points are slightly greater than the calculated points at low slips by an average percent of error of 3.6%. This is owing to ignorance of the stator core losses in the simulation program and might be due to an error in wattmeter readings.
The simulation and experimental graphs of phase current of a solid-rotor motor with its wave analyzer for light load slip value of 0.263 obtained from the experimental machine and at standstill slip value of 1 are presented respectively in **Fig. (14)** to **Fig. (15)**. In the case of computer simulated current the results in the simulation are obtained considering up to 25th harmonic order. **Table (2)** shows the simulation and experimental DF and THD of the phase current calculated and measured up to 19th harmonic order. It is seen that, the DF results are in good agreement, while THD experimental results differ slightly by 13.2% from the calculated results. It is seen that, the DF and THD results are seems to be the same for the three slip values given in the table.

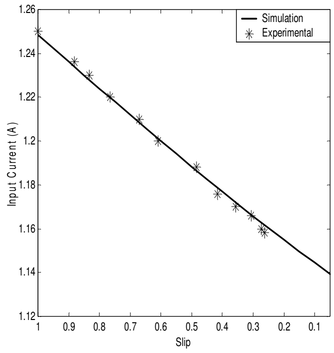

Fig. (11) Input Current versus Slip

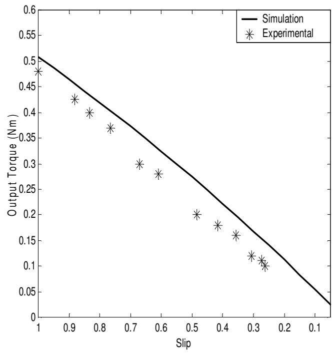

Fig. (12) Output Torque versus Slip

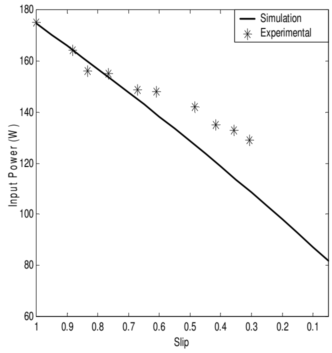

Fig. (13) Input Power versus Slip

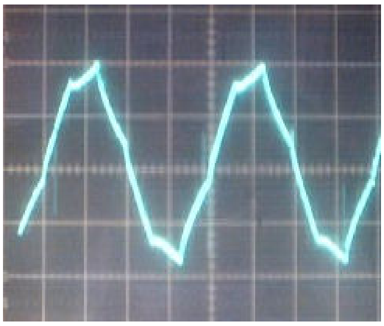

(a)

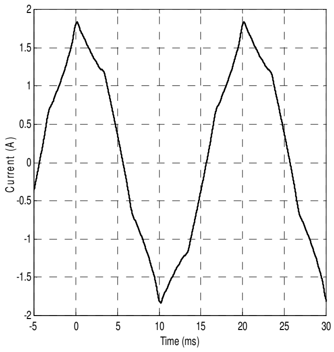

(b)

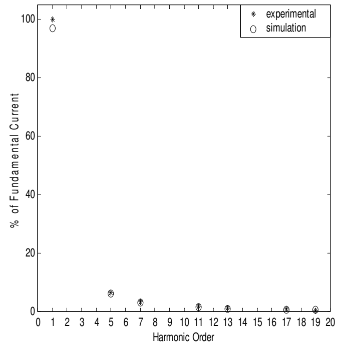

(c)

Fig. (14) Solid-Rotor Motor Phase Current at s=0.263
a) Experimental Waveform (1 A/div, 5ms/div)
b) Simulation Waveform
c) Results of Wave analyzer

(a)

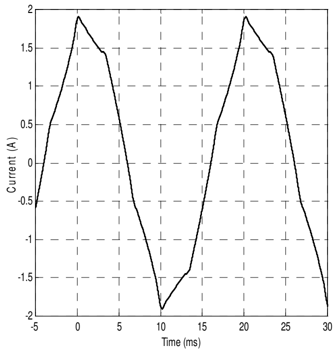

(b)

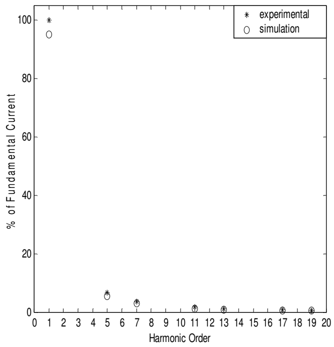

(c)

Fig. (15) Solid-Rotor Motor Phase Current at s=1
a) Experimental Waveform (2 A/div, 5ms/div)
b) Simulation Waveform
c) Results of Wave analyzer

Table (2) DF and THD of a Solid-Rotor Motor Current

Slip	Simulation		Experimental	
	DF(%)	THD(%)	DF(%)	THD(%)
0.263	99.7488	7.1	99.712	7.6
0.51	99.755	7.01	99.63	8.625
1	99.787	7	99.668	8.167

CONCLUSIONS

The most pronounce effect of harmonic voltages and currents on the induction motor is the increased heating due to the additional losses, mainly the copper losses associated with the harmonic currents. The increase in the input power of the motor due to the presence of harmonic is mainly consumed in the motor as losses forming an additional source of heat. The extra losses are dissipated within the stator and rotor of the machine. The loss increase due to presence of harmonics can consequently reduce the developed torque, due to temperature rise. The additional temperature rise increases stator and rotor resistance. Increases in these resistances reduce the fundamental torque of the machine. As a result, the overall efficiency of machine decreases as a consequence of the increase in losses. A solution to this problem could be the filtering of such harmonics at the inverter load. The steady harmonic torques are acting against each other and, at least for the machine under test, their net torque is small. The net harmonic torque is acting against the fundamental torque. The main effects of the harmonics on the operation of motors result from the low harmonics order. The harmonic content of the current depends upon the motor slip. It depends, to great extent, on the leakage reactance of the motor. A larger leakage reactance reduces the harmonic content of the current. The pulsating torques are produced by the interaction of the air-gap flux components (the fundamental flux and harmonic flux components) and rotor harmonic currents. The main torque pulsation result from the interaction between the low order rotor harmonic currents. The peak values of torque pulsation due to the low order harmonic frequency (i.e. 5^{th} and 7^{th}) is negligibly small for the motor under test. The pulsation reduces very greatly with increase of harmonic frequencies, since motor will have to withstand the pulsatio.. The calculated and measured results are in general in a close agreement for the two supplies conditions. The simulation and experimental DF results of a solid-rotor motor phase current are in good agreement. While, the THD experimental results differ by 13.2% from the calculated results. A solid-rotor motor has a lower input current than that of a conventional motor of the same frame size, when driven by inverter voltage supply. This is due to high rotor impedance of solid-rotor motor. Therefore, the stator losses are less than that in the case of conventional motor and the temperature rise of the motor is also less. As a result the efficiency of the solid-rotor motor is less sensitive than that of a cage-rotor motor with respect to supply type.

REFERENCES

I.Woolley and B.J. Chalmers; (1973), End Effects in Unlaminated-Rotor Induction Machines; Proc. IEE; vol.120; No.6; June.

J. Saari; (1998), Thermal Analysis of High-Speed Induction Machines; Dissertation for the degree of Doctor of Technology, Helsinki University, Finland;.

D. Gerling; (2000), Design an Induction Motor with Multilayer Rotor Structures and large gap; ICEM 2000, Finland; 28-30 August;; pp.458-461.

Leo A. Finzi and Derek A. Paice; (1968), Analysis of the Solid-Iron Rotor Induction Motor for Solid- State Speed Controls; IEEE Transaction on Power Apparatus and Systems; vol. PAS-87; No.2; February; p.590.

G.C. Jain; (1964), Effect of Voltage Waveshape on Performance of a 3-Phase Induction Motor; IEEE Trans.; PAS-83;; p.561.

B.J. Chalmers and B.R. Sarker; (1777), Induction Motor Losses due to Nonsinusoidal Supply Waveforms; Proc. IEE; vol.115; No.12; December 1968; p..

A.M. Saleh; (2001), Effects of Time Harmonics on Induction Gyromotors; IJCCCE; No.2; vol.2;; p.1.

B.J. Chalmers and A.M.Saleh; (1984), Analysis of Solid-Rotor Induction Machines; IEE Proc.; vol.131; No.1; pt.B; January.

B.J. Chalmers and I. Woolley; (1972), General Theory of Solid-Rotor Induction Machines; Proc. IEE; vol.119; No.9; September.

B.J. Chalmers and R.H. Abdel-Hamid; (1980), Parameters of Solid-Rotor Induction Machines with Unbalanced Supply; Proc. IEE; vol.127; No.3; Pt.B; May.

B.J. Chalmers; (1982), Application of Induction Machines with Solid-Steel Secondaries; Universities Power Engineering Conference UMIST Manchaster, England;.

B.J. Chalmers and A.M. Saleh; (1984), Single-Phase Capacitor-Run Induction Motors with Solid-Steel Rotor; Proceedings International Conferences on Electrical Machines, Lausanne Switzerland; pt.3; 18-21 September;.

A.M. Saleh; (1985), Analysis of Induction Machines with Unlaminated and Composite Secondaries; Ph.D. Thesis; University of Manchester;.

Muhammad H. Rashid; (1993), Power Elecronics; Prentice-Hall International, Inc,.

Subrahmanyam, Vedam; (1988), Thyristors Control of Electric Drives; Mc Graw-Hill: New Dellhi;.

J. Lahteenmaki; (2002), Design and Voltage Supply of High-Speed Induction Machines"; Dissertation for the degree of Doctor of Technology, Helsinki University, Finland;.

D.O'kelly; (1976), Theory and Performance of Solid-Rotor Induction and Hysteresis Machines; Proc. IEE; vol.123; No.5; May.

W.Shepherd and D.T.W. Liang; (1998), Power Electronics and Motor Control"; Cambridge University press,.

G.k. Creighton; (1980), Current-Source Inverter-fed Induction Motor Torque Pulsation; Proc. IEE; vol.127;pt.B; No.4; July.

Appendix [A]

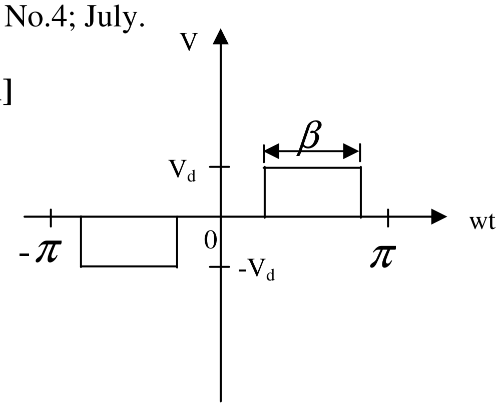

Fig. (A.1)

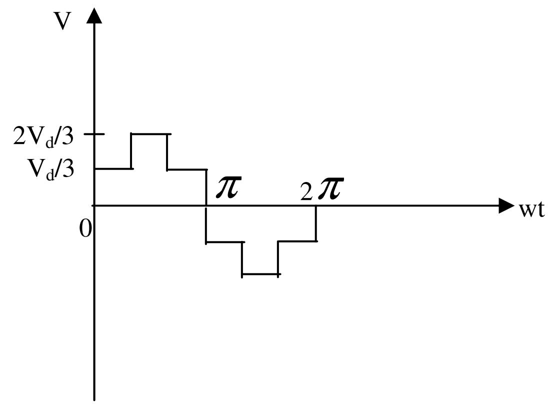

Fig. (A.2)

Consider the general form for square-wave shown in **Fig. (A.1)** where β represent conduction period.

$$v(wt)=\begin{cases} -V_d & -(\pi+\beta)/2<wt<-(\pi-\beta)/2 \\ 0 & -(\pi-\beta)/2<wt<(\pi-\beta)/2 \\ V_d & (\pi-\beta)/2<wt<(\pi+\beta)/2 \end{cases}$$

$V(-wt)=-V(wt)$ therefore $b_n=0$, i.e., no cosine term.
The function have symmetry about the x-axis therefore $a_0=0$.
$v(wt+\pi)=-v(wt)$ therefore $a_{2n}=0$

$$a_n=2V_d/\pi \int_{(\pi-\beta)/2}^{(\pi+\beta)/2} \sin(nwt)\, dwt$$

$$=-2V_d/n\pi\,[\cos n((\pi+\beta)/2)-\cos n((\pi-\beta)/2)]$$

$$=4V_d/n\pi\,[\sin n\beta/2.\sin n\pi/2]$$

For $\beta=180^\circ$,
$a_n= 4V_d/n\pi\,[\sin n\pi/2]^2$
and,

$$V=\sum_{n=1}^{\infty} 4V_d/n\pi \sin nwt$$

Let $4V_d/\pi=\sqrt{2}\,E_a$, then,

$$v=\sum_{n=1}^{\infty} \sqrt{2}\,E_a/n \sin nwt$$

Where E_a is the rms value of the fundamental component.
For $\beta=120^\circ$,
$a_n= 4V_d/n\pi\,[\sin n\pi/3]\,[\sin n\pi/2]$
$=2\sqrt{3}\,V_d/n\pi \sin m\, wt$
Where
$m=1\pm 6k$ for $k=1,2,3,\ldots,$etc.
$n= m *(-1)^{(m+3)/2}$
So if $\sqrt{2}\,E_a= 2\sqrt{3}\,V_d/\pi$, it follows that

$$v=\sqrt{2}\,E_a\,[\sin(wt)-1/5\sin(5wt)-1/7\sin(7wt)+1/11\sin(11wt)+1/13\sin(13wt)+\ldots\ldots]$$

Similarly, for the stepped-voltage waveform shown in **Fig. (A.2)**, which it is have the same properties of **Fig. (A.1)** and by applying Fourier analysis yields that: -

$$v=2V_d/\pi\,[\sin(wt)+1/5\sin(5wt)+1/7\sin(7wt)+1/11\sin(11wt)+1/13\sin(13wt)+\ldots\ldots]$$

or

$$v=\sum_{n=1}^{\infty} 2V_d/n\pi \sin(nwt)$$

Appendix [B]

Motor name plate

FB ELECTRICAL MACHINE TUTOR / ENGLAND

Type: EMT-180
Number of Poles, p: 4
Number of Phases, m: 3
Connection: Δ / Y
Power, W: 250
Voltage, V: 138/240
Frequency, Hz: 50
Current, A: 2.5
Per-phase parameters at 50 Hz obtained by Test : -

Stator data

Element	Value
Stator resistance per phase, r_1, Ω	19
Stator reactance per phase, x_1, Ω	24
Stator magnetizing reactance per phase, x_m, Ω (with solid-rotor)	98
Effective number of stator winding turns in series per phase, N	780

For Solid-Rotor

The experimental machine under test, it is the same type and rating of the experimental machine used in the test in the work presented in reference [10]. Therefore, the values of rotor saturation flux density, B_s, and rotor resistivity, ρ, used in the analysis of this work are the same that used in the reference [10] as given below:

B_s	1.8 W_b/m^2
ρ	22e-8 Ω.m

Rotor length and diameter are measured directly in the lab as given below:

L	0.034 m
D	0.1m

The value of End-effect factor (K_e), for the experimental rotor without end-plates is obtained from reference [1] as given below:

K_e	0.185

PRODUCTION OF GRAPHITE ELECTRODES BINDER FROM IRAQI ASPHALT

Abdul Halim A.K. Mohammed **Hussain K. Hussain** **Tariq M.Naief**

Chemical Engineering Department-College of Engineering
University of Baghdad-Iraq

ABSTRACT

Basrah crude oil Vacuum residue 773^+ K with specific gravity 1.107 and 4.87wt. % sulfur, was treated with hexane commercial fraction provided from Al-Taji Gas Company for preparing deasphaltened oil(DAO)suitable for hydrotreating process.

Deasphaltening was carried out with 1h mixing time, 10ml:1g solvent to oil ratio and at room temperature.

Hexane deasphaltened oil was hydrotreated on presulfied commercial Co-Mo/$\gamma - Al_2O_3$ catalyst in a trickle bed reactor. The hydrotreating process was carried out at temperature 660 K,LHSV 1.3 h^{-1}, H2/oil ratio 300 l/l and constant pressure of 4MPa.

The hydrotreated product was distillated under vacuum distillation unit. It is found that the mixture of 75% of vacuum residue with 25% anthracene satisfies with requirements for graphite electrodes binder.

الخلاصة

عومل المتبقي الفراغي لخام نفط البصرة ذو درجة غليان 773 كلفن ووزن نوعي 1.017 و4.87 نسبة وزنية كبريت بمقطع الهكسان التجاري الذي جهز من شركة تعبئة الغاز في التاجي لتحضير متبقي فراغي مفصول الاسفلتينيات مناسب لعملية الهدرجة.تم معاملة المتبقي الفراغي بالمذيب بزمن خلط 1ساعة ونسبة مذيب الى المتبقي غم 10:1 مل بدرجة حرارة الغرفة.

تم هدرجة المتبقي الذي عومل بالهكسان بوجود العامل المساعد Co-Mo/γ-Al2O3 الذي تم تحويله لصورة السلفايد في مفاعل ثلاثي الاطوار.تمت عملية الهدرجة بدرجة حرارة 660 كلفن وسرعة فراغية 1.3 ساعة $^{-1}$ ونسبة هيدروجين/المتبقي 300 لتر/لتر تحت ضغط 4 ميكاباسكال.

تم تقطير الناتج من عملية الهدرجة في وحدة التقطير الفراغي. لقد وجد ان خليط المتبقي الفراغي بنسبة 75% مع 25% من الانثراسين وافق متطلبات العجينة الرابطة لاقطاب الكرافيت.

KEY WORDS

Binder, graphite electrodes, asphalt, hydrotreating, deasphalting

INTRODUCTION

Graphite electrodes binders are the residues from petroleum refining for heavy oils,coal-tar pitches,

petroleum pitc hes, natural pitches, and the pyrolysis residues from heavy petroleum materials.These binders usually are solid and high viscous black materials, with low solubility in water but are dissolved in many organic solvents.The properties of graphite electrode binder depend on the nature of material obtained by vacuum distillation and its initial boiling point. Softening point, coke yield, sulfur content,BI and QI,are most important properties of the binder (Hatano 1989, Wagner1988).
It is well known that petroleum asphalt obtained by vacuum distillation of reduced crude oil used as basic component for binder production(Wagner1986).
Deasphalting and hydrotreating of the petroleum asphalt are the most important processes for binder production from heavy petroleum products.
Vacuum residue contained a fraction "asphaltenes" which has a particularly strong influence on the rate of HDS. Therefore,the deasphaltening process with low boiling liquid hydrocarbons for the vacuum residue before the hydrotreating process is very important, because of the most sulfur and metals could be removed with the precipitated asphaltenes.In order to obtain an acceptable level of sulfur and metals in deasphaltened oil,hydrodesulfurization should be applied(Gary (1994).
In this work,first attempt was carried out for obtaining a binder for graphite electrodes from high sulfur and metal content asphalt.Asphaltenes was separated from the vacuum residue by hexane solvent.The deasphaltened vacuum residue was hydrotreated,then ,binder was obtained by mixing the hydrotreated deasphaltened vacuum residue with anthracene.

EXPERIMENTAL WORK

Deasphaltening Unit

The deasphalting unit consists of three main stages as follows:

Mixing stage

The vacuum residue or asphalt was mixed with a light solvent in 2-neck glass flask.
The flask set on a magnetic stirrer and the mixing proceed by 12.5 mm magnetic bar. High efficiency condenser connected with upper neck of the flask for solvent recovery, this condenser already cooled by alcohol chiller at temperature of 256 K, the other neck fitted with the thermometer. The mixing carried out at room temperature with 1h mixing time and at 10ml:1g solvent to oil ratio.

Filtration and drying

The asphalt-solvent mixture introduced to the filtration process, where Buchner funnel (250 mm I.D) connected to the filtration flask fitted with filter paper for medium filtration speed. The filtration flask connected to a vacuum system includes a trap, condenser, and cooling machine. For removing of the remaining precipitate inside the mixing flask, washing solvent (hexane) was added and then filtrated. Then the filter paper placed in a hot electrical furnace (383 K) to evaporate the solvent associated with the precipitated asphaltenes for about 10 to 20 min. The dried filter paper then weighted to evaluate the percentage of asphaltenes yield.

Solvent recovery stage

The DAO-solvent mixture obtained from filtration stage introduced to a stripping stage in order to remove the solvent from the deasphaltened oil.

Hydrodesulfurization Unit

The desulfurization of deasphaltened oil was done in hydrotreating pilot plant continuous

high-pressure unit. Process flow diagram of the hydrodesulfurization unit employing a co-current up-flow. The unit consists of feed pump, reactor, high-pressure separator, and cooler.
The reactor used is a stainless steel with 19 mm inside diameter, 800 mm length and 3 mm wall thickness. The reactor supplied with 4 heaters (150 mm length for each) with 2 insulators (100 mm length). It was packed with 90 ml of the Co-Mo $/\gamma - Al_2O_3$ catalyst between two layers of inert glass balls. Catalyst presulfiding was made by passing commercial gas oil containing 0.6 vol.% Cs_2 through the catalyst bed. Firstly the catalyst treated for 3 h, at temperature 473 K, LHSV of 4 h^{-1} , pressure 2.2 MPa and no hydrogen flow. Then the operating conditions changed to 573 K, LHSV of 1 h^{-1}, pressure 2.2 MPa, H_2/oil 200 l/l and duration of experiment 16 hours. After that, the HDS run employed at reaction temperature 660 K with LHSV 1.3 h^{-1}. The gas flow was measured by gas meter by which controlled the H_2/ oil ratio (300 l/l).
The DAO was pumped co-current up-flow inside the reactor by high pressure-dosing pump (30-600 ml/h). The feed preheated and mixed with H_2 gas and entering the reactor. The reactor products were cooled in a condenser-cooler and separated from unreacted hydrogen, H_2S and hydrocarbon gases by passing into high and low-pressure separators.

Distillation of Hydrodesulfurization Products

The hydrotreating product was distilled at laboratory vacuum distillation for low boiling fractions separation. A 250 ml of the HDS product placed in a 500 ml distillation flask, supplied with a heating mantle of 2.4 kW. A voltage regulator was connected with the heating mantle for controlling the amount of heating supplied. Vertical high efficiency condenser was connected with the distillation flask, where a thermometer (623 K) fitted to measure the temperature of the vapors. Cooling machine was supplied by a cooled water (293 K) to a double shell receiver (outside shell) and though it to the condenser. The collecting flask was connected with the receiver, and a triple connector supplied for vacuum controlling, and it was already connected with the trap, trap (3-neck flask) was supplied for preventing vacuum pump damage. This trap connected with a vacuum pump through one way valve, and connected with a vacuum controller (Büch 165) from the another side. The vacuum distillation proceeded under 3 mmHg and a maximum vacuum temperature 593 K. This temperature equal to 803 K under atmospheric pressure.

Binder Preparation for Graphite Electrodes

The vacuum residue above 803 K obtained from HDS produced at 660 K and 1.3 h LHSV, was used as a basic component for binder production. Operating conditions of HDS was depended on a suitable density, viscosity as well as an acceptable level of sulfur & metals content. Anthracene with melting point 487-489 K and 1.25 specific gravity, was crushed and added at different percentages. Each mixture was mixed very well and introduced in an electrical furnace and heated to 523 K for 3 h to complete dispersion of anthracene particles in the residue media, the mixture then left for cooling overnight. A homogeneous binder was obtained.

Tests for the Feedstock and the Products

Density and Specific Gravity

The density and the specific gravity of the feedstock, deasphaltened oil and asphaltic binder were determined by using (ASTM D-287).
5.2 Viscosity
The viscosity of the feedstock, and deasphaltened oil were determined by using

(ASTM D-446).
5.3 Sulfur
The sulfur content of the feedstock determined by x-ray fluorescence (ASTM D-2622) and by quartz tube method (IP 63/55), while the deasphaltened oil and the hydrotreated product and asphaltic binder sulfur content determined by quartz tube method.

Carbon Residue
The carbon residue of asphalt, deasphaltened oil and asphaltic binder were determined by using ASTM D-189 and IP 13/66.

Ash Content
The ash content of the feedstock, deasphaltened oil and asphaltic binder were evaluated by using IP 4/65.
5.6 Softening Point (Ring and ball Method)
The softening point of the asphalt feedstock and ashaltic binder were determined by using ASTM D36-26.

Benzene and Quinoline Insolubles
The (BI) and (QI) were calculated for the asphaltic binder by using IP 47/74 standard method.

RESULTS & DISCUSSION
The properties of hydrotreated vacuum residue above 803 K distilled from the HDS of deasphaltened oil presented in **Table (1).**The standard range of graphite electrode binder properties((Hatano1989,Wagner1988and Mohammed). is shown in **Table (2).** Sulfur and ash contents are satisfies the required binder properties while softening point,density,BI and QI deviates. Therefore, anthracene is added to the binder basic component (hydrotreated vacuum residue above 803K) with different percentages. The binder properties with different anthracene content are shown in **Table (3). Figs. (1,2,3,4) and (5)** show the relationships between added anthracene weight percent and softening point, atomic C/H ratio, BI and QI respectively. The required binder must have 358K softening point[(5)]. From Fig.1 the mixture with 25wt.% anthracene has the required softening point and could be used as graphite electrodes binder. The properties of this binder are shown in Table 4.

Table (1) The properties of hydrotreated vacuum residue above 803 K.

Property	Unit	Data
Boiling Range	K	803+
Specific Gravity	-	1.017
Softening Point	K	308
Coke Yield	%	20.36
Sulfur Content	%	1.775
Ash Content	%	<0.125
BI	%	12.55
QI	%	16.21

Table (2) The standard Properties of graphite electrodes binder (Hatano1989,Wagner1988 and Mohammed)

Property	Unit	Range
Softening Point	K	312-373
Specific Gravity	-	1.16-1.3
Coke Yield	%	40.6-61.3
Sulfur Content	%	0.43-3
Ash Content	%	<0.125
BI	%	14.8-39.3
QI	%	3.4-14.1
Atomic C/H Ratio	-	1.64-1.95

Table (3) Effect of Anthracene on the Binder Properties

Binder Properties	Unit	Anthracene wt.%			
		10	20	30	40
Softening point	K	323	335	367	423
Density	g/cm3	1.25	1.13	1.85	2.05
Coke yield	Wt.%	39.9	46.0	58.23	65.60
Ash	Wt.%	0.023	0.023	0.02	0.02
Sulfur	Wt.%	1.56	1.20	1.046	0.9
Atomic C/H ratio	-	1.45	1.646	1.787	1.838
BI	Wt.%	14.0	16.05	22.20	23.0
QI	Wt.%	3.60	4.0	10.50	15.15

Table (4) Properties of the Required Binder

Binder Properties	Unit	Anthracene wt.%
		25
Softening point	K	358
Density	g/cm3	1.16
Coke yield	Wt.%	52.7
Ash	Wt.%	0.021
Sulfur	Wt.%	1.12
Atomic C/H ratio	-	1.75
BI	Wt.%	20.0
QI	Wt.%	8.60

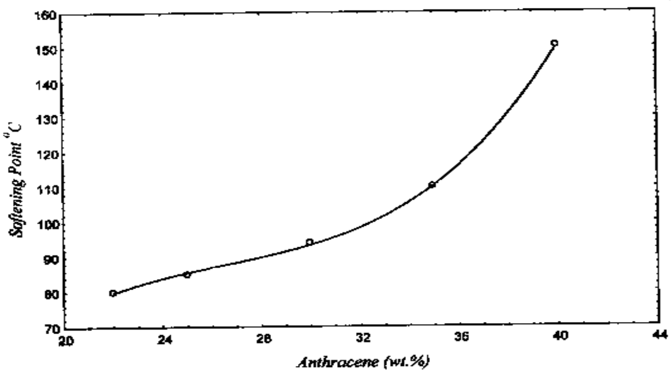

Fig.(1) Effect of Anthracene on the Softening Point

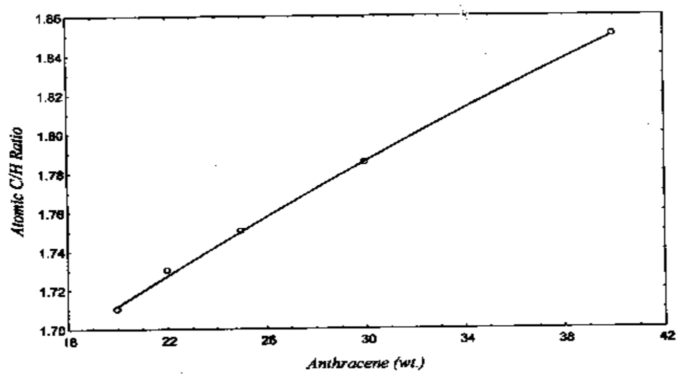

Fig.(2) Effect of Anthracene on the Atomic C/H Ratio

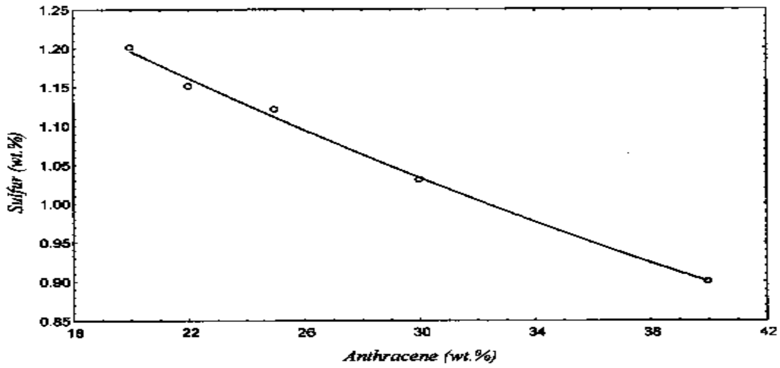

Fig. (3) Effect of Anthracene on the Binder Sulfer Content

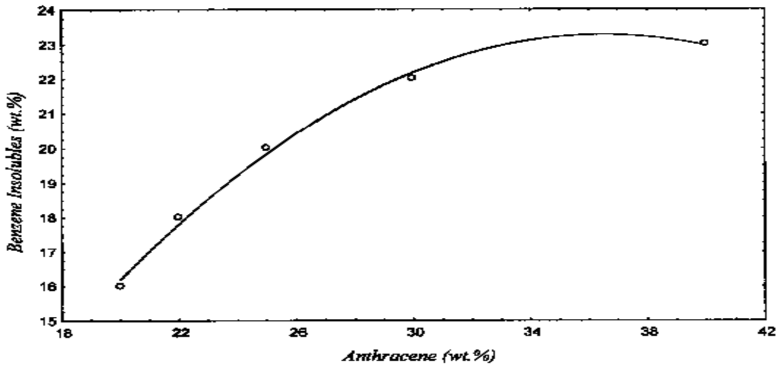

Fig.(4) Effect of Anthracene on the Binder Benzene Insoluble

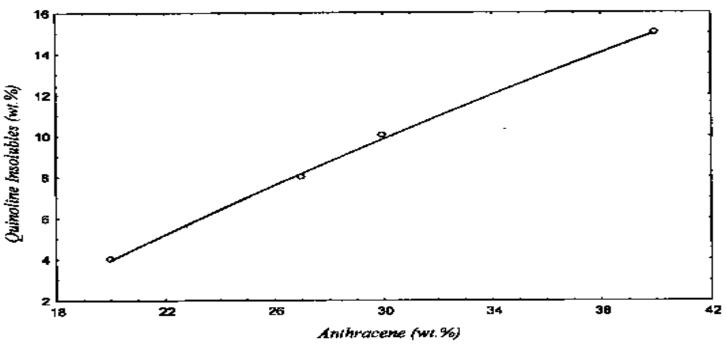

Fig.(5) Effect of Anthracene on the Quinoline Insolubles

REFERENCES

Gary,J.H., (1994), Petroleum Refining Technology and Economics, Third Edition

Hatano,H.and Suginobe,H.,Fuel,68(12),1503(1989).

Mohammed, A-H.A-H., Special Report of Al-Basil Company

Wagner, M.H., Jager, H., Letizia, I. and Wilhelmi, G., Fuel, 67(6),792(1988).

Wagner, M.H., Letizia, I., Gianini, S. and Wilhelmi, G., (1986),Int.Carbon Conference, Baden-Baden, 69

COMBINED CONVECTION HEAT TRANSFER TO THERMALLY DEVELOPING FLOW IN HORIZONTAL CIRCULAR CYLINDER

Dr. Yasin K. Salman **Hussain H. Ahmad** **Hussein A. Mohammed**
Mech. Eng. Dept., College of Engineering, University of Baghdad, Iraq.

ABSTRACT

Experiments were conducted to study the local and average heat transfer by mixed convection for hydrodynamically fully developed but thermally developing laminar air flow in horizontal circular cylinder. The experimental setup using an aluminum cylinder as test section with 30 mm inside diameter and 900 mm heated length (L/D=30), is subjected to a constant wall heat flux boundary condition. The investigation covers Reynolds number range from (400 to 1600), heat flux varied from ($60W/m^2$ to $400W/m^2$)and by using an aluminum entrance section pipes (calming sections) having the same inside diameter as test section pipe but with variable lengths as entrance sections. The entrance sections included a long calming section of length 240 cm (L/D=80) and two short calming sections with lengths 60 cm (L/D=20), 120 cm (L/D=40).

The results present the temperature variation along the cylinder surface and the local and average Nusselt number variation with the dimensionless axial distance (Z^+). For all entrance sections, the results show an increase in the Nusselt number values as the heat flux increases. Also, the mixed convection regime can be bounded by a suitable selection of (Re) number ranges and the heat flux ranges. The obtained Richardson numbers (Ri) range varied approximately from (0.1171 to 12.54).

الخلاصة

أجريت تجارب عملية لدراسة انتقال الحرارة الموقعي والمعدل بطريقة الحمل المختلط لجريان الهواء الطباقي تام التطور والمتشكل حرارياً في داخل اسطوانة دائرية أفقية. يتكون الجهاز المستخدم من اسطوانة من الألمنيوم وهي جزء الاختبار بقطر (30mm) وبطول (900mm) نسبة الطول إلى القطر تعادل (L/D= 30) تحت فيض حراري ثابت. يتراوح رقم رينولدز في هذا البحث من (400) إلى (1600) ، أما الفيض الحراري فيتغير من ($60W/m^2$) إلى ($400W/m^2$) ، وباستعمال أنابيب في المدخل (أنابيب تهدئة) من الألمنيوم لها نفس القطر الداخلي لجزء الاختبار ولكن بأطوال مختلفة . أنابيب المدخل تتضمن أنبوب مدخل طويل بطول (240cm) (L/D=80) وكذلك أنابيب قصيرة في المدخل وبأطوال (60cm) (L/D=20) و (120 cm)(L/D=40) على التوالي. وضحت النتائج تغير درجة الحرارة على طول سطح الاسطوانة وكذلك تغير رقم نسلت الموقعي (Nu_x) والمعدل ($\overline{Nu}$)مع المسافة المحورية غير البعدية (Z^+) ، لكل الأطوال المستخدمة ،وبينت النتائج زيادة رقم نسلت كلما زاد الفيض الحراري وكذلك تم الحصول على منطقة الحمل المختلط من خلال الاختيار المناسب لرقم رينولدز و قيم الفيض الحراري. يتغير رقم (Ri) الذي تم الحصول عليه تقريباً من (0.1171) إلى (12.54).

KEY WORDS

Combined Convection Heat Transfer, Thermally Developing, Horizontal Circular Cylinder.

INTRODUCTION

In convective heat transfer problems, the flow usually is classified as forced convection flow in which the flow is caused by external forces such as pumps or fans, or free convection flow in which the flow is created by the fluid density variations due to the wall to fluid temperature difference under the influence of body forces. In most physical applications, the buoyancy forces have negligible effects because they have usually a considerably smaller magnitude than those accompanying the forced flow. But in certain practical situations, however, the magnitude of the two forces may be of the same order and both may then be expected to influence the flow significantly. Therefore, when the free convection superimposed on the forced convection heat transfer process gives rise to new field of study called mixed (combined) convection. Thus, the combined convection situation extends from the extremes of free convection regime on the one hand when the motion results from buoyancy alone, to the forced convection regime on the other hand when external forces alone produce the motion and buoyancy forces are negligible (Metais and Eckert, 1964). Therefore, depending upon the relative magnitude of these two forces, the flow can be divided as pure forced, combined (forced and free) or pure free convection. The interaction of the natural and forced convection currents can be very complex and difficult because it depends not only on all the parameters determining both forced and free convection relative to one another but sometimes also on a large number of interacting parameters including the relative direction of the natural and forced convection to each other, the geometry of the arrangement, the velocity profile at tube entrance and the heating surface boundary conditions.

Laminar flow combined convection heat transfer in tubes is encountered in a wide variety because of special importance in many industrial engineering applications. The following examples can be cited: heating or cooling of heat exchangers for viscous liquids, heat exchangers for gas flows, cooling of electronic equipment, compact heat exchangers, solar collector heat exchangers, the cooling core of nuclear reactors, supercritical boilers and the cooling of rotating parts such as rotor blades of gas turbine also the pipe lines used for transporting oil (Yousef and Tarasuk, 1982). The full understanding of the prevailing velocity and temperature fields, as well as, the pressure drop and heat transfer coefficient, are necessary for the proper design. In addition, to estimate the magnitude of the thermal shock that any one of the preceding systems wall will suffer (Morcos and Bergles, 1975).

The entrance shapes, used in this experimental work, included three entrance sections (calming sections) with different length in which the flow is fully developed at entrance of the heat transfer pipe. For experimental viewpoint, very little investigations have dealt experimentally to study the effect of laminar combined convection to thermally developing flow in a circular cylinder on the heat transfer process.

McComas and Eckert (1966)studied experimentally the fully developed air flow in uniformly heated tube for different ranges of (Re) and (Gr) numbers. The experimental results have revealed that the effect of secondary flow is to reduce the wall to air bulk temperature difference compared with the pure forced convection results in the region far from the tube inlet. Variation of the wall and air temperatures and the local Nusselt number along the tube were presented.

(Mori et al, 1966) carried out experiments to study the effect of buoyancy force on forced convection for fully developed air flow under constant wall heat flux. The velocity and temperature profiles were measured for large (Re.Ra). The calculated Nusselt number was also shown to be twice as those calculated by neglecting the effect of secondary flow. The following correlation formula was obtained:

$$Nu = 0.61(\mathrm{Re}.Ra)^{1/5}\left\{1+\frac{1.8}{(\mathrm{Re}.Ra)^{1/5}}\right\} \tag{1}$$

Shannon and Depew (1968) performed an experiment to study the influence of free convection on forced laminar flow of water, initially at the ice point in a circular tube with constant wall heat flux and fully developed velocity profile at the onset of heating. The experiment was carried out with different values of (Re), (Gr) and (Gz) numbers. Experiments revealed that the Nusselt number was affected significantly far down stream but relatively little in the thermal entrance region for the tube having X/D=700. A graphical correlation with the parameter $(Gr.Pr)^{1/4}$ $/Nu_{Gz}$ (where Nu_{Gz} is the Nusselt number for pure forced convection) has been achieved giving good agreement with available experimental data.

Depew and August (1971) studied experimentally the fully developed laminar flow in an isothermal tube having an L/D ratio of (28.4). Three different liquids were used in this study: water, ethylalcohol and mixture of glycerol and water. The experiment covered a wide range of (Re), (Gr) and (Gz) numbers. The experimental results show that when dealing with flows in horizontal tubes, the term (Gr.Pr.D/L) does not correctly represents the influence of natural convection for tubes with (L/D) ratios less than 50.

Bergles and Simonds (1971) performed experiments to examine the effects of free convection on laminar water flow in an electrically heated tube having essentially constant wall heat flux. The results have revealed that the natural convection effect may be important even at relatively low Rayleigh number and show that the Nusselt number for developed flow was three times the constant property. Also (Lichtarowicz, 1971) presented the Nusselt number with the product of (Re.Ra) and the temperature profile along the tube was depicted.

(Hong et al, 1974) concluded that for $Ra=10^6$, the Nusselt number in the developing region was more than 300% above the constant property value. The data were correlated accurately by equation, which includes dimensionless groups to account for effects of variable transport properties and tube wall conduction:

$$Nu_{ff} = 0.378 Gr_{ff}^{0.28} Pr_{ff}^{0.33} \big/ f^{0.12} \tag{2}$$

Where: ($f= h.D/k_w * D/t$, t= tube thickness, k_w= tube thermal conductivity).

Morcos and Bergles (1975) conducted experiments to investigate the effect of property variation in heated glass and stainless steel tubes with distilled water and ethyleneglycol as test fluids. The measured heat transfer data were presented in a form of correlation:

$$Nu_{ff} = \left[(4.36)^2 + \left\{0.055\left(\frac{Gr_{ff}\,Pr_{ff}^{1.35}}{P_w^{0.25}}\right)^{0.4}\right\}^2\right]^{1/2} \tag{3}$$

Yousef and Tarasuk (1982) obtained the average Nusselt number based on the log-mean-temperature difference. The heat transfer results were correlated according to the influence of free convection, which was found to have a significant effect at points close to the tube entrance as follows:

$$Nu\left(\frac{\mu_w}{\mu_b}\right)^{0.14} = 1.75\left[Gz + 0.245\left(Gz^{1.5}.Gr^{1/3}\right)^{0.882}\right]^{1/3} \tag{4}$$

The purpose of the present investigation is to determine experimentally the effect of Reynolds number and the effect of the heat flux on the laminar air flow heat transfer process under mixed convection situation in uniformly heated horizontal circular cylinder.

EXPERIMENTAL APPARATUS

The apparatus was constructed to have a test section preceded with different entrance sections, as well as, different Reynolds and Grashof numbers. The open-air circuit, in this investigation, is described first, followed by details of test section and heating element. Then the measuring devices and test procedure is described. Finally, the experimental data analysis method has been presented.

The experimental apparatus shown diagrammatically in **Fig. (1)** is designed and constructed to investigate combined convection heat transfer in a circular cylinder. The apparatus consists essentially of a cylindrical test section as a part of an open-air circuit, mounted on a wooden board (A), which could be rotated around a horizontal spindle.

An open-air circuit was used including small centrifugal fan (F), rotameter(R), test section 'heat transfer pipe' (T) provided with changeable entrance section 'different calming section length'(C). The centrifugal fan derived electrically via-fine control variable resistance so that its power can be regulated accurately. An air control valve (D) was fitted at the fan inlet to obtain fine control of the airflow rate. The air was drawn by the fan in to the test section through the entrance section and then enters the rotameter through flexible hose (M) and then the air leaves the rotameter to the centrifugal fan through another flexible hose (N). Then the heated air was exhausted to the atmosphere.

The test section 'heat transfer pipe' (T) is made of aluminum cylinder with (30) mm inside diameter, (35) mm outside diameter and (900) mm length (L/D=30). The Teflon connection piece (G) represents a part of the test section inlet, with (30) mm inside diameter, (50) mm outside diameter and (80) mm long. Another Teflon piece (I) represents the test section exit and it has dimensions of (30) mm inside diameter, (88) mm outside diameter and (25) mm long. The Teflon was chosen because its low thermal conductivity in order to reduce the test section ends losses.

The air passes through the test section, is fully developed hydrodynamically by using aluminum pipes having same diameter as test section pipe but with variable length as entrance sections. These pipes are connected with the test section by a Teflon connection piece (G) bored with the same inside diameter of the test section and entrance section as shown in

The cylinder is heated electrically by using an electrical heater as shown in **Fig. (1)**, section (A-A). It consists of a (0.5) mm in diameter nickel-chrome wire (H) electrically isolated by ceramic beads, wounded uniformly along the cylinder as a coil with (20) mm pitch in order to give uniform heat flux. An asbestos rope was used as a (20) mm spacer to secure the winding pitch .The outside of the test section was then thermally insulated by asbestos (U) and fiber glass (W) layers, having thicknesses of (15) mm and (13) mm respectively.

The cylinder surface temperatures were measured by twenty-five (0.2) mm-asbestos sheath alumel-chromel (type K) thermocouples, fixed along the cylinder. The measuring junctions (which were made by fusing the ends of the wires together by means of an electric spark in an atmosphere free from oxygen) embed in grooves in the wall normal to the cylinder axis as shown in **Fig. (1)**, section (A-A).

The thermocouples were fixed by drilling twenty-five holes (V) of (1.6) mm diameter and approximately (2) mm deep and along the cylinder wall while the ends of the holes chamfered by a (2) mm drill. The measuring junctions were secured permanently in the holes by sufficient amount of high temperature application Defcon adhesive (X). All thermocouple wires and heater terminals were taken out the test section. Thermocouple positions along the cylinder are shown in **Fig.(1)** section (B-B).

The inlet bulk air temperature was measured by one thermocouple (J) placed in the beginning of the entrance section (calming section), while the outlet bulk air temperature was measured by two thermocouples (K) located in the test section exit 'mixing chamber' (B) .The local bulk air temperature was calculated by fitting straight line -interpolation between the measured inlet and outlet bulk air temperatures.

All thermocouples were used with leads and calibrated using the melting points of ice made from distilled water as reference point and the boiling points of several pure chemical substances.
To perform heat loss calculation through the test section lagging, six thermocouples are inserted in the lagging as two thermocouples at three stations along the heated section (35) cm apart as shown in **Fig. (1)** section (A-A). By using the average measured temperatures and thermal conductivity of the lagging, the heat loss through lagging can be determined.
To evaluate the heat losses from the ends of the test section, two thermocouples were fixed in each Teflon piece. By knowing the distance between these thermocouples and the thermal conductivity of the Teflon, the end losses could be calculated.
Voltage regulator (variac), accurate ammeter and digital voltmeter were used to control and measure of the input power to the working cylinder.
The following entrance sections (calming sections) were used in the present work, that in which the flow is already fully developed at the entrance to the test section. This condition is represented by the pipe with long and short calming sections at entrance as follows: -

1- A long calming section having the same diameter as the test section pipe and length equal to (240) cm (L/D=80) to provide fully developed flow at the entrance of the test section pipe.
2- Two short calming sections, also having the same diameter as the test section pipe and lengths equal to (60) cm (L/D=20) and (120) cm (L/D=40) respectively to provide fully developed flow at the entrance of the test section pipe.

Experimental Procedure

The procedure employed to carryout a certain experiment was as follows:

1- The required calming section length was fitted with the test section.
2- The centrifugal fan was then switched on to draw the air through the test section while the fan control valve was used for adjusting the required volume flow rate inside cylinder.
3- The electrical heater was switched on and the heater-input power then adjusted to give the required heat flux.
4- The apparatus was allowed to turn on for at least (4 hours) before the steady state conditions were achieved. The readings of all thermocouples were recorded every half an hour by a digital electronic thermometer until the reading became constant, then the final reading was recorded.

The input power to the heater could be changed to cover another run in shorter period of time and to obtain steady state conditions for next heat flux and for same Reynolds number.
The subsequent runs for other Reynolds numbers ranges were conducted in the same procedure.

5- During each test run, the following readings were recorded: -
a- The length of entrance section (calming section) in (cm).
b- The reading of the rotameter (air flow rate) in (m^3/hr).
c- The heater current in ampere.
d- The heater voltage in volts.
e- The readings of all thermocouples in ($^{\circ}$C).

Data Analysis Method

The following simplified steps were used to analyze the heat transfer process for the air flow in a circular cylinder when its surface was subjected to a constant wall heat flux boundary condition.
The total input power supplied to cylinder can be calculated:

$$Q_t = V * I \qquad (5)$$

The convection heat transferred from the cylinder surface:

$$Q_{conv} = Q_t - Q_{cond.} \qquad (6)$$

Where $Q_{cond.}$ = is the total conduction heat losses (lagging and ends losses).

The convection heat flux can be represented by:

$$q_{conv.} = \frac{Q_{conv.}}{A_s} \qquad (7)$$

Where $A_s = \pi * D * L$

The convection heat flux, which is used to calculate the local and average heat transfer coefficie as follows:

$$h_x = \frac{q_{conv.}}{t_{sx} - t_{ax}} \qquad (8)$$

Where: t_{sx}= local surface temperature.

t_{ax}= local bulk air temperature.

All the air properties were evaluated at the mean film temperature (Louis Burmeister, 1993).

$$t_{fx} = \frac{t_{sx} + t_{ax}}{2} \qquad (9)$$

Where: t_{fx}= local mean film air temperature.

The local Nusselt number (Nu_x) can be determined as:

$$Nu_x = \frac{h_x . D}{k_x} \qquad (10)$$

The average values of Nusselt number $(\overline{Nu})$ can be calculated based on the calculated avera surface temperature and average bulk air temperature as follows:

$$\overline{t_s} = \frac{1}{L} \int_{x=0}^{x=L} t_{sx} \, dx \qquad (11)$$

$$\overline{t_a} = \frac{1}{L} \int_{x=0}^{x=L} t_{bx} \, dx \qquad (12)$$

$$\overline{t_f} = \frac{\overline{t_s} + \overline{t_a}}{2} \qquad (13)$$

The average values of the other parameters can be calculated as follows:

$$\overline{Nu} = \frac{q D}{k(\overline{t_s} - \overline{t_a})} \qquad (14)$$

$$\overline{Gr} = \frac{g \beta D^3 (\overline{t_s} - \overline{t_a})}{\nu^2} \qquad (15)$$

$$\overline{Ra} = \overline{Gr} * Pr \qquad \text{----------}(16)$$

Where: $\beta = \frac{1}{(273 + \overline{t_f})}$, All the air physical properties $(\rho, \mu, \nu \text{ and } \kappa)$ were evaluated at t average mean film temperature ($\overline{t_f}$).

RESULTS AND DISCUSSION

A total of (48) test runs were conducted to cover the three entrance section pipes with diffe lengths 60cm (L/D=20), 120cm(L/D=40) and 240cm(L/D=80) for a horizontal circular cylin The range of heat flux from 60 w/m^2 to 400 w/m^2 and Reynolds number varied from (400 to 160

Surface Temperature Distribution

Generally, the variation of the surface temperature along the cylinder may be affected by many variables such as heat flux, Reynolds number and the flow entrance situation. The temperature variation for selected runs is plotted in **Figs. (3 - 6)**.

Fig. (3) shows the variation of the surface temperature along the cylinder for different heat flux, for Re=400 and for calming section length equal to 60 cm (L/D=20). This figure reveals that the surface temperature increases at cylinder entrance to reach a maximum value after which the surface temperature decreases. The location of maximum temperature seems to move toward the cylinder entrance as the heat flux increases. This can be attributed to the developing of the thermal boundary layer faster due to buoyancy effect as the heat flux increases for the same (Re).

Fig. (4) is similar to **Fig. (3)** but pertains to Re=1600.The curves in the two figures show same trend, but the surface temperature values in **Fig. (4)** are lower than values in **Fig. (3)** because of the forced convection domination.

Figs. (5&6) show the effect of (Re) variation on the cylinder surface temperature for low heat flux (92 w/m^2) in **Fig. (5)** and for high heat flux (294 w/m^2) in **Fig. (6)**. It is obvious that the increasing of (Re) reduces the surface temperature, as the heat flux kept constant. It is necessary to mention that as heat flux increases the surface temperature increases because the free convection is the dominating factor in the heat transfer process.

The surface temperature variation for the second calming section with length equal to 120 cm (L/D=40) and third calming section with length equal to 240 cm (L/D=80), is similar trend as mentioned for (L/D=20).

Local Nusselt Number Distribution (Nu_x)

The variation of the local Nusselt number (Nu_x) with the dimensionless axial distance (Z^+), is plotted for selected runs in **Figs. (7 - 10)**.

Figs. (7&8) show the effect of the heat flux variation on the (Nu_x) distribution for Re=400 and Re=1600 respectively. It is clear from these two figures that at the higher heat flux, the results of (Nu_x) were slightly higher than the results of lower heat flux. This may be attributed to the secondary flow superimposed on the forced flow effect increases as the heat flux increases leading to higher heat transfer coefficient. The dotted curve in each figure represents the theoretical pure forced convection (TPFC) based on constant property analysis of (Shah and London, 1978).

Figs. (9&10) show the effect of (Re) number variation on the Nu_x distribution with (Z^+), for low heat flux (92 w/m^2) in **Fig. (9)** and for high heat flux (294 w/m^2) in **Fig. (10)**. For constant heat flux, the (Nu) values give higher results than the predicted pure forced convection value and moves toward the left as (Re) increases. This situation reveals that the forced convection is dominant on the heat transfer process with little effect of buoyancy force for high (Re). As the (Re) number reduced, the buoyancy effect expected to be higher which improves the heat transfer results.

It is necessary to mention that in horizontal cylinder, the effect of secondary flow is high, hence at low (Re) number and high heat flux, situation makes the free convection predominant. Therefore, as the heat flux increases, the fluid near the wall becomes warmer and lighter than the bulk fluid in the core. As a consequence, two upward currents flow along the sides walls, and by continuity, the fluid near the cylinder center flows downstream. This sets up two longitudinal vortices, which are symmetrical about a vertical plane. These vortices reduces the temperature difference between the cylinder surface and the air flow in which led to increase the growth of the thermal boundary layer along the cylinder and causes an improvement in the heat transfer results. But at low heat flux and high (Re) number the situation makes the forced convection predominant and the vortex strength decreases which decreases the temperature difference between the surface and the air, hence the (Nu_x) values becomes higher (Mori and Futagami, 1967).

Also, the (Nu_x) distribution for higher calming section (L/D=40,L/D=80) are similar trend as mentioned in the first calming section length (L/D=20).

Average Nusselt Number Distribution $(\overline{Nu})$

The variation of the average Nusselt number $(\overline{Nu})$ with the dimensionless axial distance (Z^{+}) is depicted for selected runs in **Figs. (11 - 14).**

Figs. (11&12) show the effect of the heat flux on the $(\overline{Nu})$ for Re=400 and Re=1600 respectively and the effect of (Re) number on the $(\overline{Nu})$ for low heat flux (92 w/m^2) and high heat flux (294 w/m^2) in **Figs. (13&14)** respectively for the shorter tube (L/D=20). The $(\overline{Nu})$ variation for higher calming section (L/D=40,L/D=80) are similar trend as mentioned for (L/D=20).

CONCLUSIONS

As a result from the experimental work conducted in the present investigation to study combined convection heat transfer to thermally developing laminar air flow in horizontal circular cylinder subjected to a constant wall heat flux boundary condition, the following conclusions can be drawn:

1- The variation of the surface temperature along the cylinder has the same shape. This variation is affected by:
   a- The surface temperature increases as the heat flux increases, for the same (Re).
   b- The surface temperature for low (Re) is higher than for high (Re), for the same heat flux because of the free convection domination.
2- The variation of (Nu_x) with (Z^{+}), for all entrance lengths has the same trend. This variation is summarized as follows:
   a- For the same (Re) number, the (Nu_x) increases with the increase of heat flux.
   b- For the same heat flux and high (Re), the (Nu_x) moves toward the left of the (Nu_x) predicted for (TPFC), because the forced convection is dominant.
   c- For the same heat flux and low (Re), the (Nu_x) moves toward the right of the (Nu_x) predicted for (TPFC), because the natural convection is dominant.
3- Free convection effects tended to decrease the heat transfer results at low (Re) and to increase the heat transfer results for high (Re).
4- At the cylinder entrance the effect of buoyancy is small, but it is effects increase in the cylinder downstream.
5- The variation of the $(\overline{Nu})$ with (Z^{+}), has the same heat transfer characteristics which mentioned in the (Nu_x) results.
6- The mixed convection regime can be bounded by a suitable selection of (Re) number ranges and the heat flux ranges. The obtained Richardson numbers (Ri) range is varied approximately from (0.1171 to 12.54).

REFERENCES

Bergles, A.E. and Simonds, R.R., (1971), Combined forced and free convection for laminar flow in a horizontal tube with uniform heat flux, Int.J.Heat Mass Transfer, Vol.14 , pp.1989-2000.

Depew, C.A. and August, S.E., (1971), Heat transfer due to combined free and forced convection in a horizontal and isothermal tube, J.of Heat Transfer, ASME Trans., Vol. 93, Nov., pp.380-384.

Hong, S.W., Morcos, S.M. and Bergles, A.E., (1974), Analytical and experimental results for combined forced and free laminar convection in horizontal tubes, Int. Heat Transfer Conference 5th, Vol. 3, pap.No. NC4.6, pp.154-158, Tokyo.

Lichtarowicz, A., (1971), Combined free and forced convection effects in fully developed laminar flow in horizontal tubes, Symposium on Heat and Mass Transfer by combined free and forced convection (Int. Mech. Engrs.), pap. No. C114, (15 Sept.).

Louis C. Burmeister., (1993), Convective Heat Transfer, John wiley&sons, Inc., 2nd edition.

McComas, S.T. and Eckert, E.R.G., (1966), Combined free and forced convection in a horizontal circular tube, J.of Heat Transfer, ASME Trans., Vol.88, May, pp.147-153.

Metais, B. and Eckert, E.R.G., (1964), Forced, mixed and free convection regimes, J. of Heat Transfer, ASME Trans., Vol. 86, May, pp. 295-296.

Morcos, S.M. and Bergles, A.E., (1975), Experimental investigation of combined forced and free convection in horizontal tubes, J. of Heat Transfer, ASME Trans. ,Vol. 97, May, pp.212 –219.

Mori, y., Futagami, k., Tokuda, S. and Nakumara, M. , (1966),Forced convection heat transfer in uniformly heated horizontal tube – experimental study on the effect of buoyancy, Int.J.Heat Mass Transfer, Vol. 9, pp. 453- 463.

Mori, Y. and Futagami, K., (1967), Forced convection heat transfer in uniformly heated horizontal tubes (2nd report theoretical study), Int. J. Heat Mass Transfer, Vol.10, pp.1801-1813.

Roshenow, W.M; Hartnett and Ganic., (1985), Hand Book of Heat Transfer Fundamentals', McGraw-Hill, 2nd edition.

Shah, R.K.and London, A.L., (1978), Laminar flow forced convection in ducts, Advances in Heat Transfer, supplement 1, Academic press.

Shannon, R.L. and Depew, C.A., (1968), Combined free and forced laminar convection in a horizontal tube with uniform heat flux, J. of Heat Transfer , ASME Trans., Vol. 90 , Aug. ,pp. 353 – 357.

Yousef, W.W. and Tarasuk, J.D., (1982), Free convection effects on laminar forced convective heat transfer in a horizontal isothermal tube, J.of Heat Transfer, ASME Trans., Vol. 104, Feb., pp. 145-152.

NOMENCLATURE

Symbol	Description	Unit
A_s	Cylinder surface area	m^2
Cp	Specific heat at constant pressure	J/kg.°C
D	Cylinder diameter	m
g	Gravitational acceleration	m/s^2
h	Heat transfer coefficient	$w/m^2.°C$
I	Heater current	amp.
k	Thermal conductivity	w/m.°C
L	Cylinder length	m
Q_{cond}	Conduction heat loss	w
q_{conv}	Convection heat flux	w/m^2
Q_{conv}	Convection heat loss	w
Q_t	Total heat input	w

R	Cylinder radius	m
t	Air temperature	°C
t_1	Wall thickness	m
V	Heater voltage	volt
x	Axial distance	m

Greek

β	Thermal expansion coefficient	1/K
μ	Dynamic viscosity	kg/m.s
ν	Kinematic viscosity	m^2/s
ρ	Air density	kg/m^3

Dimensionless Group

Gr	Grashof number	$= g\beta D^3(t_s-t_a)/\nu^2$
Gz	Graetz number	= Re.Pr.D/L
Nu	Nusselt number	= h.D/ k
Pr	Prandtl number	$= \mu$. Cp/k
P_w	Wall parameter	$= h.D^2/k_w . t_1$
Ra	Rayleigh number	= Gr.Pr
Re	Reynolds number	$= \rho$. v. D / μ
Ri	Richardson number	$= Gr/Re^2$
Z^+	Axial distance	= x/D.Re.Pr

Subscript

a	Air
b	Bulk
calm.	Calming section
f	Film
f	Fully developed flow
s	Surface
w	Wall
x	Local

Superscript

—— Average

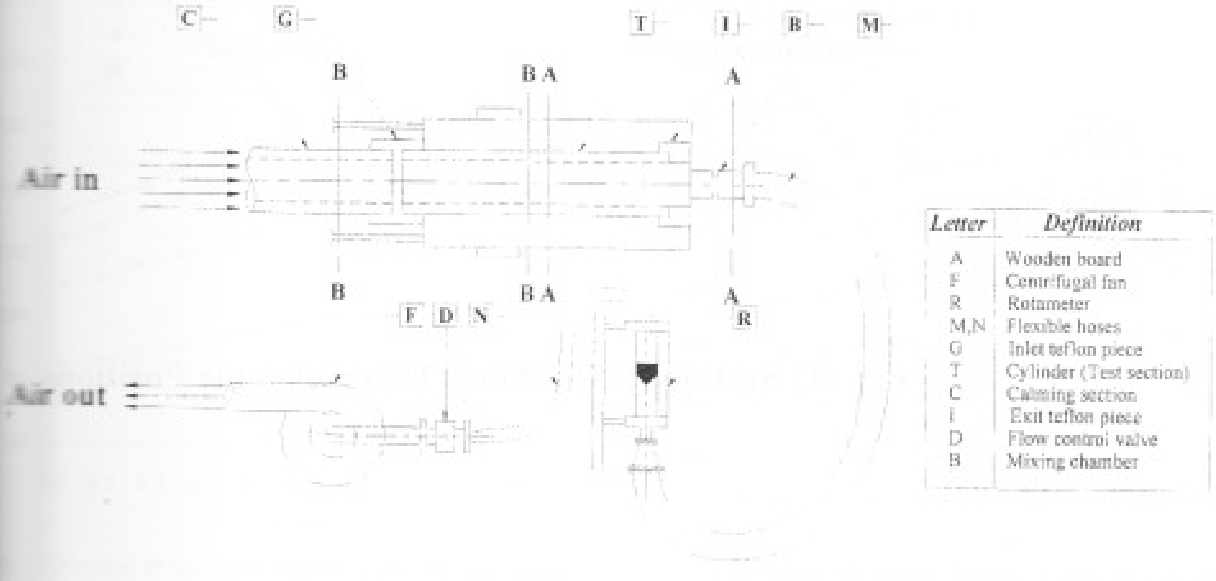

Fig. (1) Diagram of Experimental Arrangement

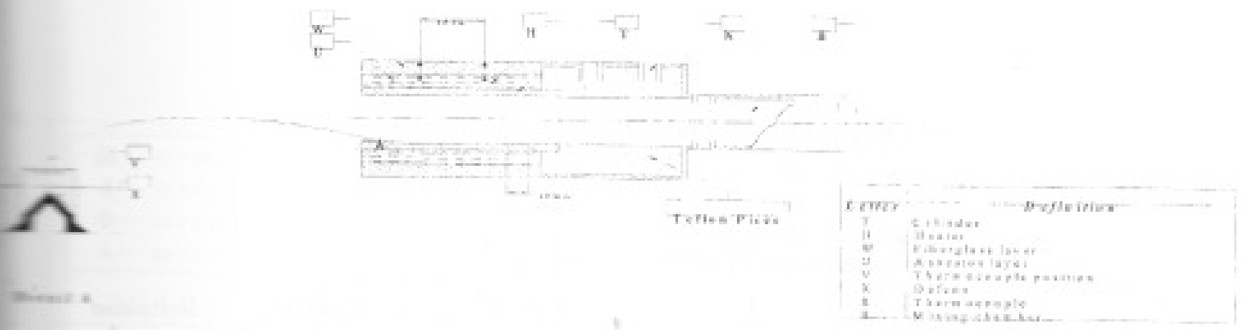

Fig.(1) Section (A-A)

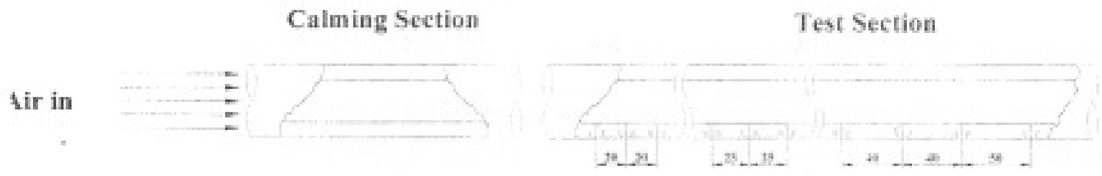

Fig. (1) Section (B-B) Shows Thermocouple Positions

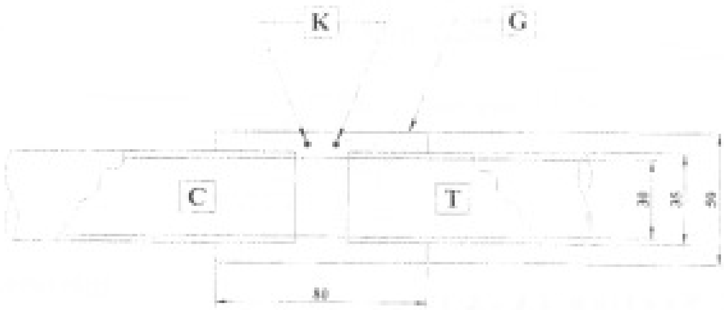

Letter	Definition
T	Test section
C	Calming section
G	Teflon connection piece
K	Thermocouple

All Dimensions in (mm)

Fig.(2) Teflon Connection Piece.

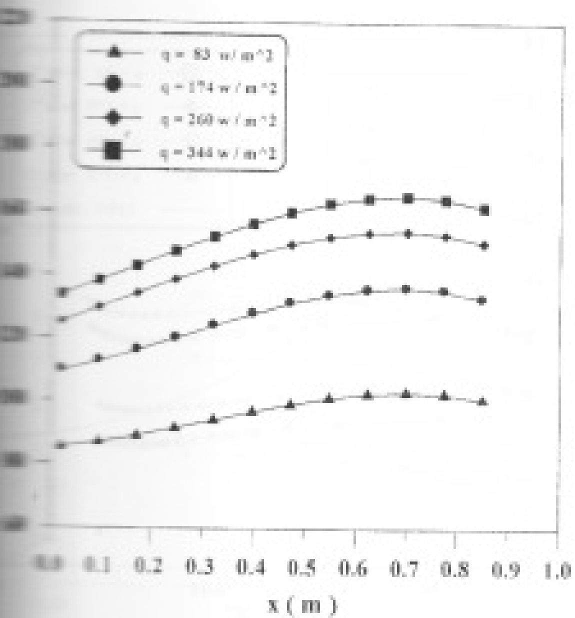

Variation of the surface temperature with the axial distance for Re=400 , Lcalm.=60 cm , L / D)calm.=20

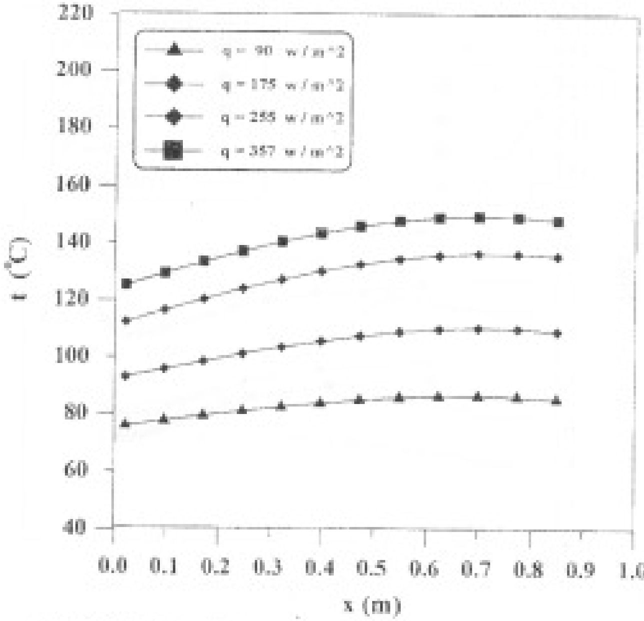

Fig.(4) Variation of the surface temperature with the axial distance for Re=1600 , Lcalm.=60 cm , L/D) calm.=20

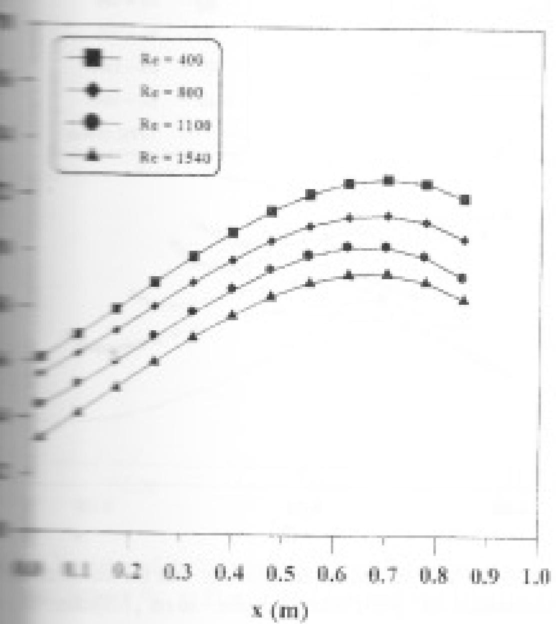

Variation of the surface temperature with the axial distance for [illegible] w/m^2 , Lcalm.= 60 cm , L/D)calm.= 20

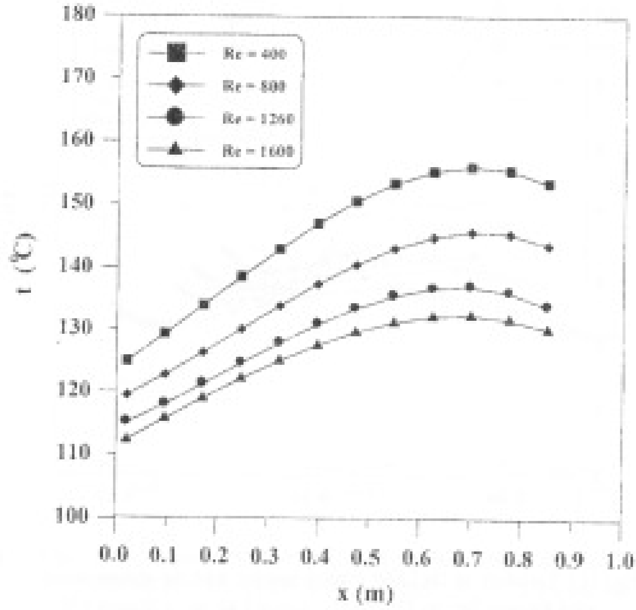

Fig.(6) Variation of the surface temperature with the axial distance for q=296 w/m^2 , Lcalm.= 60 cm , L/ D)calm.= 20

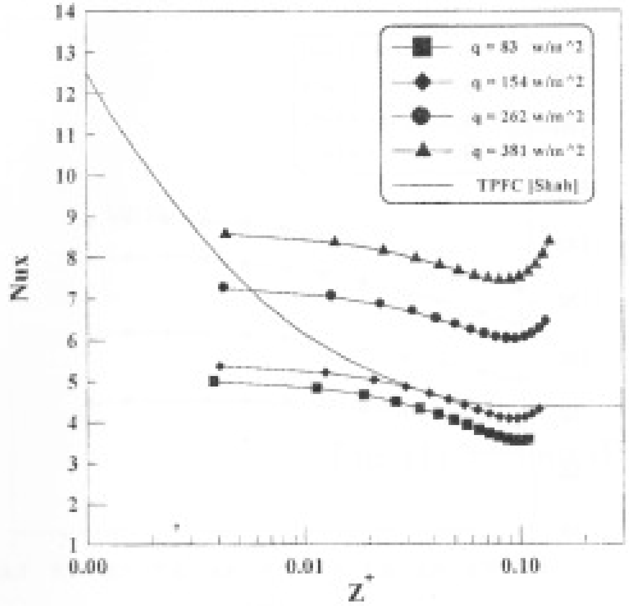

Fig.(9) Variation of the Local Nusselt number with the dimensionless axial distance for Re = 400 , Lcalm.= 60 cm , L/D)calm.=20

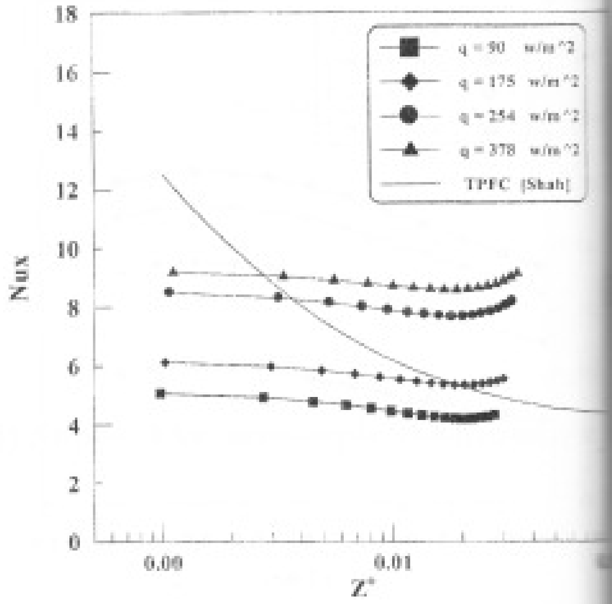

Fig.(10) Variation of the Local Nusselt number with the dimensionless axial distance for Re = 1600 , Lcalm.= 60 cm , L/D)calm.=20

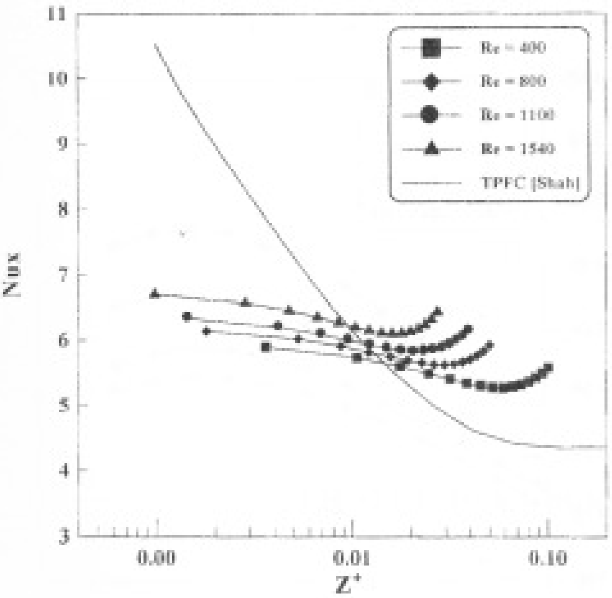

Fig.(11) Variation of the Local Nusselt number with the dimensionless axial distance for q= 92 w/m^2 , Lcalm.= 60 cm , L/D)calm.=20

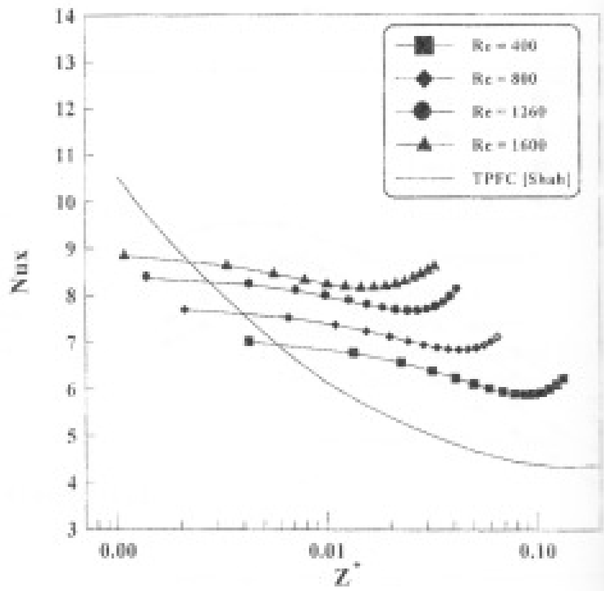

Fig.(12) Variation of the Local Nusselt number with the dimensionless axial distance for q=294 w/m^2 , Lcalm.= 60 cm , L/D)calm.=20

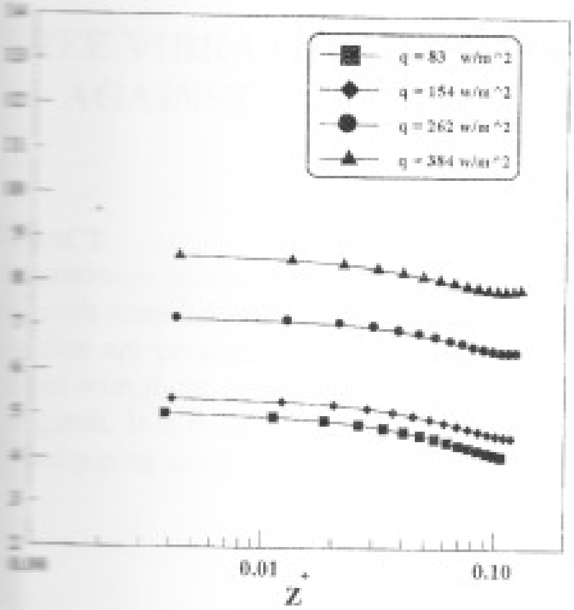

Fig.(16) Variation of the average Nusselt number with the dimensionless axial distance for Re= 400, Lcalm.= 60 cm , L/D)calm.=20

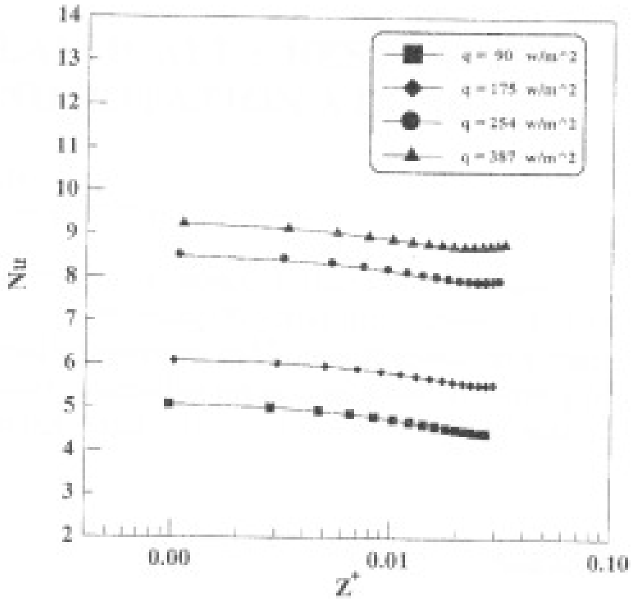

Fig.(17) Variation of the average Nusselt number with the dimensionless axial distance for Re= 1600 , Lcalm.= 60 cm , L/D)calm.=20

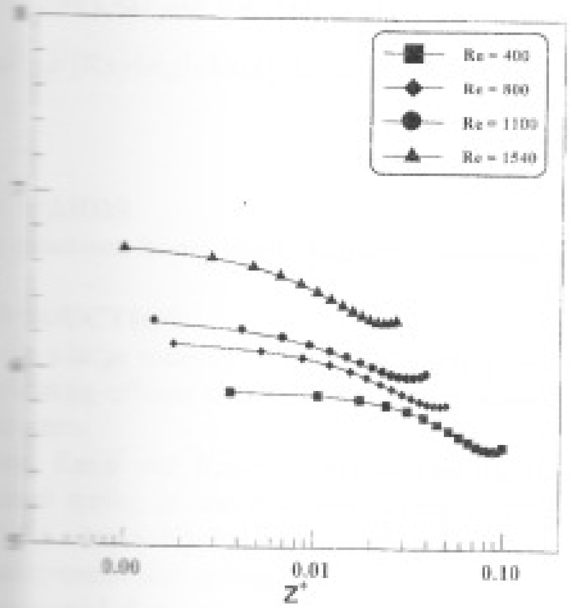

Fig.(18) Variation of the average Nusselt number with the dimensionless axial distance for q= 92 w/m^2 , Lcalm.= 60 cm , L/D)calm.=20

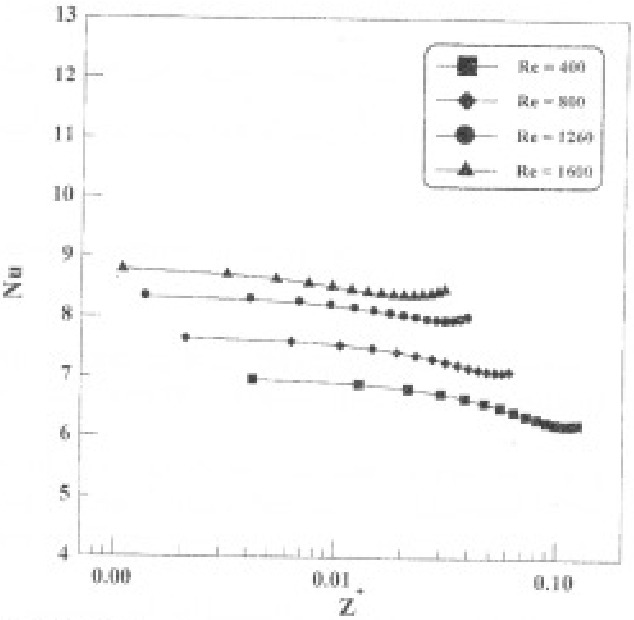

Fig.(19) Variation of the average Nusselt number with the dimensionless axial distance for q= 294 w/m^2 , Lcalm.= 60 cm , L/D)calm.=20

FREE VIBRATION OF BEAM ELASTICALLY RESTRAINED AGAINST TRANSLATION AND ROTATION AT ENDS

Nabil H.H.
Univ. of Baghdad-College of Eng.

ABSTRACT

An approximate solution of the vibration of an elastically restrained, uniform and non-uniform beams with translational and rotational springs is obtained using Rayleigh-Ritz approach. The frequencies are presented for wide range of restrained parameters and some of these have been compared with those available in the published literature illustrating the accuracy and versatility of the approach. It is believed that the results present in this paper will be of use in design of beams, shaft, and piping under dynamics consideration.

الخلاصة

في هذا البحث تم دراسة الاهتزاز الحر للعتبات ذات ظروف الإسناد المرنة حيث استخدمت طريقه الحل التقريبي (Rayleigh-Ritz) . الإسناد المرن الذي تمت دراسته هو الانتقالي والد وراني للعتبات ذات المقطع العرضي المنتظم وغير المنتظمة المقطع العرضي. النتائج التي حصل عليها لمدى واسع من معامل مرونة الإسناد الخطي والد وراني وبعد المقارنة مع نتائج البحوث ألمنشوره أثبتت دقة هذه ألطريقه وكفاءتها. كما بينت النتائج التي تم الحصول عليها في البحث امكانية ووثوقية استخدام طريقة (Rayleigh-Ritz) في تصميم الأعمدة والمساند والأنابيب الواقعة تحت تأثير الأحمال الديناميكية.

KEY WARDS

Free vibration, beam, shaft, frequency parameter, elastically restrained, Rayleigh-Ritz

INTRODUCTION

There is a large number of technical studies dealing with vibrating beam taking into account several complicating effects such as axial forces, elastic constraints, variable cross-section rotary inertia of the tip mass.

Martini, Rossi and Reyes(1976) studied the problem of free vibration of a beam supported by a rotational spring at one end and having a translational spring at the other end. Sundarajan(1979) derived a simple algebraic expression for un upper bound to the fundamental frequency of beams with unsymmetrical springs.

Freeman and Soreensen(1980) have studied the response of elastically restrained cantilever Bernoulli-Euler beams and presented exact frequencies and mode shapes for the first four modes of vibration for a number of restraint parameters. In an attempt to estimate the fundamental frequencies of vibration fuel rods, Passig(1970) derived an exact frequency equation for a beam supported by symmetrical springs at either end of the beam. Abbas(1984) has studies the problem of elastically restrant Timoshenko beams and presents some results for degenerate case of Bernoulli-Euler beam.

In the present paper the problem of free vibration of partially restrained Bernoulli-Euler is solved by using Rayleigh-Ritz approach. A simple algorithmic procedure is applied for determining the frequency parameter of the restraint beam.

APPROXIMATE SOLUTIN

The classical application of the Rayleigh-Ritz method is based upon the selection of a deflection function which is a specific function of the position .
However, as was a first shown by Rayleigh one can use a polynomial function with undefined parameters. The strain .energy of the structural system under consideration **Fig. (1).**

$$U_{\max} = \tfrac{1}{2} E \int_0^{\ell} I(x)\left(\frac{\partial^2 W}{\partial x^2}\right)^2 dx + \tfrac{1}{2}\phi_r\left(\frac{\partial W}{\partial x}\right)^2 + \tfrac{1}{2} K W^2 \Bigg|_{x=x1}^{x=x2} \qquad (1a)$$

be equal to its maximum kinetic energy

$$V = \tfrac{1}{2}\rho\omega^2 \int_0^{\ell} A(x) W^2 dx \qquad (1b)$$

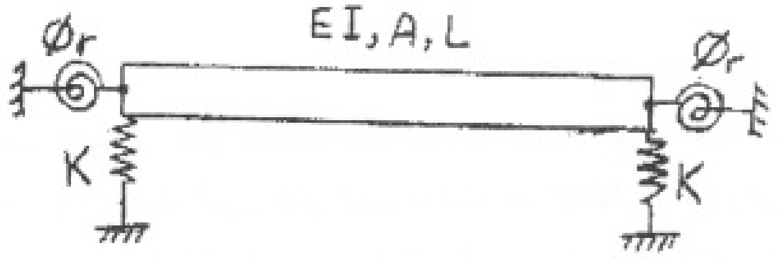

Fig.(1) The structural element under investigation, showing the support system.

Where E is the Young's modulus I(x) is the variable moment of inertia, A(x) is the variable cross-section area, ϕ_r and K are the coefficient of rotational and translational springs. The boundary conditions for the beam can be written at x=0

$$EI\frac{\partial^3 W(0,t)}{\partial x^3} = -KW(0,t)$$

$$EI\frac{\partial^2 W(0,t)}{\partial x^2} = \phi_r \frac{\partial W(0,t)}{\partial x} \qquad (2)$$

and at x=L as:-

$$EI\frac{\partial^3 W(0,t)}{\partial x^3} = KW(L,t)$$

$$EI\frac{\partial^2 W(0,t)}{\partial x^2} = -\phi_r \frac{\partial W(L,t)}{\partial x} \qquad (3)$$

The displacement deflection shape can now be approximate by means of polynomial

$$W \approx W(x,t) = (1 + \alpha_1 x + \alpha_2 x^2 + \alpha_3 x^3 + \alpha_4 x^4)\left(\sum_{n=0}^{N} A_n X^n\right) e^{i\omega t} \qquad (4)$$

Where α's are determined from the boundary conditions of equations (2) and (3). Substitution of expression (4) into equation (2) and differentiated with respect to the undefined constant A's would yield a characteristics equation of the form

$$[K - \omega^2 M]\{A\} = 0 \quad (5)$$

In which K and M are the stiffness and mass matrices of the structure, and ω is the circular frequency.

NUMERICAL RESULTS AND DISSCUSSION

The first case studied is that of uniform cantilever beam (clamped at x=0) with rotational spring supported located at the free end of the beam. The first five frequency parameters are shown in **Table(1)** and compared with the exact values from the work of Lau[1], The table shows excellent agreement with exact results .

The second case studied is that of determination of the natural frequency parameter for an uniform, single span, spring hinged beam.

Table (1) Comparison of frequency parameters $(\omega^2 ml^4 / EI)^{1/2}$ for a uniform cantilever beam with translational spring and a rotational spring at the same point (K=ϕ=10).

x/l	Mode Sequence Number				
	1	2	3	4	5
0.2	2.136 (2.1268)	5.125 (5.0431)	8.211 (8.0236)	11 . 1 32 (11 ,002)	14.431 (14,206)
0 . 6	2.786 (2.7462)	5.032 (4.9737)	8.082 (8.0698)	11 . 356 (11 .283)	14,. 165 (14. 146)
1.0	2.744 (2.7146)	5.402 (5.3348)	8.412 (8.6607)	11.512 (11.4375)	14.532 (14.5271)

Numbers in parentheses are exact values.

Table (2) Comparison of frequency parameters $(\omega^2 ml^4 / EI)^{1/2}$ for a uniform cantilever beam with translational spring and a rotational spring at the same point (K=ϕ=10).

	Mode Sequence Number				
	1	2	3	4	5
10,10	17.273 (17.2 6 9)	49.682 (49.601)	101 .891 (101.318)	172.025 (171.748)	262.124 (261.527)
100,100	19.266 (19.272)	54.961 (54.509)	110.783 (108.773)	182.642 (182.180)	275.430 (274.921)

Numbers in parentheses are exact values

Beam where both ends elastically restrained against rotational and fully translationally restrained. The results of the frequency parameters for two combinations of rotational stiffness are considered together with exact results computed by Gorman[8] as shown in **Table (2)**. Again close agreement with exact results is achieved.

Figs. (2,3,4 and 5) show the relation between the frequency parameter $(\omega^2 ml^4 / EI)^{1/2}$ and the mode number under different values rotational spring constant for uniform single span beam.

Figs. (6,7,8 and 9) show the relation between the frequency parameter $(\omega^2 ml^4 / EI)^{1/2}$ and the mode number under different values off rotational spring constant for three span beam, which is symmetrically parabolas tapered in both width and depth where the central dimensions one half of end dimension and has both end translationally and rotationally spring supported.

It can seen from the figures presented in this paper that both the translational and rotational spring constants have significant effect on thee lower mode of vibration. This study also, shows that in general the translational spring constant has relatively greater effect on the frequencies than the rotational spring constant.

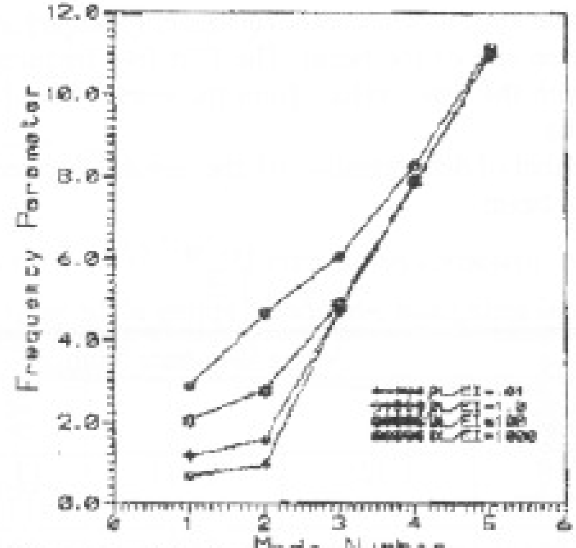

Figure(2) The relation between frequency parameter and model number for uniform restrained beam under diffrent rotary spring constant (KL/EI=0.1)

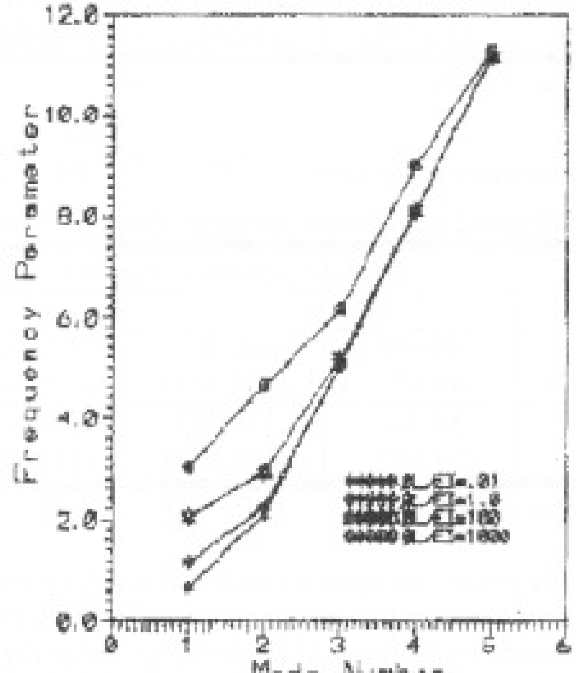

Figure(3) The relation between frequency parameter and model number for uniform restrained beam under diffrent rotary spring constant (KL/EI=1.0)

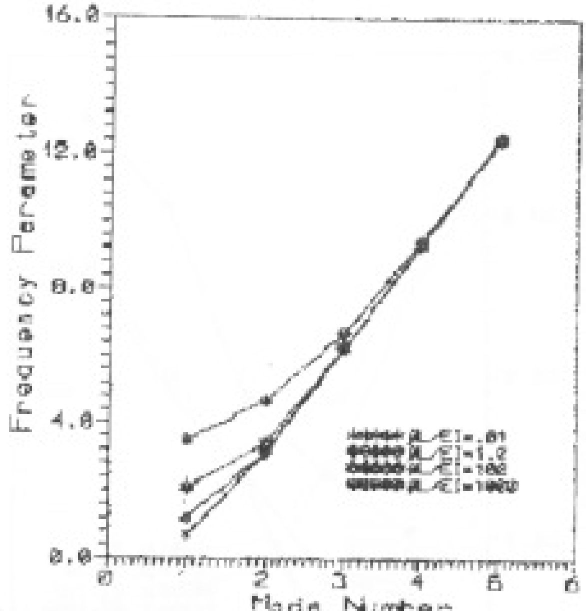

Figure(4) The relation between frequency parameter and modal number for uniform restrained beam under diffrent rotary spring constant (KL/EI=100)

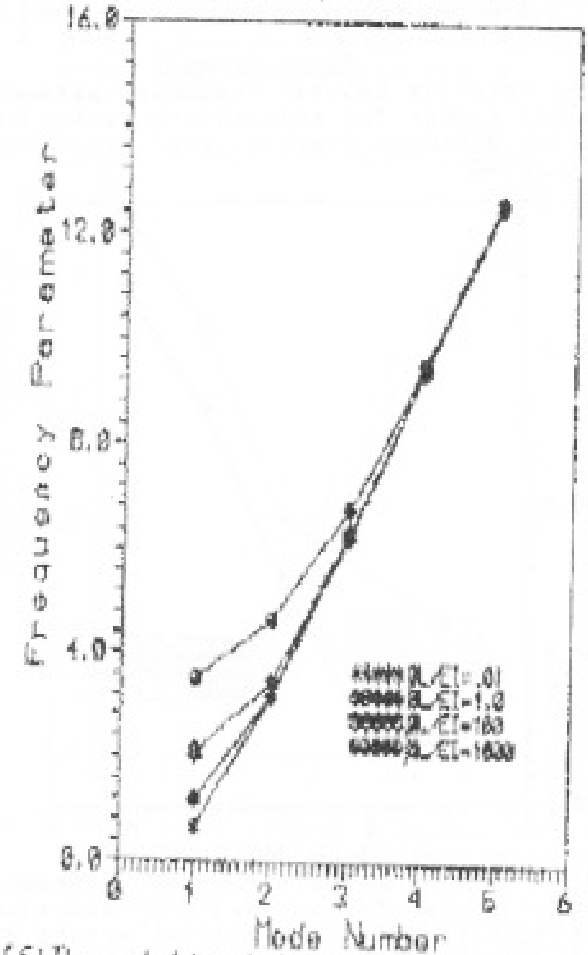

Figure(5) The relation between frequency parameter and modal number for uniform restrained beam under diffrent rotary spring constant (KL/EI=1000)

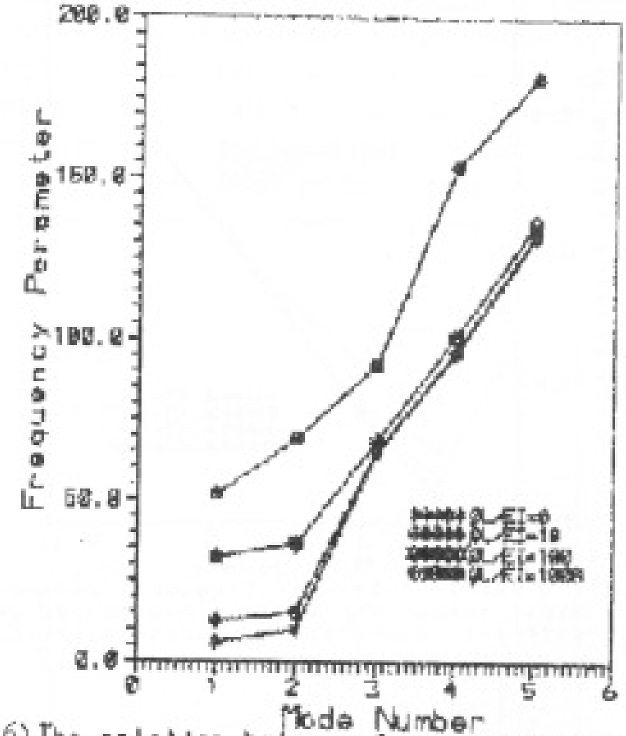

Figure(6) The relation between frequency parameter and modal number for non-uniform restrained beam under diffrent translational spring constant (KL/EI=0)

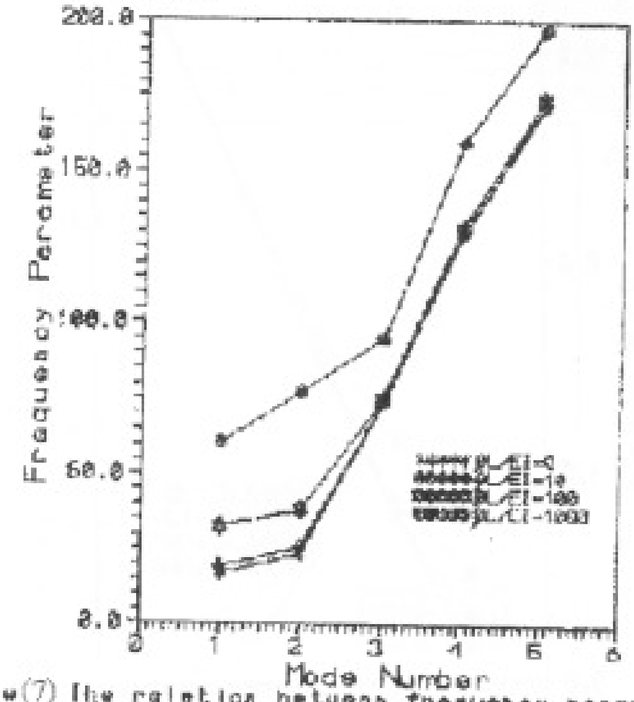

Figure(7) The relation between frequency parameter and modal number for non-uniform restrained beam under diffrent translational spring constant (KL/EI=10).

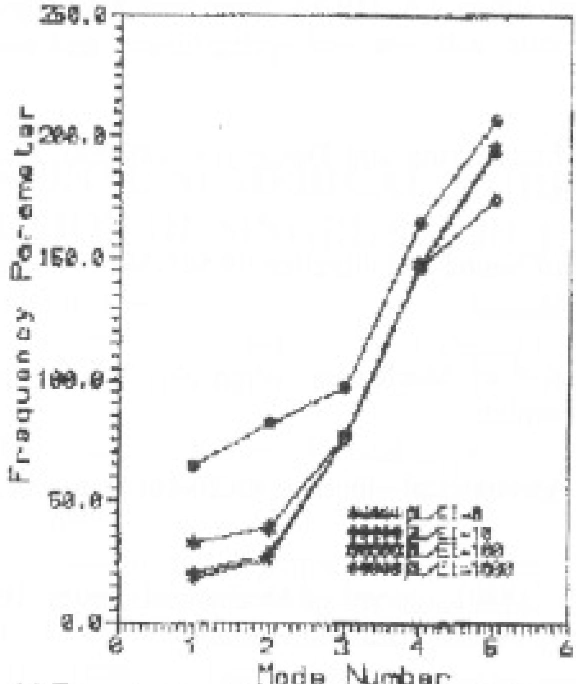

Figure(8) The relation between frequency parameter and modal number for non-uniform restrained beam under diffrent translational spring constant (KL/EI=100)

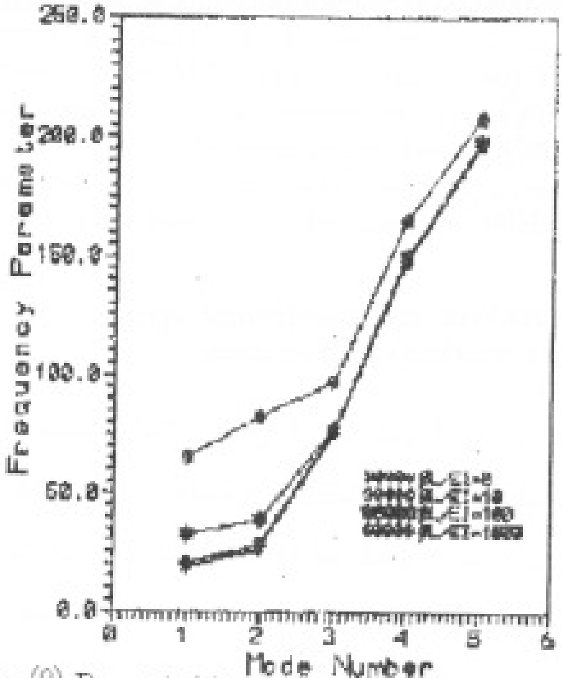

Figure(9) The relation between frequency parameter and modal number for non-uniform restrained beam under diffrent translational spring constant (KL/EI=1000).

ERENCES

H. (1984), Journal of Applied Mechanics 51, 182-187 Vibration frequencies and mode for constrained cantilever,.

Maurizi M. J. Rossi R. E. and Reyes J.A. (1976), Journal of Sound and Vibration 48, 565-568, Vibration frequencies for a beam with one end spring-hinged and subjected to a translational restraint at the other end.

Passig E.G. (1990), Nuclear Engineering and Design 14, 148-200, End slope and fundamental frequency of vibrating fuel rods.

Abbas B.A.H. (1984), Journal of Sound and vibration 99,541-548. Vibration of Timoshenko beams with elastically restrained sends,.

Sundararajan C. (1979), Journal of of Mechanical deign 101, 711-712. Fundamental frequency of beam with elastic rotational restraints,.

Abbas B. A. H.. (1985), The Aeronautical Journal 89,10-16. Dynamic analysis of thick rotating blades with flexible roots,.

Fossman R. and Sorensenjr A. (1980), Journal of Mechanical Design 102, 829-834. Influence of flexible connections on response characteristics of a beams,.

Gorman D. J. (1975), Free vibration analysis of beams and shafts, New York, John Wily.

Laura P. A. A. and Valerga Degreco B. (1988), Journal of Sound and Vibration 120(3), 537-596 Numerical experiments on free and forced vibrations of beams of non-uniform cross-section,.

NOMENCLATURE

I(x)- variable moment of inertia (m^4)
A(x)- variable cross-section area (m^2)
L- beam's length (m)
E- Young's modulus of elasticity (N/m^2)
ρ - density of the beam (kg/m^3)

ϕ_r and K - are the coefficient of rotational and translational springs.
K and M- are the stiffness and mass matrices of the structure
ω. is the circular frequency (rad/s).

TWO- DIMENSIONAL NUMERICAL MODEL FOR THERMAL POLLUTION OF SINGEL SOURCE IN RIVER

Prof. Dr. Rafa H. Al-Suhaili
College of Eng./ University of Baghdad

Mohsin Jasim Nasir
Technical institute of Mussuaib

ABSTRACT

The aim of this research was to apply a numerical model capable of describing the thermal pollution in rivers. For this purpose a two-dimensional numerical model was applied for estimating temperature distribution in a river .

Momentum Conservation Equation and Thermal Energy Equation were used to describe the distribution and diffusion of temperature along the river subjected to thermal pollution point source. Furthermore the model incorporates the (k-ε) turbulence model to calculate the distribution of turbulent viscosity .The pressure distribution was determined using hydrostatic pressure equation.

The partial differential equations were formalized and simplified to be solved using Alternative direction implicit- explicit method (ADI) with upwinding technique . The resulting system of linear simultaneous equations were then solved using Gauss-Elimination method .

A laboratory physical model was built to find experimental data . These data were used for model verification with data obtained from Al-Daura power station and Tigris river.

The model was found to be sensitive to the variation of river velocity and density difference and the model was found to be insensitive to the wind speed .The comparison of observed results from Al-Daura power station and laboratory physical model with those computed by the numerical model show a good agreement . The maximum absolute difference percentage are (16.2%, 8.6%) respectively

الخلاصة

يهدف البحث الى بناء نموذج عددي لدراسة التلوث الحراري في الانهار الناجم عن مصدر للتلوث الحراري
. ولهذا الغرض تم استنباط نموذج رياضي عددي لتمثيل هذه الظاهرة والتنبؤ بتوزيع درجات الحرارة في
النهر .تم استخدام معادلة حفظ الزخم ومعادلة حفظ الطاقة ومعادلات التوزيع الحـــراري لمعرفـــة توزيع
وانتشار درجات الحرارة خلال منطقة الدراسة وكذلك تضمن النموذج العددي معادلات الاضـــطراب
لحساب معاملات اللزوجة. كما تم اعتماد معادلة الضغط الهيدروستاتيكي لحساب الضغط في كل نقطة
بالدراسة .
تم تبسيط المعادلات التفاضلية المختلفة الاشكال بطريقة الاتجاه المتناوب (الضـــمني- الصـــريح)
المحددة (ADI) مع تطبيق منظومة Up Winding للحصول على معادلات جبرية خطية تم حلهـــا بطريقة
الحذف المتناوب (Gauss – Elimination)كما تم بناء نموذج مختبري لاغراض عمل التحقق لها

دي .لقد وجد ان النموذج حساس الى سرعة النهر والى تغير الكثافة وان النموذج غير حساس لتغير
عة الريح .

خلال مقارنة النتائج المقاسة في نهر دجلة اسفل محطة كهرباء الدورةالتي تعتبر مصدرتلوث حراريللنهر
ع النموذج المختبري مع النتائج المحسوبة من النموذج العددي الرياضي نلاحظ انها مقبولة الى حد ما
ة خطا مطلق مقداره (16.2%،8.6%) على التوالي.

INTRODUCTION

The rise of water temperature due to artificial effects is called thermal pollution .This typ[e] pollution can be defined as excessive change in the natural or ambient water temperature cause[d] the addition or removal of heat through man's activities .The heated water raise the temperatu[re] the body of water above it's normal level and can harm animals and plants living in the w[ater] (Richard,2000).

The major waste-heat producing industries are :steam-electric generation plants , petrol[eum] refineries , steel mill , chemical plants(mathur,1976).

The discharge of heated water directly to the river can be more dangerous to the health of [the] receiving water than organic pollution. Higher temperature reduces solubility of oxygen .More[over] ,the chemical reactions will proceed to a faster pace, hence , the water may go anaerobic w[ith] disastrous effects on its odor and appearance(Rute and Siliva,1997).

Al-Challabi (1994) developed a two- dimensional numerical model for the simulation of the spr[ead] and mixing of thermally polluted water disposed into the flow. This model considers the effec[t of] density difference between the pollutant density and the river water density

Li-Renyu and Righetto (1998) presented unsteady state two dimensional model to simulate [the] velocity and temperature field in the estuary of the Yangtza River in Brazil. It was found tha[t] simulation by using (K-ε)model can provide more details of flow fields and temperature distribu[tion] than that once obtained by using

Phenomenological algebraic for models of eddy viscosity and diffusivity Catirolgu and Yu[...] (1998) presented a mathematical model to predicts the long-term effects of once-through sys[tems] on local fish population. . The simulation indicates that entertainment and impingement may le[ad to] a population reduction of about 2% to 8% in the long run. Joody (2001) developed one and [two] dimensions numerical model for the simulation of the spread and mixing of thermally pol[luted] water disposed into the river flow released from the AL-Daura Power Station starting from [the] outfall up to 1000m downstream. The two dimensional model also discusses two cases, the f[irst] case neglects the effect of vertical velocity distribution while the second case include[s it]. Comparison of observed data on Feb 3, 2001 and July 27,2001 with data computed by t[he] dimensional model shows a good agreement with percentage error of 0.57% and 1.95% respect[ively]. In this research the finite difference method was used to solve the equations governing [the] phenomena of heat disposal. The solution was verified by a laboratory experimental work and field data obtained from Al-Daura power station .

NUMERICAL MODELING

Numerical model of thermal pollution is used by the formulation of the following set of pa[rtial] differential equations: (Rastogi and Rodi, 1978)

Momentum Conservation Equations

Horizontal Momentum Equation :

$$\rho\frac{\partial U}{\partial t}+U\frac{\partial U}{\partial X}+W\frac{\partial U}{\partial Z}=\frac{\partial}{\partial X}\left(\mu\frac{\partial U}{\partial X}\right)+\frac{\partial}{\partial Z}\left(\mu\frac{\partial U}{\partial Z}\right) \quad (1)$$

Vertical Momentum Equation :

$$\rho\frac{\partial W}{\partial t}+U\frac{\partial W}{\partial X}+W\frac{\partial W}{\partial Z}=\frac{\partial}{\partial X}\left(\mu\frac{\partial W}{\partial X}\right)+\frac{\partial}{\partial Z}\left(\mu\frac{\partial W}{\partial Z}\right)-\frac{\partial P}{\partial Z}+\rho g \quad (2)$$

3- Thermal Energy Equations :

$$\rho\frac{\partial T}{\partial t}+U\frac{\partial T}{\partial X}+W\frac{\partial T}{\partial Z}=\frac{\partial}{\partial X}\left(\frac{\mu}{\sigma}\frac{\partial T}{\partial X}\right)+\frac{\partial}{\partial Z}\left(\frac{\mu}{\sigma}\frac{\partial T}{\partial Z}\right)-\frac{\alpha(T-T_r)}{C_p * H} \quad (3)$$

4- K-ε turbulence model :

K-Equation :

$$\rho\frac{\partial K}{\partial t}+U\frac{\partial K}{\partial X}+W\frac{\partial K}{\partial Z}=\frac{\partial}{\partial X}\left(\frac{\mu}{\sigma_K}\frac{\partial K}{\partial X}\right)+\frac{\partial}{\partial Z}\left(\frac{\mu}{\sigma_K}\frac{\partial K}{\partial Z}\right)+G-\rho\varepsilon \quad (4)$$

ε- Equation :

$$\rho\frac{\partial \varepsilon}{\partial t}+U\frac{\partial \varepsilon}{\partial X}+W\frac{\partial \varepsilon}{\partial Z}=\frac{\partial}{\partial X}\left(\frac{\mu}{\sigma_\varepsilon}\frac{\partial \varepsilon}{\partial X}\right)+\frac{\partial}{\partial Z}\left(\frac{\mu}{\sigma_\varepsilon}\frac{\partial \varepsilon}{\partial Z}\right)+C_1\frac{\varepsilon}{K}G-C_2\rho\frac{\varepsilon}{K} \quad (5)$$

5- Density- Temperature relation ships.

$\rho = -0.0055T^2 + 0.0182\ T + 1000.1$ (6)

6- Longitudinal velocity vertical distribution:

$U = 2.5\ U_f\ Ln(Y/Y_o)$ (7)

7- Pressure distribution along the river depth $$P = g\int_0^Z \rho\, dZ \quad (8)$$

Finite difference was used for the solution of the above partial differential equations, and by using some assumption to transform these equation from non-linear to linear equations (Smith, 1978).These equations are simplified in a two-dimensional vertical and horizontal direction . Computer programming was used to perform the computations of the simulation model . It was written in Fortran-77 which works with Visual Fortran -97 language:

Equations (1,2,3) are considered as the three_ dimensional governing differential equations while Equations (4,5,6,7)are the auxiliary equations .

EXPERIMENTAL WORK

Laboratory physical model as shown in **Fig. (1)** was built to simulate the case of thermal pollution in rivers in order to obtain data for verification of the numerical model mentioned above. This model was built using galvanized steel pipes and tanks. Two pumps were used one for the heated water and one for the water that simulate the river water. The water was heated using electrical water heater .The water pipe was connected to the ground tank (feed tank),which then lifted to tanks number 1 and 2.The water in those tanks were connected to a glass flume which simulate the river through pipes ended by a tap after passing through electrical heaters (plant 1,and plant 2). The flume was fed by water from a re-circulation tank (tank no. 3). The flow was controlled by a weir

located at the end of the flume. The experiments was conducted to find the temperature along th flume downstream of the heated water outfall(the water from the tap). The temperature values we measured using thermometers distributed at selected distances from this tap.
Field data obtained from Al-Daura power station were also used to support this verificatio **Table(1)** shows the comparison of the temperature values along the Tigris river downstream of A doura Power station outfall with those obtained by the numerical model .The required informati about Tigris river obtained from (Euphrates center for studying and design or irrigatio project, 2001)

Table (1) Observed and Predicted temperature from Al-Daura power station

Distance(m)	Observed Temp.° C	Predicted Temp. °C(by Numerical model)	Absolute difference %
Outfall	44	44	0
50	32.7	38	16.2
100	30.8	34.5	12
150	30.5	32	5
200	30.3	30.6	0.004
250	30	30	0
300	29.8	29.8	0
350	29.7	29.7	0
400	29.7	29.7	0
450	29.7	29.7	0
500	29.7	29.7	0

Table(2) shows the comparison of the temperature values observed from the laboratory mo downstream of the point source outfall with those obtained by the numerical model .

Table (2) Observed and Predicted Temperature Data from Laboratory Physical Model.

Distance (m)	Observed temp.° C (in the laboratory model)	Predicted temp.° C(by the numerical model)	Absolute Differ %
0	55	55	0
0.5	38	41.3	8.6
1	32	33.1	3.4
1.5	30	30.6	2
2	30	30.1	0
2.5	30	30	0
3	30	30	0
3.5	30	30	0
4	30	30	0

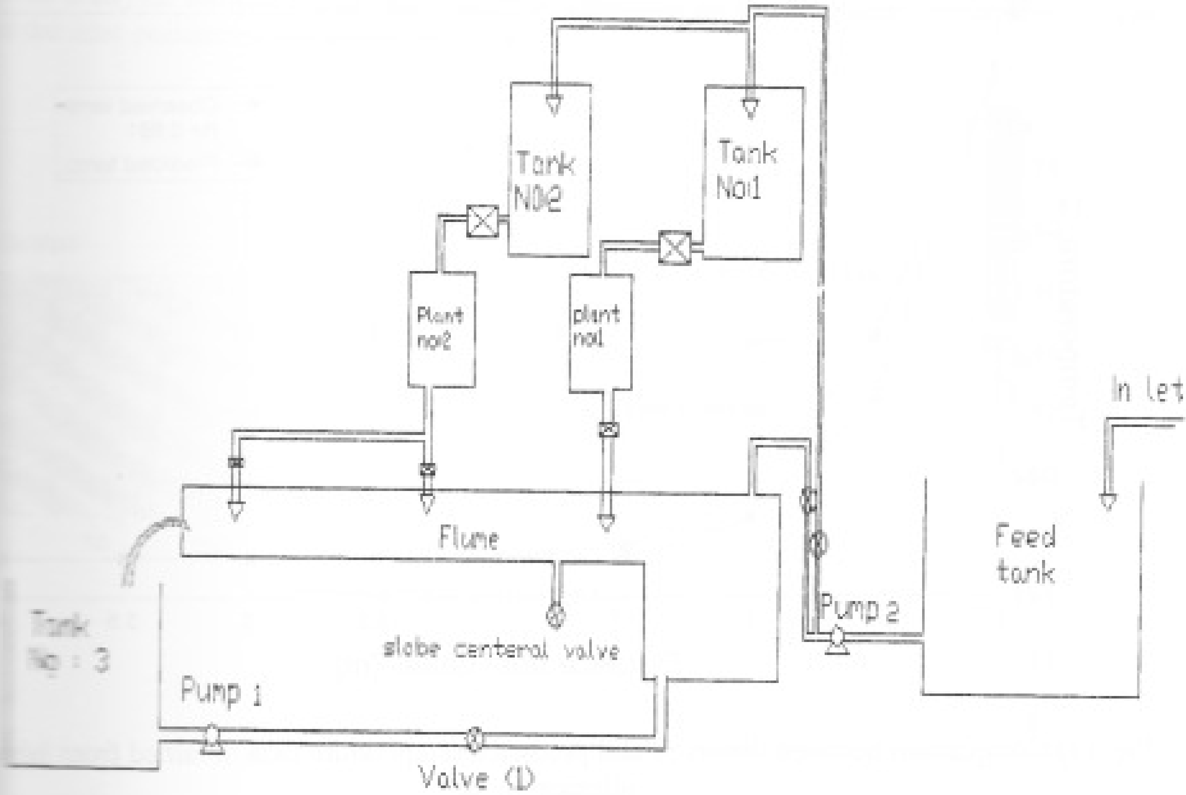

Fig. (1) Physical laboratory model

RESULTS AND DISCUSSION

Before using the results of the numerical model to study the effect of different parameters on the temperature distribution the model should be verified. The verification was carried out by conducting a comparison between the observed results from laboratory physical model and Al-Daura power station with predicted results obtained from numerical model as shown in **Figs. (2,3)**. The maximum percentage difference was found to be (16.2%,8.6%) ,and the correlation coefficient between those results are (0.917 , 0.991) respectively .

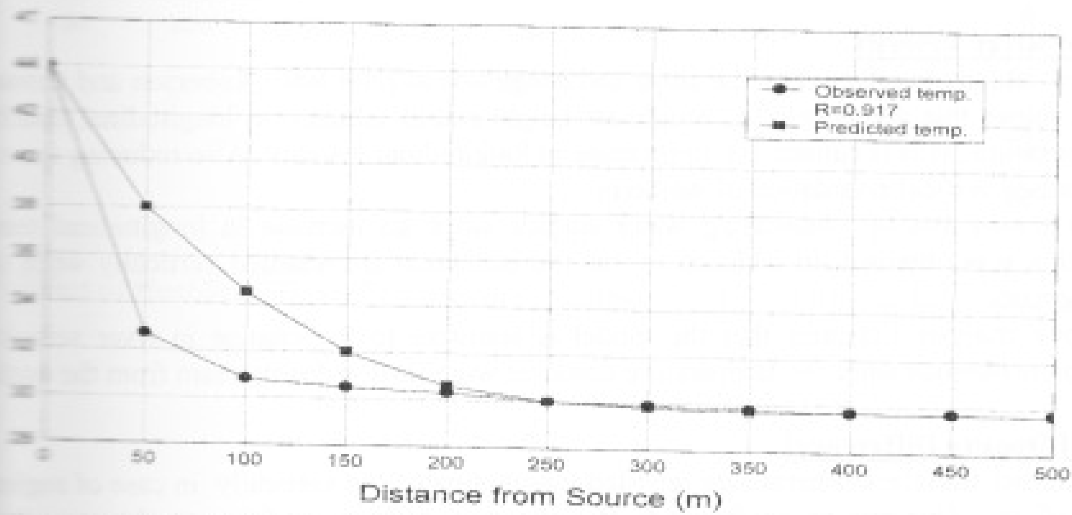

Fig.(2) Comparison between observed and predicted temperature data obtained from Al-Daura power station.

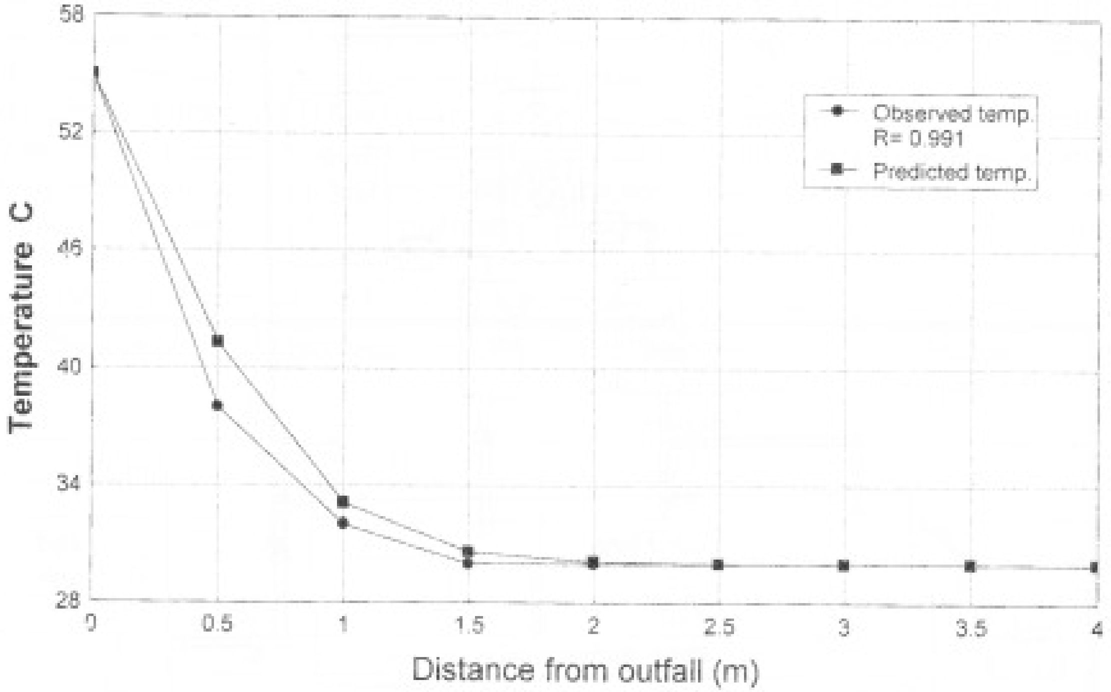

Fig. (3) Comparison between observed and predicted temperature data obtained from laborator physical model.

SENSITIVITY ANALYSIS

Sensitivity analysis was carried out to obtain the effect of the several important model parame on the temperature distribution as follows:

Effect of Wind Speed

Fig. (4) shows the comparison between the results obtained by excluding and including h transfer coefficient respectively .From this figure , it can be found that excluding or including t heat transfer from the water surface showed no noticeable change in temperature distribution .
The above analysis indicated that the model is insensitive to the variation in the wind speed. Thi obvious from the comparison of the temperature contours for the two cases which is almost simil

Effect of River Velocity

The river velocity is effected by the slope and roughness of river bed. (Roberson and Crowe, 19
Fig. (5) shows that decreasing the roughness height causes increase in longitudinal distributi the temperature .This is caused due to increase in longitudinal velocity .Also reducing the rough height causes vertical retardation of isotherms .
Fig. (6) shows that by increasing water surface slope an increase in longitudinal temper distribution was obtained, in addition to this the isotherms are retarded vertically when the wa slope increase.
The above analysis indicates that the model is sensitive to the change in river velocity . T indication is obvious since the temperature contours were shifted downstream from the outfall.

Effect of Density Difference:

Fig. (7) shows that the isotherms are retarded longitudinally and vertically in case of neglectin density effect . This can be attributed to the effect of a buoyancy force on the spreading of temperature .

e above analysis indicates that the model is sensitive to the variation of density difference ween the heat polluted water and river water .

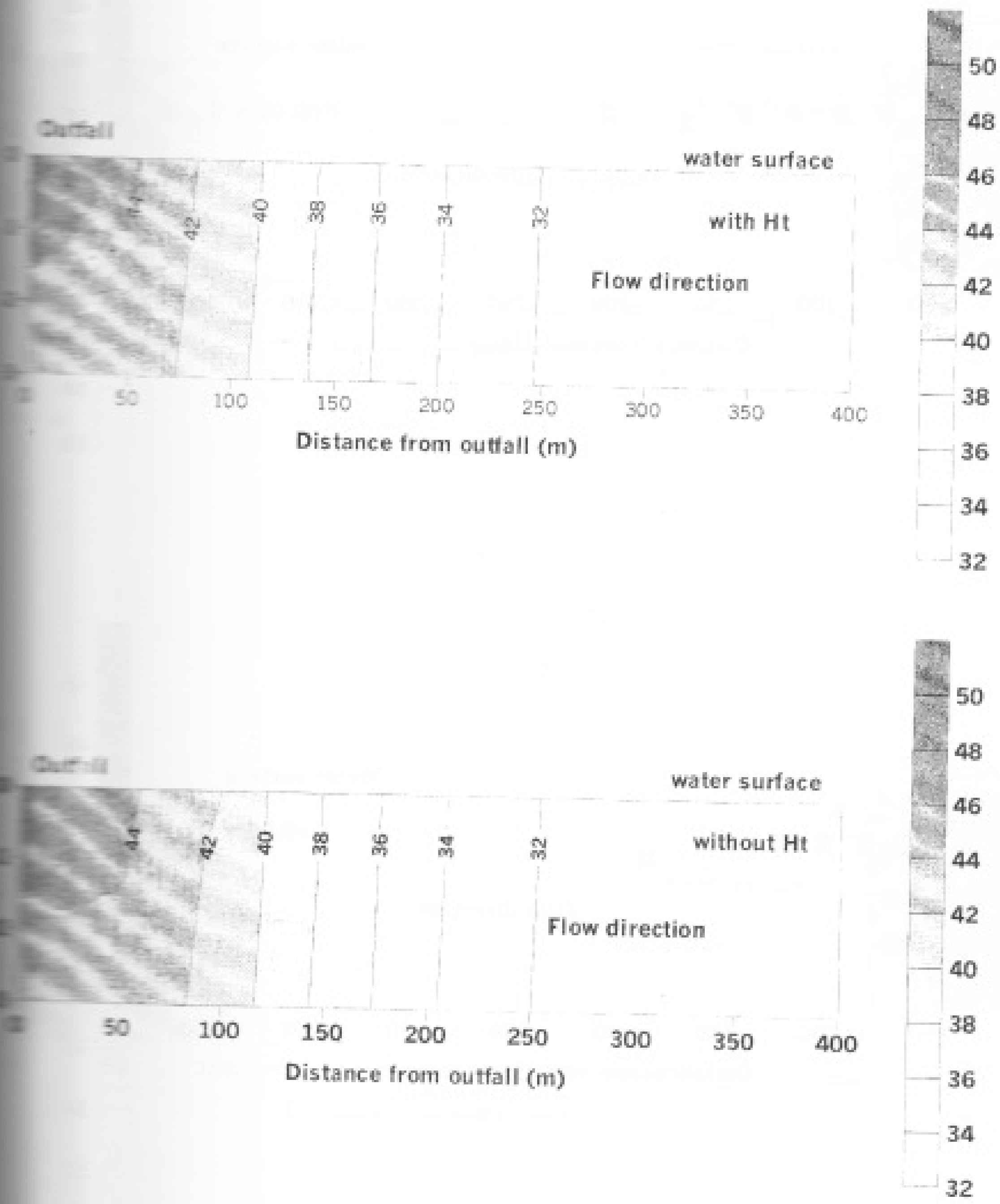

Effect of Heat Transfer on Temperature Distribution .(Td=50 °C, Tr=30 °C, t=300sec)

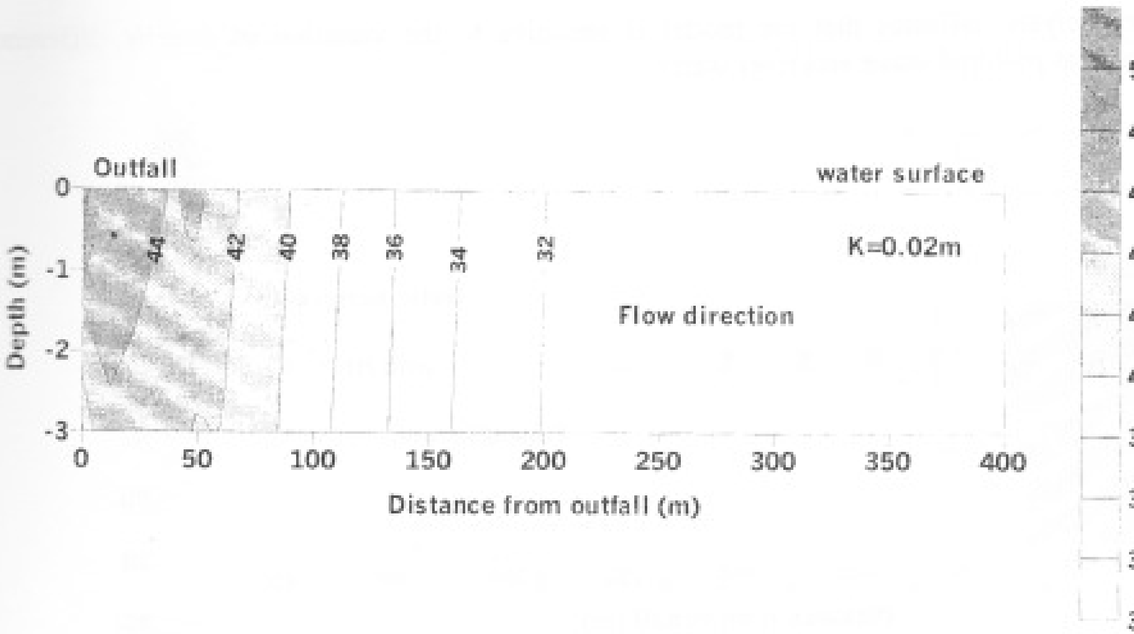

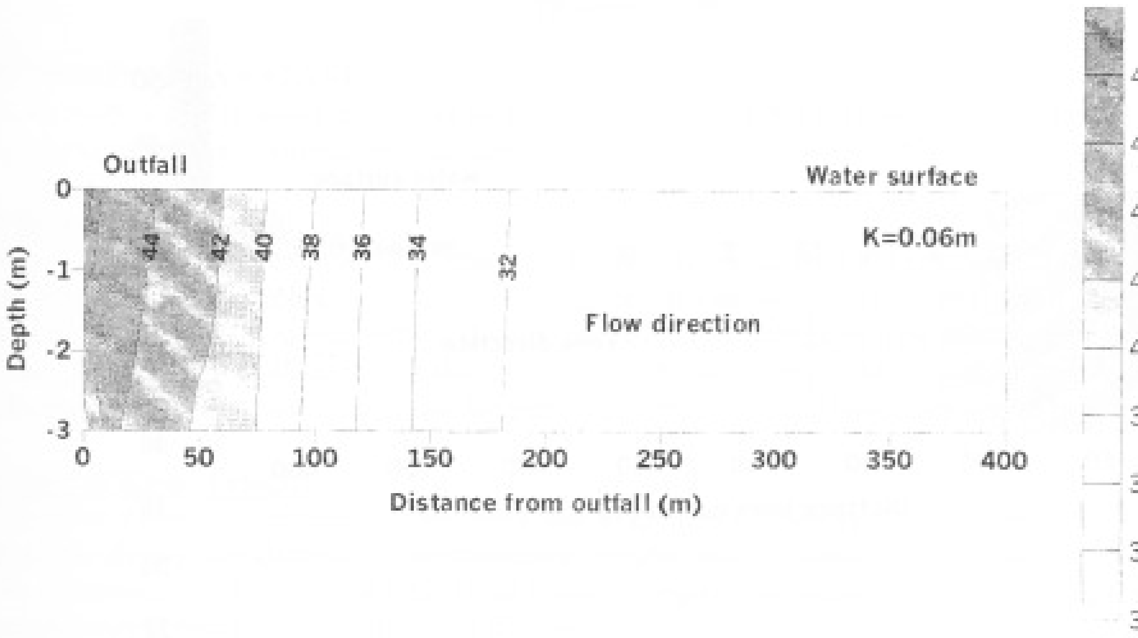

Fig. (5) Effect of Roughness Height on Temperature Distribution . (Tr=30 °C, Td=50 °C, t=300

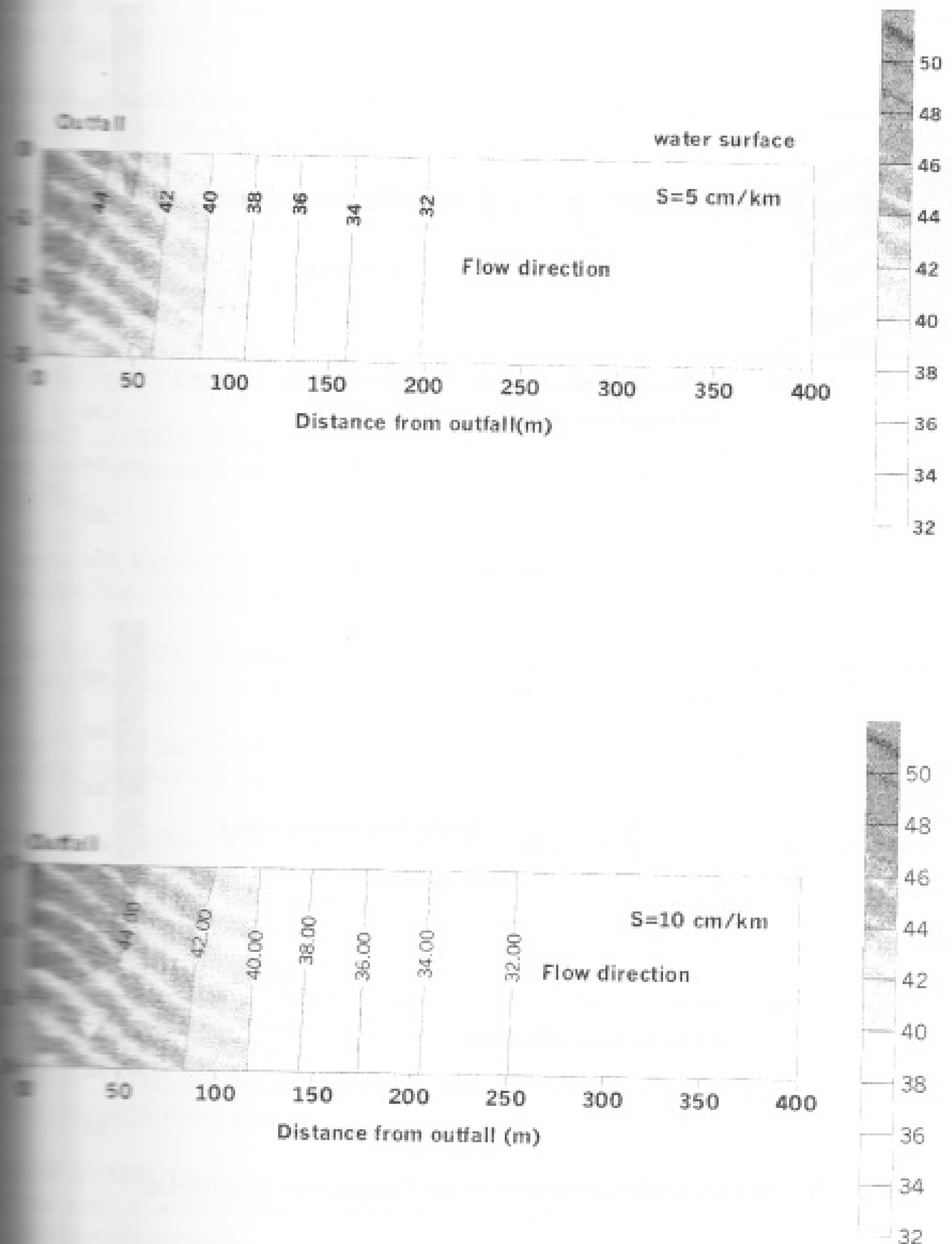

Fig. (6) Effect of River Slope on Temperature Distribution .(Tr=30 °C, Td=50 °C, t=300sec)

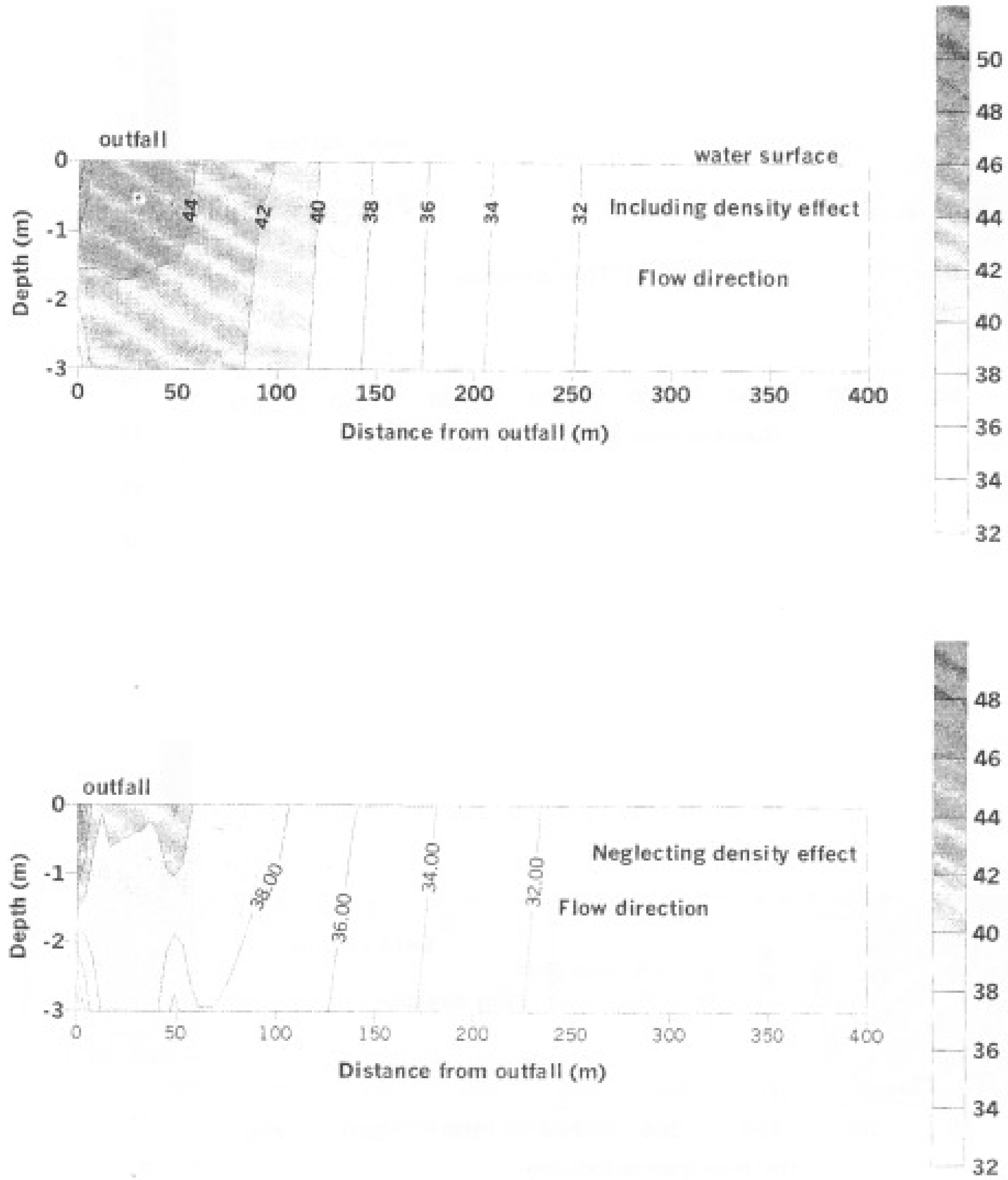

Fig. (7) Effect of Density Difference on the Temperature Distribution .

CONCLUSIONS

1- The numerical model is insensitive to the variations of wind speed .
2- The numerical model is sensitive to the variation of roughness height of the river bed , slope water surface , density difference between the heated water density and the river water density
3- The model can be utilized to study the effect of various physical parameters on temperat distribution .

REFERENCES

Al-Challabi M. A., (1994) , Numerical Model of Thermal pollution Transport in river , M.S Thesis , College of Engineering University of Baghdad.

Hermann M and T.Webster Ian, (1998), Dynamics of temperature stratification in lowland rivers Hyd. Div, Vol.124, No.10 , pp.1059-1063.

C., and Yurteri, C., (1998), Methodology for predicting cooling water effects on fish , Env. Eng., Vol.124, No.7, pp.612-618.

A.J., (1987), Validation of Three -Dimensional Numerical model of a buoyant plume , Report No.SR121, Hydraulic Research Center, Waling ford.

Company for studying and design of irrigation projects (2001) .

A.S., (2001), Studying of the Heated Water Released from AL-Doura Power Station, M.Sc. Thesis, College of Engineering, University of AL- Mustanseryya.

T.J., (2002), Design of two-dimensional numerical model for thermal effluents transport in river released from South-Baghdad electric power station, M.Sc. Thesis, University of Technology.

and Righetto A.M. (1998), Tidal and transport modeling using turbulence K-ε model, Hyd. Div, Vol.124, No.3, pp.212-221.

S.P., (1976), Thermal discharges, Handbook of water resources and pollution control , W Gehm and Jacob I.Bregrman,eds, Van Nostrand Reinhold Comp.pp.717-779.

A . K., and Rodi, W ., (1978), Prediction of heat and mass transfer in open channels, Hyd.Div. Vol.104,No.3, pp.397-420

N.L, (2000), Professor of environmental policy , department of environmental science and engineering , university of north Caroline , Email:pete_andrews@unc.edu.

J.A, and Crowe, C.T., (1997), Engineering fluid mechanics, John Wiley and Sons , New York.

Neves and Silvia Lourenco (1997), Thermal Pollution, www. physical/moor/messages/102.htm. Internet.

G.D., (1978), Numerical solution of partial differential equation, finite difference methods " University Press, England.

LIST OF SYMBOLS

the x,and,z water velocity components in x,and,z components respectively
Hydrostatic pressure
Gravitational acceleration
Surface wind velocity at distance yo from ground
Wind velocity at any depth y from ground surface
Water temperature
River Roughness Height
Water Density
Source Water Temperature
River Water Temperature

MIXED CONVECTION FROM ELECTRONIC EQUIPMENT COMPONENT AT DIFFERENT POSITION AN ENCLOUSER BY PRIMITIVE VARABILS METHOD

Dr.Jalal M.Jalil
Mech. Eng. Dept.
Military College of Eng
Assist. Prof.

Dr.Khalid.A.Ismael
Mech. Eng. Dept
Technology University
Prof.

Mr.Sattar J.Habeeb
Mech. Eng. Dept
Technology University
Assist. Teacher

ABSTRACT

A numerical study of mixed conv. . tion cooling of heat dissipating electronic component, located in a rectangular enclosure ,and cooled by an external through flow of air is carried out .A conjugate problem is solved by primitive variables method, describing the flow and thermal fields in air .The interaction between the components is of interest here, depending on their relative placement in the enclosure, and different configuration are considered. for $Re = 100$ laminar, steady flow is predicted for up to $Gr/Re^2 = 25$ according to heat source location in the enclosure. The mixed convection regime, where the buoyancy effects are comparable to the forced flow, occurs at values of Gr/Re^2 between 0.01 and 25 .The results are of values in search for suitable placement of electronic components in an enclosed region for an effective heat removal. In general , it appears that the location of the source on the left vertical wall is the most favorable in terms of cooling. Laminar results are predicted up for up to $Gr = 2.5 * 10^5$ for all configurations studied .

الخلاصة

تم دراسة تشتيت الحرارة الناتجة من أداء الأجهزة الإلكترونية الموضوعة داخل تجويف مستطيل الشكل ، من اجل تبريدها بواسطة هواء خارجي يسلط عليها، مما يؤدي إلى الاستفادة من انتقال الحرارة بالحمل المختلط الناتج من ذلك. حيث تمت الدراسة باستخدام الحل العددي التقريبي لمعادلات الكتلة والزخم والطاقة عن طريق وصف الحركة الديناميكية والحرارية للمائع. أن عملية التداخل الناتجة من وجود اكثر من مصدر حراري داخل الحيز المدروس هي المسألة المهمة هنا ، اعتمادا على موقع المصادر الحرارية نسبيًا بعضها إلى البعض الأخر داخل التجويف المستطيل الشكل . كما تم أخذ تغير موقع المصادر الحرارية داخل الحيز بنظر الاعتبار ، بالنسبة $Re = 100$ ، جريان طباقي، مستقر، إلى رقم ريشاردسون Gr/Re^2 بحدود 25 طبقا إلى موقع المصدر الحراري داخل الحيز. في منطقة الحمل المختلط فأن تأثير قوى الطفو قورنت نسبة إلى حالة الحمل القسري والتي تتكون لرقم ريشاردسون بين 25 – 0.01. النتائج كانت لقيم البحث عن افضل موقع للمصدر الحراري داخل الحيز عن طريق تأثير إزالة الحرارة .بصورة عامة أتضح أن وضع المصدر الحراري على الجدار العلوي الأيسر

للحيز المدروس يعطي أفضل أداء لعملية التبريد وإزالة الحرارة.كما كانت قيم رقم كراشوف بحدود $Gr = 2.5 * 10^5$ لكل الحالات المدروسة .

KEY WORDS
cooling of electronic component ,mixed convection , CFD ,simulation , enclosure .

INTRODUCTION

An area which has seen a considerable amount of research activity in the recent years is that of heat removal for electronic equipment with the continued effort to decrease the size of electronic equipment , the energy dissipated per unit area has increased substantially in most engineering applications . Air cooling is still the most attractive method for computer system and other electronic equipment ,due to its simplicity and low cost . Thermal engineers in the electronics industry are always trying to achieve the best possible performance out of air cooling . In this effort , the need to understand the variety of flow phenomena and convective heat transfer mechanisms that are present in air - cooled electronic systems is obvious.

A number of studies on the convective heat transfer in enclosure , such as solar collection systems , room ventilation and electronic circuit have been extensively reported regarding the cooling process. Recently, considerable attention has turned to mixed convection problems owing to many practical applications including cooling of electronic equipment and devices {G.P. Paterson and A. Ortega 1990 },{K.J. Kennedy and A. Zabib 1983}. In an enclosure , the interaction between the external forced stream and buoyancy driven flow induced by the increasing high heat flux from electronic module leads to the possibility of complex flow. Therefor its important to understand the heat transfer characteristics of mixed convection in the enclosure.

Mixed convection flow and heat transfer has been studied for inclined channels with discrete heat sources {C.Y. Choi and A. Ortega 1993 } , { C. Yucel , H. Hasnaoui, L. Robillard , and E. Bilgen 1993}. It is found by Choi that the best performance in heat transfer is obtained when the channel is in a vertical location . The Yucel is pointed out that the normalized Nusselt number is a decreasing function of the Reynolds number and an increasing function of the inclined angle .{ E. Papanicolaou and Y. Jaluria 1990 and 1993} studied mixed convection from an isolated heat source in a rectangular enclosure . They indicated that flow patterns generally consist of high- or low- velocity recirculating Celia due to buoyancy forces generated by the heat source .

In addition, the effect of the thermal conductivity of the cavity walls on the heat transfer phenomena was investigated by Jaluria . A later investigation { E. Papanicolaou and Y. Jaluria 1995} further presented turbulent flow in a cavity by **k-ε** model . Turbulent results were obtained for $Re=1000$ and 2000 , in the rang of $Gr=5*10^7$ to $5*10^8$. A detailed study of mixed convection in a partially divided rectangular enclosure was presented by { T.H. Hsu ,P.T. Hsu , and S.P. How 1997 }. It was observed that the heat transfer coefficient decrease rather rapidly as the height of the partition is more than about half of the total height of the enclosure . In the present work , therefore , where a enclosure configuration is considered , with protruding heat sources at various locations , the following conditions are considered :-

1- convection heat transfer in the enclosure only .
2- protruding heat sources (blocks) in the enclosure, mounted on surfaces that are either parallel or perpendicular to each other.
3- Interaction between a buoyancy – induced flow and a forced flow whose direction is perpendicular to the gravity vector.

The geometry of the cavity and the relevant parameters considered here are shown in **Fig(1),** for the study of the conjugate problem. The walls are assumed to be small thickness therefor the conduction through it can be neglected .The total dimensions Htot ,Wtot include the corresponding dimensions of the air – filled cavity plus the thickness of the walls.

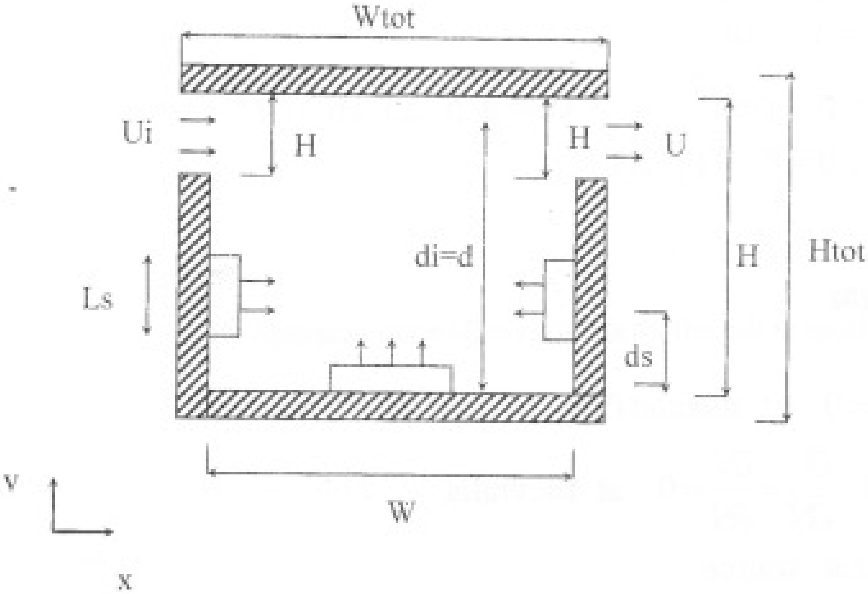

Fig.(1).Physical model of the gavity.

The configuration shown in **Fig.(1)** is a generic case , including three location of the sources , corresponding to the left , right and the bottom side walls . This case will be referred to as LRB for brevity from now on . However, most different locations and the corresponding configurations will be, respectively , named as LR (for sources on the left and right walls) , LB (left and bottom walls) , and RB (right and bottom walls) configuration s .The heat sources will be referred to as L , R, and B depending on their respective location .
The two dimensional problems is studied here , where each heat source actually represented a row of electronic components , sufficiently long in the third dimension .

MATHEMATICAL FORMULATION

Model Equations

The equation describing the problem for the configuration of **Fig.(1)** are the Navier-Stokes equations for the fluid , with buoyancy effect taken into account , as well as the energy equation , which describes the temperature variation through the fluid (air) , the flow assumed to be steady , laminar , and incompressible.
The nondimensional equations can be written as :-

$$\frac{\partial U}{\partial X}+\frac{\partial V}{\partial Y}=0 \tag{1}$$

$$U\frac{\partial U}{\partial X}+V\frac{\partial U}{\partial Y}=-\frac{\partial P}{\partial X}+\frac{1}{Re}\nabla^2 U \tag{2}$$

$$U\frac{\partial V}{\partial X}+V\frac{\partial V}{\partial Y}=-\frac{\partial P}{\partial Y}+\frac{1}{Re}\nabla^2 V+\frac{Gr}{Re^2}\theta \tag{3}$$

$$U\frac{\partial \theta}{\partial X}+V\frac{\partial \theta}{\partial Y}=\frac{1}{Re\bullet Pr}\nabla^2\theta \tag{4}$$

Where the above equation are non dimensionalized by using the dimensionless parameters defined as :-

$$X = x / Hi \ , \ Y = y / Hi$$
$$U = u / ui \ , \ V = v / ui$$
$$Pr = \nu / \alpha \ , \ P = p / \rho ui^2 \ ; \quad Gr = g.\beta.\Delta T.Hi^3 / \nu^2 \qquad (5)$$
$$Re = ui.Hi / \nu \ , \ \theta = T - Ti / \Delta T$$
$$\Delta T = Th - Ti$$

Boundary Conditions

The boundary conditions at the inflow and the outflow are, respectively :-

$$Ui=1,\ Vi=0\ ,\ \theta i=0 \quad \text{at the inlet flow.}$$
$$U=0,\ V=0 \ \text{ and } \ \frac{\partial U}{\partial N}=\frac{\partial V}{\partial N}=0 \quad \text{at the walls.} \qquad (6)$$
$$\theta i=1 \quad \text{at the heat source}$$
$$\frac{\partial U}{\partial N}=\frac{\partial V}{\partial N}=\frac{\partial \theta}{\partial N}=0 \quad \text{at the exit flow (smoth exit)}$$

The sensitivity of the solution to the outflow boundary conditions was tested by Papanicolaou and Jaluria{5}.The mean Nussult number define as :-

$$\overline{Nu} = \int_0^1 \frac{1}{\theta(y)} dy \qquad (7)$$

NUMERICAL METHOD

Governing Eqs.(1- 4) were solved numerically by the primitive variables method (finite volume method) to obtain steady state laminar flow solution , with hybrid scheme approximation for the convective terms {J.P. Simoneau , C. Inard , and F. Allard 1988}. The second upwind and central differencing scheme were also used for comparison and no significicent differences were found .

To determine the appropriate grid size with which grid independent solutions can be Obtained , the calculation were done on increasingly finer grid size distributions. A 21*21 uniform grid with a denser clustering near the walls was considered to give – independent result . To corroborate this the 21*21 grid results were compared with the solution on an 42*48 uniform grid . The two results compare very well with each other with a maximum local difference of 4.5% in the two solutions. The general transport equation for laminar flow in cartesian coordinates may be presented by :

$$\frac{\partial(\rho\Phi)}{\partial t}+\frac{\partial(\rho\Phi U_j)}{\partial X_i}=\frac{\partial}{\partial X_i}\left(\Gamma_\Phi\frac{\partial\Phi}{\partial X_i}\right)+S_\Phi$$

where

$i = 1,2,3$

$\frac{\partial(\rho\Phi U_i)}{\partial X_i}$ = convection term (8)

$\frac{\partial}{\partial X_i}\left(\Gamma_\Phi\frac{\partial\Phi}{\partial X_i}\right)$ = diffusion term

S_Φ = source term

where Φ is the dependent variable . **Table (1)** gives the expressions for the source terms S_Φ for each variable that is likely to be needed in solving cooling problems .

Table (1) Source Terms in the Transport Equations.

Equation	Φ	Γ_Φ	S_Φ
Conntinuity	1	μ	0
Momentum	U1 = U	μ	$-P_X+1/3(\mu\nabla.U)+\rho g_x$
Momentum	U2 = U	μ	$-Py+1/3(\mu\nabla.U)+\rho gy$
Momentum	U3 = U	μ	$-Pz+1/3(\mu\nabla.U)+\rho gz$
Temperature	T	Γ	Q/Cp

μ : dynamic viscosity , Γ : diffusion coefficient (diffusivity)

If we use the Boussinesque approximation, we get :-

$\rho g_x=\rho g_z=0$

$$\rho g_y=-g\left(1-\frac{\Delta T}{T}\right) \text{ where } \Delta T=T-Tr \qquad (9)$$

Tr = Reference Temperature

Solution of Governing Equations

Most of the reviewed material solve the models using the finite volume based methods. The most frequent scheme used in solving the air flow was the SIMPLE scheme and some of its variations (SIMPLEC etc...). Most investigators used the hybrid method (central / upwind Differencing), for solving the transport equation, In the following sections the equations are first discretized using finite volume methods, then a suitable difference scheme is applied. The solution process is finally concluded with the method of applying the boundary conditions.

Discretization Methods

To solve the governing equations numerically they must be discretized and formulated in such a way to preserve there nature. Two main methods of discretization are the finite element and finite difference methods. The use o f the finite element method was thought to be much better since it offers greater flexibility specially for difficult geometries. Finite difference schemes are widely used , and are the more common . Complex geometry's can be modeled when generalized coordinates are used. Finite difference scheme may be derived either by using the Taylor expansion polynomial approximation or by the use of the finite volume scheme.

Finite Volume Method (Control Volume)

The basic idea of the control volume (CV) formulation is to divide the domain into a number of non-overlapping CV's such that there is one CV surrounding each grid point. The differential equation is integrated over each CV, {H.K. Versteeg and W. Malalasekera 1995 }. The most attractive feature of the CV formulation is that the resulting solution would imply that the integral conservation of quantities such as mass, momentum and energy is exactly satisfied over each and any group of CV's and of course over the whole computational domain.

This characteristic exists for *any* number of grid points, not just in a limiting sense when the number of grid points becomes large. Then, even the coarse-grid solution exhibits *exact* integral balances.

Two Dimensional Discretization

The general transport equation may be written as,

$$\frac{\partial(\rho\Phi)}{\partial t}+\frac{\partial}{\partial X_i}\left(J_i\right)=S_\Phi \qquad (10)$$

where $J_i=\rho U_i\Phi-\Gamma_\Phi\dfrac{\partial\Phi}{\partial X_i}$

Ji represents all the flux due to both diffusion and convection. The source term may be expressed as a linear expression :-

$$S_\Phi = b\Phi_p + c \qquad (11)$$

Note the pressure term is excluded from the source term (in the momentum equation) in the solution procedure, and the linearization is done for all other terms only.

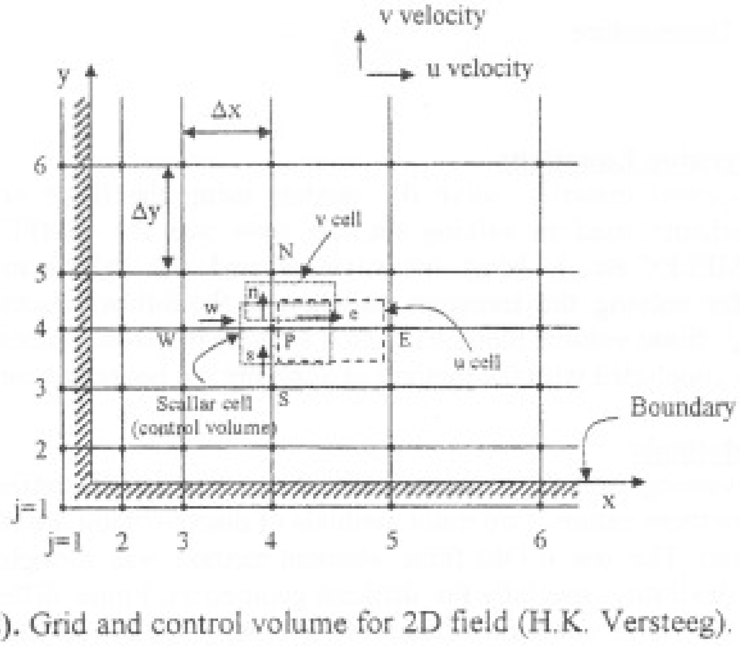

Fig.(2). Grid and control volume for 2D field (H.K. Versteeg).

Integrating using the CV we get ,

$$\left(\rho_p\Phi_p - \rho_p^o\Phi_p^o\right)\Delta A/\Delta t + J_e - J_w + J_n - J_s = \left(b\Phi_p + c\right)\Delta A \qquad (12)$$

where n (north) and s(south) are the neighbouring points of p in the y-direction , $\Delta A = \Delta X^* \Delta Y$ is the area of the CV, and the J's are the integrated total fluxes. Integrating the continuity gives,

$$\left(\rho_p - \rho_p^o\right)\Delta\rho/\Delta t + F_e - F_w + F_n - F_s = 0 \qquad (13)$$

where the F's are the mass flow rates through the control surfaces. The general two-dimensional discretization equation can be obtained from eq.(12) and eq.(13), and is given by,

$$\left(\sum_i a_i + a_p^o - b\right)\Phi_p = \sum_i a_i\Phi_i + c \qquad (14)$$

where

$$\sum_i a_i = a_p = a_e + a_w + a_n + a_s$$

$$\sum_i a_i\Phi_i = a_e\Phi_e + a_w\Phi_w + a_n\Phi_n + a_s\Phi_s \qquad (15)$$

$$a_p^o = \rho_p^o\,\Delta A/\Delta t$$

$$b = S_p\Delta A$$

$$c = S_u\Delta A + a_p^o\Phi_p^o$$

Applying any scheme to solve this will give the values of ai , for instance if the Hybrid scheme is used ,

$$a_e = \langle 0, D_e - 0.5|F_e|\rangle + \langle 0, -F_e\rangle$$

$$a_w = \langle 0, D_w - 0.5|F_w|\rangle + \langle 0, F_w\rangle \qquad (16)$$

$$a_n = \langle 0, D_n - 0.5|F_n|\rangle + \langle 0, -F_n\rangle$$

$$a_s = \langle 0, D_s - 0.5|F_s|\rangle + \langle 0, F_s\rangle$$

The convection and diffusion fluxes are given by,

$$F_e = (\rho U)_e\Delta y \quad \& \quad D_e = \Gamma_e\Delta y/\delta x_e$$

$$F_w = (\rho U)_w\Delta y \quad \& \quad D_w = \Gamma_w\Delta y/\delta x_w \qquad (17)$$

$$F_n = (\rho U)_n\Delta x \quad \& \quad D_n = \Gamma_n\Delta y/\delta y_n$$

$$F_s = (\rho U)_s\Delta x \quad \& \quad D_s = \Gamma_s\Delta y/\delta y_s$$

All the coefficients in eqs. (15) and (16) are used for solving for (Temperature , kinetic and dissipation , ..), the velocity components are calculated on a staggered grid and there values differ.

RESULTS AND DISCUSSION

Definition of Physical and Geometric Parameters

The results to be presented here will focus on the effect of certain parameters , while keeping the others fixed. More specifically , the parameters listed below in dimensionless

form, chosen to represent a cavity that would most likely appear in an electronic system, although not exclusively so, are kept fixed at the following values see **Fig(1)**).
Aspect ratio of the air – filled cavity $A = H^*/W^* = 1$, $Hi^* = Ho^* = Ls^* = 1$, $di^*/H^* = do^*/H^* = 0.8571$
The distance of the center of the sources from the bottom of the cavity is taken such that $ds^*/H^* = 0.357$, while on the bottom wall the corresponding distance is $ds^*/W^* = 0.5$, measured from the left vertical wall. The parameters to be varied here the Grashof number, the number of the sources, and the relative locations of the sources. All the alternative cases will be compared to each other. The Reynolds number is being kept fixed in this work at $Re = 100$, a value representative of the laminar regime, characterizing on incoming flow of a relatively low velocity. For instance, an air flow of about 0.1 m /s ,entering through an opening 2 cm height at $20 c^{\circ}$ would yield a Reynolds number of the above – mentioned order of magnitude .Higher values of Re have been considered before {Jaluria 1990}, and the basic flow in the cavity were not affected significantly as long as $Re \leq 1000$ The Grashof number is varied in the range $Gr = 10^3 - 2.5 * 10^5$ and this effect will be presented .

In what follows, as a variation in the Richardson number Gr/Re^2 over the corresponding range . Gr/Re^2 Is a more suitable parameter in mixed convection problems and since the Reynolds number is kept fixed, varying the value of Gr/Re^2 will be equivalent to varying the heat input from the sources. Generally , the Grashof number encountered in electronic cooling are of the order of 10^5 or higher, but in this case ,in order to get a more complete picture of the effect of Gr/Re^2 on the heat transfer, the rang of Gr has been extended to lower values.

Flow and thermal field for steady mixed convection

Fig.(3,4,5) shows the velocity vector in the enclosure at different values of Richardson number $Gr/Re^2 = 5$ and 25 of fixed value of $Re = 100$ and different location of heat source (LR , LB , RB).
All these cases leads to steady laminar solution. The flow field shows unicellular pattern at $Gr/Re^2 = 5$, but at this value a secondary flow develops due to the buoyancy effects from source R , at the base of the right side wall . At $Gr/Re^2 = 25$, the secondary cell becomes bigger and occupies more of the space originally belonging to primary cell . The temperature field (Isotherm contours , **Fig(6,7,8)**) in the fluid adjacent to source L exhibits the characteristics of a natural convection boundary layer a plumelike pattern of isotherms at all values of Gr/Re^2 chosen while for source R such a pattern makes its appearance for $Gr/Re^2 = 5$, source R is shown to be subject to an opposing recirculating flow.
For the same values of Re and Gr/Re^2 as before, the corresponding results for the LB configuration as shown in **Fig(4)** the buoyancy induced flows due to both the sources are now in the same direction ,aiding the recirculating flow .Therefore a unicellular flow pattern is observed at all values of Gr/Re^2 , with the recirculation gradually increasing with an increase in Gr/Re^2 . Thermal boundary layers are clearly observed over both sources, the BR configuration gives rise to a variety of flow patterns, as seen **in Fig(5)** .
At $Gr/Re^2 = 5$, the external flow dominates over the buoyancy effects and the flow field resembles the one generated in a driven cavity. At a higher buoyancy level , $Gr/Re^2 = 25$, the buoyancy effects from source B again add to the recirculation of the original cell , while the secondary cell is now due to buoyancy effect from the source R only and is restricted to a region

form , chosen to represent a cavity that would most likely appear in an electronic system , although not exclusively so , are kept fixed at the following values see **Fig(1))**.
Aspect ratio of the air – filled cavity $A = H^*/W^* = 1$, $Hi^* = Ho^* = Ls^* = 1$, $di^*/H^* = do^*/H^* = 0.8571$
The distance of the center of the sources from the bottom of the cavity is taken such that $ds^*/H^* = 0.357$, while on the bottom wall the corresponding distance is $ds^*/W^* = 0.5$, measured from the left vertical wall. The parameters to be varied here the Grashof number , the number of the sources , and the relative locations of the sources. All the alternative cases will be compared to each other. The Reynolds number is being kept fixed in this work at $Re = 100$, a value representative of the laminar regime , characterizing on incoming flow of a relatively low velocity. For instance, an air flow of about 0.1 m /s ,entering through an opening 2 cm height at $20 c^\circ$ would yield a Reynolds number of the above – mentioned order of magnitude .Higher values of Re have been considered before {Jaluria 1990}, and the basic flow in the cavity were not affected significantly as long as $Re \le 1000$ The Grashof number is varied in the range $Gr = 10^3 - 2.5 * 10^5$ and this effect will be presented .

In what follows , as a variation in the Richardson number Gr/Re^2 over the corresponding range . Gr/Re^2 Is a more suitable parameter in mixed convection problems and since the Reynolds number is kept fixed , varying the value of Gr/Re^2 will be equivalent to varying the heat input from the sources. Generally , the Grashof number encountered in electronic cooling are of the order of 10^5 or higher, but in this case ,in order to get a more complete picture of the effect of Gr/Re^2 on the heat transfer, the rang of Gr has been extended to lower values.

Flow and thermal field for steady mixed convection

Fig.(3,4,5) shows the velocity vector in the enclosure at different values of Richardson number $Gr/Re^2 = 5$ and 25 of fixed value of $Re = 100$ and different location of heat source (LR , LB , RB).

All these cases leads to steady laminar solution. The flow field shows unicellular pattern at $Gr/Re^2 = 5$, but at this value a secondary flow develops due to the buoyancy effects from source R , at the base of the right side wall . At $Gr/Re^2 = 25$, the secondary cell becomes bigger and occupies more of the space originally belonging to primary cell . The temperature field (Isotherm contours , **Fig(6,7,8)**) in the fluid adjacent to source L exhibits the characteristics of a natural convection boundary layer a plumelike pattern of isotherms at all values of Gr/Re^2 chosen while for source R such a pattern makes its appearance for $Gr/Re^2 = 5$, source R is shown to be subject to an opposing recirculating flow.

For the same values of Re and Gr/Re^2 as before , the corresponding results for the LB configuration as shown in **Fig(4)** the buoyancy induced flows due to both the sources are now in the same direction ,aiding the recirculating flow .Therefore a unicellular flow pattern is observed at all values of Gr/Re^2 , with the recirculation gradually increasing with an increase in Gr/Re^2 . Thermal boundary layers are clearly observed over both sources, the BR configuration gives rise to a variety of flow patterns, as seen **in Fig(5)** .

At $Gr/Re^2 = 5$, the external flow dominates over the buoyancy effects and the flow field resembles the one generated in a driven cavity. At a higher buoyancy level , $Gr/Re^2 = 25$, the buoyancy effects from source B again add to the recirculation of the original cell , while the secondary cell is now due to buoyancy effect from the source R only and is restricted to a region adjacent to the right vertical wall, this change in the flow patterns and the direction of the buoyancy-induced flow from source B can be seen in the isotherm plots(**Fig(8)**).

Average Nusselt number $\overline{Nu}$:-

Fig(9) shows the relative magnitude of the average Nusselt number $\overline{Nu}$ at the sources for mixed convection over the corresponding value for forced convection $\overline{Nuf}$, at different values of Gr/Re^2 , can be plotted , as shown in **Fig(9)** . Generally, the ratio $\overline{Nu}/\overline{Nuf}$ increase with Gr/Re^2 except in BR configuration at low Gr/Re^2 .In that case , the opposing effects of the external flow are stronger and $\overline{Nu}/\overline{Nuf}$ decreases , first with Gr/Re^2 , before buoyancy dominates and an increasing trend is observed .
This behavior was also found in the opposing forced – flow results of {11}, where the Nusselt number curves crossed the forced convection asymptote as Gr/Re^2 decrease before approaching the asymptote value. The results can be decribed by a correlation of the following form :-

$$\frac{\overline{Nu}}{\overline{Nuf}} \ \alpha \ \left(\frac{Gr}{Re^{2}}\right)^{c} \qquad (8)$$

Where c depends on the configuration and the source location and has the computed values shown in **Table (2) .**

Table (2) Magnitude of C Parameter.

CONFIGURATION	SOURCE LOCATION	C
LR	L	0.0518
LR	R	0.0248
RB	R	0.2463
RB	B	0.2391
LB	L	0.6906
LB	B	0.1859

All these have correlation coefficients close to 0.99 . It can be observed in table above , that in the LB configuration the variation of the Grashof number has a much larger effect on the heat transfer compared to the other two configuration .

CONCLUSION

A numerical procedure was developed to simulate the laminar mixed convection cooling of electronic components located in an enclosure . Results are presented for the flow field and temperature distribution in the fluid (air). The numerical method presented is very robust and capable of treating different numbers , locations of heat sources.
In general , it appears that the location of the source on the left vertical wall is the most favorable in terms of cooling . Laminar results are predicted up for up to $Gr = 2.5 * 10^{5}$ for all configurations studied .
The two-dimensional model studied here applies to two or three long rows of electronic modules mounted on either one of two vertical printed circuit boards or on a horizontal board and extending in the direction normal to the plane under consideration . The results from

the various cases studied are extremely helpful in understanding the flow patterns that develop in an air – cooled electronic enclosure and the thermal interactions between the components, this allows for an evaluation of the various alternative placements of the components and selection of the one that leads to the best thermal performance. Quantitative heat transfer result were also obtained and compared to previously existing data for configuration of relevance to the present ones.

REFERENCES

C.Y. Choi and A. Ortega , (1993), Mixed Convection in an Inclined Channel with a Discrete Heat Source; Int. J. Heat Mass Transfer , vol. (36) , no.(2), pp.(3119-3134) .

E. Papanicolaou and Y. Jaluria, (1990), Mixed Convection from an Isolated Heat Source in Rectangular Enclosure ; Numerical Heat Transfer , Part (A), vol. (18) , pp.(427-461) .

E. Papanicolaou and Y. Jaluria, (1993), Mixed Convection from a Localized Heat Source in a Cavity with Conducting Walls; A Numerical study , Numerical Heat Transfer , Part (A), vol. (17) , pp(463-484)

E. Papanicolaou and Y. Jaluria, (1995), Computation of Turbulent flow in Mixd Convection in a Cavity with a Localized Heat Source ; ASME J. Heat Transfer , vol. (17) , pp(649-658) .

G.P. Paterson and A. Ortega, (1990) , Thermal Control of Electronic Equipment and Devices Advance Heat Transfer , vol. (20) , pp.(181- 314).

H.K. Versteeg and W.Malalasekera, (1995), An Introduction to Computational Fluid Dynamics , The Finite Volume Method,

J.P. Simoneau , C. Inard , and F. Allard , (1988), Numerical Approach to Interaction Between an Injection and Laminar Natural Convection in a thermal Driven Cavity; ASME. HTD. Vol. (99) , pp.(45-51).

K.J. Kennedy and A. Zebib, (1983), Combined Free and Forces Convection between Horizontal Parallel Plates ; Int. J. Heat Mass Transfer , vol. (26), no.(3), pp.(471-474) .

L. Robillard C. Yucel, H. Hasnaoui , and E. Bilgen, (1993), Mixed Convection Heat Transfer in Open Ended Inclined Channels with Discrete Isothermal Heating; Numerical Heat Transfer , Part (A), vol. (24) , pp.(109-126) .

Patankar S.V. , (1980), Numerical Heat Transfer and fluid flow , Hemisphere, Washington, DC .

T.H. Hsu , P.T. Hsu ,and S.P. How, (1997), Mixed Convection in a Partially Divided Rectangular enclosure ; Numerical Heat Transfer , Part (A), vol.(31) , pp(655-683) .

NOMENCLATURE

A	Area
a	Coefficient values
D	Diffusion factor at control surface
d	Vertical distance from the bottom of the enclosure

e,w,n,s	Values at east,west,north,south
F	Flow rate at control volume
Gr	Grashof number
Gr/Re^2	Richardson number
g	Acceleration of gravity (body force)
H	Height of air-filled cavity
Hi , Ho	Height of the inflow and outflow channels
J	Flux due to both diffusion and convection
Ls	Length of the heat sources
$\overline{Nu}$	Average Nusselt number in mixed convection
$\overline{Nuf}$	Average Nusselt number in forced convection
P	Dimensionless local pressure
Pr	Prandtl number
Re	Reynolds number
S_{Φ}	Heat source
T	Physical temperature
ΔT	Temperature scale (Th-Ti)
U , V	Dimensionless horizontal and vertical velocity
Ui	Mean value of the horizontal velocity component at the inflow
W	Width of air-filled cavity
X ,Y	Dimensionless horizontal and vertical coordinate in general form equal N

GREEK NOMENCLATURE

Φ	Dependent variable
α	Thermal diffusivity
β	Coefficient of thermal expansion
θ	Dimensionless temperature
ν	Kinematic viscosity

SUBSCRIPTS

i	Inflow
o	Outflow
h	Hot location
C	Cold location
*	Dimensionless quantities

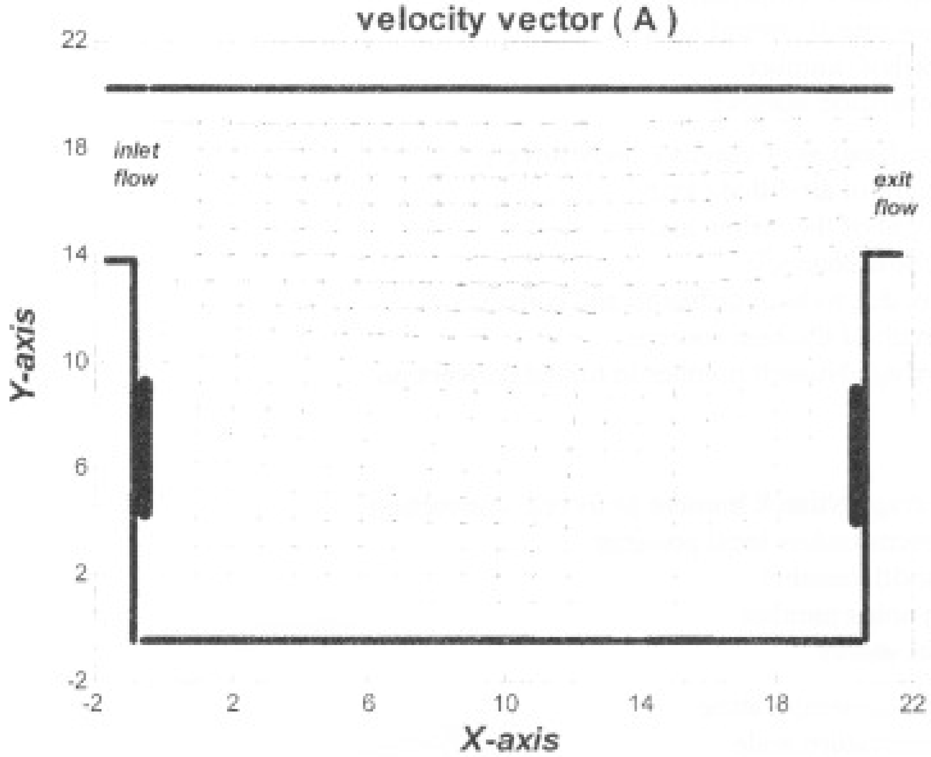

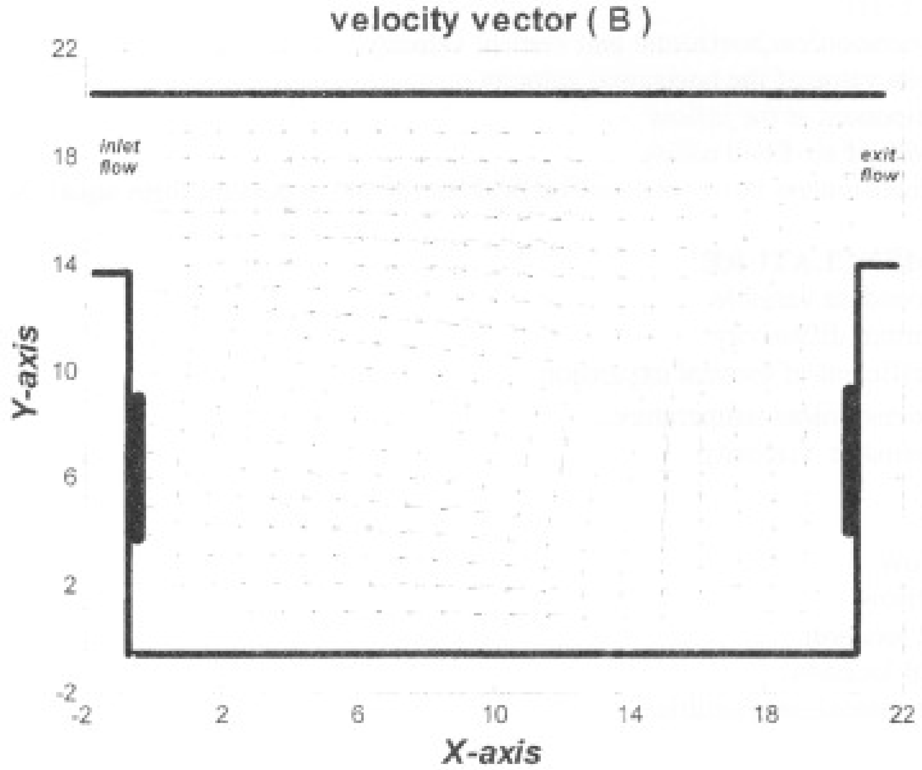

Fig.(3) Velocity Vector of the Flow Field in the Enclosure when the Location of the Heat Sources in the Left and Right Walls:

(A) $Gr/Re^2 = 5$ and $Re = 100$ (B) $Gr/Re^2 = 25$ and $Re = 100$

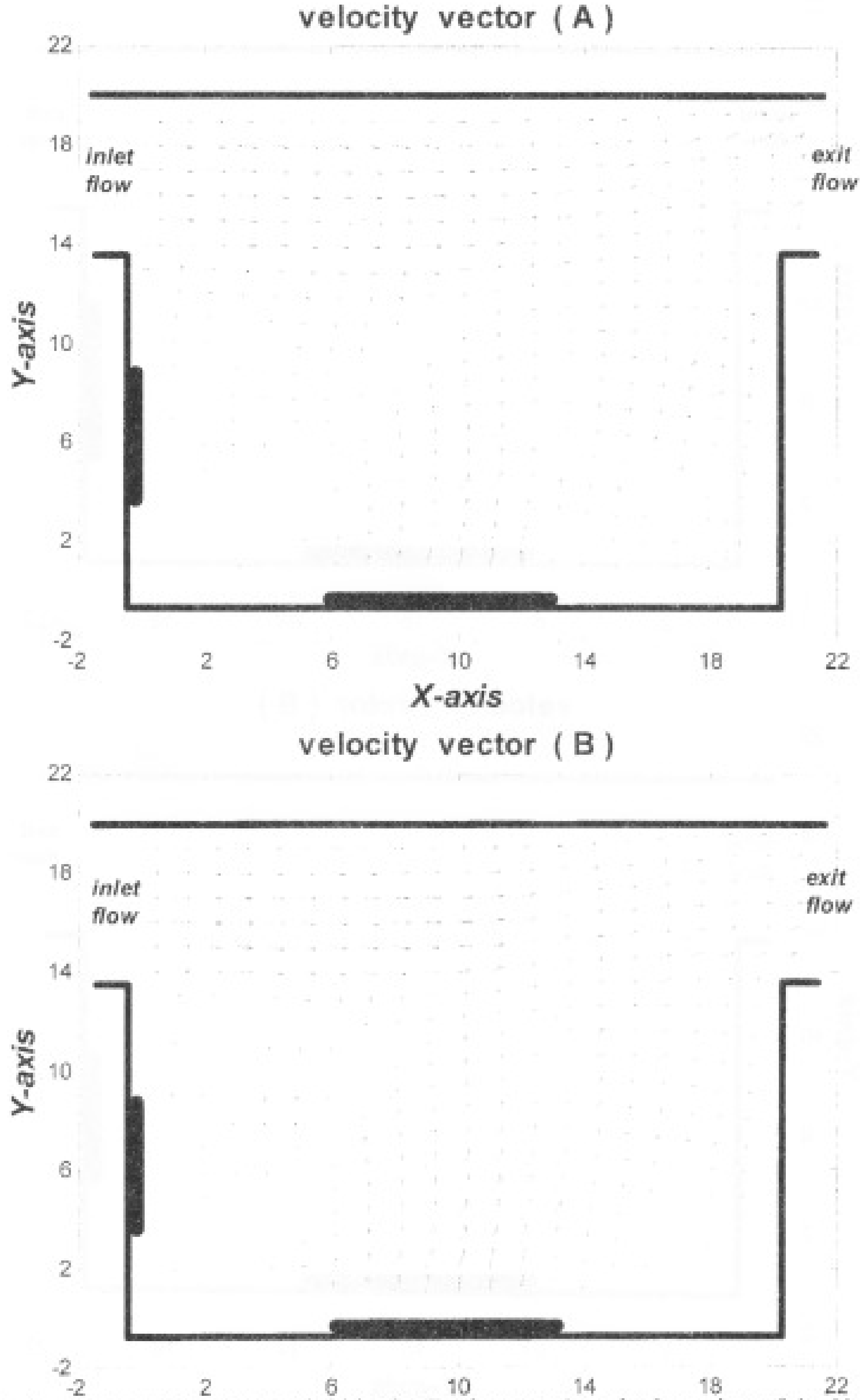

Fig.(4) Velocity Vector of the Flow Field in the Enclosure when the Location of the Heat Sources in the Left and Bottom Walls:

(A) $Gr/Re^2 = 5$ and $Re=100$ (B) $Gr/Re^2 = 25$ and $Re=100$

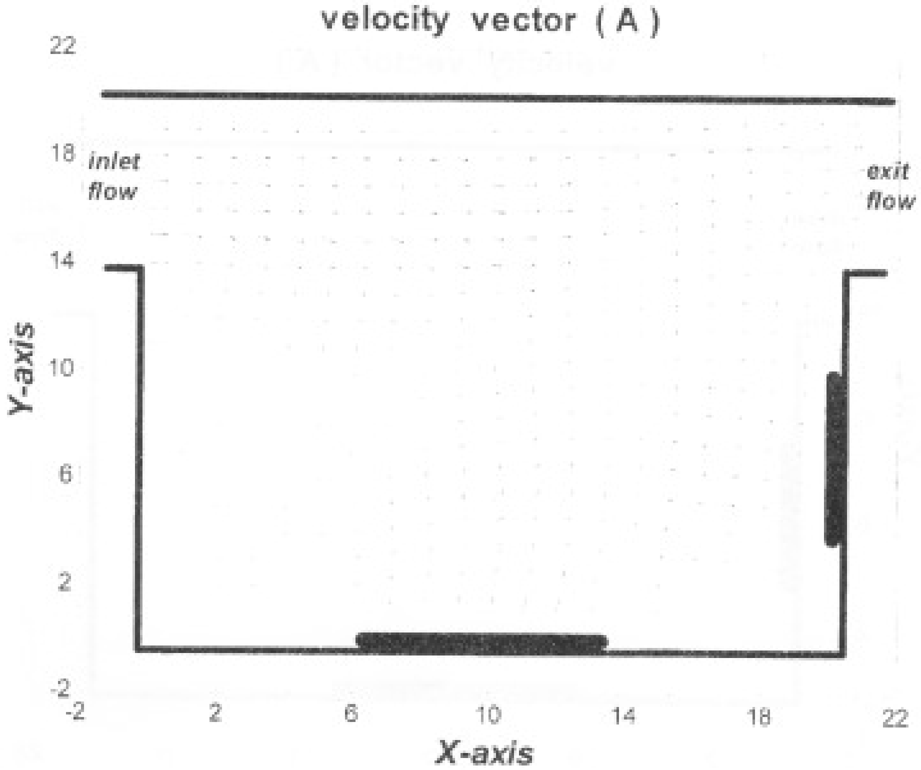

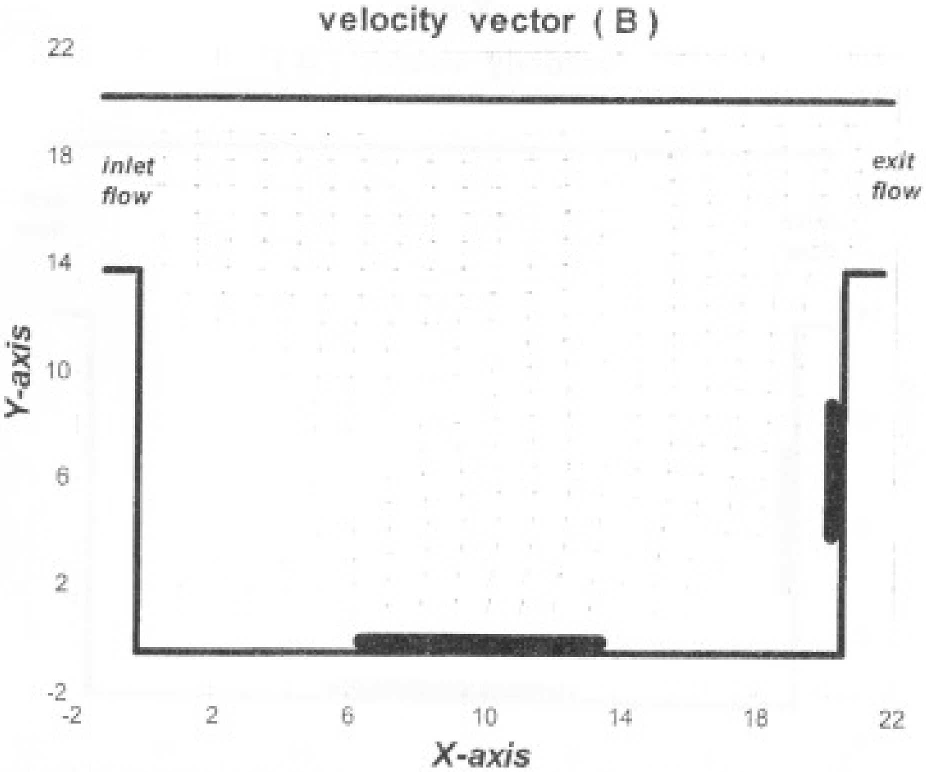

Fig.(5) Velocity Vector of the Flow Field in the Enclosure when the Location of the Heat Sources in the Right and Bottom Walls:

(A) Gr/Re^2 **=5 and Re=100** **(B)** Gr/Re^2 **=25 and Re=100**

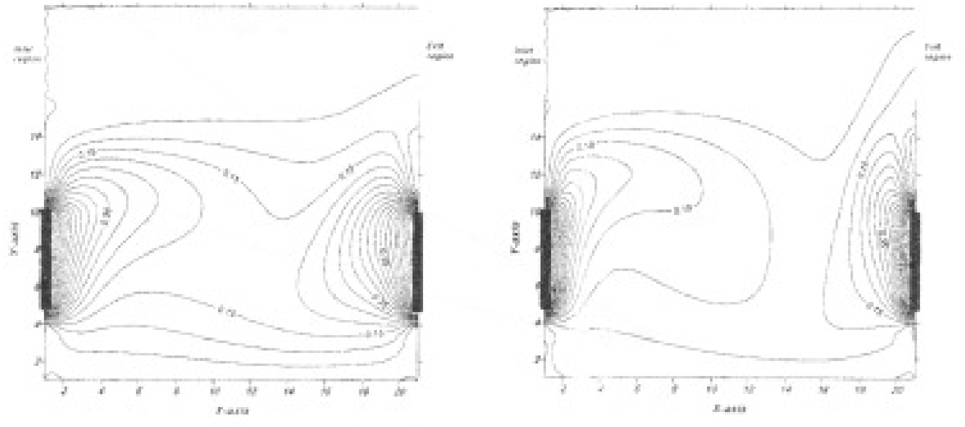

(A) (B)

Fig.(6) Isotherms Contours in LR Configuration, for Re=100 and

(A) $Gr/Re^2 = 5$ (B) $Gr/Re^2 = 25$.

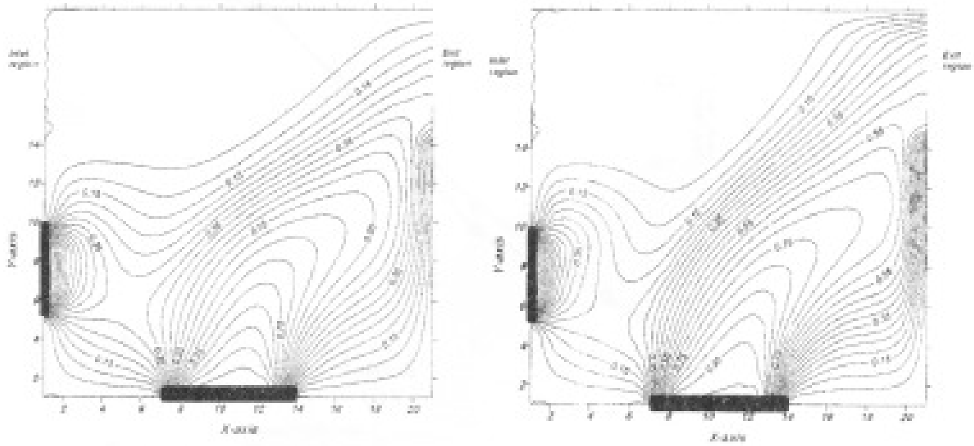

(A) (B)

Fig.(7) Isotherms Contours in LB Configuration, for Re=100 and

(A) $Gr/Re^2 = 5$ (B) $Gr/Re^2 = 25$.

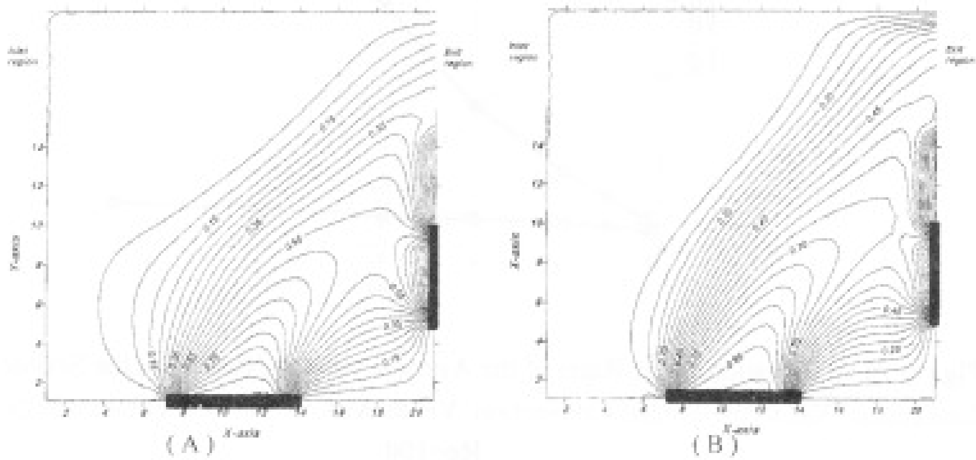

(A) (B)

Fig.(8) Isotherms contours in RB configuration, for Re=100 and

(A) $Gr/Re^2 = 5$ (B) $Gr/Re^2 = 25$.

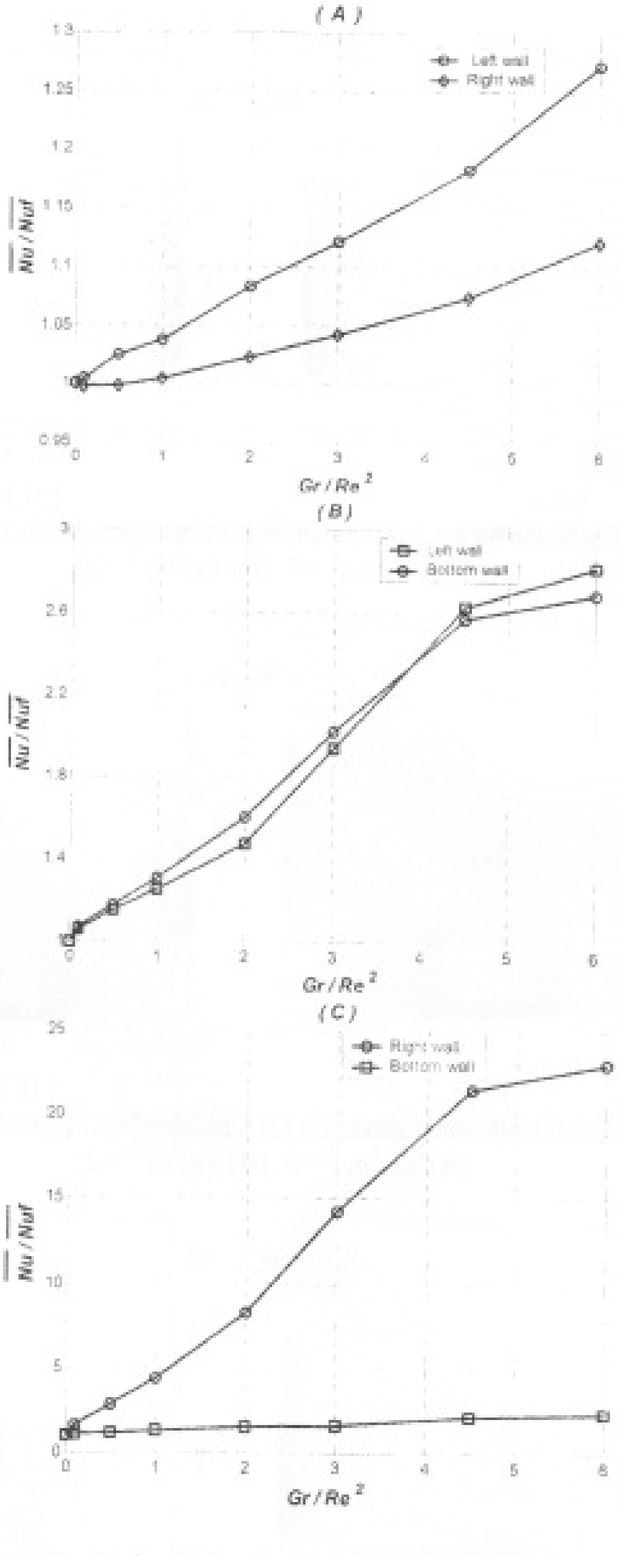

Fig.(9) The Variation of the Ratio of the Average Nusselt Number at the Source in Mixed Convection $\overline{Nu}$. to the Forced Convection Value $\overline{Nuf}$. at Various Values of Gr/Re^2 and **Re=100**

(A) LR configuration. (B) LB configuration. (C) RB configuration.

Number 1 Volume 12 March 2006 Journal of Engineering

STUDY OF THE EFFECT OF VEHICLE DRIVER BEHAVIOUR ON VEHICLE EMISSIONS OF CARBON MONOXIDE AT SIGNALIZED INTERSECTIONS

Asst. Prof. Dr. Ali H. Al-Neami **Prof. Hamed M.H. Alani** **Aso F. S. Talabany**

Department of Civil Engineering/ College of Engineering
/ University of Baghdad

ABSTRACT

Considerable concentrations of vehicular emissions at signalized intersections and streets, in urban area are health-related issues of concern to society in general. This paper presents an examination for the effect of vehicle driver behaviour on vehicular excess CO emissions. The examination process based on site observations.

Four signalized intersections in Erbil City which, satisfy the objectives and specifications of this study selected, and the necessary traffic behaviour and vehicle exhaust emission data collected. The traffic data were collected using video recording technique and the Analytical Mobile Gaseous Emissions CART P8334 machine used to measure vehicle exhaust emission data.

The required traffic data abstracted from video play back using **EVENT** computer program, which provide coded digital representation for the requisite traffic activities. The abstracted data stored on floppy disks in the form of digital computer files. These files processed using computer programs developed for this purpose to abstract the necessary information from the raw data.

Among the obtained traffic information are vehicle data classified according to the type of fuel used into two classes. The first class is gasoline powered vehicles which consisted of taxis and private cars covering different model year, engine condition and size, type of fuel injection system, number of cylinders. These data observed under different ambient air temperatures. The second class is the diesel-powered vehicles, which consists mainly of truck type vehicles.

Following the processing stage, the obtained data presented and analyzed statistically to evaluate the relationship between driver behaviour and vehicle excess of CO emission. Among the driver behaviours studied is queuing driver behaviour, which showed reasonably good relationship with the excess CO emissions.

The results of this study are useful for the Local Authorities, traffic engineers and transportation planners. This is because, the obtained results assist in the adoption of suitable method of intersection control for the purpose of reduction of CO emissions and hence, reduce level of this type of air pollution.

الخلاصة

التراكيز العالية نسبيا للغازات الملوثة للهواء الناتجة عن احتراق الوقود المستخدم لمحركات المركبات التي تمر بالتقاطعات العاملة بالاشارة الضوئية و تلك التي تسير على الطرق في المناطق الحضرية ذات تأثير سلبي على صحة الانسان مما جعلها تحظى باهتمام عموم المجتمع.

تقدم ورقة البحث دراسة لتأثير سلوكية سائق المركبة على مقدار غاز أول أوكسيد الكاربون المنبعث من عادم المركبات المختلفة. اعتمدت الدراسة على بيانات حقلية جمعت من قبل الباحثين حيث تم اختيار أربعة

تقاطعات عاملة بالاشارة الضوئية في مدينة أربيل لهذا الغرض بعد أن تم التأكد من صلاحية هذه التقاطعات في تحقيق أهداف الدراسة. جمعت البيانات المرورية باستخدام جهاز الفيديو أما البيانات المتعلقة بالغازات المنبعثة من عادم المركبات فقد جمعت باستخدام جهاز Analytical Mobile Gaseous Emissions CART P 8334.

بعد الانتهاء من عملية التصوير تم استخلاص البيانات المرورية المطلوبة من أفلام الفيديو و ذلك بإعادة عرض الافلام على شاشة التلفاز و باستخدام البرنامج الحاسبي (EVENT) تم تحويل الفعاليات المرورية الى صيغة رقمية خزنت بشكل ملفات. حفظت هذه الملفات على أقراص مرنة وتم استخدام نظام ترميز في تسمية الملفات بحيث يمكن الاستدلال على محتوى الملف من أسمه. الخطوة اللاحقة كانت تطوير برامج حاسبية لغرض معالجة البيانات لاستخراج المعلومات المطلوبة لغرض البحث. من ضمن المعلومات التي تم جمعها بيانات عن الأنواع المختلفة من المركبات مصنفة حسب نوع الوقود المستخدم ديزل أو بنزين ، طبيعة استخدام المركبة خاص أو أجرة ، سنة التصنيع، حالة المحرك، عدد الاسطوانات و درجة حرارتها و لدرجات حرارة الهواء المحيط المختلفة.

بعد الانتهاء من مرحلة معالجة البيانات، تم عرض المعلومات بشكل جداول و مخططات مع تقديم تحليل إحصائي أولي لتقييم العلاقات بين سلوكيات سائق المركبة و مقدار الانبعاث الاضافي لغاز أول أوكسيد الكاربون من عادم محركات المركبات. من بين نتائج هذه الدراسة اظهر طول الطابور علاقة جيدة مع كمية غاز اول اوكسيد الكاربون الاضافي المنبعث. ان نتائج هذه الدراسة تفيد دوائر امانة بغداد و البلديات و مهندسي المرور و مخططي النقل في اختيار نظام إدارة مرورية للتقاطع بحيث يؤدي الى للتقليل من كمية غاز اول اوكسيد الكاربون المنبعث من المركبات في التقاطعات المزودة بالاضوية المرورية.

KEY WORDS

Impact of traffic movement at intersections on environment, effect of traffic movement at intersections on air pollution. CO emission as a result of traffic at intersections.

INTRODUCTION

Air pollution is a new set of air pollutants which result from mobile, industrial, and domestic uses in urban society(our use of energy) (Al-Jamr (1997)). The use of vehicles as mode of transportation introduced a great service for the humanity. It played a major role in the development of the economical; political, and social aspects of the human life. However, the increase in the use of vehicle automobile resulted in problems to the humanity. The vehicular emissions are one of the major dangers facing the human being life, especially in congested urban areas.

To provide an insight into the increase in dependency on vehicle use, consider the statistics regarding the growth in vehicle number over the years. **Table (1)**, provides statistics for the number of registered vehicles over the period 1980-1993 in some of the world countries. The data may suggest that Iraq has one of highest number of vehicles in comparison with the other countries appeared in the **Table (1).** The implication for this growth is increase in fuel consumption. This is indicated by examination of the data presented in **Table (2),** which shows comparison between fuel consumed in transportation for the year 1989. The presented data indicates that Iraq ranked as the third country in fuel consumption for transportation purposes.

Table (1), The growth in number of vehicles (*1000) in some of the ESCWA countries (Al-Ananie 1997)

Country	Year					
	1980	1985	1990	1991	1992	1993
Bahrain	65.4	101.1	122.7	132.0	141.7	152.6
Iraq	304.8	684.1	1020.9	992.5	1007.7	1050.8
Jordan	126.0	191.2	215.1	247.5	262.5	255.5
Oman	100.2	227.3	209.9	236.2	254.9	273.8
Qatar	98.5		159.8	179.8	192.8	205.8
Saudi	2068.1	4171.8	4956.5	5117.4	5528.5	5588.0
Syria	145.3	155.7	329.4	316.6	356.2	390.1
Yaman	127.7	548.3	285.2	291.9	328.2	

Table (2), Some ESCWA countries ranked according to the fuel consumed in transportation at the end of the year 1989 (Al-Ananie 1997)

Country	Fuel consumed (Toe/10^6)
Lebanon	185.0
UAE	183.3
Iraq	174.3
Libya	162.2
Luxembourg	152.2
Jordan	117.2
USA	112.6
Argentina	103.2
EEC	80.4
Rest of the world	61.9

At present fuel consumption is one of the serious problems facing traffic and environmental engineers, and transportation planners from the standpoint of the amount of air pollutants, which result from the operations of traffic movements. This is because of the agreed world wide requirement that certain standards for CO and other exhaust gases concentrations be met (Matzoros (1988)) to minimize the harmful effect of these chemicals on human life.

The most important pollutant gases present in the air of the world's cities, namely, sulfur dioxide (SO_2), nitrogen oxides (NO or NO_2), carbon monoxide (CO), and non-methane hydrocarbons (NMHC). Natural sources (exception of volcanoes) emissions do not fluctuate from year to year. Man's made emissions, are steadily increasing as population and industry expand (Al-Jamr (1997)). For CO the figures are 1970- 79%; 1979- 89%. Thus vehicle CO emissions have been increasing as a proportion of total emissions, and they have also been increasing in absolute term's. Typical gaseous exhaust emission contents are listed in **Table (3)**, for gasoline and diesel engines. Exhaust CO emission arises as a result of incomplete combustion. It is difficult to achieve complete oxidation in practice so, instead of the products been simply water and CO_2, there are other products (Case 1982).

Table (3), Typical exhaust emissions for gasoline and diesel engines (Samara (1997))

Emissions	Gasoline engines %vol.	Diesel engines %vol.
CO	4	0.1
HC	0.03 – 0.004	0.004 – 0.002
NO_x	0.2 – 0.06	0.15 – 0.04
CO_2	9	9
O_2	4	9
SO_2	0.06	0.02

Of all vehicle types, petrol-engine cars attracted more attention in relation to emission studies and control. The reason is, car numbers more numerous and pollutant than diesel-engine vehicles. In addition car used for personal mobility easiest to control in comparison with the other types of the existing total vehicle fleet sector. This argument suggest that traffic engineers has room for maneuver and should not base their evaluation only on measures such as traffic accident reduction and vehicle, congestion, delay, number of stops, and speed. The environmental impact issue result from vehicle movement should also addressed and considered as a measure of effectiveness of particular importance when design and/or improve urban and rural traffic network operations.
To conclude the above argument, the presented data and discussion suggest that, there is need for control and regulations to restrain the increasing demand for car ownership and fuel consumption for the purpose of transportation.

LITERATURE REVIEW

The Harmful Effect of Transport Generated Co Pollutant

Man inhales about 7500 liters of air each day, so lungs and respiratory system is in direct contact with whatever harmful substances present in the air. Continuous exposure to low levels could have harmful physiological effects on human beings, whereas short exposure to high levels of CO can be lethal (Singh et. al.(1990)). At sufficiently high concentrations CO can be fatal to humans. It aggravates cardiovascular diseases and may impair psychomotor functions (e.g. reaction time, depth perception, and peripheral vision).
The adverse health effects of CO are caused by its ability to reduced the quantity of oxygen (O_2) that is delivered to the tissues by the blood and possibly to inhibit the utilization of O_2 within the tissues. CO combines with the hemoglobin of the blood to form carboxy-hemoglobin, thereby displacing O_2 from the hemoglobin molecule and reducing the blood's ability to carry O_2. It also inhibits O_2 that is bound to hemoglobin from being released to the tissues (Matzoros (1988)).
In addition to that, CO is one pollutant which produces a change in human physiology that can be directly related to concentrations which the subject was exposed; blood carboxy-hemoglobin (COHb) can be predicted from atmospheric CO concentration. CO primarily affects the cardiovascular and central nervous system. It can cause or contribute to severe cardiovascular damage or sudden death to individuals with arteriosclerotic diseases. Its potential effects on the central nervous system include changes in vigilance, sensory function and psychomotor function. The main significance of those nervous system effects is that they occur at or near carboxy-hemoglobin concentrations that can be experienced by drivers in heavy traffic. Hence, there is a possibility that it impairs driving ability and, thereby, contributes to the occurrence of traffic accidents. The clinical studies conducted, however, have found contradictory results, so that the extent to which CO exposure may impair driving abilities is still not clear (Matzoros (1988)).
Death occurs in humans exposed to concentrations around **1000 ppm** corresponding to blood levels of **60%** COHb, impaired blood function may occur at much lower levels between **10** to **20%**. Reasonable correlation between daily mortality levels and CO, in addition heart function has been shown to be altered by elevated COHb, because CO blocks the transport of O_2 in the blood stream.

Comparison of CO Sources

It is estimated that motor vehicles contribute approximately **55%** of the total anthropogenic emissions in US cities. Even in cities like Delhi, vehicular traffic is significant source of CO. The urban area of Delhi has a high pollution potential during winter especially during November to January. In the U.K. the transport in general accounts for over **90%** of total CO emissions and over **20%** of CO_2, and road transport accounts for **99%** of CO (Singh et. al.(1990)).

Signal Control Intersections and the Increase in Vehicular CO Emissions

The use of traffic signals at road intersections controls vehicle movements by allocating time intervals during which separate traffic demands make use of the available road space. Signal equipment and control techniques have evolved to cope with wide range of intersection layouts and complex traffic demands- including pedestrians crossing.

One characteristic of the transport pollutant emissions of major interest to traffic managers, is the fact that they are very much influenced by the operating mode of the engine. This, in simple terms, means that a vehicle emits different quantities of pollutants per unit time or distance, when it accelerates, decelerates, idles or cruises at a steady speed. Matzoros (1988) mentioned it is widely reported in the literature that interrupted traffic flow produces more pollution than freely moving traffic flow. This is the case of traffic flow at junctions in general and signalized intersections in particular.

In a number of papers, Patterson and Meyer (1975) has investigated the use of traffic queuing models at signalized intersections in an attempt to estimate the non-constant emission profiles caused by stop-and-go traffic at the stop line. Although subject to the limitations described below, Patterson's work indicates that the queuing process is a copious source of CO near the stop line. Thus, most CO will be emitted near the stop line while automobiles are stopped for a red light. The result is that the emissions profile will be sharply peaked at the stop line and fall off rapidly toward mid-block, leading, under most wind conditions, to a similar non-uniformity in pollution levels between stop line and mid-block.

There are, however, some limitations in Patterson's approach. The queuing model considered assume either constant or uniformly distributed arrivals to and departures from the queue. These assumptions are often violated in the field. Examples include right turn on red unprotected left turns, pedestrian blockages of left-or right-turning traffic, buses dwelling at near-side bus stop, and platoons arrivals. The inclusion of such effects requires much more comprehensive model as reported by Matzoros (1988).

Claggett et. al. (1988), measured CO, traffic and meteorology during a six week period near a signalized intersection at an arterial intersection in Melrose park, Illinois, a suburban of Chicago. Ambient air samples were collected in the queue, acceleration/deceleration, and mid-block cruise zones. Measured concentrations were highest in the zone of traffic queue and lowest at mid block. The data indicates that CO concentration may be higher at urban intersection than the near freeways that have 2-3 times higher traffic volumes.

Matzoros (1988) developed a computer model to tackle the problem of transport air pollution from urban networks. It consists of queuing, emission and dispersion models and takes vehicle-operating modes (accelerating, decelerating, and idling and constant speed) and their variable emission rates into account. The model was applied under varying conditions and it was found that, CO emissions and concentration distributions show the highest spatial variation than other pollutants.

Lee (1983), used the TEXAS-II model in series of designated experiments to obtain quantitative estimates of the effects of various traffic and intersection factors on emissions, fuel consumption, traffic delays and queue lengths.

The TEXAS-II model was used to estimate, with respect to time and location, the source of CO, HC and NO_x emissions as well as the amount of fuel consumed by individually characterized vehicles as they pass through an intersection environment which can be described accurately in terms of its geometric features, traffic control and traffic stream characteristics. He concluded that:

1- Additional emissions and fuel consumption result from interrupted traffic flow on the intersection legs and in the intersection proper, as compared with uninterrupted flow.
2- Improvements in intersection geometry and traffic signal operation generally reduce excess emissions and fuel consumption more on the inbound intersection lanes than in the intersection proper or on the outbound lanes.

3- For the practical range of cycle times and traffic volumes used in the experiment, longer cycle times cause more emissions and fuel consumption on the inbound lanes but less in the intersection proper.

DATA COLLECTION

The selection of intersections for the purpose of this study is critical, as there are various conditions (e.g. geometry, traffic and timing) which directly affect the local traffic operation. In order to fulfil the objectives of the data collection, it was necessary to collect statistically sufficient and representative data, which should represent a range of vehicle flow, signal timing, and intersection geometry and vehicle emissions.

To achieve the above objectives, it was necessary to collect data about drivers' behavior during the various aspects of the signal cycle and the hours of the day at different intersection locations and geometric. This is to allow for the impact of these parameters on driver behavior to be observed. It was also necessary to collect data about the tailpipe emissions of different types of vehicles (diesel and petrol and private and taxi) for different transient modes (idling, acceleration and deceleration). The observed data may be summarized as below:

1- Vehicle data
2- Signal data
3- Intersection and road layout data
4- Tailpipe emission data

Four intersections, which satisfied the requirements of this study and representing a range of locational, vehicle and signal timings on Kurdistan ring road in the city of Erbil, were selected. Traffic at the selected intersections was controlled by uncoordinated fixed time signal plans. At the observed intersections there was no signal control on right turn traffic movement. **Table (4)** presents some of the main traffic and geometric characteristics of the four selected intersections.

Table (4). The main traffic and geometric features observed at the selected sites

Item	Description
Roadway system	Two-way street
Type of traffic control	Pretimed control
Observed range of cycle time	70 – 80 seconds
percentage of buses	0.5 – 13 percent
percentage of trucks	0.5 – 9.5 percent
Condition of pavement marking	No marking
Grade percent	0

The data collection made during the period 7:30 AM to 8:30 AM. This is because the observed levels of traffic activities during the morning peak periods produce data, which is statistically meaningful. In addition to that, the data collected in sessions of one-hour duration for each intersection in days of good weather conditions during the spring of the year 1999.

The video recorded data were as listed below:

1- Signal timing data.
2- Vehicle arrival data.
3- Vehicle departure data.
4- Incidents that could affect the observed listed as above data.

Lane and approach widths were measured manually using tape measurement at the stop line of each approach to obtain the accurate width. While the signal phasing was obtained using a stopwatch to measure time duration of the phases at site when it was not possible to get these information from the video recording.

Data abstractions were based on sessions of 30-minute periods of recorded data. When the videotape was replayed for a period of data abstraction, the sound signal was used as a reference point for all data sets. This sound technique is useful and essential to ensure that as long as there is need to replay the recording of one session to abstract all the required data, the abstraction process start and finish at the same points in time. The recorded data were abstracted using software developed for personal computer.

The data abstraction process is mainly achieved with the aid of a computer program named EVENT developed by Al-Neami (2000). The program was developed using C-language. The accuracy of the abstracted traffic data using this program is about up to 0.01 second.

Using the developed computer programs the abstracted data from EVENT files were processed. These programs calculate the given below traffic parameters:

1- The time headway between successive arriving vehicles.
2- The time headway between successive departing vehicles in queue.
3- The travel time for successive departing vehicles in queue.
4- Saturation flow data were calculated by taking the reciprocal of the average headway.
5- Calculates the frequency distribution of the video observed departure and arrival headways
6- The average video observed delay of an approach.
7- Duration of video observed data session.
8- Vehicle arrival and departure flow.

Remark

It should be noted that not all listed as above data used in this paper.

The link speeds data for the links between the surveyed intersections were measured by observations made from a moving vehicle during the morning peaks. This is because this method is efficient and practical, and is particularly suitable when a general evaluation of traffic conditions on a network of streets required (McShane and Roess (1990)).

The observers in the test car made a number of test runs (at least 6) for each link and they record their journey times, count opposing traffic, and keep a tally of overtaking and overtaken vehicles. From these observations, the mean speeds and numbers of vehicles passing along a street can be obtained for all classes of selected vehicles.

The vehicle emission data were collected using ANALYTICAL MOBILE GASEOUS EMISSION CART P 8334. The observed samples were 100 diesel engine buses and trucks, and 600 gasoline cars were tested at ambient temperature between 20 – 25 °C for transient modes (idling, accelerating and decelerating). Most of the vehicles were at cold start situation.

In this research, the intention was to produce typical emission values for the existing vehicle traffic composition in Erbil City. Therefore, the observed vehicles were mostly of models in the range of 1975-1990, with kilometers traveled between 100000 and 400000 km at the time period of surveys. A few older models with higher mileage vehicles also included in the survey for the observed data to be representative.

PRESENTATION AND ANALYSIS OF OBSERVED DATA

The abstracted data were analyzed statistically. The statistical analysis performed using SPSS statistical package. The traffic parameters analyzed are those of driver behaviour which initially assumed to have an effect on amount of car exhaust emission.

Observed emissions rate data

The idle vehicle emission data obtained by direct measurement of CO and HC emission from the vehicle exhaust. Emission data for other modes of vehicle operation obtained from the conducted surveys of moving car method. Achieved results of data collection of the observed various modes of vehicle operation presented in **Table (5)**.

The idle vehicle emissions data, used in the analysis of the effect of driver perception-reaction behaviour on air pollution at the onset of green for vehicles. Emission data for dynamic mode of vehicle operation used in the analysis of driver behaviour during intergreen periods in relation to air pollution and in the development of emission models for vehicle queue and delay. Examination of the presented data indicates that on average, kinematics and dynamic modes of operation of gasoline engine vehicles have the highest CO and HC emission rates.

Table (5), Observed CO and HC emission data

Operating mode	CO & HC Emissions ($* 10^{-3}$ g/sec)							
	Gasoline vehicles						Diesel Vehicles	
	Taxi Cars		Private Cars		Average			
	CO	HC	CO	HC	CO	HC	CO	HC
Cruise (50 kph)	37	15	36.7	15	36.9	15	11*	3*
Deceleration (50-0) kph	147	38	142	37	145	37.6		
Idle	134	17	131	16.6	132.8	16.8		
Acceleration (0-50) kph	139	28	136	27.3	137.8	55.7		

* FOR ALL OPERATING MODES

Observed Effect of Driver Behaviour on Vehicular CO Emissions

Driver starting delay time behaviour

Driver starting delay defined as the time lag between the start of green indication for stopped vehicles and the movement of first vehicle in queue. This time lag depends primarily on waiting driver perception – reaction time. **Table (6)**, provides a summary for the results of the descriptive statistical analysis performed. The observed data covers the behaviour of 1986 driver. The presented statistics indicates the existence of substantial difference in perception-reaction times among the observed drivers as may be inferred from the range of the data.

The obtained data presented graphically in **Fig.(1)**. This Figure is a scatter plot used to examine the relation between starting delay and the excess vehicular CO emissions. The presented data suggest that as the starting delay increase the excess vehicular CO emission increase. This trend may be attributed for two reasons. The first is that the perception component of the starting delay time increases the idling time of the vehicle engine and hence, the CO emission. The second reason attributed to the reaction – action time component of the starting delay behaviour.

Table (6), Results of descriptive statistical analysis of the observed starting delay behaviour

Sample size	Minimum	Maximum	Mean	Standard deviation
1985	0.22	9.61	2.13	1.14

During this time interval the driver change his vehicle state from kinematics to moving condition to cross the stop-line. This has the implication of increase the excess CO emission as a result of the difference in time between the two modes of vehicle condition of idling and moving at constant speed before passing over the stop line.

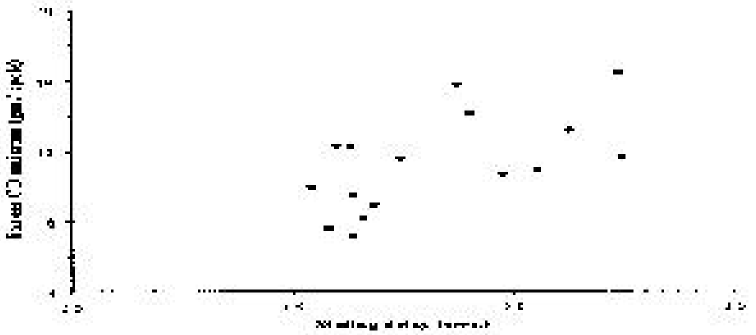

Fig. (1), Effect of observed mean driver starting delay behaviour on excess CO emission

Based on the above obtained result and argument, it is decided to examine the distribution of observed drivers starting delay behaviour. The obtained distribution presented in **Fig.(2)**, in the form of a standardized frequency polygon.

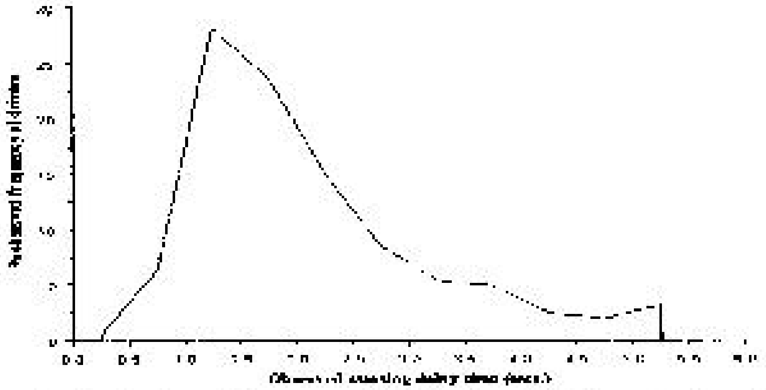

Fig.(2), Observed standardized frequency distribution of driver starting delay behaviour

The shape of the frequency polygon suggests that the observed driver behaviour skewed to the right. This indicates that the majority of drivers have starting delay times greater than the observed mean value of 2.13 seconds. This conclusion is consistent with the observed range of starting delay values presented in Table-6-. However, it should be noted that driver behaviour is not the only factor which contribute to the mean starting delay value. Type of vehicle has also an effect on starting delay value. An indication to this can be found by examination of the data presented in **Table (7)**-below. The presented data indicate that passenger car and truck-trailer type of vehicles have the lowest and highest mean starting delay of 1.692 and 3.953 seconds respectively. The reason for this substantial difference is attributed to the variation in kinematics characteristics between vehicles.

Table (7), Observed mean starting delay values for different types of vehicles

Type of vehicle	Mean starting delay	Observed sample size
Mixed traffic	2.129	1985
Passenger car	1.692	1497
Mini bus	3.005	60
Normal bus	3.185	36
Truck	3.034	43
Truck-trailer	3.953	20
Tractor	3.104	7
Total	3648	

Average vehicle queue length

The number of vehicles waiting at the commencement of green is usually referred to as vehicle queue length. This number depends on traffic factors such as vehicle arrival flow, saturation flow, phasing, cycle time and duration of red indication. The time required for vehicle queue to discharge has a substantial effect on the excess vehicular CO emissions. The increase in queue length can cause an increase in excess vehicular CO emission. An indication to this can be found by examination of the data presented in **Fig. (3)**.

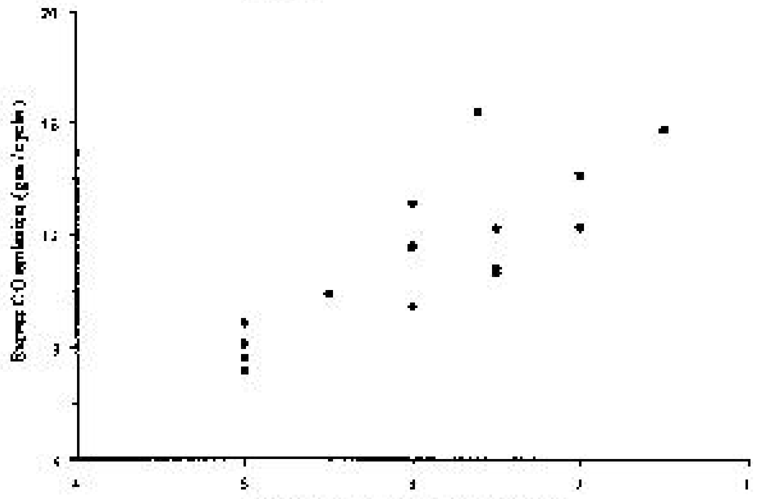

Fig. (**4**). Effect of average vehicle queue length on excess CO emissions

This is attributed for two major reasons. Firstly, an increase in the queue length means increase in the number of CO emitters, and hence, in the amount of CO gas. Secondly, an increase in queue length result in an increase in the time required for vehicles to dissipate during green. This has the implication of increase CO emissions while queuing vehicles are in idle, kinematics and dynamic modes of movement.

By contrast, vehicle queue length can result in decrease in vehicle discharge headway with the increase in vehicle position in queue. An indication to this can be found by observing the data presented in **Table (8)**. As a consequence of this driver behaviour, it is possible to argue that vehicle CO emission decrease with the increase in vehicle queue length. This decrease in vehicle discharge headway with the increase in vehicle position in queue can be attributed to the decrease in driver perception-reaction time. This decrease can result from the possible impact of queuing time on driver.

However, the resultant effect of vehicle queue length is that CO emission increase with the increase in the average queue length.

Table (8)-, Effect of vehicle position in queue on vehicle discharge headway

Vehicle position in queue	2	3	4	5	6	7	8	9	10
Discharge headway	2.53	2.45	2.35	2.22	2.01	1.89	1.65	1.70	1.32
Total	**1882**	**1675**	**1315**	**889**	**500**	**229**	**71**	**15**	**3**

Percent Stopped Vehicles

As the percent stopped vehicles increases the excess vehicular CO emission also increase. This is clear in **Fig.(4)**, which is a scatter plot of percent stopped vehicles and the excess vehicular CO emissions. The reason may be attributed for fact that as the percent stopped vehicles increases the idling, accelerating and decelerating times increase and the constant speed time decrease. Hence, the difference in CO emission rates between these modes namely the excess CO emission increase with the increase in percent stopped vehicles.

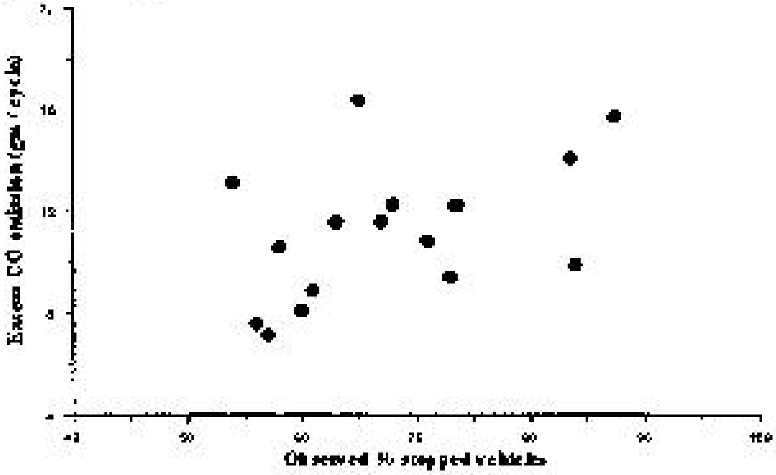

Fig.(4), Effect of percent stopped vehicles on vehicle excess CO emissions

Driver end lost time

The amber signal indication period follow the green signal used to provide the driver with a safe transition interval before the signal change into red. Therefore drivers arriving during this interval face the situation of either, decelerate to stop the vehicle before the stop-line or continue movement and accelerate if necessary to cross the intersection area before the commencement of the red signal. The choice of the proper action can vary between drivers. The end lost time defined as the unused portion of the amber interval result from the behaviour of those drivers who choose to stop during amber.

The effect of end lost time on vehicular CO emission is similar to that described for the effect of vehicle starting delay, that is CO emission increase with the increase in vehicle end lost time. Indication to this trend can be found by examination of the data presented in **Fig.(5)**. This trend in the data can be attributed for reasons similar to that described as above in the section of effect of driver start lost time on excess CO emissions.

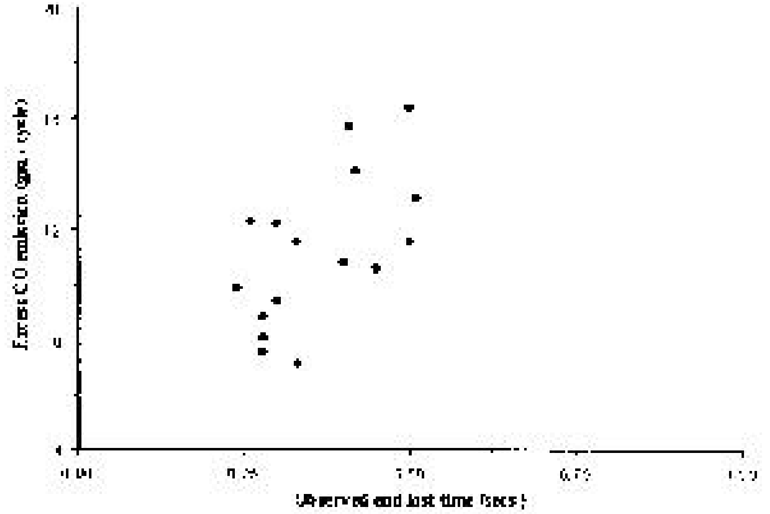

Fig. (5), Observed effect of driver behaviour during amber on CO emissions

Driver behaviour during amber is further examined by observation of the effect of time since start of amber on driver decision. Result of the statistical analysis made presented graphically in **Fig. (6)**, in the form of a standardized frequency polygon. The presented data indicate that the majority of the observed drivers pass over the stop-line when they arrive during the first 1.5 seconds following the start of amber. However, this behaviour vary with the type of vehicle observed. An indication to this variation can be seen by examination of the data presented in **Table (9)**.

Table (9). Observed variation of amber mean time used by vehicles with type of vehicle

Type of vehicle	Observed No. of vehicles	Mean time used by vehicles since start of amber
Passenger car	644	1.06
Small truck	52	1.46
Mini bus	42	1.20
Normal bus	39	1.52
Large truck	14	1.65
Tractor	8	1.34

In general excess CO emission increases with the increase in end lost time and the majority of the observed drivers pass over the stop-line when they arrive during the first half of the amber period.

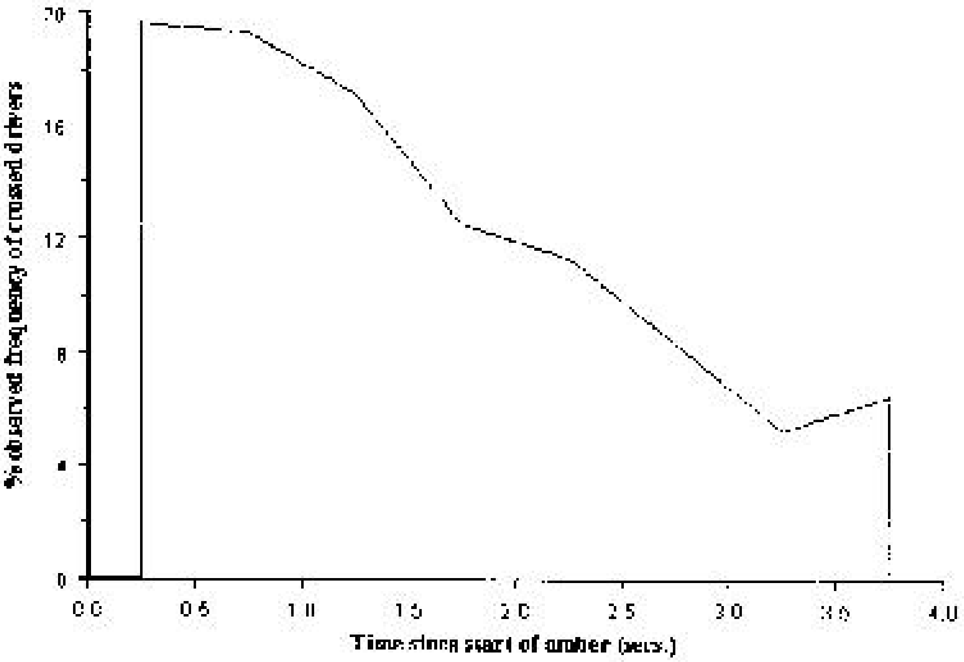

Fig.(6). Variation of excess CO emissions with the used time by vehicles since start of amber

Concluding remarks

The obtained results of this research work summarized as below:

1- Transient modes have substantial effect on CO emission rates, with decelerating mode having the highest CO emission rate. This conclusion is in agreement with that reported by the presented literature.
2- Gasoline powered vehicles emit higher percentages of CO emissions than diesel powered vehicles.
3- The obtained emission rates are based on the observed driver behaviours and vehicle types. It is rather unlikely that different vehicle compositions would produce similar results.
4- High driver precipitation-reaction time values, can result in an increase in vehicle excess CO emission rates.

5- Vehicle average queue length has a considerable effect on vehicle excess CO emissions, which increases with the increase in average queue length.
6- Improve vehicle movement during amber period can result in reduction in the excess CO emissions if safety can be maintained.

REFERENCES

Al-Neami, Ali H. (2000), Event- A Computer Program For Abstraction Of Traffic Data, The Scientific Journal Of Tikrit University, Engineering Sciences, Vol.(7). No.(2), Sept.

Al-Omari, B. (1997), Techniques to Reduce Vehicular Emission (US Practice). Proceedings of the First Jordanian Conference on Traffic Engineering and Environment, Amman, Jordan. 13-15 May. pp. 125-133.

Benson, Paul E. (1992), A Review of the Development and Application of the CALINE 3 and CALINE 4 Models, Atmospheric Environment, Vol.(26B), No.(1), pp. 378-390.

Case, D. J. (1982), Emissions from Motor Vehicles, Traffic Engineering and Control, March, pp. 139-145.

Claggett, M., Shrock, J. and Noll, K. (1981), Carbon Monoxide near Urban Intersection. Atmospheric Environment. Vol. (15), No. (9), pp. 1633-1642.

Cohen, S. L. (1977), Use of Traffic Simulation in Analysis of Carbon Monoxide Pollution. Transportation Research Board, TRB 648, pp. 74-76.

Dr. Al-Jamr, A. (1997), Air Pollution, Workshop on Traffic Engineering and Environment, held at Jordan Engineers Association, Amman-Jordan, 10-12 May.

Lee, F. P. (1983), Vehicle Emissions at Intersections. Ph.D. Thesis, University of Texas at Austin, Austin, U.S.A.

Lieberman, Edward B.(1976), New Techniques for Evaluating Urban Traffic Energy Consumption. TRB, 599, pp. 41-45.

Matzoros, A. (1988), A Junction Based Model of Air Pollution from Urban Road Networks. Ph.D. Thesis, University of Leeds, U.K.

McShane, W. R. and Roess, R. R. (1990), Traffic Engineering. Prentice Hall Polytechnic Series in Traffic Engineering, Prentice Hall, Englewood Cliffs, New Jersey, U.S.A.

Patterson, R. M. and Meyer, E. L. (1975), An Approach for Relating Traffic to Ambient CO Concentrations at Signalized Intersections. The 68th Annual Meeting of Air Pollution Control Association. Paper No. (75), Boston, U.S.A.

Singh, M. P., Goyal, S., Agarwal, S., Kumari, M. and Panwar, T. S. (1990), Predicted Measured Concentrations of Traffic CO Over Delhi. Atmospheric Environment, V 24A, N4, 1990, pp. 801-810.

د. بسام العناني "تأثير سير المركبات داخـل المـدن علـى البيئـة" (1997), Proceedings of the First Jordanian Conference on Traffic Engineering and Environment, Amman, Jordan, 13-15 May, pp.199-212.

نضال محمد سمارة (1997) . "التلوث البيئي من وسائط النقل" , Proceedings of the First Jordanian Conference on Traffic Engineering and Environment, Amman, Jordan, 13-15 May, pp.178-198.

APPLICATION OF DECISION SUPPORT SYSTEM IN CONSTRUCTION PROJECTS USE IN COST MANGEMENT

Sidqi I. Razzouqi
Instructor
Civil Engineering Department
College of Engineering
University of Baghdad

Ahmed M. R. Mahjob
Civil Engineering Department
College of Engineering
University of Baghdad

ABSTRACT

This work is concerned with introducing new methods and techniques for the projects management in construction industry. This research suggest that the Iraqi engineering staff, who work in construction sector, have a poor knowledge about the subject of Decision Support System (D.S.S.) in spite of that this subject have a wide uses in construction companies in the world. So the researcher presents this study to introduce and to increase the knowledge about the concept of Decision Support System.

This research consist of the questionnaire process for construction companies, then the research use the questionnaire results in building a proposed Decision Support System, also the questionnaire process indicate the relation between the decision structure and the organizational levels.

The results obtained from the questionnaire process shows that there is a requirement for Decision Support System in cost control decisions support. So the researcher build a Decision Support System for cost control process which can be used by the planner and estimator for different types of projects. The researcher also applies and evaluates the proposed system in some Iraqi construction companies.

The application and evaluation process recommended the needs for applying the Decision Support System for project management in construction companies.

الخلاصة

يتعلق هذا العمل البحثي بتقديم الطرائق والتقنيات الحديثة لإدارة مشاريع الصناعة الإنشائية. يفترض البحث أن الكادر الهندسي العراقي، الذي يعمل في قطاع الإنشاءات، لديه معرفة قليلة حول موضوع نظام دعم القرار بالرغم من أن هذا الموضوع له استخدامات عديدة في شركات الإنشاء في العالم. لذلك يقدم الباحث هذه الدراسة لإدخال وزيادة المعرفة حول مفهوم نظام دعم القرار.

يضم البحث عملية استبيان لشركات الإنشاء، يقوم الباحث بعدها باستخدام نتائج الاستبيان في تطبيق نظام دعم قرار مقترح، كما تؤشر عملية الاستبيان العلاقة بين هيكلية القرار والمستويات الإدارية. لقد بينت نتائج عملية الاستبيان الحاجة إلى نظام دعم القرار في قرارات السيطرة الكلفوية. لذلك قام الباحث ببناء نظام دعم قرار للسيطرة الكلفوية والذي يمكن استخدامه من قبل المخططين والمخمنين لمختلف أنواع المشاريع الإنشائية. كما قام الباحث بتطبيق وتقويم للنظام المقترح في بعض شركات الإنشاء العراقية.

KEY WORDS
Decision support system, Project management, Cost control. Decision structure and Organization level.

INTRODUCTION

When ever a decision is made, one of the proposed alternatives is chosen. Future activity focused on the chosen alternative uses time, money and other resource, and excludes any efforts on the alternatives rejected. Thus, if a poor choice was made and later decided to revise the decision, all the intervening time is lost and expenditure are, for the most parties. Thus all decisions commit the decision makers and other parties related for further efforts to make better decisions.

Successful project management depends on the ability to make good decisions. The ability to make good decisions depends on the availability of timely, accurate, and organized information in the right format at the right time. To handle such task, project managers, should use a proper planning and management system. One of these systems which has received considerable attention in the recent years is the Decision Support System.

In spite of that construction industry founded and developed from thousands of years, but, it is still less organized and controlled as compare with other industries (e.g. Manufacture industries). Also construction industry consists a lot of decision making with uncertainties situations.

To work in such environment and to increase the project organization and control, in construction industry, many researchers working in the construction management field began highlighting new techniques and methods to achieve this target.

From this start point the idea of making this study have been crystallized to show Decision Support System as a modern method used in project planning and control, also, to show its basic concepts, to identify its types, to find areas in project management working with Decision Support System. Then, this study derives results and recommendations that develop and support this method in project management.

DEFINITION OF DECISION SUPPORT SYSTEM

Decision Support System can be defined as "An organized collection of people, procedure, software, database and devices used to provides support in three main categories: data collection, analysis of models and presentation to help in making decisions".(Post and Anderson 2000; Stair and Georgy 1997)

DECISION SUPPORT SYSTEM OBJECTIVES

There are six major objectives of D.S.S. which are (Turban 1988).

1- D.S.S assists managers in their decision processes in semi-structured (or unstructured) tasks.

2- D.S.S support rather than replace managerial judgment.

3- D.S.S improve the effectiveness of the decisions, not the efficiency with which decisions are being made.

4-It incorporates data and models, as well as, other analytical techniques.

5-It focus on features that make them easy to use by non-technical users in interactive mode.

6-It emphasize flexibility and adaptability to make accommodate changes in the environment and decision making approach of the user.

TYPES OF DECISION SUPPORT SYSTEM

There are seven type of D.S.S as follows (Mallach 2000).

1-File drawer systems: -

Allow immediate access to data items.

2-Data analysis systems: -

Allow the manipulation of data by means of operators tailored to the task and setting or operates of
general nature.

3-Analysis information systems: -
Provide access to a series of database and small models.

4-Accounting models: -
Calculate the consequences of planned actions on the basis of accounting definitions.

5-Representational models: -
Estimate the consequences of action on the basis of models that are partially non definitional.

6-Optimization systems: -
Provide guidelines for action by generating the optimal solution consistent with a set of constraints.

7-Suggestion systems: -
Perform mechanical work leading to a specific suggested decision for a fairly structured task..

The first three types are data-oriented while the remaining four types are model- oriented as shown in **Fig. (1)**.

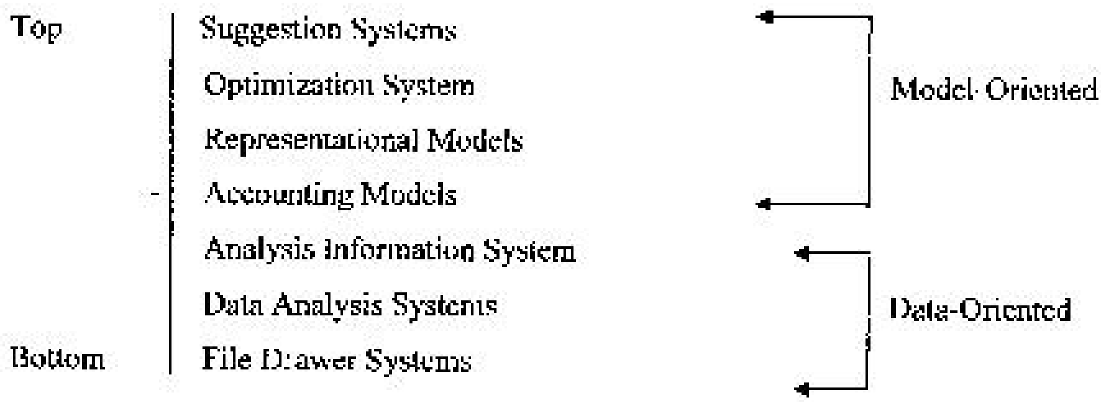

Fig (1) The seven types of decision support system (Mallach 2000).

THE QUESTIONNAIRE PROCESS

The questionnaire form is designed for the processes in project management and to achieve this goal the researcher employed the processes included in the Specification of the International Organization of Standardization (ISO 10006) down the title "Quality management -Guideline to quality in project management", because this specification involves all the processes and activities in project management.

There main two targets of the questionnaire process is to investigate the process in project management that requires a D.S.S to help in dealing with its decision. and indicate the relation between the decision structure and the organizational level.

THE RESEARCH SAMPLE

The research sample represents the major factor that the questionnaire success depends on the success of selecting them. The research sample represents the tool that tells us the information we need from the field of engineering work. The research sample consists of individuals working in four engineering fields (planning and scheduling, estimating and pricing, designing and construction), because many decision appear in these field in construction projects.

The research sample involves (25) individuals who working in construction companies and have experience in the engineering fields listing above. The results of the questionnaire process are as shown in **Table (1)** through **Table (11)** below.

Table (1)

Process	Importance	Top management	Middle management	Operational management
Strategic	4/25=16%	25/25=100%		
Interdependency management			24/25=965	1/25=4%
Scope related		18/25=72%	7/25=28%	
Time related		5/25=20%	20/25=80%	
Cost related	18/25=72%	6/25=24%	19/25=76%	
Resource related	2/25=8%	1/25=4%	24/25=96%	
Personal related			2/25=8%	23/25=92%
Communication related operational			3/25=12%	22/25=88%
Risk related	1/25=4%	2/25=6%	22/25=88%	1/25=4%
Purchasing related			23/25=92%	2/25=8%

Table (2) The Strategic Process

Process	Structured	Semi-structured	Un-structured
Strategic		5/25=20%	20/25=80%

Table (3) The Interdependency Process.

Process	Importance	Structured	Semi-structured	Un-structured
Project initiation and plan development	19/25=76%	20/25=80%	5/25=20%	
Interaction management		6/25=24%	18/20=72%	1/25=4%
Change and configuration management	6/25=24%		7/25=28%	18/25=72%
Closure		22/25=88%	3/25=12%	

Table (4) The Resource Related Process.

Process	Importance	Structured	Semi-structured	Un-structured
Resource planning	9/25=36%	4/25=16%	21/25=84%	-
Resource control	16/25=64%	19/25=76%	4/25=16%	2/25=8%

Table (5) The Scope Related Process.

Process	Importance	Structured	Semi-structured	Un-structured
Concept development	4/25=16%		5/25=20%	20/25=80%
Scope development and control			8/25=32%	17/25=68%
Activity definition	4/25=16%	3/25=12%	22/25=88%	
Activity Control	17/25=68%		21/25=84%	4/25=16%

Table (6) The Time Related Process.

Process	Importance	Structured	Semi-structured	Un-structured
Activity dependency planning	6/25=24%		19/25=76%	6/25=24%
Duration estimation	1/25=4%		23/25=92%	2/25=8%
Schedule development		9/25=36%	16/25=64%	
Schedule control	18/25=72%	6/25=24%	18/25=72%	1/25=4%

Table (7) The Cost Related Process

Process	Importance	Structured	Semi-structured	Un-structured
Cost estimation	12/25=48%		21/25=84%	4/25=16%
Budgeting		2/25=8%	23/25=92%	
Cost control	13/25=52%	1/25=4%	22/25=88%	2/25=8%

Table (8) The Personal Related Process.

Process	Importance	Structured	Semi-structured	Un-structured
Organizational structure definition	17/25=68%	25/25=100%		
Staff allocation process	2/25=8%	3/25=12%	22/25=88%	
Team development	6/25=24%	24/25=96%	1/25=4%	

Table (9) The Communication Related Operation Process.

Process	impotence	structured	Semi-structured	Un-structured
Communication planning	1/25 4%		25/25=100%	
Information management	23/25=92%	5/25=20%	20/25=80%	
Communication Control	1/25=4%	19/25=76%	6/25=24%	

Table (10) The Risk Related Process.

Process	Importance	Structured	Semi-Structured	Un-structured
Risk identification	3/25=12%		8/25=32%	17/25=68%
Risk estimation	21/25=84%		3/25=12%	22/25=88%
Risk response development	1/25-4%	1/25=4%	18/25=72%	6/25=24%
Risk control		16/25=64%	9/25=36%	

Table (11) The Purchasing Related Process.

Process	Importance	Structured	Semi-structured	Un-structured
Purchasing planning and control			4/25=16%	21/25=84%
Requirement documentation	5/25=20%	22/25=88%	3/25=12%	
Subcontractor evaluation	2/25=8%		1/25=4%	24/25=96%
Subcontracting		23/25=92%	2/25=8%	
Contract control	18/25=72%	10/25=40%	15/25=60%	

THE QUESTIONNAIRE RESULT

1- That regarding the process or activity that needs a D.S.S. to help in solving its problem. The result show that (72%) of the respondents confirmed that the cost related process need a D.S.S. in dealing with its decisions.
2- that regarding the divisions of the process selected (the cost related). The result shows that a (48%) of the respondents agreed that the cost estimation need a D.S.S., while (52%) of the respondents agreed the cost control need a DSS in dealing with its decisions. So it's recommended developing a D.S.S. to help in making decision for both cost estimation and control.
3- That regarding the organization level and for the project management process and the type of structure for each division in the processes the result is summarized in **Table (12)** below. Most of the results agreed with the theories listed in the review of literature. that's didn't mean (100%) of agreement, but more than (70%) in most cases, because there are many interactions between the processes as well as between the organization levels. But the main goal of this result is to give an indication about the relationship between the organizational levels and type of structure for the processes.

4- In **Table (12)** below, there is a mismatch some between processes and the organizational level performed it, like in (Scope related and Time related processes). **Table (12)** indicates that these processes performed by Top Management, but actually, these processes performed by Middle Management. This may be related to the interaction between some processes in project management as well as between the persons who performed these processes. More of that there is a misunderstanding may happen for the authority and responsibility for some respondents of the questionnaire, and that may gives a misleading answers that gives incorrect results.

Table (12) The Relationship Between the Organizational Level and Type of Structure for the Project Management Processes.

Levels / Type Of structure	Operational Management	Middle Management	Top Management
Structured	*Organizational structure definition *Team development *Communication control	*Project initiation and project plan development *Resource control *Risk control *Requirement documentation *Subcontracting	
Semi-structured	*Staff allocation process *Communication planning *Information management	*Interaction management *Cost estimation *Budgeting *Cost control *Resource planning *Risk response development *Contract control	*Activity definition *Activity control *Activity dependency planning *Duration estimation *Schedule development *schedule control
Un-structured		*Change configuration management *Risk identification *Risk estimation *Purchasing planning and control *Sub contractor evaluation	*Strategic process *Concept development *Scope development and control

BUILDING PROPOSED D.S.S. FOR COST CONTROL PROCESS

According to ISO 10006- Claus (5.6.3) "The information needed to ensure the timely release of funds should be made available and provided as input to the resource control process" after reading this statement, it can be understood that the cost control should provide an information about the amount of money required in every stage of the project, as well as, compare the amount of funds spent on the project in every stage with similar projects implemented in the past. This comparison be available when use the cash flow forecasting for the project. The cash flow will provide regular payments.

represent the expenditure of the project, and by making use of these data which had been documented in the companies for the projects implemented in the past, the estimator or the planner could compare the amount of money expend for constructed project with a similar type of project, accomplished in the past, or he could calculate the required amount of money for the project in the next payment.

OVERVIEW OF THE SYSTEM

The main idea of the system (program) is to collect the data, which represented by the cash flow for completed projects, and then calculate the maximum and the minimum percentage of expenditure for the projects with the same type of the required project, which represented as a percentage from the total cost. For example: if the total cost of a project equal to (10000000 I.D) and the expenditure at (70%) of completion equal to (65000000 I.D) then the percentage of expenditure at (70%) equal to{65000000/10000000=65%}. This percentage represents the result of the data for on project, so the program will repeat this process on the other data of the projects with the same type (for example school projects) and then calculate the maximum and the minimum percentage for all project of the same type in the database. **Fig (2)** through **Fig (6)** shows the windows for the proposed system.

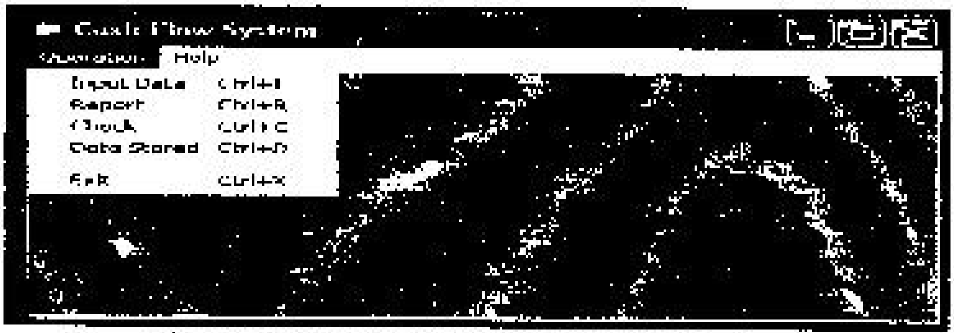

Fig (2) The main window for the proposed system.

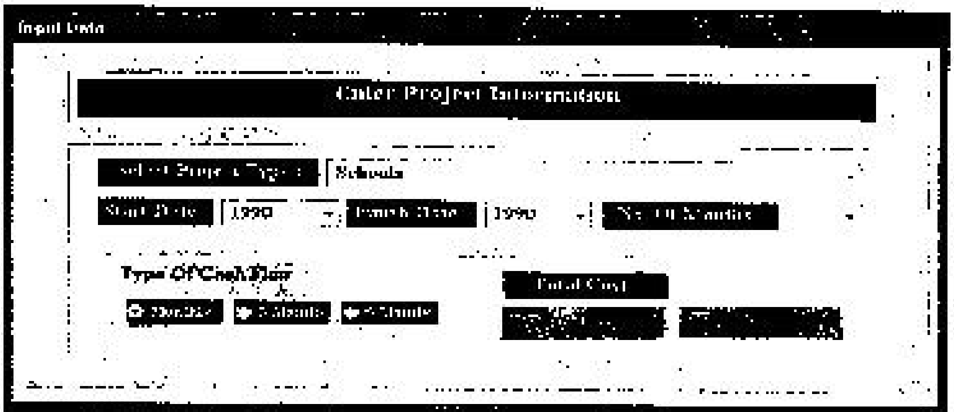

Fig (3) Input data window for the proposed system.

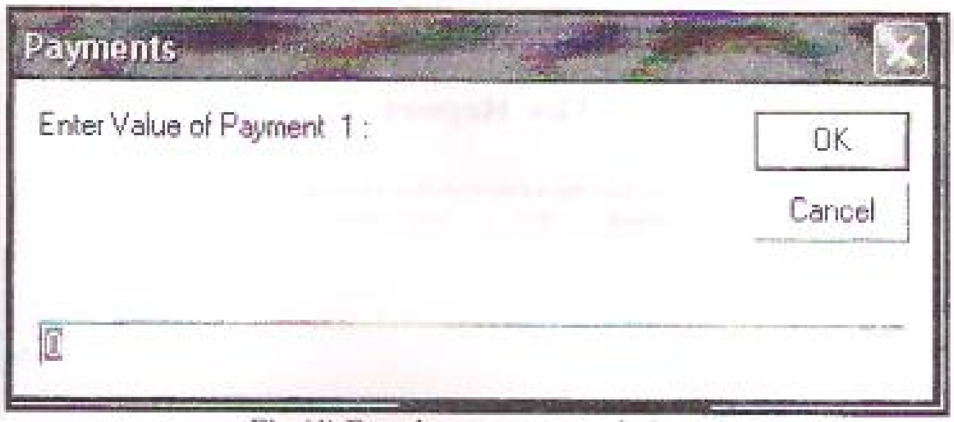

Fig (4) Entering payments window.

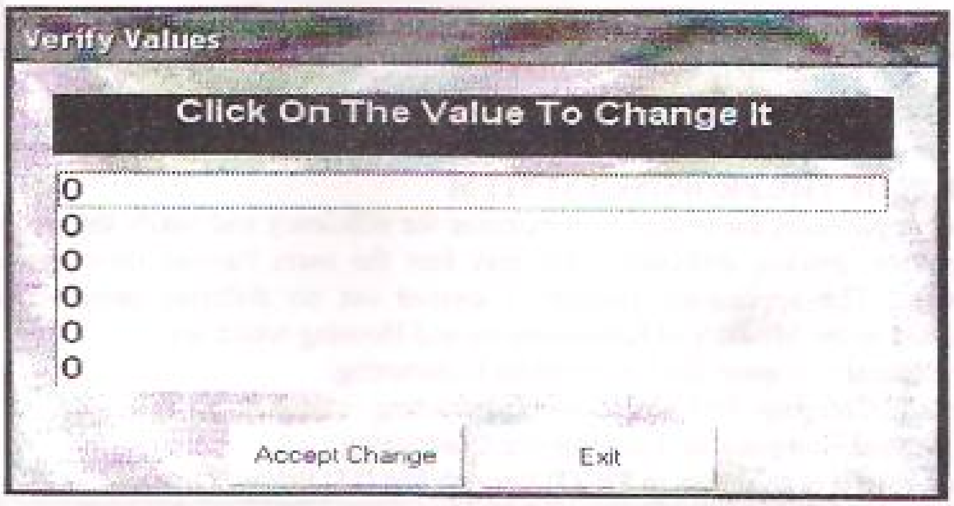

Fig (4) Payments Verifying window

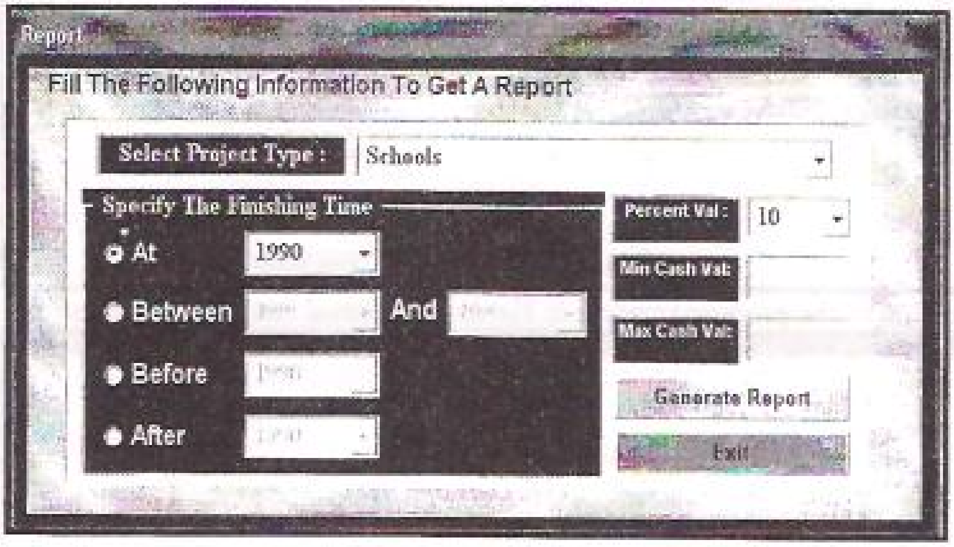

Fig (5) Information entering for the report.

Fig (6) Out put of the proposed system.

APPLICATION OF THE PROPOSED SYSTEM

The purpose of application the system is to examine the efficiency and verify the performance, also to detect any error, defects, difficulties that may face the users through their application of the proposed system. The application process is carried out on different projects in three state companies related to the Ministry of Rehabilitation and Housing which are:

1- Al-Farooq General Company for Construction Contracting.
2- Asuour General Company for Construction Contracting.
3- Hamorabi General Company for Construction Contracting.

The application results is as shown in **Fig (7)** through **Fig (11)** below.

Fig (7) Application of the proposed system in Hamorabi general company (Bridges projects).

Fig (8) Application of the proposed system in Hamorabi general company (Roads projects).

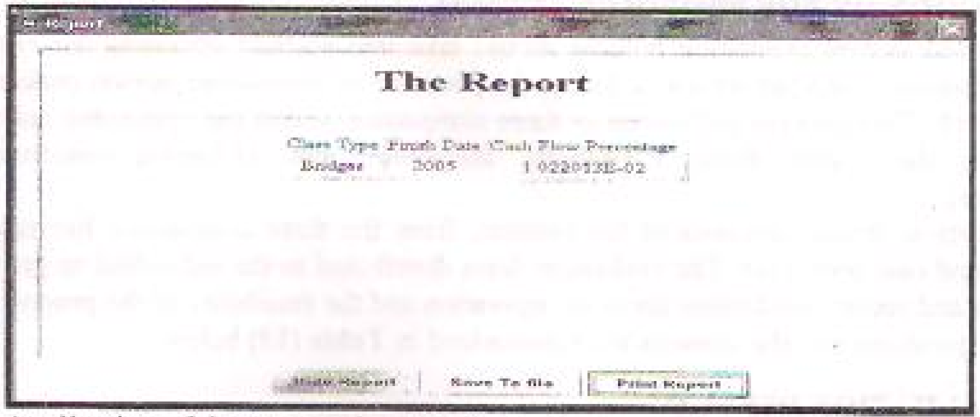

Fig (9) Application of the proposed system in Asuour general company (Bridges projects).

Fig (10) Application of the proposed system in Asuour general company (Roads projects).

Fig (11) Application of the proposed system in Al-Farooq general company (University project).

EVALUATION OF THE PROPOSED SYSTEM

The proposed system evaluation process should take into account operating the system before an open discussion connected with and during the presence of specialized person concerning with this type of work. This process performed in three companies, which the researcher collect the data of application the system from it (Ashour, Hamorabi, and Al-Farooq construction Contract Companies).

The evaluation process consists of ten persons, from the three companies, having experience in planning and cost processes. The evaluation form distributed to the individual to get their opinions, comments and recommendations about the operation and the feasibility of the proposed system. The evolution questions and the answers are summarized in **Table (13)** below.

THE EVALUATION RESULTS

The answer of the evaluation questions shows the following:

A- The proposed DSS is very good in collecting and entering the data and that give an indication of a very good user interface with the system.

B- The proposed DSS provide a very good assistance for the planners and the estimator.

C- The proposed DSS provide excellent information for the user.

D- The proposed DSS have a very good role in cost control process.

E- The answers agreed that the accuracy of the information provided by the system is very good.

F- The proposed DSS have a very good importance for the three companies.

CONCLUSIONS

1- The procedure followed in Iraqi construction companies, by the financial department and planning and follow up department, haven't the ability to play the actual role in cost control
2- Three is a mismatch between the authority, responsibility and the functional position when making managerial decisions.
3- There is lack of documentation process for management activities, especially, that related to the cost control and cost estimation.
4- The evaluation result of the proposed Decision Support System shows that the importance of implementing such system in construction companies.

Table (13) The Evaluation Questions and the Results.

No	The Questions	Excellent 100-90	V. Good 90-80	Good 80-70	Accept 70-60	The Degree	The Evaluation
1	The flexibility of collect and entering the data in the system (user interface).	1	7	2		84	V. Good
2	The assistants that the system provides to the planners and estimators	1	8	1		85	V. Good
3	The type and importance of the information provided by the system	8	2			93	Excellent
4	The role of the proposed system in cost control.	2	8			87	V. Good
5	The accuracy of the information provided by the system.	2	6	2		85	V. Good
6	The important of the proposed system to your company.	3	7			88	V. Good

REFERENCES

ISO 10006 (1996), Quality Management-Guide Line to Quality in project Management, International Organization for Standardization

Mallach, Efrem G. (2000), Decision Support and Data Warehouse Systems, McGraw-Hill Book, 1ST Edition.

Post, Gerald V. and Anderson, David L. (2000), Management Information System, Irwin/ McGraw-Hill, 2nd Edition.

Stair, Ralph M. and George W. Reynolds (1997), Principles of Information Systems: A Managerial Approach, Course Technology, Cambridge, Mass.

Turban, Efraim. (1988), Decision Support and Expert Systems, Macmillan Publishing Company, 1st Edition.

REMOVAL OF SCALE DEPOSITED ON THE INTERNAL SURFACES OF PIPES IN COOLING SYSTEMS

Prof.dr. Abbas h. Sulaymon **Dr. Ajwa saber majeed**
Chem.Eng.Dept. -Engineering College -University of Baghdad

ABSTRACT

The possibility of using inhibited hydrochloric acid in descaling of water deposits on heat exchanger and cooling system tubes have been investigated. A dynamic flow system was designed for this state. Experiments were carried out using different, temperatures, solution flow rates,times,and different hydrochloric acid concentrations inhibited with Hexamine .
Kinetics of acid – iron oxide scale reaction was studied using hydrochloric acid .The kinetics analysis showed that the acid- FeO scale reaction followes 1st order reaction. It was found that the FeO scale removal was mass transfer controlling process.
Iron- oxide scale removal process was analyzed as mass transfer operation and adequate semi-empirical correlations for scale removal (or mass transfer rate) under different conditions, in a dimensionless form have been obtained. The results of iron- oxide scale removal (or mass transfer rate) are compared with many proposed models particularly those based on the concept of analogy among momentum and mass transfer.
Prandtl- Taylor analogy showed a good agreement with experimental mass transfer results.

الخلاصة

يهدف البحث الى إمكانية استخدام الطرق الكيمياوية في إزالة الترسبات مـن السـطوح الداخليـة لأنابيـ
المبادلات الحرارية وانابيب المياه الحارة والمراجل وأجهزة التبريد.
تم الحصول على نماذج لأنابيب نقل المياه الساخنة من مصفى بيجي (شركة مصافي الشمال) وقد اجـر
تحليل كامل لهذه الترسبات واعتمادا على هذا التحليل تم اختيار المواد الكيمياوية المناسبة للإزالة.
لقد استعمل حامض الهيدروكلوريك مع الهكسامين كمادة مثبطة للتأكل.
درست حركية تفاعل حامض الهيدروكلوريك مع تكلسات أوكسيد الحديد الموجودة ضمن خليط التكلـ
وباستعمال حامض الهيدروكلوريك . وبين التحليل الحركي ان التفاعل هو من الدرجة الأولى نسبة إلى الحـ
. وتبين ان تفاعل إزالة تكلسات الحديد مسيطر عليه فيزياويـــا
(أي عملية انتقال الكتلة هي المسيطرة على سرعة التفاعل).
تم تحليل عملية إزالة التكلسات كعملية انتقال كتلة ووضعت علاقات تجريبية وضعية لحساب معدل إزا
التكلسات تحت ظروف مختلفة. وقد تم مقارنة النتائج العملية مع عدة علاقات موضوعية للتعبير عن ا
الكتلة بين الجدار والمائع وخاصة العلاقات المبنية على التشابه في ميكانيكية الانتقال بـين الكتلـة والـ

وة إمكانية حساب معدل إزالة التكلسات باستخدام هذه العلاقات. وقد تم اعتماد احد هذه العلاقات للتعبير عن معدل إزالة التكلسات في بداية العملية.

ت علاقة Prandtl Taylor توافقا جيدا مع النتائج العملية لكل قيم درجات الحرارة في بداية عملية الإزالة.

KEY WORDS
Scale,Chemical cleaning,Deposit,Hydrochloric acid,Descaling

INTRODUCTION

The deposition of solids occur on industrial equipments surfaces like heat exchanges ,boilers, cooling towers or any surface which water contacts minders along with salts and corrosion products.

Scale deposition in the industrial equipments occurs by any, or all of four mechanisms: crystallization-scaling, deposition of particulate matter, corrosion with subsequent transfer of corrosion products, and microbiological growth(Mansfield,G.H.and Terrell(1990).

Various cleaning methods have been used; mechanical, chemical and thermal or a combination of them.Cleaning up by chemicals is probably the most widely adopted procedure(Powell,S.T.(1954)). There is no physical damage to the tube bundle in chemical cleaning although there is a possibility of chemical reaction and corrosion inhibitor. Mineral acids used in chemical cleaning include hydrochloric and (HCl), sulfuric acid,and sulfamic acid (H_2NSO_3H). Other solvents used are organic acids.

Hydrochloric acid is the most commonly used solvent(NACE,T-8A on cleaning,corrosion 15,... and 15,17t(1959)), because this acid is safer, less expensive, can be diluted easily, soluble reaction product. Corrosion caused by the acid cleaning can be prevented or reduced by an inhibitor. Type and amount of the corrosion inhibitor depends on the acid concentration and temperature at which the cleaning solvent is used .

Cleaning solution usually passed in turbulent flow through the system, during acid cleaning process. When turbulent flow occurs in circular tubes, momentum is transferred between layers of fluid, this momentum transfer manfests itself as a frictional resistance and at the wall shear stress, which is equivalent to the time rate of momentum transfer per unit area(Philip J.W.Roberts and Donald R.Webster(2002)).

Mass transfer may occur during turbulent flow. Most of the experimental studies showed that there is a relation exists between mass transfer and skin friction, knowledge of such relationship would allow prediction of the rate of mass transfer from friction loss data.

The work of Osborne Reynold's (Reynolds,O.(1874) in 1874 has led to useful, simple equations relating the friction factor and the mass transfer coefficient by Reynold's analogy(Bennett,C.O.and J.E.Myers,(1982)).

The present investigation of the problem of scale removal is being studied mainly on tubes of heat exchangers obtained from Baiji Refinery using chemical solution (hydrochloric acid).

A special flow system has been designed where parts of these piping were being fixing in exposed to the treatment solution.

Percentages and rates of scale removal were studied as a function of temperature, circulation rate and concentration of an inhibited hydrochloric acid.

Furthermore a mathematical model to describe the solution mechanism was attempted and presented in this investigation.

EXPERIMENTAL WORK

1- Scaled carbon steel pipes from the main hot water lines were used. (10 cm long, 25mm O.D and 20 mm I.D). List of the scale materials was shown in **Table (1).**Hydrochloric acid with concentration of (3-10 wt%) was used.

Table(1) Complete Analysis of Baiji Refinery Scale Deposited on Heat Exchanger Tubes*.

Element Analysis	Wt.%
Iron (FeO)	51.8
CaO	2.2
$CaCO_3$	6.02
Al_2O_3	17.3
$MgCO_3$	7.74
ZnO	2.636
Silical (SiO)	4.12
Chlorine	0.05
SO_4	Traces
L.O.I.(loss on Ignition)	7.214
Total	99.08

* The analysis was carried out in Baji Refinery Laboratories

Hexamine was used as corrosion inhibitor with concentration of 0.1 wt%

2- A flow system for the descaling investigation was made of Q.V.F. glass. It consisted of 10 liters round bottom container with four necks, the container was connected from the bottom with the tuping through which hot solution circulated.

A controlled heating tapes were rapped around the insulated Q.V.F. glass tuping for heating the circulating solution.

The circulation of the chemical solution was effected using a centrifugal pump (0.2 KW) and the flow rate was measured using rotameter ranged (0-2000 L/hr).

The solution passed through the scaled metal specimen, and returned to the round bottom container as shown in **Fig.(1).**

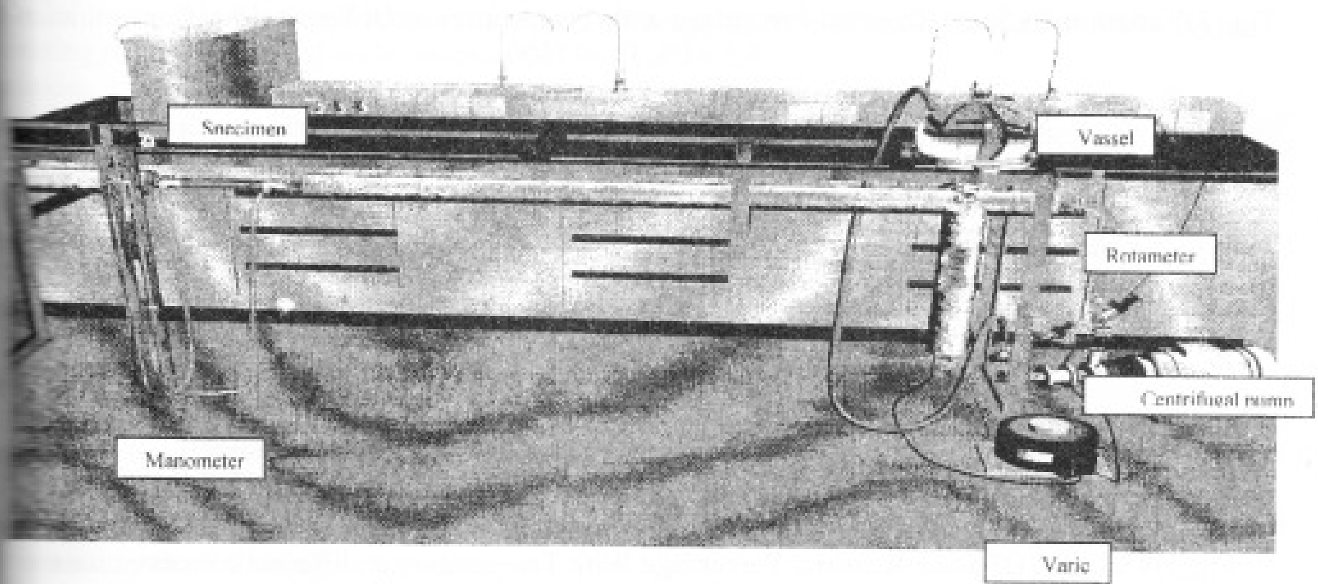

Fig(1) Experimental diagram of the system

The pressure drop through the specimen was measured using inverted U-tube manometer. The temperature of the test solution was measured by means of thermometer of the range (0-100 C°).

The concentration of the acid was measured using simple titration method.

The concentration of iron in the acid solution was measured by using Shimadiza UV-160 by determining the absorbance of the ferrous ions.

The amount of scale deposits which has been removed at each run was calculated by weight difference of the scaled tube before and after the tests.

RESULS AND DISCUSSION

Effect of experimental variables on percentage of scale removal:

Figures (2), (3) and (4) show the effect of temperature with the range of (25-70C°), acid concentration of (3-10wt%), solution circulation rate (as Re no.) with the range of (10000-25000) and descaling time of (2-6 hrs) on the scale removal process.

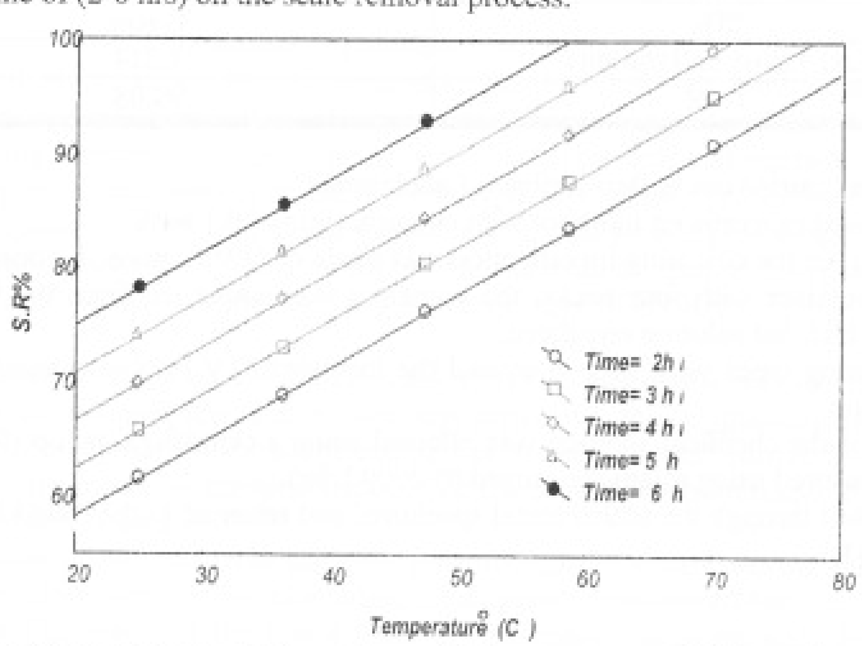

Fig.(2)Variation Of Scale Removal Percentage with Temperature at Different time, Concentration =6.5 wt%, Re=17500

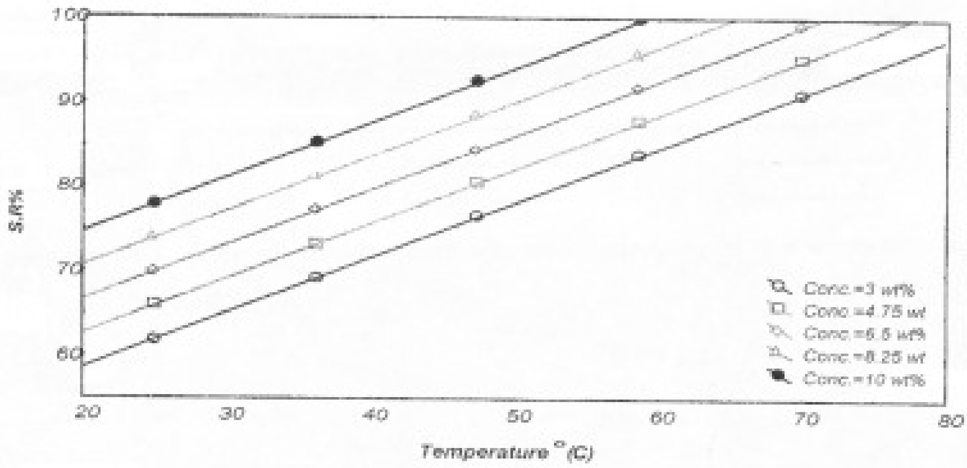

Fig(3)Variation Of Scale Removal Percentage With Temperature at different concentrations ,Time=4hr,Re=17500

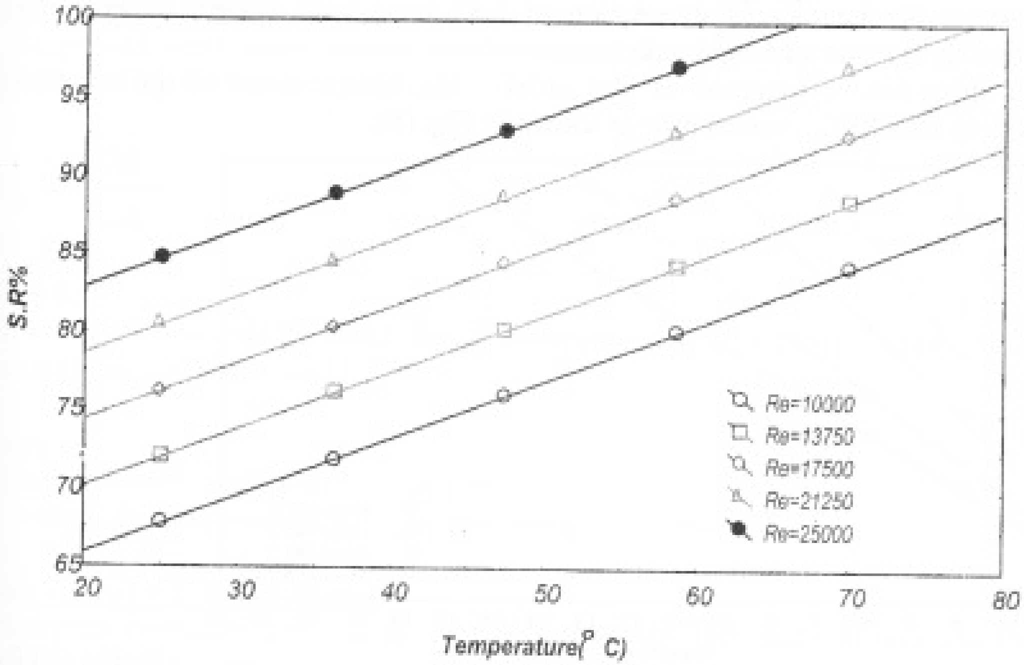

Fig.(4)Variation Of Scale Removal Percentage With Temperature at Different Re ,Time=4hr,Concetration=6.5 wt%

was shown that the increase of any of the above variables causes to increase the percentage of ale removal.The increasing of percentage of scale removal with increasing the temperature plained by the fact that increasing the temperature cause to increase the reaction rate constant and s its maximum value at the highest temperature. Also increasing the temperature cause to increase e convective mass transfer due to decreasing the solution viscosity and increasing the diffusivity the solution compounds.

e investigations of Charles and Moor (Charles,M.Loucks(1962) and Moore,R.E.(1972)) agrees th this conclusion.

e increase of acid concentration increases the percentage of scale removal which is due to the rease in concentration gradient between the bulk and the solid solution interface.

reasing the descaling time cause to increase the percentage of scale removal, that is due to the on of the acid to break the bound it. Hence increasing the time of scale exposed to acid solution reasing the percentage of scale removal.

reasing the circulation rate in the cleaning processcause to increase the percentage of scale oval, this behavior can be explained as follows, as the circulation rate increases the laminar -layer will be very small in thickness as the turbulence is high due to hindrance of fluid at the erogeneous surface of several compounds in the solid phase of the scale, then the chemical ction will also increases as the chemical materials has more chances to touch the particles of the face due to renwal of the chemicals as the boundary laminar sub-layer becomes more thin or will neglected.

etics of FeO Scale Removal

m the analysis of the scale composition **Table (1)**, it was clear that the most fraction of scale position is (FeO), then the most important reaction is the reaction of FeO scale with rochloric acid, which was studied in this research.

e stoichiometry of the reaction between iron oxide (FeO) and hydrogen ion in solution is sented by the following equation:

$$eO+2H^{+} \longrightarrow Fe^{+2} + H_2O \quad \text{------------(1)}$$

In order to determine the kinetics of dissolution of FeO scale with respect to Fe^{++} ion, the concentration of ferrous ion was measured with time .
The reaction rate order can be assumed as first order . The kinetic order of the reaction was determined by plotting Ln C_{A0}/C_A versus time as shown in **Fig. (5).**

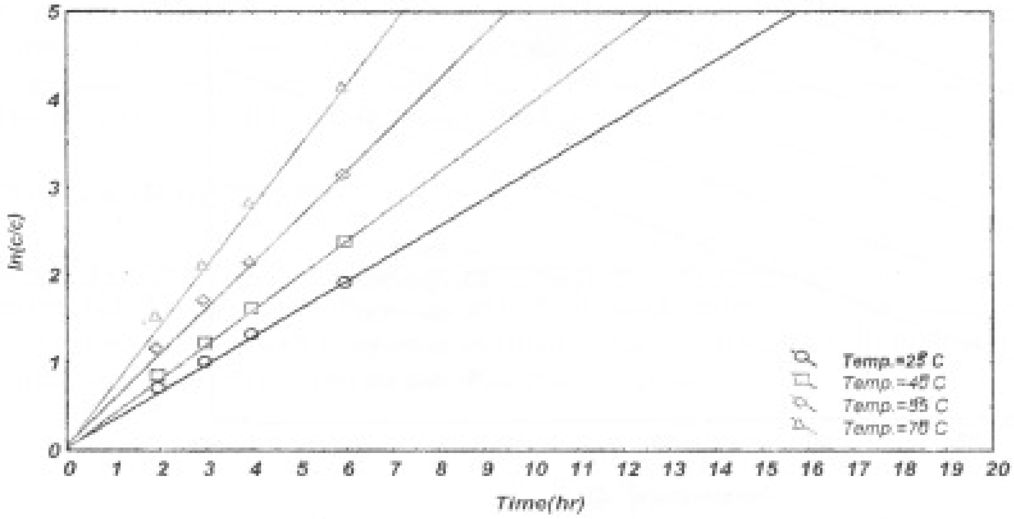

.(FigFig.(5) Rate of Desolution at Re=10000

This figure clearly establishes that the dissolution of iron oxide scale is first order with respect to ferrous ion.
The rate constant is a function of temperature and can be expressed by Arrheniu's equation :

k_r=A exp (–E/RT) (2)

Where :
A : exponential constant.
E : activation energy.
R : gas universal constant.
T : absolute temperature.

According to Arrheniu's equation (2) plot of Ln k_r versus $^1/_T$ as shown in **Fig. (6)** gives the slope equal to –E/R.
Activation energy (E) can be determined from the slope of the line. The value of the activation energy of the desolution process of FeO scale with hydrochloric acid = 15 KJ/mole.

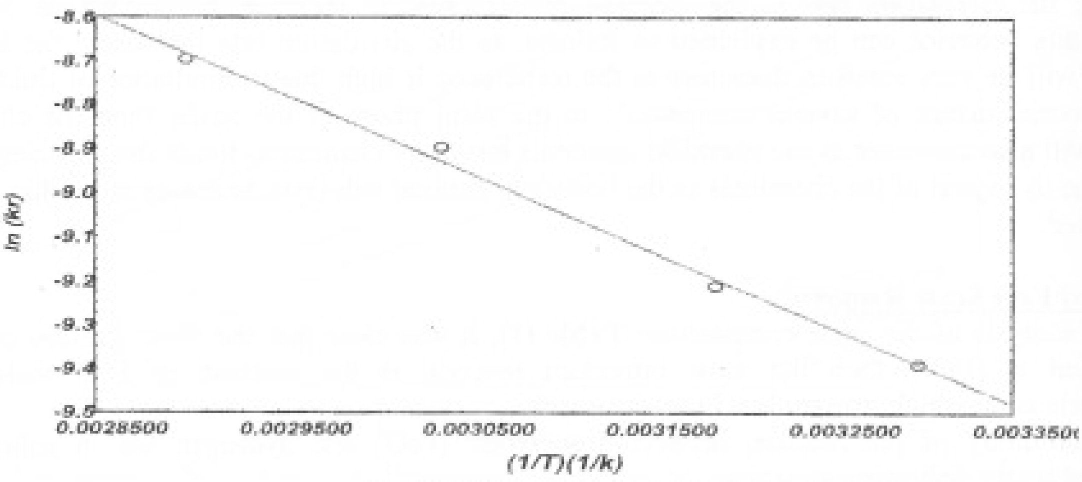

Fig.(6) Ln Kr Versus 1/T

Mass Transfer Results

In the present work mass transfer coefficient was calculated by estimating the mass flux of FeO (Fe^{+2}) ion using the following equation :

$$N_A = \frac{M}{t.A} \quad (3)$$

$$N_A = k\Delta C \quad (4)$$

It is worthy to note that the molar flux of hydrogen equal 2 times that of (Fe^{+2}) ions according to the chemical reaction equation(1).

Where :

k = mass transfer coefficient of hydrogen ion.

ΔC = the bulk concentration of hydrogen ions in the solution

Mass Transfer Limited Model

A complete formulation of the rate equation must take into account both the mass – transfer and chemical reaction rates.

In some instances, one of the rates, mass transfer or reaction, is so much smaller than the other that it becomes the controlling one.

The dominant mechanism can be deflected by observing the effects of certain changes in operating condition experimentally.

The fact that mass transfer rather than a chemical reaction is controlling the rate of reaction indicated by the law activation energy(Schmidt,N.O.(1976))which is in good agreement with the value obtained in this work, (activation energy about 15 KJ/mol for mass transfer controlled process, Tewari and, Campbell(1976).presented that the activation energy is (12-24 KJ/mol). and by the fact that the rate of desolution is increased by increasing the rate of liquid past the scale(Schmidt,N.O.(1976)).

Factors Affecting FeO Descaling And The Mass Transfer Coefficient

Effect of reynolds number and temperature

Figs. (7) and (8) show the variation of mass transfer coefficient and descaling rate with Re at various temperatures respectively. It is clear that (k) and descaling rate increases with increasing Re for all temperature values (25 to 70 °C).

The increase in k with Re can be explained according to the following equation(Bradley,G.W.(1977)and Poulson,B.(1983)).

$$k = \frac{D + \varepsilon_D}{\delta_d} \quad (5)$$

As Re No. increases the convective mass transport of hydrogen will increase, i.e. mass transfer by eddy diffusion (ε_D) due to the increased turbulence.

Increasing turbulence leads to decrease the thickness of viscous sub-layer and the diffusion layer that represents the main residence to momentum and mass transport respectively(Mahato,B.K.(1980) and Coulson,J.M.(1977)),hence the hydrogen concentration gradient at the surface will be increased leading to increase (k).

Increasing (k) with Re leads consequently to increases (Sh) over the whole range of temperature (or Sc) **Fig.(9)**

The increase in (Sh) with (Re) indicates that increasing Re leads to increase the mass transport by convection (or eddy diffusion) over that by molecular diffusion because Sh is the ratio between the two. The molecular diffusive mass transport (Diffusivity of hydrogen) is independent on Re, it varies only with Sc and temperature.

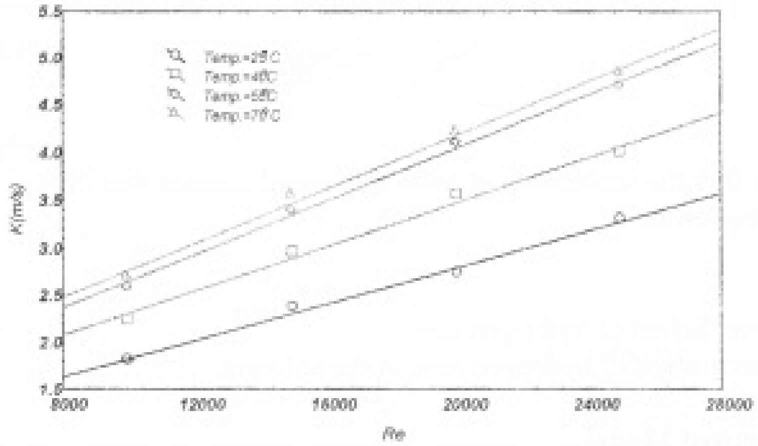

Fig.(7) Variation Of Mass Transfer Coefficient With Re at Various Temperature and t=300sec.

Using statistical analysis the following correlation is obtained for the whole range of Re No. and temperature (Sc) assuming the dependence of Sh on Sc is 1/3 as customary found(Coulson,J.M.(1977) and Hasan ,B.O.(2003)).

$$Sh = 0.053\ Re^{0.6208}\ Sc^{1/3} \qquad (7)$$

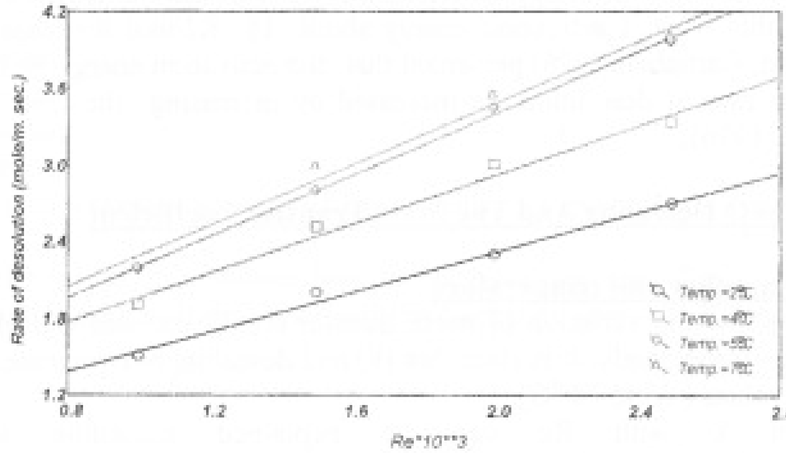

Fig.(8) Variation Of Desolution Rate with Re at time =300 sec.

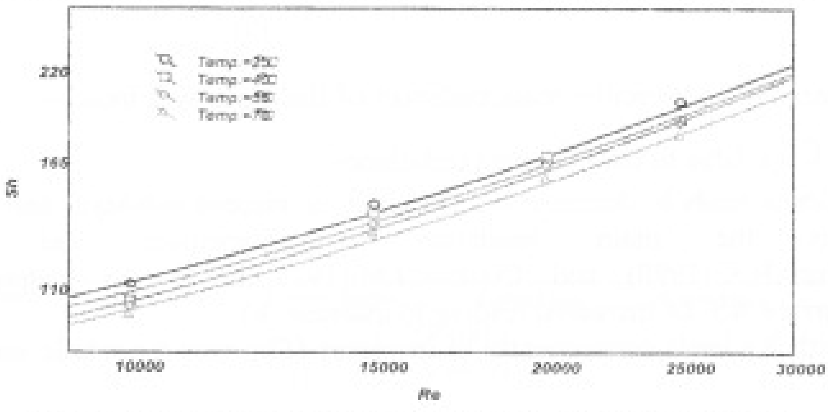

Fig.(9)Variation Of Sh With Re at Different Temperatures

The effect of increasing temperature on Sh is due to the increase two variables acting in opposing way on the value of Sh. These two variables are the mass transfer coefficient (k)) and the molecular diffusivity(D). Hence, the net effect of temperature on Sh will be determined by the change of the ratio k/D.

Effect of Time

Fig. (10) shows the variation of k or Sh with Re No. at various temperatures and time as a parameter. This figure indicate that at all the temperatures , the time causes a significant decrease in k for all Re range. This can be explained by the decrease of roughness as the time increases due to the scale removal, hence decreasing the mass transfer rate due to decreasing mass transfer area(Knudsen,J.G.(1958),Petulchov,B.S.(1970),Colburn,A.P.(1964),and Kandikar,S.G.,(2001)). Also formation of the chemical reaction product of the scale with the acid influence the mass transfer rate by influencing the hydrogen ion diffusion from the bulk to the scale surface (Brodkey,R.S.(1988).

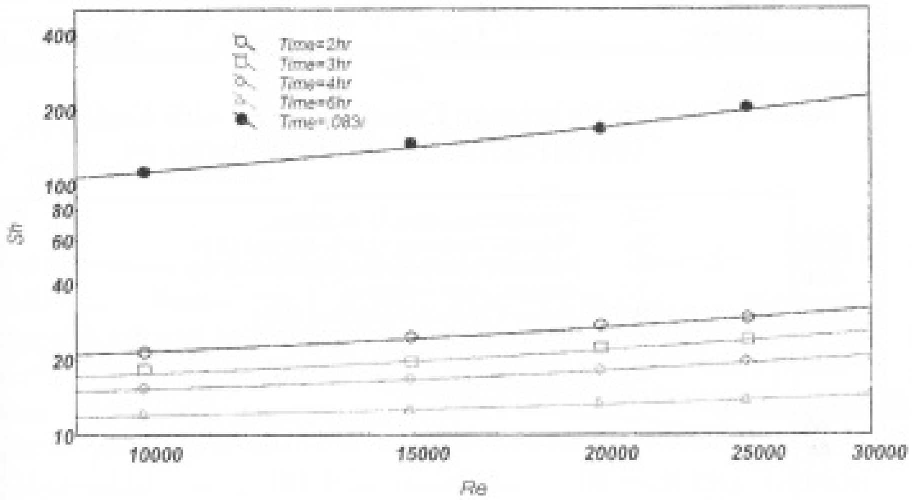

Fig.(10)Variation Of Sh With Re at Different Intervals and Temperature=25 °C

Comparison with The Proposed Model

In this section it is aimed to compare the experimental results of mass transfer with the proposed correlations particularly those which are based on the concept of analogies among momentum and mass transfer.

This comparison serves to investigate how far is the derived correlation deviate from the proposed models.

Making a comparison enable to adapt best correlation that can be employed to estimate scale removal rate through (sh).

The experimental mass transfer results were compared with other correlations presented in the appendix, such as prandtl and Taylor (Eq-1a) and Eq.(1b) and Prandtl–Taylor (Eq.2), Von Karman(Eq.3), Chilton –Colburn (Eq.4) and, Darshnalal (Eq.5).

Graphical comparison is shown in **Fig.(11).** Best agreement found to be with Prandtl-Taylor analogy. Eq.(1a) and Eq.(1b), (with a small difference due to the assumption that the calculated friction factor from the experimental work is equal to the friction factor of Iron-oxide scale) i.e. the scale removal can be well represented by this analogy for the entire range of Re and at the early period of the scale removal process.

Time (or scale removal) affects the capability of analogy correlation to estimate the mass transfer coefficient and mass transfer group (Sh) ,i.e. removing the scale increases the difference between the experimental mass transfer coefficient and that obtained from analogy models .

Fig.(12), shows a comparison between experimental Sh and that obtained from analogies for (t = 4,6 hr) i.e. when most of the scale removed at all temperatures it is evident that time causes large difference between the mass transfer rate (Sh) during scale removal process that predicted by analogy correlations and experimented results.

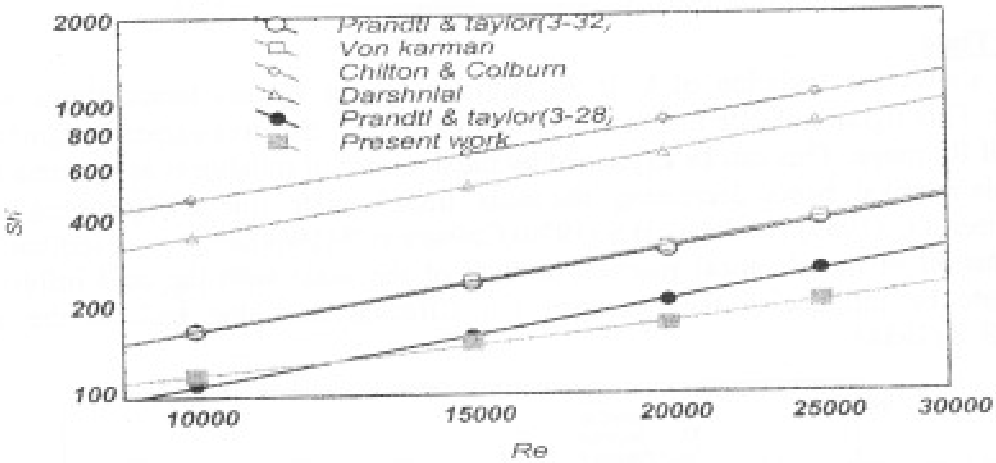

Fig.(11) Comparison between Experimental Sh with Analogies.
108108108108108108108108108

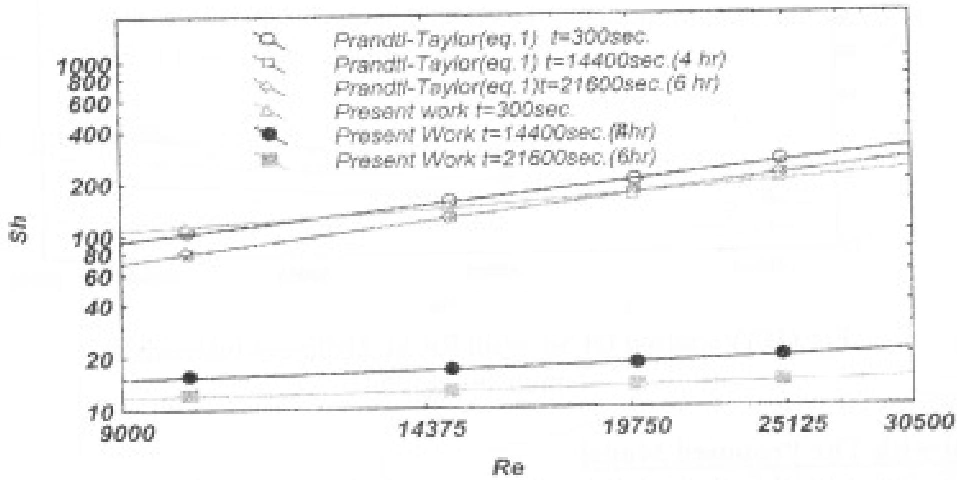

Fig.(12)Comparison of Analogy Models and Experimental Results In Present Work at t=25 ° C

According to above conclusions ,the analogy models can be employed to estimate the mass transfer controlled FeO scale removal rate (for the scale type used in this work) at particular Re and Sc determining the friction factor experimentally .

Table(2) lists the values of (Sh) estimated from various analogy models using the friction factor besides experimental values obtained by concentration difference of Fe^{+2} ion for all ranges of Re. The chosen analogie are Prandtl and Taylor analogy (Eq.1a) using (Eq.1b) for estimation of (u_x/u_c).

A modification has been done on the correlation to estimated(α) of (Prandtl-Taylor analogy Eq.1a and Eq.1b) to make this analogy can be employed for the descaling process at time (2,4,6) hr respectively. using statistical analysis the following correlations for (α)values estimation were obtained.

$\alpha = 0.00244Re^{0.516}$ for time 2hr ------ (8a)

$\alpha = 0.0013 Re^{0.8}$ for time 4hr ------ (8b)

Table (2) Comparison of experimental Sh No. with analogies t= 300 s and T= 25°C, Sc=378

	Sh No.					
Re .No.	Prandtl Tayler **(Eq.1a)**	Von Karman	Chilton Colburn	Darshnlal	Prandtl Tayler **(Eq.2)**	Present work
10000	104.2	162.18	467.7	346.7	161.18	112.2
15000	152	239.88	660.69	512.8	234.4	144.5
20000	201	309.02	853	660.6	301.9	165.9
25000	255	389.04	1047.12	831.7	380.1	199.5

$\alpha = 0.00294 Re^{0.803}$ for time 6hr ------ (8c)

CONCLUSIONS

1- Scale removal by means of inhibited Hydrochloric acid is dependent upon the temperature of reaction, solution circulation rate (as Re) , time of reaction and, acid concentration, it was concluded that the amount of scale removal increases with increasing any factor of them, the condition to obtain high high percentage of scale removal (80-100%) should be ; for Reynolds number values over 17500, reaction temperature over 50°C , acid concentration not below 6.5wt%,and time over four hours.

2- Reaction of Hydrochloric acid with Iron oxide scale is followed first order kinetics model, with activation energy of 15kJ/mole which indicating that the process of Iron-oxide scale desolution is mass transfer controlling process.

3- Correlation for the variation of (Sh) (or mass transfer rate) with Re for the whole range of Re and temperature values

$Sh = 0.0537\ Re^{0.6028}\ Sc^{1/3}$

4-The experimental results for Iron- oxide desolution rates show good agreement with Prandtl – Taylor analogy, (Eq.1) , (using $\alpha = 2\ Re^{-1/8}$) at the early periods of the process, but at the later periods the rate divat from Prandtl –Taylor analogy.

Modification of analogies was obtained, correlations for α values estimation were obtained at different time to make Prandtl –Taylor analogy can be employed for the process.

$\alpha = 0.00244\ Re^{0.516}$ at time = 2hr

$\alpha = 0.0013\ Re^{0.8}$ at time = 4hr

$\alpha = 0.0029\ Re^{0.803}$ at time = 6hr

REFERENCES

Bennett, C.O. , and J.E. Myers, (1982), Momentum heat and mass transfer, 3rd ed. , Mc Graw – Hill Unit States,.

Berger, F.B. , (1977), and K.F. Hau, Int J. heat mass trans, vol. 20, P.1185,.

Bradley, G.W. and J.A. Smith, (1973), Mtls Prot. And performance, 12,48.

Brodkey, R.S. and HC.Hershey, (1988), transport phenomena; Aunified approach, MC Graw-Hill PP. 516-20

Charles M.Loucks, (1962), chemistry tackle plant maintenance, chemical engineering vol.69 Mar 5,.

Colburn , A.P. , (1964), Trans. AICHE, vol. 29,p. 174, 1933, Republished in J.Heat Mass Transfer vol. 7, p. 139,.

Coulson, J.M. , and J.F. Richardson, (1977), chemical engineering, 3rd edition.

Darshanlal, T., T. Wasan, and C.R. Wike, (1964), Int. J. heat mass trans., vol. 7, P.87,.

Hasan AL- AUAS, B.O., (2003), PhD. Thesis , Dept. Chem. Eng., Saddam University, Baghdad February.

Kandikar, S.G., (2001), S.Joshi,S.Tian, Heat Transfer For Conference, 35th National, AMSE California,.

Knudsen, J.G. and D.L.Katz, (1958), Fluid Dynamics and heat transfer, Mc Graw-Hill, New York.

Mahato, B.K. , B.K. , (1980), C.Y. Cha, and W. Schemlit, Corro, Sci., vol. 20, P421,.

Mansfield, G.H. and R.J. (1990), Terrell I.C.I.Engineering Division Winington, General water treatment to prevent fouling in cooling water (internet document).

Moore, R.E., A.E. Bischof, J.D. Robins, and D.R. Brenneman, (1972), Mtls Prot. and Perform. 11,3,41.

Precautionary procedures in chemical cleaning report of NACE Technical Unit Committee T-8A on Chemical Cleaning. Corrosion,15,17t (1959), January.

Chloride Stress Corrosion Cracking of Austenitic Stainless Steels, Report of NACE Unit Committee T-8A On Chemical Cleaning Corrosion, 15,69t (1959) February.

Petukhov, B.S. , (1970), Heat transfer and friction in Turbulent pipe flow with variable physical properties, Advances in heat trans.,vol.6, 503,.

Philip J.w. Roberts and Danald R. Webster, (2002), Turbulent Diffusion, School of Civil and Environmental Engineering, Georgia, Institute of Technology , Altantas.

-Powell,S.T., (1954), Water conditioning for industry, 1st ed., Mc Graw - Hill.

-Poulson, B., (1983), corrosion science, vol. 23, No.1 P.391,.

-Reynolds , O., (1874), Process Manchester Lit. phil soc. 14:7, (cited in 55)

-Schmidt, N.O., and W.S., (1958), wise, Ind. Eng. Chem, 50,5,811.

-Tewari, P.H. and Campell, A.B. J.phys Chem., (1976), vol. 80, P.1844.

APPENDIX

Mass and momentum transfer analogy equations

Prandtl and taylor analogy

$$\frac{k}{u_\infty} = \frac{f/2}{1+\left(\frac{u_x|_\delta}{u_\infty}-\right)(Sc-1)} \quad (1a)$$

$$\alpha = 2Re^{-1/8} \quad (1b)$$

$$Sh = \frac{(f/2\ )Re.Sc}{1+5\sqrt{\frac{f}{2}}(Sc\ -1)} \quad (2)$$

-Von- Karman analogy(Brodkey,R.S.(1988)).

$$Sh = \frac{(f/2)Re.Sc}{1+5\sqrt{\frac{f}{2}}\{\ Sc-1+\ln(1+\frac{5}{6}Sc)\ \}} \quad (3)$$

Chilton – Colburn analogy(Berger,E.B.(1977)).

$$Sh = \frac{f}{2} ReSc^{1/3} \quad (4)$$

Darshnlal et.al analogy(Darshanlal,T.(1964)).

$$Sh = 0.058\sqrt{\frac{f}{2}}Re\ \ Sc^{0.34} \quad (5)$$

The friction factor and wall shear stress for rough surface were obtained by measuring the pressure drop across the test section for each value of Re, temperature and time and applying the equations ;

$$f = \frac{d.\Delta\ P}{2\rho u^2 L} \quad (6)$$

since,

$$\Delta p = \Delta h\rho g \quad (7)$$

hence,

$$f = \frac{\Delta hdg}{2\ u\ ^2 L} \quad (8)$$

NOMENCLATURE

A:Surface area of specimen,m^2

C:Concentration,mole/m^3

d:Pipe diameter,m

D:Diffusivity,m/s
f:Friction factor
k:Mass Transfer coefficint,m/s
N_A:Flux of mass transfer,mole/m^2.s
P:Pressure drop,N/m^2
Re:Reynold 's Number
Sc:Schimdt Number
Sh:Sherwood Number
S.R%:Scale removal percentage,wt%
t:Time,h or s
T:Temperature,C°
u:Velocity

APPLICATION OF VIBRATION MEASUREMENT TO DETECT DAMAGE IN CASTING

Dr. Adnan N. Jameel Al-Tamimi
Baghdad University
Mech. Eng. Dept

Ehab N. Abbas
D.G. of Vocational Education
Senior Researcher in Scientific Affairs Dept

ABSTRACT
Modal testing has become commonplace in many industries today as a research and development tool. In this capacity, it is used primarily during product prototype development and for vibration problem in general. Many types of structural or parts faults will cause changes in the measured dynamic response of a structure. These changes will, in turn, cause change in the structure's modal parameter.
The purpose of the present work is to propose an improved damage detection and location based on the measurement of modal parameter (natural frequency and mode shape) before and after faults, which they have varying extents, for three different sizes of Aluminum casing plates. This local damage can be translated into or characterization as a reduction of the local stiffness which, simulated in the presented numerical models using software package. After measured natural frequency, if a change is detected a statistical method is used to make the best match between the measured changes in frequencies and the family of the theoretical predictions. This predicts the most likely defect location. Analytical results are also used to check numerical results, which showed a good agreement with it. Standard Aluminum plates were also investigated in this work. It results were compared with casting results for two boundary conditions. Also, the defect location charts that plotted with the support of deriving stiffness sensitivity equation showed a good agreement between the predicted defect site and the actual defect location for most of the study cases.

الخلاصة
إن الاختبارات الشكلية أصبحت هذه الأيام شيئا مألوفا في عدة صناعات كبحوث أو أداة تطوّر. وضمن هذه ألا مكانيه ، فقد استخدمت أولا أثناء إنشاء النموذج الأولى للأجزاء وكذلك لمشاكل الاهتزاز بشكل عام. أن أنواع عديدة من العيوب البنيوية سوف تحدث تغيرات في الاستجابة الديناميكية المقاسه لتركيب هيكلي ما. و هذه التغيرات سوف تحدث، تباعا، تغيّر في البارامترات الشكلية للتركيب الهيكلي. إن الغرض من العمل الحالي هو اقتراح تقنية مع إدخال بعض التحسينات لكشف وتعيين موقع العيب مستنده على قياس البارامتر الشكلي (التردد الطبيعي وشكل الموجه) قبل وبعد حدوث العيوب، والتي لها أحجام أو مديات مختلفة، لثلاثة أحجام مختلفة من ألواح الألمنيوم المسبوكة. إن هذه العيوب الموضعية يمكن نقلها أو تمثيلها على شكل تقليل في الجساءة الموقعية، والتي مثلت في النماذج العددية المقدّمة باستخدام برنامج جاهز. بعد قياس الترددات الطبيعية، إذا تم كشف تغيّر في الترددات الطبيعية فسوف يتم استخدامها ومن خلال طريقه إحصائية لحساب أفضل توافق بين التغيرات المقاسة والمجموعة المتنبأ بها نظريا. هذه الطريقة تنبأ عن الموقع الأكثر احتمالا

للعيب. كذلك تم استخدام النتائج النظرية لفحص دقة النتائج العددية، والتي أظهرت تطابق جيد معها. ذلك تم استخدام ألواح قياسية من الألمنيوم حيث تم التحقق منها في هذا العمل. هذه النتائج تم مقارنتها مع نتائج الألواح المسبوكة ولنوعين من الحدود الشرطية. كذلك فأن مخططات موقع العيب، والتي رسمت وبمساعدة المعادلة المشتقة لحساسية الجساءة، أظهرت توافق جيد بين مكان العيب المتنبأ به والموقع الحقيقي للعيب لاكثر الحالات المدروسة.

KEY WORDS
Non- destructive test, Modal Analysis, Damage, Detection, Location, Casting.

INTRODUCTION

The physical mass, stiffness, and damping properties of a structure determine how this structure can vibrate. Vibration is caused by an exchange of energy between the mass (inertia) property and stiffness (restoring) property of the structure. The damping property dissipates vibrational energy.

A structure's modal properties are directly related to its physical properties. That is, changes in structure's mass, stiffness, or damping properties will cause change in its modal properties (modal frequencies, modal damping, and mode shapes). Also, changes in the structure's boundary conditions (mountings) can be viewed as changes in the mass, stiffness, or damping plus its surroundings, and will change its modal parameter.

The modal parameter solutions to the differential equation of motion which are themselves functions of the mass, stiffness, and damping of the structure [Mannan 1991].

Changes in structure's modal parameters are to be used as a reliable means of detecting, and possibly even locating and quantifying structural faults. "Faults" means the following occurrences:

- Flaws voids, cracks, thin spots, etc. caused during manufacturing processes such as casting or forming operations. Faults of casting are the type of fault that we need it in this paper.
- Failure of the structural material, e.g. cracking, breaking, or delamination.
- Loosening of assembled parts, e.g. loose bolts, rivets, or glued joints.
- Improper assembly parts during manufacturing.

Now we can asked that what is the smallest physical change in a structure that can be detected, located, and quantified from changes in its modal parameters? The best answer to this question is "the smaller the better". This answer presumes that it is always better to detect the onset of structural faults as early as possibly when it is still small.

Non destructive damage detection can be broken up into four categories. *Level I* test for the presence of damage. *Level II* test for the presence and location of the damage on the structure. *Level III* test for the presence, location, and severity of the damage. Finally *level IV* tests for the presence, location, and level of the imparted damage as well as predicting the change in physical properties of the structure due to the damage. In this work, we used level II techniques to detect and locate faults in casting.

The main objective of the current work is to build a vibration technique capable of detecting and locating faults in Aluminum casting plates as a mean of quality control, where there are large numbers of the same component produced.

A computer model is developed to study the effect of damage in the casting plates on the natural frequencies and mode shapes using a package deal with finite element analysis. This technique is highly accurate, and can be used for analysis in any structure with any type of structural vibration. Also calculate the change in the model parameters of the casting plates due to the introduction of suggested defect models. The defect model must be able to represent the defect that have a sensible effect on the structure stiffness and also must be simple for calculating.

Test rigs will be designed and built to study the vibration behavior of the model structures before and after damage to predict the measured change in natural frequencies. Finally, develop a statistical method for the best match between the measured changes in frequencies and the family of numerical predictions. This model in true will then locate the most likely damage sites. A comparison was made between the experimental and the theoretical results and between casting plates and Aluminum plates.

Advantages of Modal Parameter Measurements as Continuous Monitoring

Measurement and the estimation of modal parameter changes have some inherent advantages for continuous monitoring applications that are not available with other methods.

1- Modal parameters can be measured on any structure that vibrates.
2- Modes of vibration are sensitive indicators of physical changes.
3- Changes in modes can localize a fault.
4- Faults can be detected in a measured region of the structure (measurements at single point in the structure is enough for detection).
5- Only a small number of measurements are required.
6- A wide variety of excitation and signal processing methods can be used.
7- Modal testing is non-destructive test.

ANALYTICAL ANALYSIS

A plate is a two-dimensional sheet of elastic material, which lies in a plane. The general assumptions and equations used in the analysis of plates in this section are:

For plate laying in the x-y plane the normal strains (ε_x and ε_y) and shear strain (ε_{xy}) in the plane of the plate are [Srinivasan 1982]:

$$\varepsilon_x = z\frac{\partial^2 w}{\partial x^2}\ ,\ \varepsilon_y = z\frac{\partial^2 w}{\partial y^2};\ \varepsilon_{xy} = 2z\frac{\partial^2 w}{\partial x \partial y} \qquad (1)$$

The out of plane strains are zero:

$$\varepsilon_{xz} = \varepsilon_{yz} = \varepsilon_{zz} = 0$$

These strains are associated with the following stresses for a homogenous isotropic material:

$$\sigma_{xx} = \frac{E}{1-\upsilon^2}(\varepsilon_x + \upsilon\varepsilon_y)\,;\sigma_{yy} = \frac{E}{1-\upsilon^2}(\varepsilon_y + \upsilon\varepsilon_x) \qquad (2)$$

$$\sigma_{xy} = G\varepsilon_{xy};\ \sigma_{xz} = \sigma_{yz} = \sigma_{zz} = 0$$

If w is the transverse deflection of the plate, the elementary kinetic energy dT and the elementary potential energy dV of the plate is given by:

$$dT = \frac{1}{2}\rho\left(\frac{\partial w}{\partial t}\right)^2 dx\,dy\,dz \qquad (3)$$

$$dV = \frac{1}{2}(\sigma_x\, dydz)[\varepsilon_x\, dx] + \frac{1}{2}(\sigma_y\, dxdz)[\varepsilon_y\, dy] + \frac{1}{2}(\sigma_{xy}\, dydz)[\varepsilon_{xy}\, dx] \qquad (4)$$

The total kinetic energy T and potential energy V of the plate is given by integrating:

$$T = \frac{1}{2}\int_0^a \int_0^b \rho h \left(\frac{\partial w}{\partial t}\right)^2 dx\,dy \tag{5}$$

$$V = \frac{D}{2}\int_0^a \int_0^b \left[\left(\frac{\partial^2 w}{\partial x^2}\right)^2 + \left(\frac{\partial^2 w}{\partial y^2}\right)^2 + 2\upsilon \frac{\partial^2 w}{\partial x^2} \times \frac{\partial^2 w}{\partial y^2} + 2(1-\upsilon)\left(\frac{\partial^2 w}{\partial x \partial y}\right)^2\right] dxdy \tag{6}$$

Where: $D = \dfrac{Eh^3}{12(1-\upsilon^2)}$ is called the plate bending stiffness element

Forming the Lagrangian $L=T-V$ and applying the Hamilton's principle: $\delta \int_{t_1}^{t_2} L\,dt = 0$, we obtain:

$$\frac{1}{2}\delta \int_{t_1}^{t_2} \int_0^a \int_0^b \left\{\rho h w_t^2 - D\left[w_{xx}^2 + w_{yy}^2 + 2\upsilon w_{,xx} w_{,yy} + 2(1-\upsilon) w_{xy}^2\right]\right\} dxdy = 0 \tag{7}$$

Performing the operations as per the rules of the calculus of variation term by term, we use the variational operation (δ) to extract the analytical term for vibrating plate:

$$D\nabla^4 w + \rho h \ddot{w} = 0 \tag{8}$$

Suppose the plate is supported on all the four edges, and the plate is vibrating with a frequency p given by:

$$w = w_0 \cos(pt) \tag{9}$$

The equation of motion of the plate (8) becomes:

$$\nabla^4 w = \gamma^2 w : \qquad \text{Where } \gamma^2 = \frac{\rho h}{D} p^2$$

We shall assume the deflection w_0 as [2]:

$$w_0(x,y) = \sin\left(\frac{m\pi x}{a}\right)\sin\left(\frac{n\pi y}{b}\right) \quad ; m, n = 1,2,3,.... \tag{10}$$

So that frequency equation for simply supported plate becomes:

$$P_{m,n} = \pi^2\left(\frac{m^2}{a^2} + \frac{n^2}{b^2}\right)\sqrt{\frac{D}{\rho h}} \qquad \text{i, j=m, n=1,2,3,...} \tag{11}$$

Equation (11) represent the analytical term for finding natural frequency for the above boundary

condition. In the same manner we can find the frequency equation of a plate subjected to other boundary conditions.
While the subject of vibration analysis of the completely free rectangular plate has a history, which goes back nearly two centuries, it remains a fact that most theoretical solutions to this case are considered to be at best approximate in nature. This is because of the difficulties, which have been encountered in trying to obtain solutions that satisfy the free edge conditions as well as the governing differential equation [Gorman 1978]. Since no analytical solution exist for this boundary [Victor 2001], so that the eigenvalues for plate vibrate under this boundary condition is governed by the approximate natural frequency expression (in Hertz) of the form presented below [Blevins 1979]:

$$Pij = \frac{\pi}{2}\left[\frac{G_1^{\ 4}}{a^4} + \frac{G_2^{\ 4}}{b^4} + \frac{2J_1J_2 + 2\upsilon(H_1H_2 - J_1J_2)}{a^2b^2}\right]^{1/2}\left[\frac{Eh^3}{12\gamma(1-\upsilon^2)}\right]^{1/2} \tag{12}$$

Where, $i = 1,2,3,....$ and $j = 1,2,3...$
The dimensionless parameter G, H and J are functions of the indices i and j and the boundary conditions on the plate.The approximate natural frequencies predicted by equation (12) are directly analogous to the analytical solutions. The approximate natural frequencies can be expected to be within 5% of the exact solutions [Blevins 1979].

NUMERICAL ANALYSIS

The finite element analysis applied to vibration problems is now becoming well known and the study of vibrational behavior of a structure is of great importance because it can be used to determine the eigenvalue and the eigenvector solutions.
In contrast to the early days, it can use computer software to generate complex geometry, at either component or reassemble level. It can (with some restrictions) automatically generate elements and nodes, by merely indicating the desired nodal density. Software is available that work in conjunction with finite element to generate structure of optimum topology, shape, or size.
In order to select the suitable mesh for the plates, in the numerical calculation, the plates must be investigated for different number of (D.O.F.). **Figs. (1), (2), and (3)** show the variation of natural frequency with the number of (D.O.F.) for the three different sizes of free-free plates used in this work respectively. For the work purpose, natural frequencies have been calculated numerically using ANSYS FE software package and the mode shapes have been observed for all the Aluminum casting plates and Aluminum plates tested in this work. The plates were drawn to the scale 1:1 on this software and a study was performed in two boundary conditions, free-free and simply supported boundaries. Natural frequencies for some cases have been listed in **tables (1), and (2)** which are compared with the theoretical natural frequencies. Also the first three dynamic modes are shown in **Figs. (4), and (5)** for some cases.

EXPERIMENTAL WORK

The objective of this section is to detail the testing procedure, which gives as possible as accurate values of the natural frequencies of the structure. The procedure requires that the structure under test is excited by harmonic force and the response at various points of the structure must be measured. An arbitrary choice of the point of excitation could be lead to difficulties in producing the resonance at certain natural frequencies of the structure. For example, exciting the structure at a nodal point (point of zero amplitude of vibration) of a certain natural frequency would result in missing out the resonance at the natural frequency. It useful to change the position of the excitation of a structure to exist the different modes of vibration or by drawing the theoretical mode shapes.

A natural frequency was distinguished by observing the sharp increase in amplitude of the pickup output and by the intensity of the tone emitted, which was amplified and displayed on the oscilloscope. This procedure was represented to measure the pre and post damage natural frequencies. The test procedure must establish homogeneous conditions throughout all phases of the experimental work. Thus, the method used for supporting the structure during each investigation should be simple to set-up and must be reproducible.

The test plates was suspended horizontally in the test rig using a very soft elastic cords attached to the mid-points of its four sides in order to approximate the free-free boundary condition, the procedure was used by several researchers [Lauwagie 2002]. Also in order to approximate the simply-supported conditions the tested plates was putted on a four sides sharp edge frame made for the purpose. Each plate was set-up in precisely the same fashion in attempt to minimize the effects of human factors on the frequency changes. Damage was represented in all tests carried out by putting the saw cut and then change the dimension of the saw cut by extends it. Also, a drill was used to make all sizes of holes damage in the plates. The natural frequencies have been measured for undamaged free-free and simply supported rectangular sand casting Aluminum plates, also we use a standard Aluminum plates to compare there results with casting Aluminum plates results. Then natural frequencies for the same plates have been damaged by making six damage cases which used in the all tests. The cast Aluminum used is C443.0: S5C ASTM, which it mechanical and physical properties are (Tensile strength is 230 Mn/m^2, Yield strength is 110 Mn/m^2, Modulus of elasticity is 71.0 Gn/m^2, Percentage elongation is 9%, Density is 2690 Kg/m^3, and Poisson's ratio is 0.33).

DEFECT LOCATION TECHNIQUE

The stress distribution through a vibrating structure is non-uniform and is different for each natural frequency (mode shape). This means that any localized defect would affect each mode differently, depending on the particular location of the defect. The defect may be modeled as a local decrease in stiffness of the structure. So, if it is situated at a point of zero stress such as the nodal lines in a given mode, it will have no effect on the natural frequency of that mode. On the other hand if it is at a point of maximum stress, it will have the greatest effect. Therefore the location of the defect site requires the computation of the relative effect on several modes of vibration at different sites within the structure .The experimentally measured changes in natural frequencies may be then be compared with the theoretically calculated changes for defect at different sites and the position of the defect deduced. If natural frequency measurements are to be curried out, the effect of defect may be determined by modeling the defect as a local decrease in the stiffness, rigidity, or thickness of the structure and currying out the dynamic analysis of the system.

Following Cawley et.al. [Cawley 1979], it is assumed that, in theory, the change in the natural frequency of mode (i) of a structure due to damage in the structure is a function of the position vector of the damage (r), and the reduction in stiffness caused by the damage (δK), thus:

$$\delta\omega_i = f(\delta K, r) \tag{13}$$

A formula expansion about the undamaged state ($\delta k = 0$), and ignoring second and higher-order terms, yields:

$$\delta\omega_i = f(0,r) + \delta K \frac{\partial f}{\partial(\delta K)}(r,0) \tag{14}$$

Assuming that there is no frequency change with out damage, it follows that $f(r,0)=0$ for all (r) and so, writing the partial derivative as $g_i(r)$, equation (14) then simplified to:

$$\delta\omega_i = \delta K\, g_i(r) \qquad (15)$$

If it is assumed further that (δK) is independent of frequency, it follows that the ratio of frequency changes is dependent only upon the damage location as specified by (r):

$$\frac{\delta\omega_i}{\delta\omega_j} = \frac{g_i(r)}{g_j(r)} = h(r) \qquad (16)$$

Measurements of the frequency changes in one pair of modes will yield in a locus of possible damage sites, that the point where the ration of the experimentally determined changes equals the theoretical ratio. With symmetrical structures, two or more sites will be predicted, the number depending on the degree of geometric symmetry. So that an "error "which is denoted by (e_{rij}), in assuming the defect to be at position (r), given frequency changes (δ_{wi}) and (δ_{wj}) in modes (i) an (j) respectively, as:

$$e_{rij} = \frac{S_{ri}/S_{rj}}{\delta_{\omega i}/\delta_{\omega j}} - 1, \qquad \frac{S_{ri}}{S_{rj}} > \frac{\delta_{\omega i}}{\delta_{\omega j}} \qquad (17)$$

The value of the error function (e_{rij}) is computed for each mode pair according to equation (17). These values are then assumed to give a measure (e_{rt}) of the total error in assuming the damage to be at position (r) given the experimentally measured frequency changes. Thus:

$$e_{rt} = \sum_{all\ pairs\ (i,j)} e_{rij} \qquad (18)$$

The most probable defect site is taken to be the one at which the value (e_{rt}) is minimum .Let this minimum value is (e_{min}). This was then used to normalize each total error, which was expressed as the "normalized error" for failure at theoretical position (r), defined as:

$$ne_r = 100 \times e_{\min}/e_{rt} \qquad (19)$$

A very attractive alternative to repeat the full dynamic analysis in order to compute the changes in the natural frequencies due to localized damage is to use a sensitivity (perturbation) analysis. The basic principles of the method are described by, for example, Courant and Hilbert [Courant 1953]. By this method, the sensitivities of the natural frequencies of a system to small changes in the stiffness matrix, mass matrix, and damping matrix are calculated from mode shapes of the unmodified structure (structure with no faults) produced by the initial full dynamic analysis.

The orthogonality property of the modes "almost" simultaneously diagonalizes the mass, stiffness, and damping matrices, and therefore "almost" uncouples the equations of motion. The term "almost' is used because strict diagonalization occurs if there is no damping ([C] = [0]). Probably the most sought after cause of a structural fault is a reduction in local stiffness, which might be caused by the formation of a crack, delamination, voids, or a loose fastener.

$$\{U_k\}^t[dK]\{U_k\} = \omega_{1k}^2 - \omega_{0k}^2 \qquad (20)$$

This formula only required the mode shapes for the unmodified structure plus changes in the stiffness matrix [dK]. A fault that causes local stiffness change can then be detected and located by simply tracking the stiffness change of the structure, and using equation (20).

RESULTS AND DISCUSSION

The validity of any theoretical approach may be examined by one of two methods, the first method is by making a comparison between the suggested approaches and well known analytical methods, while in the second method, the comparison is made with the experimental results.

In this section, the performance of the proposed NDT has been checked. Several tests were carried out for different casting plate structures with readily qualifiable forms of damage in order to check the operation of the technique and the supporting analysis.

Fig. (6), (7) shows a comparison between the exact and approximate natural frequencies. It may be observed from the figure that the results compare very favorably with the exact values. **Table (3)** give the predicted and measured natural frequencies (Hz) for the undamaged state of the 600*500*6 mm free free casting plate. The maximum error in predicting natural frequencies was (1.969) in the second mode. These errors are from variations in dimensions due to casting process and material properties. The data in table shows that the FEA model of the casting plate without fault tended to give slightly higher natural frequency than the test data as the modes increased in frequency. Instead of soaking time in frequency measurement experiment by placing the shaker and the accelerometer at different positions in order to avoid the possibility of having the accelerometer and / or the shaker at a nodal line. The best position can be predicted from the mode shapes of the tested plate. The node lines are drawn by connecting node points, which are computed as points where the mode shapes is zero in a normal direction to the surface of the plate.

The results obtained from ANSYS FE software package showed that the maximum displacement (especially in the first mode) is in the corners of the plate (for free free boundaries). Therefore, the shaker and the accelerometer were mounted in one of the Four Corners of the tested plate. Also the results showed that the maximum displacement is around the center of the plates (for simply supported boundaries). Therefore, the shaker and the accelerometer were mounted in the center of the tested plate. If we want to plot the mode shapes after the fault made in the plate. We expected that there are large differences with the shapes for unmodified plate, but also we expected that they don't pinpoint the location of the fault. One explanation for this is that all of these modes are "global" in nature (which is true for most simple structures and hence will change globally even due to a "local" change such as the hole damage.

Different cases of damage have been investigated for this casting plate. **Table (3)** also gives the experimentally measured frequency reduction (Hz) for all cases of damage. It is apparent that the reduction in the natural frequencies increased as the damage size increased. From the analysis it is observed that at least three modes are needed to detect damage existing any were in the casting plate. Individual modes have relatively different sensitivities to potential damage location in casting plate. For example modes 1 and 3 are sensitive to the location near the center while modes 2 and 4 are not sensitive. The table values reveal that the frequency reduction clearly indicates the presence of the 10 mm and 5 mm holes, by the frequency shift of the modes. Due to the relatively small magnitude of damage they don't detect the 3 mm hole. Also **Table (4)** has been presented for another case.

The defect location chart will consist of a plot of the plate, with elements labeled using the normalized error. The predicted damage site being represented by the value 100 (see eq. 19). Series of tests for defect location analysis were carried out on the casting plates using different damage models. Sensitivity analysis was used to simulate damage by the reduced thickness of the whole element. From these results it will be possible to establish the generality and validity of the method used in order to deal with such structures. **Fig. (8)** shows the location chart produced from a test on a rectangular Aluminum casting plate of dimension 600*500*6 mm. The analysis used a 16*16 finite element mesh with a total of 1024 grid points. The plate was damage by drilled a 10 mm hole at site A. It will be observed that, due to symmetry, the location chart shows four possible damage sites. It can be seen from the figure that the damage was correctly located.

CONCLUSIONS

This paper presented a method of non-destructively detect faults in casting plates for which only a few natural frequencies are available. Also, we presented an improved damage location algorithm which was used a set of modal parameters for an unmodified(undamaged) casting plates with experimental data with the support of sensitivity equations, which consider the orthogonality conditions of the undamaged plate mode shape.

The final scheme has the advantage that only one dynamic FEA need to perform on the casting plate structure. The dynamic analysis may be stored on disc and used as input to the damage location program, along with the experimentally determined natural frequencies.

The major conclusions that can be obtained from the present work can be summarized as follows:

1- For this work, in frequency measurement the best position of attachment between the shaker/ accelerometer and the tested plate was predicted from the theoretical mode shape of the tested plate. It was found that this position was in one of its four corners for free free boundaries and around the center for simply supported boundaries, where maximum displacement was found numerically at these positions.
2- Any set of measurements that are repeatedly made over time will exhibit variations. These variations are caused either by the "natural" statistical variation in the measurement process, due to numerous sources of measurement error, or they are caused by a physical change in the structure, i.e. an "assignable cause".
3- It is possible to use the method of health monitor without need to have measured the frequency of the virgin structure by using a damaged state as the baseline for future measurement. This is an important property in the job field, where there are a large number of products. Also a key advantage of this technique is that it can be used on the type of data, namely natural frequency, which is commonly measured in a structure testing laboratory using the experiments system.
4- The experimental results indicated that the smallest defect size that can be located, using the proposed defect location method, depends upon the accurate measurements of natural frequency. The error in the measurement of natural frequency is come from the error in simulating the actual boundary conditions, the change in material properties, and the error in dimensions of casting plates due to casting process.
5- Individual modes have relatively different sensitivities to potential damage location. Thus, we observed that they were appreciable changes in some natural frequencies and comparatively small in other. The effect depends on the location of damage and increases as the damage size increase.
6- Good agreement was obtained between the experimental and theoretical results both for undamaged and damaged plates.

REFERENCES

Blevins Robert D. (1979), Formula for Natural Frequency and Mode Shape, Van Nostrand Reinhold Company, USA,.

Cawely P. and Adams R.D. (1979), The Location of Defects in Structures From Measurements of Natural Frequencies, J. of Strain Analysis. Vol.14, No.2, PP.49-57,.

Courant R. and Hilbert D. (1953), Method of Mathematical Physics, IntelliSense Publishers, Vol. I, first edition, London,.

Gorman D.J. (1978), Free Vibration Analysis of The Completely Free Rectangular Plate by the

Method of Superposition, J. of Sound and Vibration, Vol. 57, No.3, PP. 437-447,.

Lauwagie T., Sol H., and Guill P. (2002), Identification of Distributed Material Properties Using Measured Modal Data", Proceeding of ISMA Conference,.

Mannan M.A. and Richardson M.H. (1991), Determination of Modal Sensitivity functions for Location of Structural Faults", 9th IMAC Proceeding, Florence, Italy, April.

Srinivasan R. (1982), Mechanical Vibration Analysis, McGraw-Hill Book Company (UK) Limitec London,.

Victor Giugriutiu and Andrei Zagrai (2001), electro-Mechanical Impedance Method for Crack Detection in Metallic Plate", 6th Annual Int. symposium on NDE for Health Monitoring and Diagnostics, 4-8 March.

NOMENCLATURES

a	Length of plate (mm)
b	Width of plate (mm)
f	Functions
h	Thickness of plate (mm)
i , j	Modes i , j
L	Lagrangian multiplier
G_1, G_2 / H_1, H_2 / J_1, J_2	Dimensionless parameter for natural frequencies formulas
e_{rij}	Error function
e_{rt}	Total error function
ne	Normalized error
$P_{i,j}$	Natural frequency (Rad/Sec)
n	Number of DOFs of the Structure
m	Number of Modes
r	Position vector of damage
Sr_i	Sesitivity of mode i to damage at **r**
$[dK]$	changes in the stiffness matrix
T	Total kinetic energy
V	Total potential energy
[U]	Mode shape matrix
D.O.F.	Degree of freedom
N.D.T.	Non destructive testing
w	Transverse deflection of The plate midsurface
σ	Stress Vector
ε	Strain Vector
ρ	Density (Kg/m^3)
ν	Poisson's Ratio
δK	Reduction in stiffness caused by damage
$\delta\,\omega_i$	Change in natural frequency (Rad/Sec)
ω_i	Natural frequency (Rad/Sec)
ω_{0k}	Natural frequency of the unmodified structure (Rad/Sec)
ω_{ik}	Natural frequency of the modified structure (Rad/Sec)

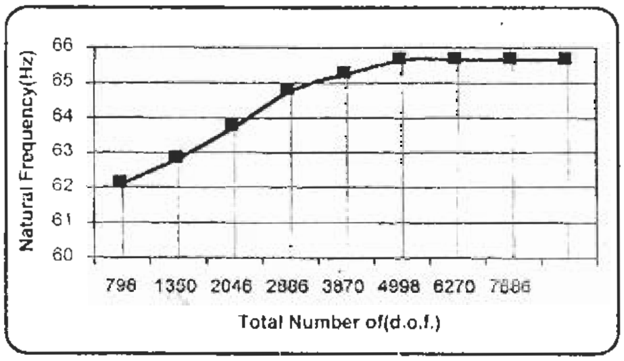

Fig. (1) Variation of natural frequency with total number of (d.o.f.) for 600*500*6 mm free-free casting plate.

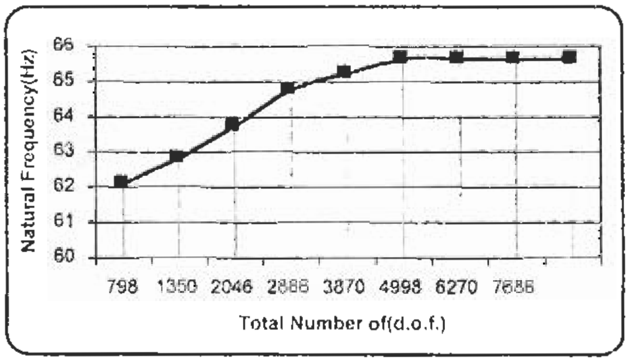

Fig. (2) Variation of natural frequency with total number of (d.o.f.) for 600*500*3 mm free-free casting plate.

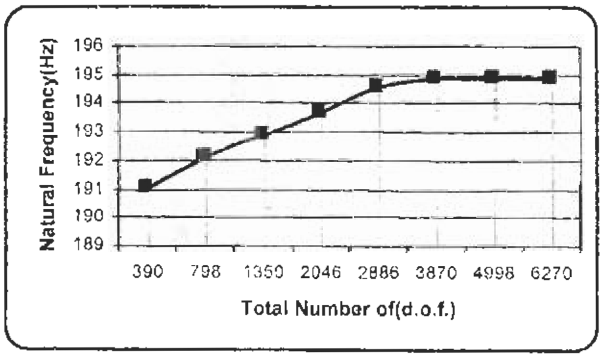

Fig. (3) Variation of natural frequency with total number of (d.o.f.) for 400*250*6 mm free-free casting plate.

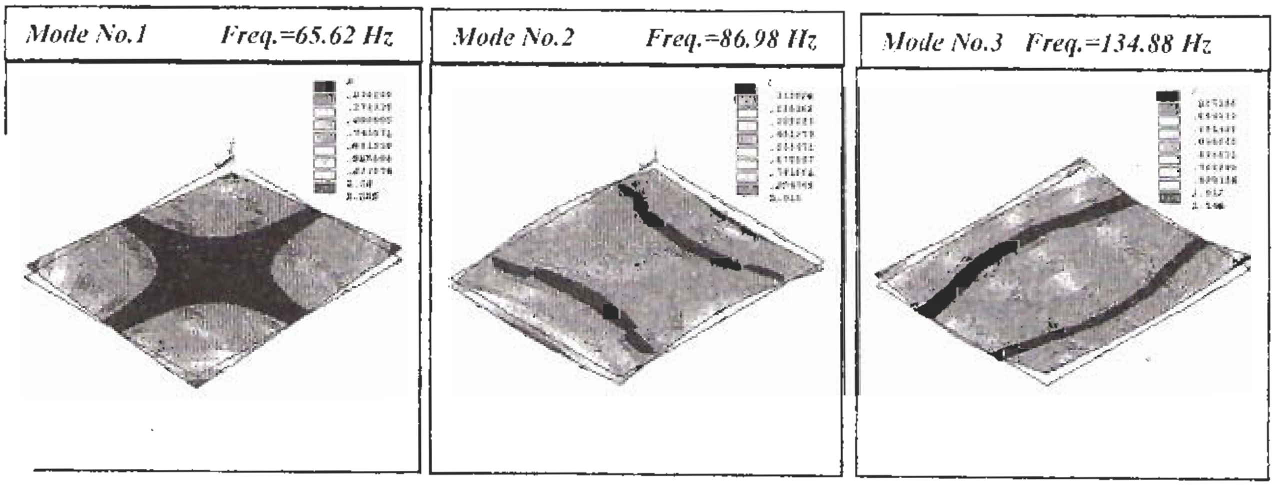

Fig. (4) Mode shape for the 0.6*0.5*0.006m free-fee casting plate.

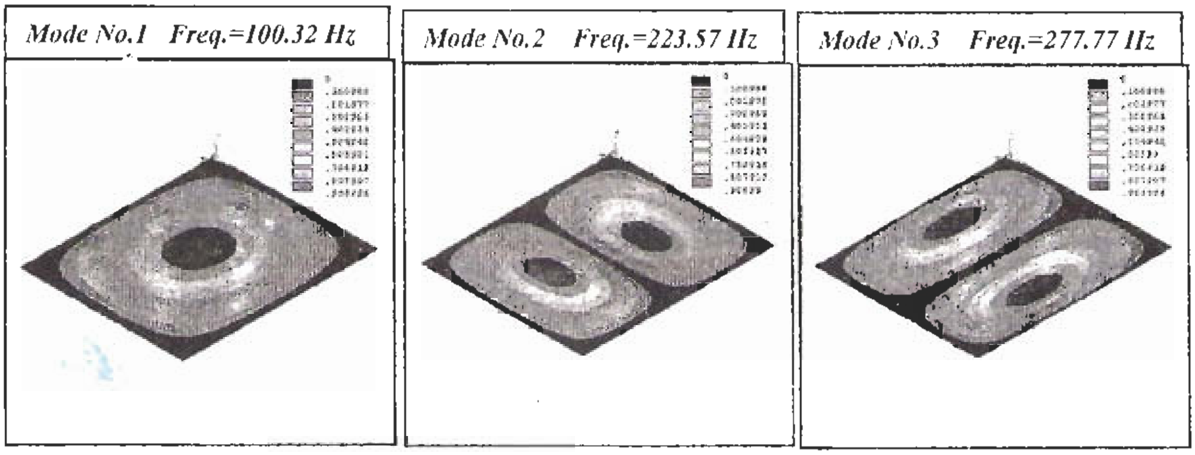

Fig. (5) Mode shapes for the0.6*0.5*0.006m simply-supported casting Plate.

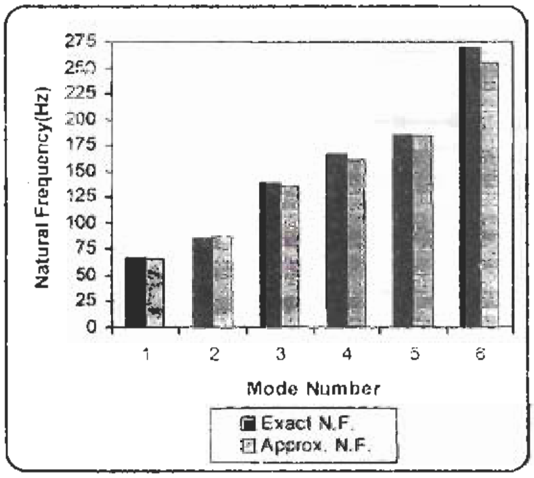

Fig (6) Comparison between the exact and approximate natural frequency for 600*500*6 mm free free casting plate.

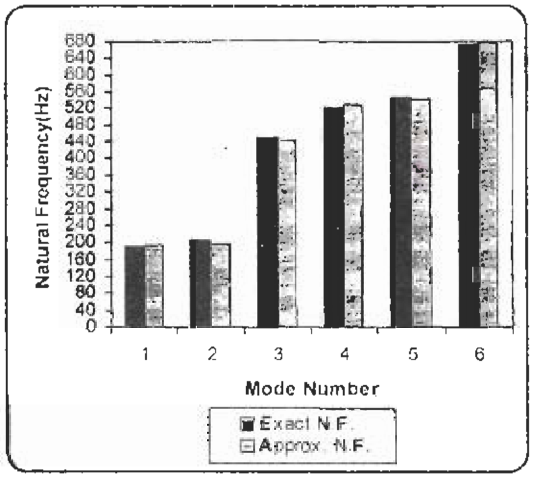

Fig. (7) Comparison between the exact and approximate natural frequency for 400*250*6 mm free free casting plate.

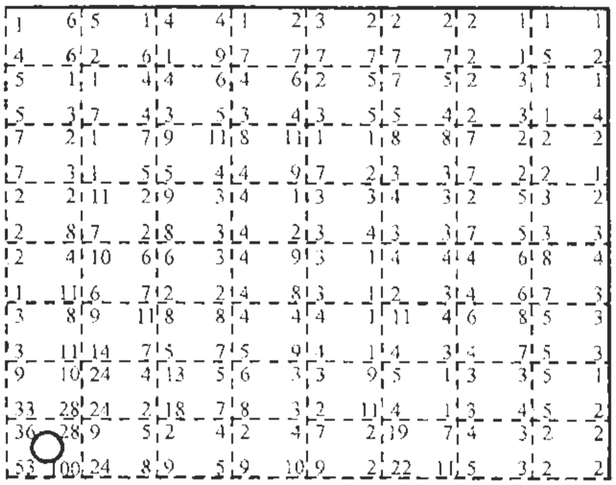

Fig. (8) Location chart for quarter of the 600*500*6 mm casting plate with 10mm hole damage at site A.

Table (1) Numerical and theoretical pre-damage frequency of the first six modes for the 600*500*6 mm fre-free casting plate.

Mode No.	Natural Frequency (Hz)		Percentage Error %
	ANSIS 5.4	Analytical	
1	65.62	67.28	2.4673
2	86.98	85.49	1.7429
3	134.88	138.85	2.8592
4	160.42	166.39	3.5879
5	183.23	184.58	7.2658
6	255.25	269.35	5.2348

Table (2) Numerical and theoretical pre-damage frequency of the first six modes for the 400*250*6 mm fre-free casting plate.

Mode No.	Natural Frequency (Hz)		Percentage Error %
	ANSIS 5.4	Analytical	
1	194.86	190.168	2.4674
2	198.80	203.80	2.4533
3	445.00	450.07	1.1265
4	529.20	522.42	1.2978
5	542.93	545.32	0.4382
6	676.23	671.23	0.7449

Table (3) Experimental and theoretical frequencies for 600*500*6mm free free casting plate with six damage case.

	Unmodified Frequency (Hz)					
Mode No.	**Mode 1**	**Mode 2**	**Mode 3**	**Mode 4**	**Mode 5**	**Mode 6**
Exp.	64.8	85.3	134.0	159.1	182.5	254.5
Theo.	65.62	86.98	134.88	160.42	183.23	255.25
Error %	1.265	1.969	0.656	0.829	0.400	0.0.294
Damage Case	**Frequency Reduction (Hz) Exp.**					
3 mm Hole	0.2	0.3	0.2	0.1	0.2	0.4
5 mm Hole	3.2	2.1	3.6	2.4	3.6	4.1
10 mm Hole	7.0	5.9	6.8	5.1	8.1	6.2
All Holes	11.4	8.6	11.2	8.1	11.7	10.6
20mm Saw Cut	2.6	4.2	4.5	8.9	5.8	3.9
40mm Saw Cut	6.2	8.2	10.8	11.9	10.9	8.3

Table (4) Experimental and theoretical frequencies for 400*250*6mm free free casting plate with six damage case.

	Unmodified Frequency (Hz)					
Mode No.	**Mode 1**	**Mode 2**	**Mode 3**	**Mode 4**	**Mode 5**	**Mode 6**
Exp.	192.3	196.0	442.8	526.8	540.3	673.7
Theo.	194.86	198.80	445.00	529.20	542.93	676.23
Error %	1.331	1.428	0.496	0.455	0.486	0.370
Damage Case	**Frequency Reduction (Hz) Exp.**					
3 mm Hole	0.3	0.2	0.3	0.5	0.3	0.6
5 mm Hole	4.0	3.1	4.9	3.5	2.8	2.2
10 mm Hole	6.5	5.8	7.2	6.3	7.9	5.6
All Holes	11.1	9.1	9.0	9.4	11.5	12.0
25mm Saw Cut	6.3	7.2	5.0	7.2	9.6	7.3
40mm Saw Cut	7.6	9.7	8.5	11.6	13.0	13.6

IMPLEMENTATION OF FPGA-BASED RISC FOR LNS ARITHMETIC BY SOFTWARE & HARDWARE

Asst. Lecturer N. H. Abbas
Dept. of Elect. College of Eng. – University of Baghdad
Baghdad- Iraq

ABSTRACT

Field Programmable Gate Arrays (FPGAs) have some difficulty with the implementation of floating-point operations. In particular, devoting the large number of slices needed by floating-point multipliers prohibits incorporating floating point into smaller, less expensive FPGAs. An alternative is the Logarithmic Number System (LNS), where multiplication and division are easy and fast. LNS also has the advantage of lower power consumption than fixed point. The problem with LNS has been the implementation of addition. There are many price/performance tradeoffs in the LNS design space between pure software and specialised-high-speed hardware. This paper focuses on a compromise between these extremes, and on a small RISC core design (loosely inspired by the popular ARM processor) in which only 4 percent additional investment in FPGA resources beyond that required for the integer RISC core more than doubles the speed of LNS addition compared to a pure software approach. This approach shares resources in the data path of the non-LNS parts of the RISC so that the only significant cost is the decoding and control for the LNS instruction. The preliminary experiments suggest modest LNS-FPGA implementations, like the algorithms under consideration, are more cost effective than pure software and can be as cost effective as more expensive LNS-FPGA implementations that attempt to maximise speed.

الخلاصة

ترتيبات بوابة برمجة المجال (FPGAs) عندها بعض الصعوبة بتطبيق عمليات النقطة الطائفة. بصورة خاصة، يكرس عدد كبير للشرائح التي يحتاجها المضروبون فيهم للنقطة الطائفة ويحرم دمج النقطة الطائفة في ترتيبات بوابة برمجة المجال الى اصغر واقل كلفة . خيار اخر هو نظام العدد اللوغاريتمي (LNS) حيث الضرب والقسمة تتمان بسهولة وبسرعة . نظام العدد اللوغاريتمي (LNS) له فائدة اخرى هي استهلاك الواطيء للقدرة مقارنتا بالنقطة الطائفية . المشكلة مع نظام العدد اللوغاريتمي (LNS) هي في بناء عملية الجمع هناك العديد من المقايضات بين السعر والاداء في نظام العدد اللوغارتمي (LNS) وهذا النظام له تصحيحي بين البرامج الصافية واجهزه خاصة سريعة . هذه المنشورة تركز على المساومة بين النهايات التي كتبت عن RISC core الصغير في تصحيحي الخاص (يعمل بشكل طليق بمعالج ARM شعبي) التي استثمار 4% اضافي في مصادر ترتيب بوابة برمجة المجال عن المطلوبة لتصميم RISC core السرعة تتضاعف لجمع في نظام العدد اللوغارتمي (LNS) مقارنة مع طريقة برنامج صافي. هذه الطريقة

تي اخترناها تحصل فيها مشاركة بالمصادر في طريق البيانات لغير جزء من نظام العدد اللوغارتمي RISC
ان الكلفة مهمة في فك الجفرة والسيطرة على ايعاز ال LNS. في تجاربي الاولية اقترحت بناء
FPGA – LNS معتدل الذي هو اكثر فعالية للكلفة عنه عن البرنامج الصافي واذا مارفعنا الكلفة فانه سوف
نحصل على سرعة اعلى .

KEY WORDS
Addition, ARM, Interpolation, Logarithmic Number System, Low-power Arithmetic, RISC, Verilog.

INTRODUCTION

The Logarithmic Number System (LNS) uses inexpensive hardware for multiplication: an adder [Pal 2000]. This is possible because the sum of logarithms is the logarithm of the product $\log(x)+\log(y)=\log(x\ y)$. LNS can be more cost effective and less power-hungry than fixed- or floating-point for multiply-intensive signal-processing applications, including sound and screen computations (constrained by the limited resources of portable communication devices like WAP phones) where moderate accuracy is acceptable [Kadlec].

However, multiplication is not the only arithmetic operation such multimedia applications require. There is usually about an equal mix of addition and multiplication. One approach would be to convert to the logarithmic format only for multiplication, and convert back to conventional fixed-point for the summation [Pan 1999]. This has two drawbacks: two conversions, each requiring a look-up table (LUT), are required at each multiplication, and the resulting fixed-point representations often requires more bits (and correspondingly more power for transmission). In fact, logarithmically-based formats, such as μ-law encoding, have been used in telecommunications for decades because of the compression they afford compared to fixed-point methods like PCM.

For the multimedia and signal-processing applications are interested in, the number of input values given to an algorithm is much smaller than the number of additions and multiplications performed on these values. For example, it might have $O(n^{3/2})$ computations for $O(n)$ inputs and outputs. Thus, it is desirable from a power-consumption standpoint to keep data in the more compressed logarithmic format during addition as well as during multiplication, and only convert to fixed-point at the end of the computation.

The problem is that LNS addition also requires LUTs [Kadlec, Waz 1995]. Yet FPGAs, the central component in reconfigurable computing, are rich in LUTs [Sto 1988]. Three ways to implement LNS are listed by increasing speed (and cost):

1- Software running on LUT-based RISC;
2- Hybrid software with some LUT-based hardware dedicated to LNS; and
3- LUT-based hardware dedicated to LNS [Kadlec].

This paper will discuss such FPGA design alternatives using LNS arithmetic. For design reuse between these alternatives, it synthesize the FPGA aspects of the design from a high-level (C-like) notation, known as implicit-style Verilog, using a tool called VITO [Arn 1997] to create the hardware state machines automatically.

It is investigate in this paper the implementation of a conventional CPU inside the FPGA together with some unconventional hardware for LNS. This paper describes using an FPGA to implement a RISC core inspired by a subset of the Advanced RISC Machine's ARM microprocessor [arm]. Rather than simply emulating the ARM, this core is intended to be a platform for an experiment measuring the cost-effectiveness of LNS arithmetic. Thus, it named this project the ARM Work-alike Experiment (AWE) The ARM has been the subject of other academic-design experiments [Woo 1997] and has compiler tools available; also ARM is popular in many multimedia systems-on chip applications where LNS may be useful. Such applications typically need a large memory space for software and data, and thus must assume the logarithm tables required by LNS can fill in what otherwise might be wasted space in a large fixed-size memory chip. AWE is presently targeted for the Virtex-300-FPGA-based VW-300 board from Virtual Computer Corporation. This excellent board has a 1MBx16 external RAM. Since LNS tables occupy an insignificant fraction of this external memory, relatively modest FPGA resources yield numeric speed-up compared to conventional techniques. Putting tables onto the FPGA instead accelerates operations further but at significant-LUT cost. Thus, LNS offers a range of tradeoffs for reconfigurable computing not possible with conventional arithmetic techniques.

AWE reconfigures the meaning of some instructions to assist with LNS implementation. Some flexibility appeared because the processor is implementing only as the configuration of an FPGA. The only constraint is that the instructions under consideration reconfigure should not be ones that are commonly generated by the compiler. For example, the Add-with-Carry (ADC) instruction of the ARM instruction set is infrequently used. It is possible to replace the ADC instruction with a sequence of a few other instructions in the rare instances in which ADC is required. Thus, one option for introducing LNS into our system would be to reconfigure the opcode of the ADC instruction to implement logarithmic multiplication, reducing signed LNS multiply from five cycles to one using insignificant FPGA resources. The ARM instruction set also includes coprocessor instructions, and it will focus on whether it is cost effective to reconfigure this opcode to implement logarithmic addition.

The essential idea with LNS is to convert values into logarithms once and keep them in this representation throughout the entire computation. For example, when a positive value X is input, it is converted into $x = \log_b(X)$. I use capital letters for variables that describe values perceived by the end user, and lower case for the LNS representation. LNS multiplication and division are easy, involving only the addition or subtraction of the logarithmic representation, with some special cases to deal with signs and overflow. (These cases are why reconfiguring the ADC instruction may be desirable.) These special cases are ignored since they have been covered elsewhere [Arn Aug. 1992, King 1971]. Given the LNS representations, $x = \log_b(X)$ and $y = \log_b(Y)$ of the positive values, X and Y, the representation of the product can be formed simply as $x + y$. The difficult part of LNS is the implementation of addition. LNS addition involves the following steps:

1- Obtain $z = y - x$, which corresponds to $\log_b(Z) = \log_b(Y/X)$.

2- Approximate $s_b(z) = \log_b(1 + b^z)$, which corresponds to $\log_b(1+Z) = \log_b(1+ Y/X)$.

3- Obtain $y = x + s_b(z)$, which corresponds to $\log_b(X(1+ Y/X)) = \log_b(X + Y)$.

The benefit of this algorithm is that it only needs one lookup from a table (step 2), instead of the three lookups for the more natural approach, $\log_b(X + Y) = \log_b(b^x + b^y)$.

Two facts affected early LNS implementations [King 1971]: 1) practical results for many applications can be achieved using low-precision LNS, and 2) prices were low enough that direct-memory lookup could approximate $s_b(z)$ for such low-precision systems. Since its memory requirements grow exponentially with word length, high precision cannot be obtained with direct-memory implementation.

Over one hundred papers [xlns] have described variations on LNS techniques, with many showing how to approximate $s_b(z)$ at lower cost than direct lookup. The most common improvement is that the size of the s_b table can be cut in half [King 1971] (without affecting accuracy) by interchanging y and x so that z is positive because $s_b(-z) + z = s_b(z)$. Since

$$\lim_{z \to \infty} s_b(z) = z,$$

thus $s_b(z) \approx z$ for large z, the entire domain of z need not be tabulated [Tay 1988]. Also, interpolation [Arn june1992, Lew 1990, Lew 1994] can increase precision possible with smaller table size than direct lookup.

Power consumption and battery life are important issues in the design of large FPGA systems. Recently, Palourias showed that LNS-based circuits can consume less power than a comparable fixed-point (scaled integer) representation since, on average, the high-order bits of LNS-words exhibit less switching activity [Pal 2000].

LNS is most naturally compared [Arn Aug.1992] against floating-point arithmetic, which is typically larger and more accurate than fixed-point arithmetic. The goal of this project is to implement LNS arithmetic on the AWE in a 32-bit format that is roughly as precise as the 32-bit single-precision floating-point format of the IEEE-754 standard (23 bits of precision). It is considered both a software LNS implementation on a version of the AWE that lacks any special hardware devoted to LNS, and a hardware implementation of LNS for an alternate version of the AWE that consumes only modest additional FPGA resources.

It is also considered how aggressively the designer should pursue high-speed hardware solutions for LNS arithmetic by comparing the modest LNS hardware to a more sophisticated (and expensive) LNS design in the literature [Kadlec] implemented in the same FPGA family as our design.

AWE INSTRUCTION SET ARCHITECTURE

This section describes the non-LNS aspects of the AWE core. The AWE is a 32-bit microprocessor that supports a subset of the ARM's instruction set. It must be chose this subset to be large enough to run the benchmark programs i were interested in and to enable faithful emulation of those ARM instructions that it did not implement in hardware. Like the later versions of the ARM, the AWE supports a full 32-bit address space. (Early versions of the ARM supported a 26-bit address space with the processor's state in the high bits.) The AWE has sixteen general-purpose registers, of which R15 acts as the program counter. Unlike the ARM, the AWE does not have additional registers used for supervisor mode, but instead saves the processor's state in memory. The following describes the binary-compatible instructions of the AWE that behave identically to those of the ARM and describes those ARM instructions not implemented in hardware on the AWE.

The primary class of instructions for the AWE is the data-processing instructions. Like any RISC processor, these instructions operate on two operands with the result going into a third register. For example,

```
ADD R1,R2,R3
AND R4,R5,15 ROR 2
SUB R6,R7,R8 LSL 7
```

There are 16 such AWE instructions, either involving only an addition/subtraction or a Boolean operation. The last operand can be a (possibly rotated) 8-bit immediate value or a register (possibly shifted/rotated a fixed distance). Unlike the ARM, the AWE does not support shifting or rotating by a variable distance, but, as explained below, the AWE has provisions for software emulation of ARM instructions not implemented in hardware.

The second class of instructions on the AWE is the multiply/accumulate instruction:

```
MUL R1,R2,R3
MLA R1,R2,R3,R4
```

The latter instruction is the only AWE instruction implemented in hardware that processes four operands. Like early versions of the ARM, the AWE only multiplies unsigned 32-bit values producing only the low-order 32 bits of the product.

The third class of instructions on the AWE is for relative branch instructions:

```
B  label
BL label
```

The branch-and-link instruction (BL) saves a return address in R14. The ARM lacks a halt, but it is useful for testbenches. I have defined a branch back to itself (eafffffe) as the halt for the AWE.

The final class of instructions on the AWE is the load/store instructions:

```
LDR R1,[R2,4]
STR R3,[R4],-4
```

The AWE supports pre- and post-increment and decrement modification of the index register by an unsigned 12-bit constant. The AWE also supports pre-indexed addressing without modification of the indexed register. Unlike the ARM, the AWE does not support modification of the index register by another register.

The AWE supports conditional execution of instructions, based on four bits of the program-status register (negative, zero, carry and overflow). These bits are optionally set by data-processing or multiply instructions. The sixteen conditions supported include signed and unsigned inequality.

The AWE does not support multi-register transfer, swap or supervisor mode instructions. The non-NS version of the AWE does not support the coprocessor instructions and raises an exception if a program attempts to execute such an instruction.

Although the AWE does not support special supervisor mode instructions, it does have a primitive supervisor mode used for unimplemented instruction traps and external interrupts. The way in which the AWE supervisor mode processes interrupts is completely different from the way the ARM supervisor modes process interrupts.

In the ARM, an interrupt causes a subset of the registers to be switched for a bank of supervisor registers. For "FIQ" interrupts, R8-R14 are switched, with R14 containing the return address. In the other four interrupt modes, R13-R14 are switched. So, in total, there are 16+(14-8+1)+4*(14-13+1) = 31 ARM registers, of which only 16 are available to the software at any instant. Although this makes the ARM well suited for context switching, the complexity of this scheme makes the hardware realisation of this on an FPGA undesirable.

Instead, the AWE uses a minimalist technique borrowed from the classically elegant PDP-8 [Bell 1971]. On that machine, an interrupt causes the return address to be saved at a fixed location in memory and execution to proceed from the location following the return address with the interrupt flag disabled. Interrupts can only occur when the interrupt flag is enabled. The interrupt flag provides a semaphore that controls writing to that fixed location. The PDP-8 returns from the interrupt service routine by turning the interrupt flag back on and doing an indirect jump through the fixed location in memory.

In the AWE, an interrupt causes the program counter, R15, to be saved at a fixed location in memory and execution to proceed from the following location. Because the AWE implementation is pipelined, the value of the R15 at that moment is somewhat offset from the correct return address, but the correct address can be computed from the information saved in memory. The AWE instruction set includes load instructions with relative addressing (pre-indexed R15 without modification). When R15 is loaded by such an instruction, the effect is identical to a jump indirect. For example, if the following AWE code is located so that the label UR15 is at the address where the hardware saves the user's R15 and ISR is the label where the hardware resumes execution after an exception:

```
UR14                ;saved user R14
UR15                ;AWE saves user R15 here
ISR STR R14,[R15,-16] ;save user R14 in UR14
    LDR R14,[R15,-16] ;get UR15 into R14
    SUB R14,R14,12    ;adjust ret addr for pipe
    STR R14,[R15,-24] ;ret addr to UR15
    ...
    LDR R14,[R15,-32] ;restore UR14 into R14
    LDR R15,[R15,-32] ;indirect jump to UR15
                      ;LDR R15 supervisor off
```

Execution proceeds at the label ISR; the interrupt will be processed; and the user's R14 will be saved by the software in UR14. Of course, a realistic service routine would have more details at the place indicated by the ellipsis (which must be empty for the offsets to be correct here). To exit, the user's state is restored (in this case, just the restoration of UR14 into R14 is shown). The final step to resume execution of the user's code is the LDR R15. The AWE has a feature of the LDR R15 instruction not present on the ARM: the LDR R15 instruction turns supervisor mode off on the AWE. This feature causes no problems with a user-mode program having an LDR R15 instruction. This feature does mean that LDR R15 can only be used in AWE supervisor mode for the purpose of returning to AWE user mode, as shown above.

Because this return address scheme is non-reentrant, AWE interrupts (and unimplemented instruction traps) can only occur in user mode. All supervisor software must be restricted to the instructions supported by the hardware. In order to support ARM supervisor mode software, it should be possible to write a small kernel that runs ARM supervisor modes under AWE user mode.

VERILOG CODING

The design was done in the implicit style of Verilog [Arn 1999], which allows easy coding of register transfers in an Algorithmic State Machine (ASM). It has a register file with two read ports and one write port. The register file is simply declared as reg[31:0]r[15:0]. At present, I have chosen a pipeline depth of 3 stages (instruction fetch, instruction decode, execution) as was done on early versions of the ARM . For example, the execution stage for the following:

```
ADD R1,R2,R3
SUB R4,R1,1
```

will cause the Verilog non-blocking assignment, r[1] <= `NCLK r[2]+r[3], to execute in one cycle (reading r[2] and r[3] in the same cycle that the sum is written back into r[1]). Then, in the next cycle (when r[1] contains the sum) the non-blocking assignment r[4] <= `NCLK r[1]-1 will execute, again causing two reads and one write. It is may decide to increase the pipeline depth in order to increase the clock frequency, but my initial experiments suggest that a depth of 3 stages is usable to at least 25MHz. (The B instruction is natural [Arn 1999] for a pipeline depth of 3, although versions of the ARM, such as the StrongArm [Mon 1997], went to a pipeline depth of 5 in order to operate above 200MHz.)

The starting point for our design of the AWE was the tiny textbook example of an ARM subset [Arn 1999]. That example was intended to be an illustration of the concepts of pipelined execution, and it only supports ADD, SUB, MOV and B instructions and the N bit in the program status register. That example does not implement the logical, compare, shift, load, store, multiply or subprogram instructions. That example assumes that the program counter is physically part of the register file and that the ARM could be regarded as a Harvard architecture. The load, store, multiply and subprogram instructions use multi-cycle implementation on the AWE (as on the ARM). My reconfigured LNS instruction also uses a multi-cycle implementation.

Like the ARM, the AWE is a Princeton architecture, with the same memory used to store programs and data. I made the implementation choice that there is only one port to the memory. Because of the one-port memory, LDR and STR instructions on the AWE (as on the ARM) take multiple cycles (one to fetch the instruction, another to calculate the effective address and a third to access the data). R15 is not the actual program counter on the AWE. Instructions that modify R15 (such as the LDR R15 above) cause the AWE to copy the value from R15 back into a separate program counter in an extra state that only occurs for R15. In a similar way, the BL instruction takes an extra cycle to save the return address in R14. The multiply/accumulate on the AWE performs the multiply of two register operands and then inserting an appropriate ADD instruction in the pipeline to fetch the fourth operand. In this sense, the implementation is similar to microcode. The features of the AWE listed in this

...uire multiple states to implement. The ease with which the implicit style allows design of a ...mplex-state machine is an important factor. Unlike a pure multi-cycle implementation, the AWE ...st enter and leave these special states aware of the contents of the pipeline, and this complicates ...e state machine considerably.

...e other version of the AWE that is augmented with an LNS-addition instruction also uses multi-...cle implementations, similar in complexity to the integer multiply/accumulate. It was possible to ...egrate this quickly into the AWE because of the convenience of the implicit style of Verilog.

...FTWARE IMPLEMENTATION

...ear interpolation computes $s_b(z_H) + c(z_H) \cdot z_L$ as an approximation for $s_b(z)$, where $c(z_H)$ is the ...pe of an interpolation line and $s_b(z_H)$ is obtained from a table in RAM. Here i split z into two ...oint components so that $z = z_H + z_L$, where z_H is the high portion of z used to access the table and ...note that $0 \leq z_L < \Delta = 2^{-N}$) is the low portion which is multiplied by the slope. The division ...ween z_H and z_L occurs N bits after the radix point. It is do not considered partitioning [Bell ...71, Arn 1999], which is a more complicated form of interpolation in which Δ varies depending ...z.

...ere are several alternative forms of interpolation, which differ in how $c(z_H)$ is defined and in how ...h accuracy it can guarantee for the result . For example, choosing $c(z_H) = s_b'(z_H)$ gives $2N + 3$ ...s of accuracy. Instead, it will be use Lagrange interpolation, which gives $2N + 5$ bits. The linear-...grange approach computes $c(z_H)$ as $(s_b(z_H + \Delta) - s_b(z_H)) / \Delta$. Thus a choice of $N = 9$ gives 23 ...s of accuracy, which is roughly what IEEE-754 provides, leaving 23 - 9 = 14 bits for z_L. (Lewis ...ew 1994] argues for better-than-floating-point accuracy, which can be achieved with larger table ...d guard bits.) Here is the AWE code for the LNS addition algorithm without using any LNS-...ific instructions:

```
SUBS  R2,R2,R1          ;R2=z=y-x
ADDMI R1,R1,R2          ;if(x>y){ R1=y
RSBMI R2,R2,0x00        ;      z=|z| }
CMP   R2,0xcf ROR 12    ;if z is big
BCS   L                 ; skip interpolate
MOV   R4,R2 LSR 14      ;R4=zH=z>>14
SUB   R2,R2,R4 LSL 14   ;R2=zL=z-(zH<<14)
ADD   R6,R3,R4 LSL 2    ;R6=addr + (zH<<2)
LDR   R5,[R6],0x004     ;R5 = sb(zH)
LDR   R4,[R6],0x000     ;R4 = sb(zH+Dt)
SUB   R4,R4,R5 ;c(zH)=(sb(zH+Dt)-sb(zH))/Dt
MUL   R6,R4,R2          ;R6 = c(zH)*zL
ADD   R2,R5,R6 LSR 14   ;R2 = sb(z)
ADD   R0,R1,R2          ;R0 = min(x,y)+sb(z)
```

...ming R1 contains x, R2 contains y and R3 contains the starting address of the $s_b(z_H)$ table, the ...itional instructions (ADDMI and RSBMI) put the absolute value of their difference (z) into R2 ...the smaller of the two of them into R1. The compare and branch instructions avoid ...rpolation when z is outside of the domain in which the function needs to be tabulated. The ...wing seven instructions implement the interpolation formula. The final ADD combines the ...polated approximation for $s_b(z)$ with the minimum of x and y, forming the logarithm of the sum ...and Y. On the AWE, the LDR instruction takes three cycles, and the 32-bit integer multiply ...s 36 cycles. (In order to simplify its implementation, the AWE does not exit early on ...iplication in the way the ARM does—the testing of the 32-bit word would slow the cycle time in our FPGA implementation.) The other eleven instructions are single cycle. The total time for the LNS-addition software on the AWE is 53 cycles.

FPGA IMPLEMENTATION

An advantage of an FPGA is that its functionality can be reconfigured to optimise operations that are important for the application at hand. In this case, the LNS-addition algorithm (including interpolation) can be transformed from the above software into equivalent Verilog, making LNS addition part of the instruction set of the AWE. This has the potential to speed up the operation. FPGA implementation allows some steps that were done sequentially in §4 to proceed in parallel. For example, the summing of $s_b(z_H)$ to the minimum of x and y occurs simultaneously with the fetching of $s_b(z_H + \Delta)$. Also, the first three instructions are reduced to one or two cycles in the hardware implementation as shown in the following implicit Verilog code:

```
...
else if (ir1[27:24] == 4'b1110)
 begin
  ir2 <= `CLK{12'hf05,ir1[19:0]};
  //NOPed SUB --same ops as LADD
  ...
  @(posedge sysclk) `ENS;
  t <= `CLK `PC;
  minreg <= `CLK ir1[3:0]; //Y
  maxreg <= `CLK ir1[19:16];//X
  z <= `CLK aluout; // X-Y
  ir2 <=`CLK{12'hf06,ir2[19:0]};//RSB
  if (aluout[31]) //msb from SUB
   begin //Y>X, use RSB aluout
    @(posedge sysclk) `ENS;
     maxreg <=`CLK ir1[3:0]; //Y
     minreg <=`CLK ir1[19:16];//X
     z <= `CLK aluout; //Y-X
   end
  ...
 end
```

Here, `ENS indicates Entering a New State, ir1 is the instruction register for the decode stage of the pipeline (ir1[19:16] points to the register that contains X and ir1[3:0] points to the register that contains Y), ir2 is the instruction register for the execute stage of the pipeline (ir2[25:20] determines which data-processing operation the AWE's ARM-compatible ALU performs: 05 is subtract, and 06 is reverse subtract, Y-X), aluout is the output from that ALU, and minreg and maxreg are bit pointers to registers that contain min(X, Y) and max(X, Y), respectively. The above code ... SUB and RSB instructions into the instruction register to obtain z. It takes an extra cycle when the roles of X and Y need to be interchanged in order to make z positive. Together with Verilog ... shown above, it takes seven or eight cycles outside of the multiplication for LADD to compute ... Since z_L only needs 14 bits, the multiply in the interpolation can stop after 14 cycles. Thus the total time for the Logarithmic-Add instruction (LADD) is either 21 or 22 cycles.

Unlike the actual coprocessor instructions of the ARM, LADD on the ... (coded in the coprocessor group, 1110) accesses the processors' general-purpose registers. (A few additional internal registers that are not accessible to the programmer, like minreg and maxreg, are also used.) To simplify the design of LADD, it was assumed that the destination ... different register than the registers that contain X or Y, and it was also assumed that either ...

erand registers may be used by LADD as a scratchpad. LADD chooses the one that contains the ger of the operands (pointed to by maxreg) as the scratchpad, leaving the minimum value changed for use at the end of the logarithmic addition algorithm. (Such assumptions are possible ause this is an FPGA-RISC implementation, where optimisations may be shared between the cessor and its software—a luxury not possible for conventional processors.)
h designs were synthesised for the Virtual Computer Corporations' VW-300 board, which uses Xilinx Virtex-300 FPGA. This FPGA has 3,072 logic slices.

Table 1. Comparison of Implementations
(Assuming these are placed and routed in the same V300 chip)

	AWE no LNS	AWE with LNS	LNS/noLNS ratio	HSLA (ALU only)	HSLA ALU + AWE
Hz	27	25	0.92	17	17
cles	53	21-22	0.4	8	8
tes	19	27	1.4	n/a	n/a
ces	2,471	2,560	1.04	2,325	4,796
GA utilisation	80 %	83 %	1.04	75 %	won't fit
p-flops	784	850	1.08	n/a	n/a
Ts	3,651	3,875	1.06	n/a	n/a
es	35,114	37,045	1.05	n/a	n/a

a = not available)
Cycles indicate how many clock cycles are required to perform the logarithmic addition ation. The States are the total number of states in the state machine that controls the hardware. s are the internal lookup tables used as the basic component of the FPGA. A slice consists of s plus other logic and flip-flops. The equivalent gates are those reported by the Xilinx hesis tool, and should be viewed as only a hypothetical estimate of the complexity of the gn.

53 cycles for the software implementation does not include one cycle to initialise R3 to contain address of the table. This cycle is not needed in the hardware implementation because, unlike a mercial VLSI processor, an FPGA processor can be resynthesised to customise the table ess for a particular software program. This is one of the advantages of the reconfigurable oach—A CISC instruction like LADD need not be quite so complex because i can make some lifying assumptions.

LNS-addition aspect of the AWE shares many resources with its non-LNS-aspects. The ginal cost of implementing LNS addition is only 2,560 - 2,471 = 89 slices because of this urce sharing. These slices are mostly devoted to implementation of the extra states of the rithm.

present design does not implement subtraction. Although for the same accuracy, subtraction s more of the external memory than addition[10], the algorithmic complexity of subtraction is ilar to addition. It can thus estimate that at most another 89 slices would be required for raction, yielding a total of 2,560 + 89 = 2,649 slices

MPARISON WITH OTHER LNS FPGAS

re are a few other reports in the literature of FPGA implementations for LNS arithmetic with ch the AWE might be compared. Wazlowski et al. [Waz 1995] report much more limited-ision use of LNS than that proposed here in a re-configurable platform specialised for hidden-kov speech recognition.

Kadlec et al. [Kadlec] report a 32-bit LNS ALU, with comparable precision to the design considered here. It is based on a design promoted by the HSLA project [col 2000], and like my design, has the logarithm tables residing off-chip. Kadlec synthesized this for a larger member of the same family of FPGAs used here, and thus can be compared to my design. (A more recent version of Kadlec's design uses Virtex-E part, and thus cannot be compared directly to my design.) The available data for Kadlec's original design [Kadlec] is shown in the right column in Table above. The clock frequency is roughly two-thirds of that in my design. Kadlec appears to use a significant portion of the resources in a fast integer multiplier for quadratic interpolation, and yet, given the limitations of the FPGA, is only able to achieve 8-cycle operation. It should be remembered that Kadlec only implements an ALU—there is no processor mentioned to control its operation. A fairer comparison is one between my AWE and Kadlec's ALU plus a processor. Since he reports no processor, let us assume that he is using a processor of the same size as the non-LNS AWE. Since his ALU and processor stand alone from each other, this combination would require 2,325 + 2,471 = 4,796 slices.

The LNS AWE can achieve 25/21.5 = 1.16 MFLOPs using no more than 2,560 + 89 = 2,649 (including the estimate for subtraction) slices. Kadlec's ALU with a processor could achieve 17/8 = 2.125 MFLOPs using no more than 4,796 slices. A reasonable figure of merit to compare Kadlec against the LNS AWE is MFLOP/slice. This is roughly $4.4 \cdot 10^{-4}$ for either system. Thus, Kadlec is no more cost effective than the LNS AWE. In contrast, my non-LNS AWE with software LNS has a lower figure of merit: $2 \cdot 10^{-4}$. Thus i conclude that it pays to move from software to modest hardware reconfiguration (which is done easily within my V300 FPGA), but there is no additional gain in developing a system as complex as Kadlec (which would require a larger, more expensive FPGA).

CONCLUSIONS

In this paper the results shown that a modest investment in FPGA resources, on top of what is required for a minimal integer-RISC processor, allows significant improvement in the implementation of LNS arithmetic. For the particular example of 32-bit LNS, an increase of about 4 percent of the FPGA's resources allows a speedup of about 2.5 for logarithmic addition. This improvement is possible because a significant amount of the resources required can be shared with the non-LNS RISC core. In contrast, an earlier attempt [Kadlec] to make a faster LNS ALU does so at a much higher FPGA cost. Since the justification for LNS must be stated in terms of its cost effectiveness, this preliminary experiment with AWE suggests that a faster LNS implementation [Kadlec] is no more cost effective than an economical implementation (like mine). Since mine takes half the FPGA resources (in a similar RISC-processor context), my design can be used in smaller, less expensive FPGAs, such as the Virtex-300 used in our experiment.

Were able to conduct this experiment rapidly because of the convenience of the implicit style of Verilog, which allows efficient multi-cycle state machines to be coded in a natural algorithmic form. The enhanced preprocessor described in the following appendix (VITO 1.4) enables us to use implicit Verilog to produce a one-hot state machine that is accepted by a conventional synthesis tool (in my case, Xilinx's WebPack). VITO is available for download [Arn 1997], as is WebPack [Xil 1999].

APPENDIX. ENHANCEMENTS TO VITO

In order to synthesize the AWE, i had to extend the semantics of my VITO preprocessor beyond the previously published [Arn 1997, Arn 1999] specifications to cope with memories. As an example of this extension, let's consider something much simpler than the AWE. Here is a two-state nonsensical machine specified in implicit Verilog (the macros `ENS and `CLK are explained elsewhere [Sto 1986]):

```
reg [31:0] a;
```

```
reg [31:0] data1, data2;
always
 begin
  @(posedge clk) `ENS;
   a <= `CLK data1;
  @(posedge clk) `ENS;
   a <= `CLK data2;
 end
```

The labels on the left correspond to wires in a one-hot controller. The previous version (1.2) of VITO creates a one-hot controller and a corresponding datapath that implements the algorithm specified in implicit-style Verilog. Here the controller has two states, one for each @(posedge clk)`ENS. The datapath has only the one register, a, in this example. For the above implicit Verilog source code, all versions of VITO (including the improved version 1.4 described here) translate this into a one-hot controller, with two outputs, whose names are based on the statement numbers of the original Verilog (s4 and s6 here), as shown in **Fig. (1):**

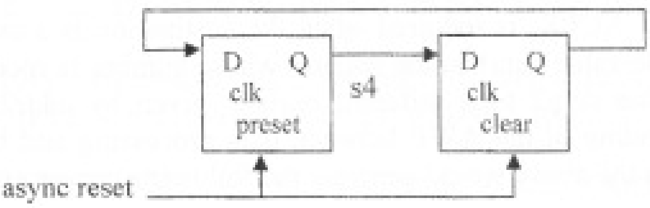

Fig (1). A two-state one-hot controller.

The asynchronous reset makes sure that the flip flop for the starting state contains a one in the first clock cycle and the other flip flop(s) contain zero(s). (An additional flip flop involved in the reset is not shown.) Control statements, such as if or while, would cause the corresponding one-hot controller to be more complicated. The outputs of the controller are used to tell the datapath what to do. The difference between older versions of VITO and the new version used here is in the datapath. VITO 1.2 generates the datapath by extracting all the non-blocking assignments (sorted by destination). These then specify continuous assignment(s) to wire(s) (whose names derive from the concatenation of "new_" to the destination register):

```
wire [31:0] new_a;
assign new_a = s4 ? data1 : s6 ? data2 : a;
```

This corresponds to a series of two input multiplexors, as shown in **Fig. (2).**

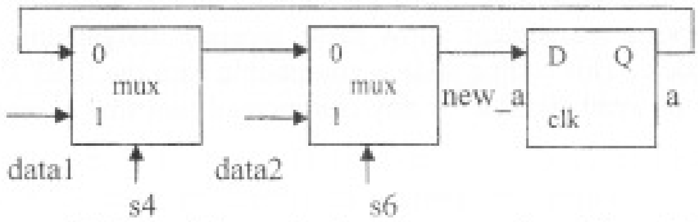

Fig (2). A datapath that corresponds to Figure 1.

The wire (new_a) is the Q input to the destination register (whose D output is a in this case):

```
reg [31:0] a;
always @(posedge clk)
```

```
a <= new_a;
```

Although this works adequately for simple designs up to the complexity of accumulator-based general-purpose computers [Arn 1999], this datapath-generation technique is not powerful enough to handle the Verilog coding for the register file of a RISC processor in a correct fashion. For example, different addresses may be used to access the register file in different states:

```
   reg [31:0] r[15:0];
   reg [31:0] data1, data2;
   reg [3:0] addr1,addr2;
s1: always
s2:  begin
s3:   @(posedge clk) `ENS;
s4:     r[addr1] <= `NCLK data1;
s5:   @(posedge clk) `ENS;
s6:     r[addr2] <= `NCLK data2;
s7:  end
```

For simulation, a different macro, `NCLK, is required when the destination is a memory, such as r[addr1]. The first state assigns the value data1 to the register whose number is specified by addr1. The second state assigns the value data2 to a different register given by addr2. For instance, situations like this occur in the coding of the AWE between data-processing and branch-and-link instructions. Using VITO 1.2 with the above would generate the following erroneous code:

```
wire [31:0] new_r[15:0];
assign new_r[addr1]=s4 ? data1 : m[addr1];
assign new_r[addr2]=s6 ? data2 : m[addr2];
```

This is illegal since Verilog does not allow an array of wires. In order to overcome this restriction, we developed a new version (1.4) of VITO that generates the datapath in a new way:

```
reg [31:0] r;
...
always @(posedge clk)
 begin
  r[addr1] <= s4 ? data1 : r[addr1];
  r[addr2] <= s6 ? data2 : r[addr2];
 end
```

The semantics of the non-blocking assignment allow these separate assignments to be grouped together into a single always block. This coding style is compatible with the IEEE P1364.1 Verilog synthesis standard, and should be synthesizable by any commercial tool that accepts only this style.

REFERENCES

M. Arnold, T. Bailey, and J. Cowles, (1992), Comments on 'An architecture for addition and subtraction of long word length numbers in the logarithmic number system, IEEE Trans. Comput., 41, pp. 786-788, June.

M. Arnold, T. Bailey, J. Cowles, and M. Winkel, (1992), Applying features of IEEE 754 to sign/logarithm arithmetic, IEEE Trans. On Comput., 41, pp.1040-1050, Aug..

Arnold and J. Shuler, (1997), A preprocessor that converts implicit style Verilog into one-hot designs, 6th International Verilog HDL Conference, Santa Clara, CA, pp. 38-45, March 31-April 3,. See www.verilog.vito.com for more recent versions.

Arnold, (1999), Verilog Digital Computer Design: Algorithms into Hardware, PTR Prentice Hall, Upper Saddle River, NJ,.

G. Bell and A. Newell, (1971), Computer Structures: Readings and Examples, ch. 5, McGraw-Hill, New York, NY,.

N. Coleman, E. I. Chester, C. I. Softley, and J. Kadlec, (2000), Arithmetic on the European Logarithmic Microprocessor, IEEE Trans. Comput., 49, no. 7, pp. 702-715, July.

King 1971] N. Kingsbury and P. Rayner, (1971), Digital Filtering Using Logarithmic Arithmetic, Electron.Lett.,7, pp.56-58, Jan.

Kadlec et al., LNS ALU core for FPGA, http://www.utia.cas.cz/idealist-east/vilach/sld001.htm

M. Lewis, (1990), An architecture for addition and subtraction of long word length numbers in the logarithmic number system, IEEE Trans. Comput., 39, pp. 1325-1336, Nov..

M. Lewis, (1994), Interleaved memory function interpolators with application to accurate LNS arithmetic units, IEEE Trans. Comput., 43, pp. 974-982, Aug..

Montanaro, et al., (1997), A 160-MHz, 32-b, 0.5-W CMOS RISC microprocessor, Digital Technical Journal, 9, No. 1,. See also www.intel.com/design/strong/.

Paliouras and T. Stouraitis, (2000), Logarithmic number system for low-power arithmetic," PATMOS 2000: International Workshop on Power and Timing Modeling, Optimization and Simulation, Gottingen, Germany, 13-15 September, pp. 285-294,.

The Programmable Logic Data Book, Xilinx, San Jose, (1999), See www.support.xilinx.com for information on WebPack.

Stouraitis, (1986), Logarithmic Number System Theory, Analysis, and Design, PhD Dissertation, University of Florida, Gainesville, pp. 122-124,.

F. Taylor, R. Gill, J. Joseph, and J. Radke, (1988), A 20 Bit logarithmic number system processor, IEEE Trans. Comput., C-37, pp. 190-199,

Wazlowski, A. Smith, R. Citro, and H. Silverman, (1995), Performing log-scale addition on a distributed memory MIMD multicomputer with reconfigurable computing capabilities, Proceedings of the 1995 International Conference on Parallel Processing, pp. III-211 - III-214,.

Woods, P. Day, S. B. Furber, J. D. Garside, N. C. Paver, and S. Temple, (1997), AMULET1: asynchronous ARM microprocessor, IEEE Trans. on Comput., 46, No. 4, pp. 385-398, April.

] www.arm.com.

] www.xlnsresearch.com.

Pan et al., (1999), A 32b 64-matrix parallel CMOS processor, IEEE International Solid-State Circuits Conference, San Francisco, pp. 15-17, Feb.

ANODIZING OF ALUMINUM-MAGNESIUM ALLOY USING CHROMIC ACID PROCESS

Adil A. Al-Hemiri **Khalid A. Al-Zameli**
Chemical Engineering Department-College of Engineering
University of Baghdad-Iraq

ABSTRACT
Aluminum-magnesium alloy has been anodized using chromic acid as an electrolyte. The effect of voltage in the range of 15-60V, electrolyte concentration in the range of 20-110 g/l, electrolyte temperature in the range of 30-60 °C and time of exposure in the range 25-85 minutes on the coating weight of the anodic film are studied. The experimental data was fitted in terms of the coating weight and the coefficients of third order polynomial are estimated. Optimum conditions of the studied variables are predicted and found equal to 32V, 85 g/l, 50 °C and 70 minutes.

الخلاصة
تم انودة سبيكة المنيوم-مغنسيوم باستخدام حامض الكروميك كمحلول الكتروليتي. تم دراسة تأثير كل من الفولتية من 15-60 فولت وتركيز المحلول الالكتروليتي من 20-110 غم/لتر ودرجة الحرارة من 30-60 م° وزمن تعرض من 25-85 دقيقة على وزن التغطية. تم ملائمة القيم التجريبية بدلالة وزن التغطية حيث تم ايجاد معاملات معادلة من الدرجة الثالثة ومن ثم استخراج القيم المثلى للمتغيرات ووجدت 32 فولت، 85 غم/لتر، 50 م° و70 دقيقة.

KEY WORDS
Anodizing, Chromic Acid Process, Aluminum Alloy

INTRODUCTION

The main processes in use for the anodizing of aluminum employ solutions of sulfuric acid, chromic acid or a mixture of sulfuric acid and oxalic acid as electrolytes. Other processes have been used in specific applications. The chromic acid process is used where a high resistance to corrosion is required with a minimum loss of metal section. They are also used where an enamel-like decorative finish is required and for the detection of flaws in castings and for the treatment of riveted and other assembled parts (Canning, 1970; Al Anodizing Council 2001).
The chromic acid anodizing process for corrosion protection of structural aluminum alloys was invented and subsequently patented by Bengough and Stuart in 1923. Their process utilized a complex voltage control procedure for time intervals applied to aluminum alloys in a 3-5% by weight chromic acid aqueous solution operated at 38-42 °C, the voltage is increased in steps from 0 to 40/50 volts (Henley, 1982). In 1937, Robert W. Buzzard at the National Bureau of Standards found that by increasing the chromic acid concentration to 10% by weight, the complicated voltage variance cycle could be eliminated and the process time decreased (10% chromic acid process). Their process operated at a temperature of 55 °C and 30 volts (Canning, 1970).

The universal chromic acid anodizing process invented and subsequently patented by Turns and Forrester in 1981. This invention provide a universally acceptable chromic acid anodizing process that could be employed for all of the aluminum alloy parts that were to be anodized. A universal process involves a 3-20% by weight chromic acid. In general the optimum conditions obtained were: 20V, 40 °C and 45 minutes. It should be noted that an applied voltage value of 20V was due to the fact that the alloys used have a relatively high content of total alloying element (7.5%).

Sulfuric acid anodizing requires 600 mg/ft^2 (64.6 mg/dm^2) to provide corrosion resistance equivalent to 200 mg/ft^2 (21.5 mg/dm^2) for chromic acid anodizing as stated in Mil-A-8625 (Defence Dept. USA, 1993). Unlike the sulfuric acid process, in the chromic acid anodizing, any electrolyte remaining after inadequate washing, or due to seepage from flaws in the metal, will leave an easily detected yellow stain. For this reason this process is mandatory for anodized items which will be in contact with explosives, propellants or pyrotechnics and is preferred for anodized items which are to remain in close proximity to explosives, propellants or pyrotechnics (Ministry Of Defence UK, 1997) .

In this investigation the coating weight of anodic film of aluminum-magnesium alloy in chromic acid anodizing process was studied. The effect of the operating conditions on the coating weight were also studied and optimized.

EXPERIMENTAL WORK

The specimens used for this study were aluminum-magnesium alloy cut into a dimension of (12 x 1 x 0.24) cm. The analysis of aluminum-magnesium alloy by weight percent as follows: aluminum 98%, copper 0.023%, zinc 0.45%, magnesium 1.51%, lead 0.002% and silicon 0.015%.

The variables studied were: voltage, temperature, acid concentration and time. The first three variables were studied by factorial method and the last variable was studied at the best conditions of the first three. Their arrangement is shown is as shown bellow.

The range of the operating conditions studied were as follow:

X_1 = Voltage (V) 15-60V

X_2 = Acid concentration (C_A) 20-110 g/l

X_3= Temperature (T) 30-60 °C

X_4 = Time (t) 25-85 min.

The relationships between the coded levels and the corresponding real variables as follows:

$$X_{1,coded} = \frac{3(X_{1,actual} - 37.5)}{22.5} \tag{1}$$

$$X_{2,coded} = \frac{3(X_{2,actual} - 65)}{45} \tag{2}$$

$$X_{3,coded} = \frac{3(X_{3,actual} - 45)}{15} \tag{3}$$

$$X_{4,coded} = \frac{2(X_{4,actual} - 55)}{30} \tag{4}$$

Procedure

1- Pretreatment: Prior to anodizing the specimen was treated with the following processes:

- -Chemical Cleaning: Oil, grease and general dirt were properly removed with trichloroethylene at 25 °C. Grease tends to float on surface, which was removed later by filtration. After this stage the specimen rinsed in running water then by distilled water to remove the excess trichloroethylene on the specimen (Ministry of Defence UK, 1995).
- -Stripping Anodic Coating: Defective anodic coatings cannot conveniently be touched up; stripping and re-anodizing are necessary. Anodic coating was stripped in a solution containing

phosphoric acid (3.5 vol.%) and chromic acid (2.0 wt.%) at 99 °C and for 10 min., after this stage the specimen rinsed in running water then by distilled water to remove the excess solution on the specimen (Ministry of Defence UK 1997).

- *-Etching*: 5% by weight sodium hydroxide solution was used with an operating temperature of 40-50 °C. The specimen was placed in the etching solution for a period of 5 min., after this stage the specimen rinsed in running water then by distilled water to remove the excess sodium hydroxide on the specimen (Alubook-Lexical, 2002).
- *-Desmuting*: The specimen was treated in solution contain (30 vol.%) nitric acid and (5 vol%) hydrofluoric acid for about 5 min. at 25 °C to remove the black layer that formed on the surface and to activate the surface for the anodizing afterward the specimen was rinsed with running water followed by distilled water, dried by means of air (Ministry of Defence, UK, 1995).

2- Anodizing: A schematic representation of the experimental apparatus is shown in **Fig. (1).** Two direct current power supplies connected in series were incorporated with the anodizing cell to supply the electrodes a maximum current of 5A and a voltage of 60V. The anodizing cell (one liter capacity) was placed on a magnetic stirrer heater to heat the electrolyte solution and maintains good mixing of the solution to prevent temperature layering in the anodizing cell. A thermostat was connected with power supply heater to control the temperature desired for the solution throughout anodizing time. The aluminum specimen was connected to the positive terminal where it becomes anode, while the stainless steel article was connected to the negative terminal to be the cathode. The two electrodes were held by means of jigs and PVC rack, such only 25 cm^2 of each electrodes surface was immersed. The ammeter and voltmeter were connected to the electric circuit, to measure the current and voltage for the circuit during the process.

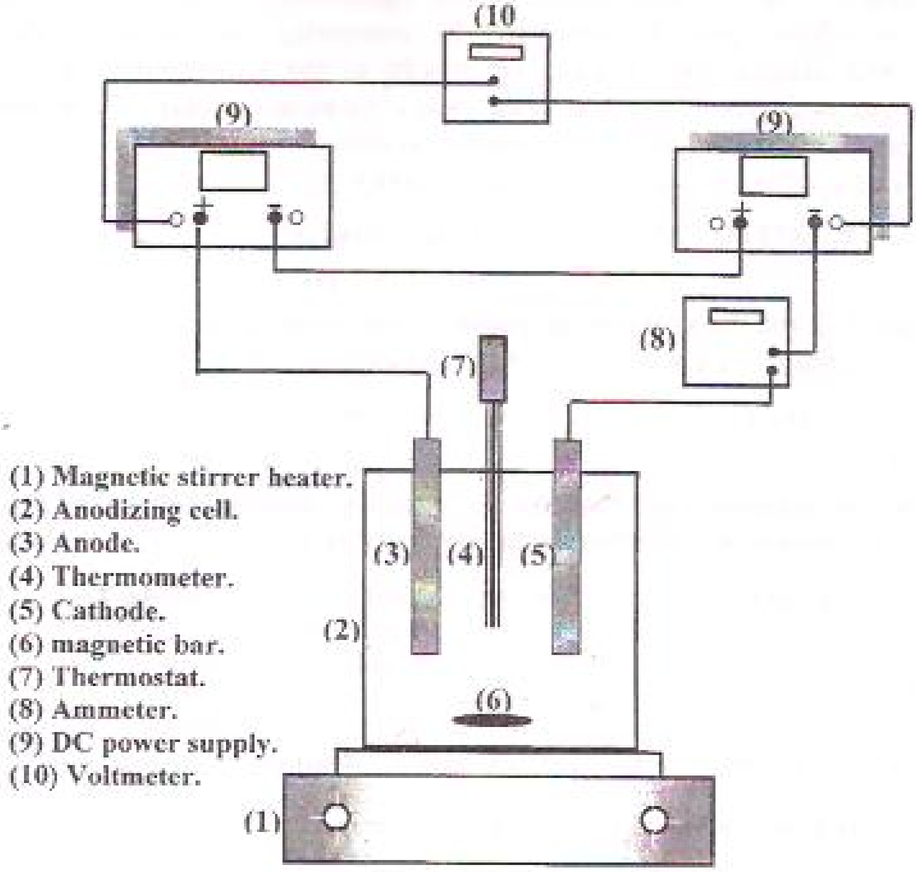

Fig. (1) Schematic diagram for the whole assembly of experimental work.

3- Sealing: The final stage is the sealing process where the specimen was immersed in a one liter solution containing 100 g of potassium dichromate and 18 g of sodium carbonate in distilled water. The solution was kept at temperature 99 °C. The immersion time was 10 min. and the pH of solution was maintained between 6.3-7.4 by the addition of chromic acid or sodium hydroxide (Ministry of Defence UK, 1997).

DISCUSSIONS

A third order polynomial equation is employed for the three variables (voltage"X_1", acid concentration"X_2" and temperature"X_3"). The coating weight is represented by the response Y of the model equation to be constructed. The general form of third order polynomial is written as follows:

$$Y = a_0 + a_1 X_1 + a_2 X_2 + a_3 X_3 + a_4 X_1^2 + a_5 X_2^2 + a_6 X_3^2 + a_7 X_1 X_2 + a_8 X_1 X_3 + a_9 X_2 X_3 + a_{10} X_1^3 + a_{11} X_2^3 + a_{12} X_3^3 + a_{13} X_1 X_2 X_3 + a_{14} X_1 X_2^2 + a_{15} X_1 X_3^2 + a_{16} X_2 X_1^2 + a_{17} X_2 X_3^2 + a_{18} X_3 X_1^2 + a_{19} X_3 X_2^2 \quad (5)$$

The coefficients of equation (5) can be determined by Quasi-Newton method using software program "STATISTICA, Version 5".

The fitted response of the equation (5) is:

$$Y = 273.555 - 8.874 X_1 + 4.5 X_2 + 32.167 X_3 - 6.923 X_1^2 + 0.21 X_2^2 - 8.901 X_3^2 - 3.454 X_1 X_2 + 2.615 X_1 X_3 - 2.83 X_2 X_3 + 0.757 X_1^3 - 0.654 X_2^3 - 2.401 X_3^3 - 0.76 X_1 X_2 X_3 + 0.349 X_1 X_2^2 + 0.41 X_1 X_3^2 - 0.054 X_2 X_1^2 - 0.223 X_2 X_3^2 - 0.554 X_3 X_1^2 - 0.201 X_3 X_2^2 \quad (6)$$

The analysis of variance (F-test) is used for testing the significance of each effect in equation (6). The significance of effects may be estimated by comparing the value of the ratio a2/(standard errors)2 with critical value $F_{0.95}(1, 44) = 4.06$ of the F-distribution at 95% level of confidence with 1 and 44 degree of freedom. If the ratio $a^2/(\text{standard errors})^2 > 4.06$ then the effect is significant. The new response function is then written as follows:

$$Y = 273.555 - 8.874 X_1 + 4.5 X_2 + 32.167 X_3 - 6.923 X_1^2 - 8.901 X_3^2 - 3.454 X_1 X_2 + 2.615 X_1 X_3 - 2.83 X_2 X_3 + 0.757 X_1^3 - 2.401 X_3^3 - 0.76 X_1 X_2 X_3 - 0.554 X_3 X_1^2 \quad (7)$$

Employing equations (1, 2 and 3) to convert the coded values to real values as follows:

$$W_C = 995.4 + 3.875 V - 0.2362 V^2 + 0.0018 V^3 + 0.57 C_A - 84.442 T + 2.237 T^2 - 0.019208 T^3 + 0.0134 T C_A + 0.3056 V T + 0.03 C_A V - 0.00137 C_A V T - 0.00199 V^2 T \quad (8)$$

It is important to find the optimum conditions for the operating variables. Taking the first derivative of equation (8) for the response W_C with respect to each variable and equating to zero as follow:

$$\frac{\partial W_C}{\partial V} = 3.875 - 0.4724 V + 0.0054 V^2 + 0.3056 T + 0.03 C_A - 0.00137 C_A T - 0.00398 V T = 0 \quad (9)$$

$$\frac{\partial W_C}{\partial C_A} = 0.57 + 0.0134 T + 0.03 V - 0.0137 V T = 0 \quad (10)$$

$$\frac{\partial W_C}{\partial T} = -84.442 + 4.474 T - 0.0576 T^2 + 0.0134 C_A + 0.3056 V - 0.00137 C_A V - 0.00199 V^2 = 0 \quad (11)$$

Solving these three equations, it is found that the values were:

$V = 32\ volt$

$C_A = 85\ g/l$

$T = 50\ ^oC$

A third order polynomial equation is employed for the time variable (X_4) at best operating conditions.

The coating weight is represented by the response Y of the mathematical model to be constructed. The general form of third order polynomial is written as follows:

$$Y = b_0 + b_1 X_4 + b_2 X_4^2 + b_3 X_4^3 \quad (12)$$

The fitted response of equation (12) is:

$$Y = 336.086 + 28.8 X_4 - 11.893 X_4^2 + 0.95 X_4^3 \quad (13)$$

Employing equation (4) to convert the coded value to real value as follow:

$$W_C = 23.8 + 10.289 t - 0.0993 t^2 + 0.0002815 t^3 \quad (14)$$

Taking the first derivative of equation (14) for the response W_C with respect to t and equating to zero as follows:

$$\frac{dW_C}{dt} = 10.289 - 0.1986t + 84.45*10^{-5} t^2 = 0 \quad (15)$$

Solving this equation, it is found that the value was: $t = 77$min.

The statistical analysis of the response function showed that the temperature is the factor which has the largest effect on the coating weight, since its coefficient in equation (6) is greater than the coefficients of the other variables. **Figs. (2 and 3)** show the effect of temperature on the coating weight at different voltages and acid concentrations respectively.

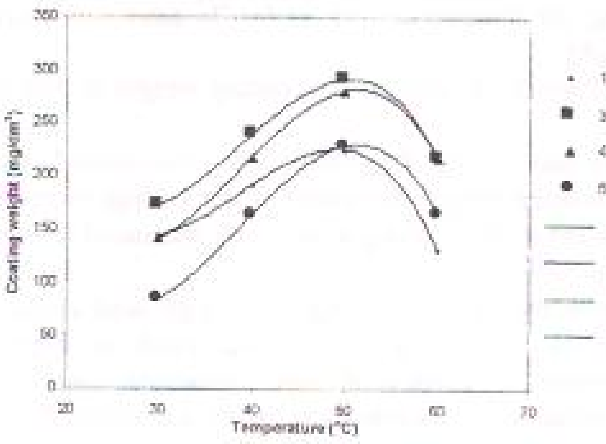

Fig. (2) Effect of temperature on coating weight at different voltages (C_A= 65 g/l, t= 55min.).

Examining these figures one can see that the coating weight or thickness of anodic film increased as the temperature increased in the range between 30-50 °C. But the coating weight decreased as the temperature increased from 50 °C to 60 °C.

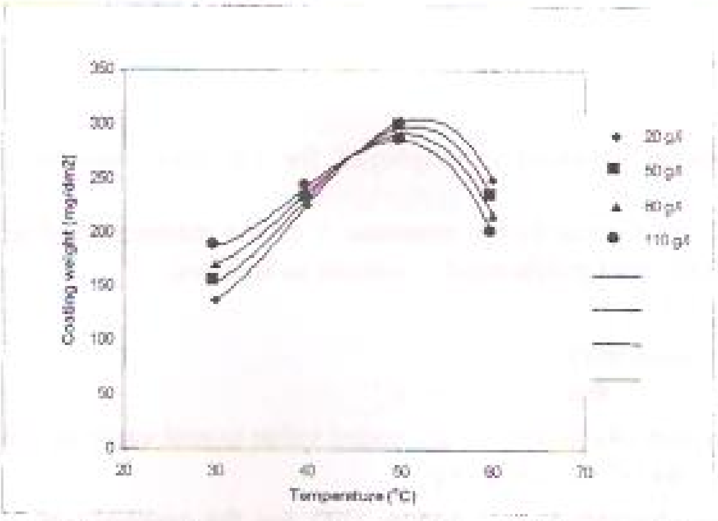

Fig. (3) Effect of temperature on coating weight at different acid concentrations (V= 37.5V, t= 55min.).

This behavior is due to the effect of increasing temperature on coating weight by two inverse ways. The first way, when the temperature increased, the current density increased therefore the formation rate of anodic coating increased, this behavior is in agreement with Arhenious theory. On the other hand further increase in temperature results in the increase of the dissolution rate of anodic coating increased.

From **Fig. (2)**, it is clear that, increasing the temperature from 30 °C to 50 °C gave an increase in the formation rate of anodic coating larger than the increase in the dissolution rate of anodic coating therefore the positive net from these two factors represented by the increase in the coating weight. On the contrary, increasing the temperature up to 60 °C gave a negative net represented by the decrease in the coating weight.

Figs. (4 and 5) show the effect of voltage on the coating weight at different temperatures and acid concentrations respectively.

Examining these figures one can see that the coating weight increased as the voltage increased from 15V to 30V. Moreover the coating weight decreased as the voltage increased from 45V and higher.

Fig. (4) shows that the gradient in the coating weight was increased as temperature decreased, when increasing the voltage above 30V.

From **Fig. (5)** it can be seen that at low voltage with high acid concentration a good result for coating weight. Beside that the same result can be achieved at high voltage with low acid concentration. This behavior is consistent with operation conditions of known processes (Bengough Stuart process using acid concentration 50 g/l and 40/50 V, 10% chromic acid process using acid concentration 100 g/l at 30V).

Figs. (6, 7) show the effect of acid concentration on the coating weight at different temperatures, voltages respectively. Fig. (6) shows that the coating weight increased as the acid concentration increased for low temperature (30-40 °C), and a large rising is achieved as temperature decreases in this range. On the contrary the coating weight decreased as acid concentration increased for high temperature (50-60 °C) and large gradient is achieved as temperature increases in this range. From **Fig. (3)**, it is clear that the reflection point of this behavior occur at 45 °C.

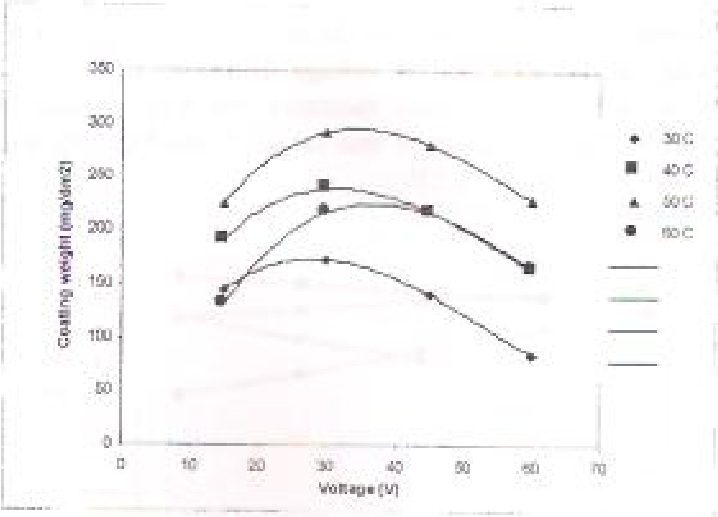

Fig. (4) Effect of voltage on coating weight at different temperatures (C_A= 65 g/l, t= 55 min.).

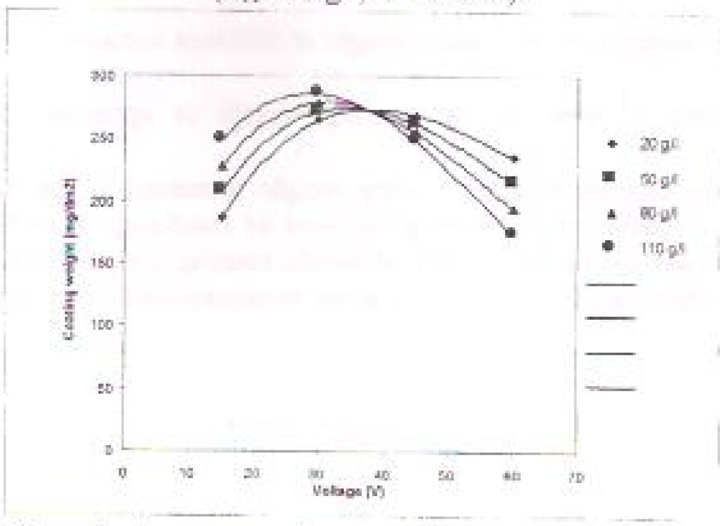

Fig. (5) Effect of voltage on coating weight at different acid concentrations (T= 45 °C, t= 55 min.).

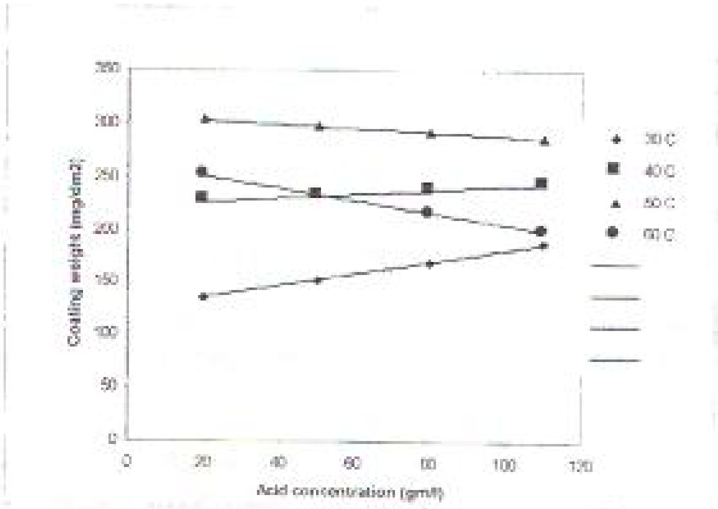

Fig. (6) Effect of acid concentration on coating weight at different temperatures (V= 37.5V, t= 55 min.).

Fig. (7) shows that the coating weight increased as the acid concentration increased for low voltage (15-30V) and a large rising can be achieved as voltage decreases in this range. Farther more the coating weight decreased as acid concentration increased for high voltage (45-60V) and a large gradient can be achieved as voltage increases in this range. From **Fig. (5)**, it can be noted that the reflection point of this behavior occurs at 37.5V.

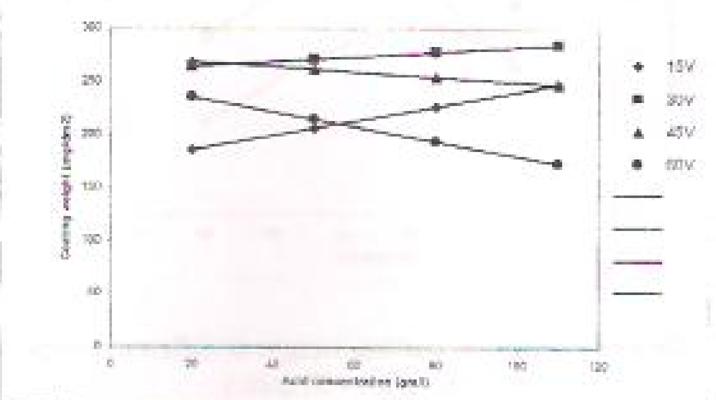

Fig. (7) Effect of acid concentration on coating weight at different voltages (T= 45 °C, t= 55 min.).

Fig. (8) shows the effect of time on the coating weight at optimum operating conditions (32V, 85 g/l, 50 °C).
Examining this figure one can see that the coating weight increased as the time increased in the range between 25-70 min. Moreover increasing the time of anodizing more than 70 min. had no significant effect. In this case the formation rate of anodic coating is equal to the dissolution rate of the anodic coating. Thus the time 70 min. is taken as the recommended optimum time.

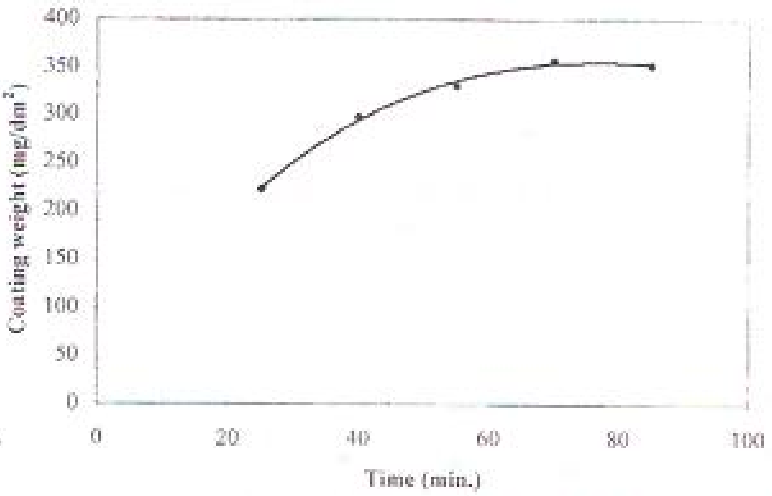

Fig. (8) Effect of time on coating weight (C_A= 85 g/l, V= 32V, T= 50 °C).

While, the mathematical optimum time is equal to 77 minutes. This time value is obtained due to that a small change in coating weight between 70 and 85 min. gave a maximum point at 77 min.

CONCLUSIONS

A third order polynomial of the objective function (coating weight) gave adequate description of the process in terms of temperature, acid concentration and applied voltage (equation 8). While equation 14 describe the process variation with time at optimum values of temperature, concentration and voltage. And these are given below.

It was, also, found that the recommended operating conditions for anodizing aluminum alloy by chromic acid process were:

a- Temperature: 50 °C.

b- Voltage: 32V.

c- Acid concentration: 85 g/l.

d- Time: 70 min. (during the first ten minutes the voltage gradually raised at a rate of 3.2V/min.).

REFERENCES

W. Canning and Co. Ltd., (1970), Canning Handbook on Electroplating, 21 ed.

Aluminum Anodizers Council, (2001), Anodizing Reference Guide, (www.anodizing.org/index.html).

Bengough, G. D., Stuart, J. M., (1923), Improved Process of Protecting Surfaces of Aluminum or Aluminum Alloys, GB Pat. 223,994.

Henley, V. F., (1982), Anodic Oxidation of Aluminum and Its Alloys, Pergamon Press, 1 St. ed.

Turns, E. W. and Forrester, R.E., (1981), Universal Chromic Acid Anodizing Method, US Pat. 4,256,547.

Mil-A-8625F, Military Specification, (1993), Anodic Coatings for Aluminum and Aluminum Alloys, The Department of Defence, USA.

Defence Standard 03-24/Issue 3, (1997), Chromic Acid Anodizing of Aluminum and Aluminum Alloys, Ministry of Defence, UK.

Defence Standard 03-2/Issue 3, (1995), Cleaning and Preparation of Metal Surfaces, Ministry of Defence, UK.

Alubook-Lexical, (2002), About Aluminum, (www.alu-info.dk /Html/alul.ib/ modul/abook40.html)

PROBABILISTIC APPROACH TO MACHINE-COMPONENTS GROUPING IN CELLULAR MANUFACTURING SYSTEMS

Dr. Zuhair I.A. Al-Daoud
Assistant Professor
College of Engineering/ Baghdad University

ABSTRACT

In this paper existing group technology techniques are reviewed and an alternative method using probabilistic approach to machine-components grouping in cellular manufacturing systems is introduced where it is based on production flow analysis, which uses routing information. A common feature of this approach is that it sequentially rearranges row and columns of the machine part incidence matrix according to predefined index and block diagonal is generated. The steps of this method are to assign the 1's in each row and column a probability weight, which alternately rearranged in descending order until a block diagonal matrix is created. It does not need to decide in advance, the number of required cells. It also overcomes the limitation of computational complexity, inherited in exiting group technology methods, especially for large scale and complex problems.

الخلاصة

يتناول البحث دراسة لطرق تكوين الخلايا التكنولوجية و من ثم طرح طريقة جديدة باستعمال الاحتمالية في تكوين المجاميع التكنولوجية في الخلايا التصنيعية التي يتكون منها المصنع. ان الطريقة تعتمد على التسلسل التكنولوجي للاجزاء المكونة للمنتجات المراد تجميعها في المجاميع التكنولوجية. ان هذه الطريقة تقوم في اعادة تنظيم السطر و العواميد للمصفوفة المكونة للاجزاء و المكائن التي تنتج عليها و بالتالي تكوين مصفوفة من مجاميع مستقلة. في هذه نقوم بتخصيص احتمالية لكل من الاجزاء التي تعمل على المكائن و من ثم تنظيمها لحين ظهور مجاميع مستقلة للأجزاء العاملة على المكائن. ان هذه الطريقة لا تحتاج الى تحديد العدد المطلوب من الخلايا. وفي الوقت نفسه تتجاوز الصعوبات المترتبة في الحسابات، التي تعاني منها الطرق المعروفة حاليا و خاصة في الخلايا التي تحوي على عدد كبير من الاجزاء و المكائن.

KEY WORDS

Group Technology. Celluar Manufacturing. Flow Production. Rank Order Clustring.

INTRODUCTION

Group technology (GT) is one of the important techniques used in the formation of cellular manufacturing system. It is used for the purpose of transferring the advantages of flow production organization to be obtained in what otherwise would be jobbing or batch manufacture. GT is defined as the discipline of identifying things; such as parts, processes, equipment, tools, people, and customers; by their attributes. These attributes are then analyzed to identify similarities between

among them. These things are then grouped according to similarities. GT is used to increase efficiency and effectiveness of managing the cellular manufacturing system (Hunt, 1989).
Cellular manufacturing system as an application of group technology concept is defined as the pursuit of smaller batch production of discrete parts, in which the manufacturing system is decomposed into sub-systems (clusters of dissimilar machines located in close proximity) each of which is viewed as an independent entity dedicated to the production of sub-set of similar parts (Ballakur and Steudel, 1987).
Production flow analysis is a method for group technology, developed by Burbidge (1971), which has particular appeal in that it requires no special part coding system, is relatively simple to implement and can be applied to the reorganization of existing, as well as the design of a new manufacturing systems. The method involves a number of stages, which are described in more details by Burbidge (1975).
Using route card data, a machine-component matrix is prepared, in which the rows represent machines and the columns represent components, or vice-versa. If the cell entry $A_{ij}=1$, it indicates that machine "i" makes component "j", or if =0, then there is no relation between the two. So, the complete matrix is a random array of 0's and 1's. The clustering algorithms, which this paper discusses, rely on these assumptions that the machines and components can be partitioned into matched groups of machines and components. These will be represented as clusters along the diagonal of the matrix. This visual presentation of the possible constitution of the cells is the key merit of these methods.
In this paper, the probabilistic relation between the occurrence of the operations of the components on the machines that will perform it and the order that it is performed is taken into considerations so as the final 0-1 matrix, representing the clustering gives the groups of machines that will be assigned to the manufacturing of the components. It is more accurate and quicker to evaluate the machine-component groups.

GROUP TECHNOLOGY METHODS

There are several methodologies developed based on cluster analysis. These are:

Matrix Formulation

In matrix formulation a (0-1) machine-part incidence matrix a_{ij} is constructed, in which elements 1(0) indicate that machine i is used (not used) to process part j. Normally the machine-part incidence matrix constructed based on the production route data. To arrange the matrix into block diagonal form, a number of methods were developed such as:

a- Similarity coefficient, the procedure uses the route information represented by the machine-part incidence matrix to compute the similarity coefficient between machines (i) and (k). The similarity coefficient S_{ik} is the number of parts, which visit both machines 'i' and 'k' divided by the number of parts, which visit at least one of them. Then based on this machine groups are generated. The 1st research that involved in developing this type of technique was (McAuley, 1972). Then he was followed by many others as have been evaluated and/or surveyed by (Shafer and Rogers, 1993 and 1994), (Seifoddini and Hsu, 1994), (Loh and Taylor, 1994), (Seifoddini and Djassemy, 1995) and (Mosier et la, 1997).

b- Array Based Clustering, this method is based on production flow analysis, which uses routing information. A common feature of this approach is that it sequentially rearranges rows and columns of the machine-part incidence matrix according to a predefined index and block diagonal is generated. King (1980) developed the Rank Order Clustering (ROC). The limitation of the ROC method was overcame by introducing the improved method (ROC2), (King and Nakornchai, 1982). The method was furtherly developed by introducing the block and slice method known as (MODROC), (Chandrasekharan and Rajagopalan, 1986). A non-hierarchical clustering algorithm was developed, called " GRAFICS", (Srinivasan and Narendran, 1991).

c- Fuzzy Clustering, the presence of uncertain or vague information of part features, demand or processing time etc., create an inefficient solution, if grouping problem is solved by deterministic type of algorithms. Fuzzy clustering or fuzzy mathematical programming provides a good solution for cell formation with vague information. The 1st presentation of a fuzzy mathematics for part family formation problem was introduced by (Xu and Wang, 1989). Method based on fuzzy set theory was introduced by (Zhung and Wang, 1991), while a method based on a fuzzy c-means clustering algorithm for cell formation was proposed by (Chu and Hayya, 1991), and fuzzy logic approach to consider parts features was presented by (Narayanaswamy and others, 1996). A fuzzy mixed-integer programming is proposed to minimize the cost to exceptional elements, (Tsai and others, 1997).

Rank Order Clustering Algorithm

The rank order-clustering algorithm (ROC), introduced by (King, 1980), represents route card data as a binary matrix. Using a positional weighing technique for the "1" entries in the matrix, the rows and columns are alternatively rearranged in order of decreasing rank. The result is a diagonalization of the 1's into several clusters. If independent machine-component groups do exist in the sample data provided, each machine will occur in only one cluster. Components will be uniquely assigned to any one of the clusters. Using this algorithm, the analyst can obtain a visual assessment of the machine groups and the associated families of parts simultaneously. With such an approach, a very valuable preliminary assignment of machines can be obtained because, if a large number of machines are shared over several clusters, plans for cellular manufacture can be shelved at the outset. There are few weaknesses in this algorithm, which affect its performance, caused by two types of cell entries, which prevent cluster formation and create dispersion away from the diagonal. These are (Tsai and others, 1997):

a- Exception elements: these are a few cell entries that occur outside a pair of clusters. However, only one cluster can contain that machine, resulting in an inter-cell move of the other components requiring that machine to complete their processing. The occurrence of such entries is expected but the ROC solution is disrupted, due to the method adopted for ranking. It reacts on pairwise comparison of cell entries in the leftmost column (when ranking rows) and topmost (when ranking columns). So if the positional occurrence of these elements is such that they influence the ranking, poor cluster formation will result.

b- Bottleneck machines: these are machines that are used by a large number of components. Since these components can be expected to be dispersed over more than one cluster, such machines must appear in more than one row in the matrix. Otherwise, the ranking procedure creates large dispersed cluster with many machines and components contained in them.

The ROC algorithm work only after these two types of elements are identified and suppressed after visual analysis of the initial matrix solutions. Such prior assumptions bias solution, especially as the algorithm must indicate exceptions and bottleneck machines, not rely on their temporary suppression to be effective. Other drawbacks are:

- An inability to analyze large matrices since the binary words lengths increase. Rows and columns are compared pair wise increasing the number of comparisons necessary for a solution. The ranking being dependent on the positional coordinates of the entries in the matrix. The complete matrix needs to be analyzed, which increases computational time.
- *Inconsistency in the number of clusters, the identity of the exceptional elements and the machine

–component constitution of the clusters, is depending on the initial input matrix.

- Total neglect of load figures to decide the allocation of bottleneck machines among the clusters.

PROBABILISTIC APPROACH ALGORITHM

To overcome most of the limitation of other methods, the following approach is suggested. It will:

a- Use the machine-component matrix only, with no need for special coding or rearrangement to fit particular solution.

b- Simplify the identification of both exceptional elements and bottleneck machines by grouping correctly all the machines.

c- Ability to analyze large matrices, since it is only dealing with small values in comparison.

If there are M machines processing N components, then a machine i is assigned to process component j, hence their relation can be expressed by an incidence matrix A(i,j)=0, otherwise A(i,j)=1. The objective of the method is to rearrange the machine-component incidence matrix such that the element "1" focuses on the diagonal blocks of the matrix. This is achieved by introducing the probability of each component j processed on machine i, by means of determining the total number of components and then finding the probability of occurrence of each one independently by using the formulas:

Total number of components performed on machine i, which is indicated by ($TOTC_i$), is:

$$TOTC_i = \sum_{j=1}^{N} X_{i,j}$$

Probability of occurrence of component j on machine i, which is indicated by ($P\{X_{i,j}\}$), is:

$$P\{X_{i,j}\} = \frac{1}{TOTC_i}$$

Therefore the sum of each machine i, which is indicated by ($SUMC_i$), is: $SUMC_i = \sum_{j=1}^{N} P\{X_{i,j}\} * j$

Then this is sorted in decreasing value order, the ones with the same value are arbitrary ordered in the same order in which they appear in the current matrix.

Similarly, the same is done for the machines, i.e.:

Total number of machines used by component j in accordance to its process technology, indicatedby ($TOTM_j$), is: $TOTM_j = \sum_{i=1}^{M} Y_{i,j}$

Probability of occurrence of machines i used by component j for processing, which is indicated by $(P\{Y_{i,j}\})$, is: $(P\{Y_{i,j}\}) = \frac{1}{TOTM_j}$

Therefore the sum of each component j, which is indicated by ($SUMM_j$), is:

$$SUMM_j = \sum_{i=1}^{M} P\{X_{i,j}\} * i$$

Then this is sorted in decreasing value order; the ones with the same value are arbitray ordered in the same order in which they appear in the current matrix.

At the end of each stage the total of the rows and columns for the current matrix, indicated by $GRDTOT_k = SUMC_i + SUMM_j$, where k=1,.......,n; is determined and then compared with previous one. If they are equal then the method is terminated i.e. it has reached its optimum and then they are the clusters which gives the groups. Otherwise it is repeated with same steps as above. **Fig. (1)** indicates the flow chart for the algorithm.

The algorithm can start with any form of a machine-component matrix since it is an iterative approach that will converge to the optimal solution in a finite number of iterations.

PRACTICAL APPLICATION

The algorithm then was programmed on a computer using data from a company so as to find the optimum number of g oups. The application uses (42) machines and (72) components, as shown in **Table (1)** below.

Table (1) Machine- Component Original Matrix

```
0000000000111111111122222222223333333333444444444455555555556666666
66666777
0012345678901234567890123456789012345678901234567890123456789012345
56789012
011                          1
0211  1  1 1 1     1 11        11  11            1    1    1
031
041                                 1   1 1               1      1
051                     1
06 1  1    1 1                   1
07  1          1
08   1                 1 1                                    1
09    1                   1           1    1        1  11      1
10    1
11    1                            1  1                    1
12    11 1 111        1      1  1      1      1   1    11
13     1  1 1            1       11    1111 1 111 11
1
14      1                   11       1       1              1
15      1                   11       1       1              1
16        1
17        1   1 11       1                                   1
18        1              1                1            1
19        1    1       1                            1   1
20          1            1       1 1        1
21           1     1                                1
1
22            1 11  1                                        1
23                1
24                      1
25                      1
26                      1      1
27                      1
28                      1
29                      1
30                      1
31                        1                1           1       1
32                        1           1    1              11  1 11
33                              1
34                                1   1
35                                                   1            1
1111111
36                                                   1
111111
37                                                   1
38                                                             1
39                                                              1
40                                                                1
41                                                                1
42                                                                1
```

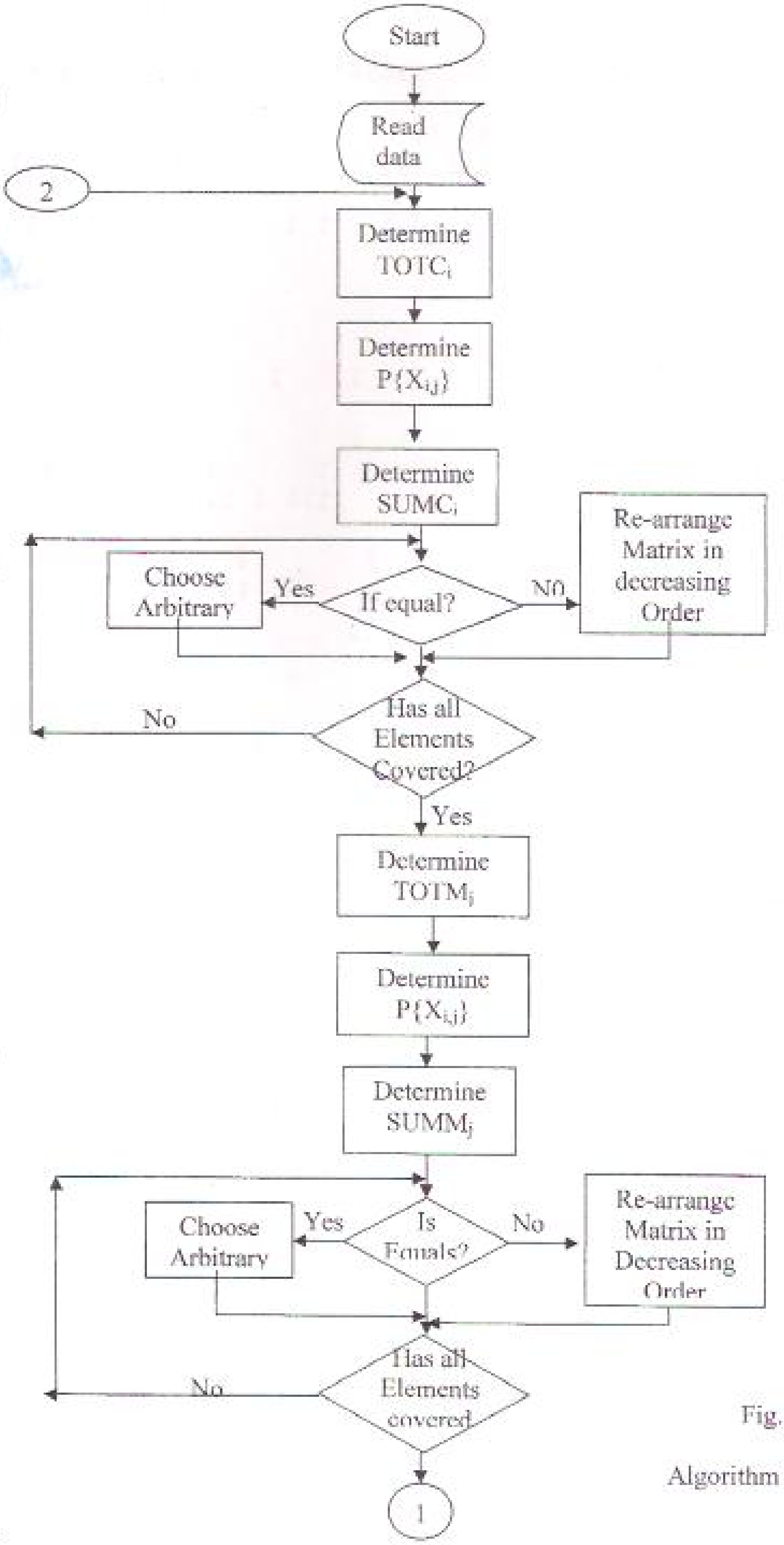

Fig. (1)

Algorithm Flowchart

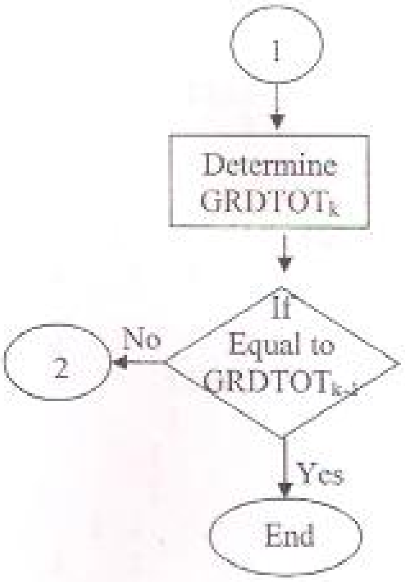

Fig. (1) continued

Then applying the algorithm produced, the result shown in Table (2).:

Table (2) The resulted matrix after the application of the algorithm

```
000301100235132245356422351304453524567246603344462156666776011150
10223451
001452028137800972863038241165956051312420297946852416789014435693
97675387
0211111111111111
0411              1111
051                   1
011                    1
031
06  1111                1
12  111 11        1    1
11  1     11
09  1
10  1
21   1      1
20        1
32         1       11
26           1        1
33           1
13                1  1  1
18                   1
24                    1
25                    1
27                    1
28                    1
29                    1
30                    1
34                      1
```

```
12    1111111
11           1
09    1      111111
21            1     1
20     11            11
32           1  11     11
13     11111         11  1111111
18                1  1   1
34           1
19    1       1          1      11
31              1111
38                 1
35                  1
42                  1
08                   1 1        1
17                   1   1
39                      1
16                       1
07                               1
35                                   11111111
08                                           1
17                                            1111
07                                                1
36                                   1111111
37                                   1
40                                          1
41                                          1
22                                            1111
1
14
111111
15
111111
23
1
```

EXCEPTIONAL ELEMENTS

There were many exceptional elements in the final matrix, and then a re-assignment was made to these elements. This has resulted in determining the group matrix as shown in **Table (3).** This group matrix contains three groups, without any exceptional parts.

Table (3) Groups after re-assignment

```
000301100235132245356422351304453524567246603344462156666776011150
10223451
001452028137800972863038241165956051312420297946852416789014435693 .
97675387
021111111111111111
0411              1111
051                   1
011                    1
031
06  1111                1
12  111 11        1    1
11  1     11
09  1
10  1
21   1      1
20        1
32         1       11
26           1        1
33           1
13                1  1  1
18                   1
24                    1
25                    1
27                    1
28                    1
29                    1
30                    1
34                      1

12                       1111111
11                              1
09                       1      111111
21                               1    1
20                        11           11
32                              1 11     11
13                        11111        11  1111111
18                                  1  1   1
34                              1
19                       1       1         1      11
31                                1111
38                                   1
35                                    1
42                                    1
08                                     1 1        1
17                                     1   1
39                                          1
16                                         1
07                                                 1
```

```
35   11111111
08           1
17            1111
07                1
36   1111111
37   1
40          1
41          1
22            1111
14           111111
15           111111
23                1
```

CONCLUSIONS

The method introduced in this study has simplified the calculation for the (0-1) matrix because of the use of probability which lead to the use of small numbers in calculations and therefore less time needed in the manupalation of the group matrix.

Also the introduced method is able easily to deal with a large number of components and machine without having to extend memory or splitting of matricies.

REFERENCES

Ballakur, A. and H.J. Steudel, (1987), A Within Cell Utilization Based Heuristic for Designing Cellular Manufacturing Systems, Int. J. Prod. Res., Vol. 33, No. 10.

Burbidge, J.L., (1971), Production Flow Analysis, Prod. Engr., Vol.50, No. 4.

Burbidge, J.L., (1975), The Introduction to GT, Heinemann, London, U.K.

Burbidge, J.L., and D.M. Zelenovic, (1983), Using Production Flow Analysis to plan Group Technology for a New Factory, Mater. Flow 1.

Chandrasekharan, M.P. and R. Rajagopalan, (1986), MODROC; An Extension of Rank Order Clustering for Group Technology, Int. J. Prod. Res., Vol. 24 No 5.

Chu, C.H. and J. Hayya, (1991), A Fuzzy Clustering Approach to Manufacturing Cell Formation, Int. J. Prod. Res., Vol. 29 No. 7.

Gallagher, J.L., T.J. Grayson, A. Philips; (1971), A Review of Development and Applications of Group Technology at the University of Birmingham, Int. J. Prod. Res., Vol. 9 No 9, 1971.

Gallagher, J.L., and W.A. Knight, 1973, Group Technology, Butterworth, UK.

Gallagher, C.C., and W.A. Knight, (1986), Group Technology Production Methods in Manufacturing, John Wiley and sons, USA.

Ham, I., K. Hitomi, and T. Yoshida, (1985), Group Technology Application to Production Management, Kluwer-Nijhoff Pub., USA.

Hunt, V.D., (1989), Computer Integrated Handbook, Chapman & Hill, U.S.A.

Kamrani, A.K., and R.P. Hamid, (1994), A Methodology for Design of Manufacturing Systems Using Group Technology, J. Prod. Planning and Control, Vol. 5, No. 5.

King, J.R., (1980), Machine-component Grouping Production Flow Analysis; an Approach Using Rank Order Clustering Algorithm, Int. J. Prod. Res., Vol. 18 No. 2.

King, J.R.' and V. Nakornchai, (1982), Machine-Component Group Formation in Group Technology: Review and Extension, Int. J. Prod. Res., Vol. 20 No. 2.

Loh, S. and G.D. Taylor, (1994), An Evaluation of Product Commonality and Group Technology Production Methods in a Pre-defined Multiple-machine Scenario, Prod. Planning and Control, Vol 5 No 6.

McAuley, J., (1972), Machine Grouping for Efficient Production, Prod. Engr.

Mosier, C.T., J. Yelle, and G. Walker, (1997), Survey of Similarity Coefficient Based Methods as Applied to the Group Technology Configuration Problem, Omega Int. J. Mgt. Sci., Vol. 25 No 1.

Narayanaswamy, P., C.R. Bector and D. Rajamani, (1996), Fuzzy Logic Concept Applied to Machine-Component Matrix Formation in Cellular Manufacturing, Europ. J. Op. Res., Vol 93.

Optiz, H. and H.P. Wiendahl, (1971), Group Technology and Manufacturing Systems for Small and Medium Quantity Production, Int. J. Prod. Res., Vol. 9 No 1.

Schafer, H., N.H. Darracot, C. O'Brien, and J.R. Wilson; (1992), The Consideration of Human Factors in the Design of Group Technology Manufacturing Systems, Proc. 2nd Int. FAIM Conf. Ed., Osama K. Eyada & M. Munir Ahmed, CRC Press Inc., Virinia, U.S.A.

Seifoddini, H. and C. Hsu, (1994), Comparative Study of Similarity Coefficient and Clustering Algorithm in Cellular Manufacturing, J. Manuf. Sys., Vol. 13 No. 2.

Seifoddini, H. and M. Djassemi, (1995), Merits of Production Volume Based Similarity Coefficient in Machine Cell Formation, J. Manuf. Sys., Vol. 14 No. 1.

Shafer, S.M., and D.F. Rogers, (1993), Similarity and Distance Measures for Cellular Manufacturing, Part I, A Survey, Int J. Prod. Res., Vol. 31, No. 5.

Shafer, S.M., and D.F. Rogers, (1993), Similarity and Distance Measures for Cellular Manufacturing, Part II, An Extension and Comparison, Int. J. Prod. Res., Vol. 31, No. 5.

Srinivasan G. and T.T. Narendran, (1991), GRAFICS: A Non Hierarchical Clustering Algorithm for Group Technology, Int J. Prod. Res., Vol. 29 No 3.

Tsai, C.C., C.H. Chu and T.A. Batra, (1997), Modeling and Analysis of a Manufacturing Cell Formation Problem with Fuzzy Mixed-integer Programming, IIE Trans., Vol. 29 No. 7.

Xu, H. and H. Wang, (1989), Part Family Formation for GT Application Based on Fuzzy Mathematics, Int. J. Prod. Res., Vol 27 No 9.

Zhung, C. and H.P. Wang, (1991), Formation of Machine Cells: A Fuzzy Set Approach, CAD/CAM Robotic and Factories of the Future 90, Volume 1, Ed. Dwivedi, S.N., A. K. Verma, and J.E. Snekenberger, Springer Verlag, USA.

PROBABILISTIC APPROACH TO MACHINE-COMPONENTS GROUPING IN CELLUAR MANUFACTURING SYSTEMS

Dr. Zuhair I.A. Al-Daoud
Assistant Professor
College of Engineering/ Baghdad University

ABSTRACT

In this paper existing group technology techniques are reviewed and an alternative method using probabilistic approach to machine-components grouping in cellular manufacturing systems is introduced where it is based on production flow analysis, which uses routing information. A common feature of this approach is that it sequentially rearranges row and columns of the machine part incidence matrix according to predefined index and block diagonal is generated. The steps of this method are to assign the 1's in each row and column a probability weight, which alternately rearranged in descending order until a block diagonal matrix is created. It does not need to decide in advance, the number of required cells. It also overcomes the limitation of computational complexity, inherited in exiting group technology methods, especially for large scale and complex problems.

الخلاصة

يتناول البحث دراسة لطرق تكوين الخلايا التكنولوجية و من ثم طرح طريقة جديدة باستعمال الاحتمالية في تكوين المجاميع التكنولوجية في الخلايا التصنيعية التي يتكون منها المصنع. ان الطريقة تعتمد على التسلسل التكنولوجي للاجزاء المكونة للمنتجات المراد تجميعها في المجاميع التكنولوجية. ان هذه الطريقة تقوم في اعادة تنظيم السطر و العواميد للمصفوفة المكونة للاجزاء و المكائن التي تنتج عليها و بالتالي تكوين مصفوفة من مجاميع مستقلة. في هذه نقوم بتخصيص احتمالية لكل من الاجزاء التي تعمل على المكائن و من ثم تنظيمها لحين ظهور مجاميع مستقلة للأجزاء العاملة على المكائن. ان هذه الطريقة لا تحتاج الى تحديد العدد المطلوب من الخلايا. وفي الوقت نفسه تتجاوز الصعوبات المترتبة في الحسابات، التي تعاني منها الطرق المعروفة حاليا و خاصة في الخلايا التي تحوي على عدد كبير من الاجزاء و المكائن.

KEY WORDS

Group Technology. Celluar Manufacturing. Flow Production. Rank Order Clustring.

INTRODUCTION

Group technology (GT) is one of the important techniques used in the formation of cellular manufacturing system. It is used for the purpose of transferring the advantages of flow production organization to be obtained in what otherwise would be jobbing or batch manufacture. GT is defined as the discipline of identifying things; such as parts, processes, equipment, tools, people, and customers; by their attributes. These attributes are then analyzed to identify similarities between among them. These things are then grouped according to similarities. GT is used to increase efficiency and effectiveness of managing the cellular manufacturing system (Hunt, 1989).

Cellular manufacturing system as an application of group technology concept is defined as the pursuit of smaller batch production of discrete parts, in which the manufacturing system is decomposed into sub-systems (clusters of dissimilar machines located in close proximity) each of which is viewed as an independent entity dedicated to the production of sub-set of similar parts (Ballakur and Steudel, 1987).

Production flow analysis is a method for group technology, developed by Burbidge (1971), which has particular appeal in that it requires no special part coding system, is relatively simple to implement and can be applied to the reorganization of existing, as well as the design of a new manufacturing systems. The method involves a number of stages, which are described in more details by Burbidge (1975).

Using route card data, a machine-component matrix is prepared, in which the rows represent machines and the columns represent components, or vice-versa. If the cell entry A_{ij}=1, it indicates that machine "i" makes component "j", or if =0, then there is no relation between the two. So, the complete matrix is a random array of 0's and 1's. The clustering algorithms, which this paper discusses, rely on these assumptions that the machines and components can be partitioned into matched groups of machines and components. These will be represented as clusters along the diagonal of the matrix. This visual presentation of the possible constitution of the cells is the key merit of these methods.

In this paper, the probabilistic relation between the occurrence of the operations of the components on the machines that will perform it and the order that it is performed is taken into considerations so as the final 0-1 matrix, representing the clustering gives the groups of machines that will be assigned to the manufacturing of the components. It is more accurate and quicker to evaluate the machine-component groups.

GROUP TECHNOLOGY METHODS

There are several methodologies developed based on cluster analysis. These are:

Matrix Formulation

In matrix formulation a (0-1) machine-part incidence matrix a_{ij} is constructed, in which elements 1(0) indicate that machine i is used (not used) to process part j. Normally the machine-part incidence matrix constructed based on the production route data. To arrange the matrix into block diagonal form, a number of methods were developed such as:

a- Similarity coefficient, the procedure uses the route information represented by the machine-part incidence matrix to compute the similarity coefficient between machines (i) and (k). The similarity coefficient S_{ik} is the number of parts, which visit both machines 'i' and 'k' divided by the number of parts, which visit at least one of them. Then based on this machine groups are generated. The 1st research that involved in developing this type of technique was (McAuley, 1972). Then he was followed by many others as have been evaluated and/or surveyed by (Shafer and Rogers, 1993 and 1994), (Seifoddini and Hsu, 1994), (Loh and Taylor, 1994), (Seifoddini and Djassemy, 1995) and (Mosier et la, 1997).

b- Array Based Clustering, this method is based on production flow analysis, which uses routing information. A common feature of this approach is that it sequentially rearranges rows and columns of the machine-part incidence matrix according to a predefined index and block diagonal is generated. King (1980) developed the Rank Order Clustering (ROC). The limitation of the ROC method was overcame by introducing the improved method (ROC2), (King and Nakornchai, 1982). The method was furtherly developed by introducing the block and slice method known as (MODROC), (Chandrasekharan and Rajagopalan, 1986). A non-hierarchical clustering algorithm was developed, called " GRAFICS", (Srinivasan and Narendran, 1991).

c- Fuzzy Clustering, the presence of uncertain or vague information of part features, demand or processing time etc., create an inefficient solution, if grouping problem is solved by deterministic type of algorithms. Fuzzy clustering or fuzzy mathematical programming provides a good solution for cell formation with vague information. The 1st presentation of a fuzzy mathematics for part family formation problem was introduced by (Xu and Wang, 1989). Method based on fuzzy set theory was introduced by (Zhung and Wang, 1991), while a method based on a fuzzy c-means clustering algorithm for cell formation was proposed by (Chu and Hayya, 1991), and fuzzy logic approach to consider parts features was presented by (Narayanaswamy and others, 1996). A fuzzy mixed-integer programming is proposed to minimize the cost to exceptional elements, (Tsai and others, 1997).

Rank Order Clustering Algorithm

The rank order-clustering algorithm (ROC), introduced by (King, 1980), represents route card data as a binary matrix. Using a positional weighing technique for the "1" entries in the matrix, the rows and columns are alternatively rearranged in order of decreasing rank. The result is a diagonalization of the 1's into several clusters. If independent machine-component groups do exist in the sample data provided, each machine will occur in only one cluster. Components will be uniquely assigned to any one of the clusters. Using this algorithm, the analyst can obtain a visual assessment of the machine groups and the associated families of parts simultaneously. With such an approach, a very valuable preliminary assignment of machines can be obtained because, if a large number of machines are shared over several clusters, plans for cellular manufacture can be shelved at the outset. There are few weaknesses in this algorithm, which affect its performance, caused by two types of cell entries, which prevent cluster formation and create dispersion away from the diagonal. These are (Tsai and others, 1997):

a- Exception elements: these are a few cell entries that occur outside a pair of clusters. However, only one cluster can contain that machine, resulting in an inter-cell move of the other components requiring that machine to complete their processing. The occurrence of such entries is expected but the ROC solution is disrupted, due to the method adopted for ranking. It reacts on pairwise comparison of cell entries in the leftmost column (when ranking rows) and topmost (when ranking columns). So if the positional occurrence of these elements is such that they influence the ranking, poor cluster formation will result.

b- Bottleneck machines: these are machines that are used by a large number of components. Since these components can be expected to be dispersed over more than one cluster, such machines must appear in more than one row in the matrix. Otherwise, the ranking procedure creates large dispersed cluster with many machines and components contained in them.

The ROC algorithm work only after these two types of elements are identified and suppressed after visual analysis of the initial matrix solutions. Such prior assumptions bias solution, especially as the algorithm must indicate exceptions and bottleneck machines, not rely on their temporary suppression to be effective. Other drawbacks are:

- An inability to analyze large matrices since the binary words lengths increase. Rows and columns are compared pair wise increasing the number of comparisons necessary for a solution. The ranking being dependent on the positional coordinates of the entries in the matrix. The complete matrix needs to be analyzed, which increases computational time.
- *Inconsistency in the number of clusters, the identity of the exceptional elements and the machine
–component constitution of the clusters, is depending on the initial input matrix.
- Total neglect of load figures to decide the allocation of bottleneck machines among the clusters.

PROBABILISTIC APPROACH ALGORITHM

To overcome most of the limitation of other methods, the following approach is suggested. It will:

a- Use the machine-component matrix only, with no need for special coding or rearrangement to fit particular solution.

b- Simplify the identification of both exceptional elements and bottleneck machines by grouping correctly all the machines.

c- Ability to analyze large matrices, since it is only dealing with small values in comparison.

If there are M machines processing N components, then a machine i is assigned to process component j, hence their relation can be expressed by an incidence matrix A(i,j)=0, otherwise A(i,j)=1. The objective of the method is to rearrange the machine-component incidence matrix such that the element "1" focuses on the diagonal blocks of the matrix. This is achieved by introducing the probability of each component j processed on machine i, by means of determining the total number of components and then finding the probability of occurrence of each one independently by using the formulas:

Total number of components performed on machine i, which is indicated by ($TOTC_i$), is:

$$TOTC_i = \sum_{j=1}^{N} X_{i,j}$$

Probability of occurrence of component j on machine i, which is indicated by ($P\{X_{i,j}\}$), is:

$$P\{X_{i,j}\} = \frac{1}{TOTC_i}$$

Therefore the sum of each machine i, which is indicated by ($SUMC_i$), is: $SUMC_i = \sum_{j=1}^{N} P\{X_{i,j}\} * j$

Then this is sorted in decreasing value order, the ones with the same value are arbitrary ordered in the same order in which they appear in the current matrix.

Similarly, the same is done for the machines, i.e.:

Total number of machines used by component j in accordance to its process technology, indicatedby ($TOTM_j$), is: $TOTM_j = \sum_{i=1}^{M} Y_{i,j}$

Probability of occurrence of machines i used by component j for processing, which is indicated by$(P\{Y_{i,j}\})$, is: $(P\{Y_{i,j}\}) = \frac{1}{TOTM_j}$

Therefore the sum of each component j, which is indicated by ($SUMM_j$), is:

$$SUMM_j = \sum_{i=1}^{M} P\{X_{i,j}\} * i$$

Then this is sorted in decreasing value order; the ones with the same value are arbitray ordered in the same order in which they appear in the current matrix.

At the end of each stage the total of the rows and columns for the current matrix, indicated by $GRDTOT_k = SUMC_i + SUMM_j$, where k=1,.......,n; is determined and then compared with previous one. If they are equal then the method is terminated i.e. it has reached its optimum and then they are the clusters which gives the groups. Otherwise it is repeated with same steps as above. **Fig. (1)** indicates the flow chart for the algorithm.

The algorithm can start with any form of a machine-component matrix since it is an iterative approach that will converge to the optimal solution in a finite number of iterations.

PRACTICAL APPLICATION

The algorithm then was programmed on a computer using data from a company so as to find the optimum number of g oups. The application uses (42) machines and (72) components, as shown in **Table (1)** below.

Table (1) Machine- Component Original Matrix

```
00000000000111111111122222222223333333333444444444455555555556666666
66666777
0012345678901234567890123456789012345678901234567890123456789012345
56789012
011                          1
0211  1  1 1 1     1 11       11  11            1    1    1
031
041                                1   1 1               1      1
051                     1
06 1  1    1 1                   1
07  1          1
08   1                 1 1                                   1
09    1                   1          1    1        1  11      1
10    1
11    1                           1  1                    1
12    11 1 111        1      1  1      1      1   1    11
13     1  1 1            1      11    1111 1 111 11
1
14      1                  11       1       1              1
15      1                  11       1       1              1
16        1
17        1   1 11       1                                  1
18        1              1               1            1
19        1    1       1                           1   1
20          1            1      1 1        1
21           1     1                               1
1
22            1 11  1                                       1
23                1
24                      1
25                      1
26                      1      1
27                      1
28                      1
29                      1
30                      1
31                        1               1           1       1
32                        1          1    1              11  1 11
33                               1
34                                 1   1
35                                                  1            1
1111111
36                                                  1
111111
37                                                  1
38                                                            1
39                                                             1
40                                                               1
41                                                               1
42                                                               1
```

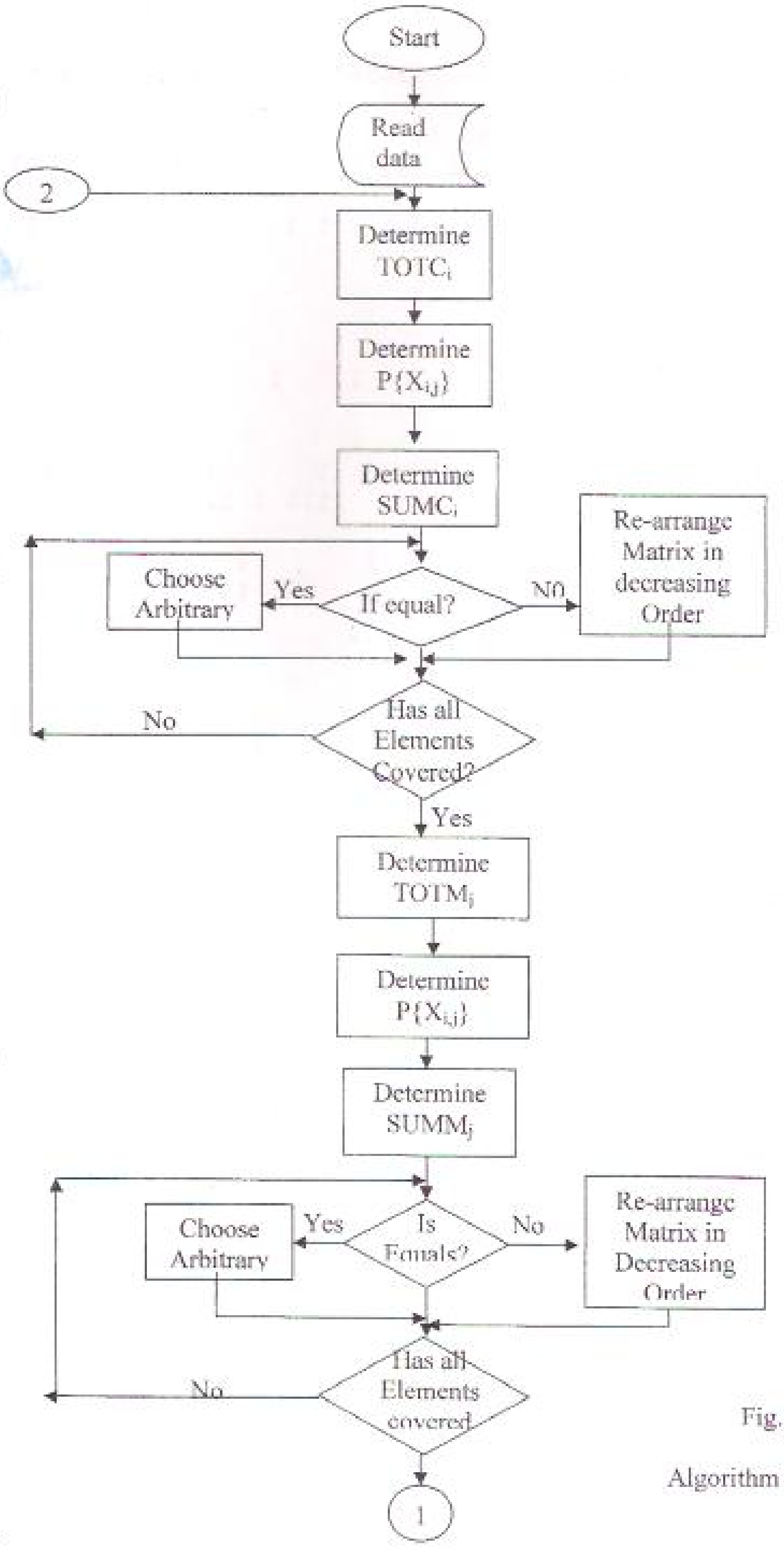

Fig. (1)

Algorithm Flowchart

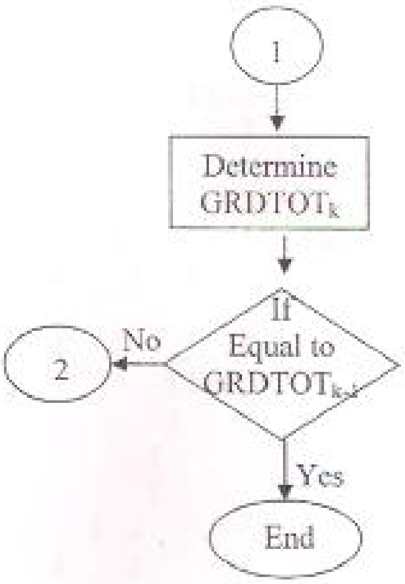

Fig. (1) continued

Then applying the algorithm produced, the result shown in Table (2).:

Table (2) The resulted matrix after the application of the algorithm

```
000301100235132245356422351304453524567246603344462156666776011150
10223451
001452028137800972863038241165956051312420297946852416789014435693
97675387
021111111111111111
0411              1111
051                   1
011                    1
031
06  1111                1
12  111 11        1    1
11  1     11
09  1
10  1
21   1      1
20        1
32         1       11
26           1        1
33           1
13                1  1  1
18                   1
24                    1
25                    1
27                    1
28                    1
29                    1
30                    1
34                      1
```

```
12                       1111111
11                              1
09                       1      111111
21                               1    1
20                        11           11
32                              1 11     11
13                        11111        11  1111111
18                                  1  1   1
34                              1
19                       1       1         1      11
31                                1111
38                                   1
35                                    1
42                                    1
08                                     1 1        1
17                                     1   1
39                                        1
16                                         1
07                                                 1
35                                                  1111111
08                                                          1
17                                                           1111
07                                                               1
36                                                  1111111
37                                                  1
40                                                         1
41                                                         1
22                                                           1111
1
14
111111
15
111111
23
1
```

EXCEPTIONAL ELEMENTS

There were many exceptional elements in the final matrix, and then a re-assignment was made to these elements. This has resulted in determining the group matrix as shown in **Table (3).** This group matrix contains three groups, without any exceptional parts.

Table (3) Groups after re-assignment

```
000301100235132245356422351304453524567246603344462156666776011150
10223451
001452028137800972863038241165956051312420297946852416789014435693
97675387
021111111111111111
0411              1111
051                   1
011                    1
031
06  1111                1
12  111 11        1    1
11  1     11
09  1
10  1
21   1      1
20        1
32         1       11
26           1        1
33           1
13                1  1  1
18                   1
24                    1
25                    1
27                    1
28                    1
29                    1
30                    1
34                      1

12                       1111111
11                              1
09                       1      111111
21                               1    1
20                        11           11
32                              1 11     11
13                        11111        11  1111111
18                                  1  1   1
34                              1
19                       1       1         1      11
31                                1111
38                                   1
35                                    1
42                                    1
08                                     1 1        1
17                                     1   1
39                                        1
16                                         1
07                                                 1
```

```
35   11111111
08           1
17            1111
07                1
36   1111111
37   1
40          1
41          1
22            1111
14           111111
15           111111
23                1
```

CONCLUSIONS

The method introduced in this study has simplified the calculation for the (0-1) matrix because of the use of probability which lead to the use of small numbers in calculations and therefore less time needed in the manupalation of the group matrix.

Also the introduced method is able easily to deal with a large number of components and machine without having to extend memory or splitting of matricies.

REFERENCES

Ballakur, A. and H.J. Steudel, (1987), A Within Cell Utilization Based Heuristic for Designing Cellular Manufacturing Systems, Int. J. Prod. Res., Vol. 33, No. 10.

Burbidge, J.L., (1971), Production Flow Analysis, Prod. Engr., Vol.50, No. 4.

Burbidge, J.L., (1975), The Introduction to GT, Heinemann, London, U.K.

Burbidge, J.L., and D.M. Zelenovic, (1983), Using Production Flow Analysis to plan Group Technology for a New Factory, Mater. Flow 1.

Chandrasekharan, M.P. and R. Rajagopalan, (1986), MODROC; An Extension of Rank Order Clustering for Group Technology, Int. J. Prod. Res., Vol. 24 No 5.

Chu, C.H. and J. Hayya, (1991), A Fuzzy Clustering Approach to Manufacturing Cell Formation, Int. J. Prod. Res., Vol. 29 No. 7.

Gallagher, J.L., T.J. Grayson, A. Philips; (1971), A Review of Development and Applications of Group Technology at the University of Birmingham, Int. J. Prod. Res., Vol. 9 No 9, 1971.

Gallagher, J.L., and W.A. Knight, 1973, Group Technology, Butterworth, UK.

Gallagher, C.C., and W.A. Knight, (1986), Group Technology Production Methods in Manufacturing, John Wiley and sons, USA.

Ham, I., K. Hitomi, and T. Yoshida, (1985), Group Technology Application to Production Management, Kluwer-Nijhoff Pub., USA.

Hunt, V.D., (1989), Computer Integrated Handbook, Chapman & Hill, U.S.A.

Kamrani, A.K., and R.P. Hamid, (1994), A Methodology for Design of Manufacturing Systems Using Group Technology, J. Prod. Planning and Control, Vol. 5, No. 5.

King, J.R., (1980), Machine-component Grouping Production Flow Analysis; an Approach Using Rank Order Clustering Algorithm, Int. J. Prod. Res., Vol. 18 No. 2.

King, J.R.' and V. Nakornchai, (1982), Machine-Component Group Formation in Group Technology: Review and Extension, Int. J. Prod. Res., Vol. 20 No. 2.

Loh, S. and G.D. Taylor, (1994), An Evaluation of Product Commonality and Group Technology Production Methods in a Pre-defined Multiple-machine Scenario, Prod. Planning and Control, Vol 5 No 6.

McAuley, J., (1972), Machine Grouping for Efficient Production, Prod. Engr.

Mosier, C.T., J. Yelle, and G. Walker, (1997), Survey of Similarity Coefficient Based Methods as Applied to the Group Technology Configuration Problem, Omega Int. J. Mgt. Sci., Vol. 25 No 1.

Narayanaswamy, P., C.R. Bector and D. Rajamani, (1996), Fuzzy Logic Concept Applied to Machine-Component Matrix Formation in Cellular Manufacturing, Europ. J. Op. Res., Vol 93.

Optiz, H. and H.P. Wiendahl, (1971), Group Technology and Manufacturing Systems for Small and Medium Quantity Production, Int. J. Prod. Res., Vol. 9 No 1.

Schafer, H., N.H. Darracot, C. O'Brien, and J.R. Wilson; (1992), The Consideration of Human Factors in the Design of Group Technology Manufacturing Systems, Proc. 2nd Int. FAIM Conf. Ed., Osama K. Eyada & M. Munir Ahmed, CRC Press Inc., Virinia, U.S.A.

Seifoddini, H. and C. Hsu, (1994), Comparative Study of Similarity Coefficient and Clustering Algorithm in Cellular Manufacturing, J. Manuf. Sys., Vol. 13 No. 2.

Seifoddini, H. and M. Djassemi, (1995), Merits of Production Volume Based Similarity Coefficient in Machine Cell Formation, J. Manuf. Sys., Vol. 14 No. 1.

Shafer, S.M., and D.F. Rogers, (1993), Similarity and Distance Measures for Cellular Manufacturing, Part I, A Survey, Int J. Prod. Res., Vol. 31, No. 5.

Shafer, S.M., and D.F. Rogers, (1993), Similarity and Distance Measures for Cellular Manufacturing, Part II, An Extension and Comparison, Int. J. Prod. Res., Vol. 31, No. 5.

Srinivasan G. and T.T. Narendran, (1991), GRAFICS: A Non Hierarchical Clustering Algorithm for Group Technology, Int J. Prod. Res., Vol. 29 No 3.

Tsai, C.C., C.H. Chu and T.A. Batra, (1997), Modeling and Analysis of a Manufacturing Cell Formation Problem with Fuzzy Mixed-integer Programming, IIE Trans., Vol. 29 No. 7.

Xu, H. and H. Wang, (1989), Part Family Formation for GT Application Based on Fuzzy Mathematics, Int. J. Prod. Res., Vol 27 No 9.

Zhung, C. and H.P. Wang, (1991), Formation of Machine Cells: A Fuzzy Set Approach, CAD/CAM Robotic and Factories of the Future 90, Volume 1, Ed. Dwivedi. S.N., A. K. Verma, and J.E. Snekenberger, Springer Verlag, USA.

EXPERIMENTAL INVESTIGATION OF LAMINAR MIXED CONVECTION IN AN INCLINED ANNULUS

Prof. Dr. Khalid A. Ismael
Mech. Engr. Dept.
University of Technology
Baghdad-Iraq

Asst. Prof. Dr. Ihsan Y. Hussain
Mech. Engr. Dept.
College of Engr.
University of Baghdad
Baghdad-Iraq

Asst. Lecturer Akeel A. Mohammed
Mech. Engr. Dept.
University of Technology
Baghdad-Iraq

ABSTRACT

Experiments were carried out to study the local and average heat transfer by mixed convection to a simultaneously developing air flow in a horizontal , inclined, and vertical concentric cylindrical annulus. The experimental setup consists of an annulus has a radius ratio of 0.555 and inner cylinder with a heated length 1.2m subjected to the constant heat flux while the outer cylinder is subjected to the ambient temperature. The investigation covers Reynolds number range from 154 to 845, heat flux varied from 96 W/m^2 to 845 W/m^2, and annulus angles of inclinations α =0° (horizontal), 40°, 70°, and 90° (vertical). Results demonstrate the temperature variation along the inner cylinder surface and the local Nusselt number Nu_z variation with the dimensionless axial distance , for all angles of inclinations which shows an increase in the Nu_z values as the heat flux increases and as the angle of the inclination moves from the vertical to the horizontal position.

الخلاصة

أجريتْ تجارب عملية لدراسة انتقال الحرارة الموقعي و المعدّل بالحمل المختلط لجريان الهواء المشكّـل تراكبياً (أي تزامن التشكيل الحراري مع التشكيل الهيدروديناميكي) بتجويف حلقي بين اسطوانتين متحدي المركز، نسبة نصف القطر لهما تعادل 0.555 و بطول 1.2 m ، بالوضع الأفقي، المائل، و العمودي. سخنت الاسطوانة الداخلية تحت فيض حراري ثابت ، بينما عرّضت الاسطوانة الخارجية إلى درجة حرارة الجو. يتراوح معدّل رقم رينولدز Re في هذا البحث من 154 إلى 845 أما الفيض الحراري فيتغير من 96 W/m^2 إلى 860 W/m^2 ، و زوايا ميل التجويف الحلقي هي 0° (أفقي)، 40° ، 70° ، 90° (عمودي). . وضحت النتائج العملية تغير درجة حرارة الأسطوانة الداخلية مع الاتجاه الطولي و كذلك تغير رقم نسلت الموقعي مع المسافة المحورية الغير بعدية ، حيث أظهرت النتائج زيادة رقم نسلت مع زيادة الفيض الحراري و مع انحراف زاوية الميل من الوضع العمودي إلى الوضع الأفقي.

KEY WORDS

Heat Transfer, Mixed Convection, Concentric Annulus

INTRODUCTION

Laminar flow heat transfer in annuli is encountered in a wide variety of engineering situations, including the barrel- type expitaxial reactor (chemical vapor deposition reactor) in the semi conductor manufacturing industry (Hanzwa 1986), heat exchangers designed for viscous liquids in chemical process and food industries (Hessami 1987), the cooling of electrical cables, the collection of solar energy (Ciampi 1987), etc. In many of these applications, flow through the annular passage is characterized by small Reynolds numbers for which buoyancy effects may be significant. Even though such applications are now being used widely, there is a lack of understanding of many details of laminar flow and heat transfer physics concepts. The difficulties with laminar flows are associated with the fact that fluids which in practice are in this flow regime usually have properties which are strongly dependent on temperature. As a result, to cover this lack, the present study is motivated and concerned with the experimental investigation of laminar mixed convection in the thermal and hydrodynamic entrance region of concentric annulus with uniformly heated inner cylinder, and outer cylinder subjected to ambient.

Many experimental and theoretical investigations have been conducted to study the effect of free convection on laminar flow inside horizontal, inclined, and vertical annulus.- (Lundberg, et-al 1962). studied experimentally and theoretically the mixed convection of simultaneously developing laminar upward air flow in a vertical annulus. The experimental study included four annulus radius ratios (0.132, 0.25, 0.375, and 0.5).The thermal condition of the inner wall was isothermal and the outer wall was adiabatic, while Re varied from 800 to 1500. Variation of the inner surface temperature and the heat transfer coefficient along annulus were depicted. While the theoretical study included evaluation of the four fundamental solutions in the thermal energy regions by solution of the eigen value problem.

(Hanzawa, ét-al 1986), performed experiments to study the mixed convection of upward gas flow in a vertical annulus of radius ratio range from 0.39 to 0.63 and hydraulic diameter to heating section length range from 0.34 to 1.4 . A part of the inner tube was isothermally heated while the outer tube was kept adiabatic. Study covered Gr range from 1.5×10^5 to 2.6×10^8 , Re range from 20 to 100. The effects of operating conditions on the temperature profiles, flow pattern and heat transfer coefficient were investigated. (Falah & Yaseen 1993) performed experiments to study the local and average heat transfer by mixed convection to a simultaneously developing upward air flow in a vertical , inclined and horizontal concentric cylindrical annulus with a radius ratio of 0.41 and the inner cylinder with a heated length of 0.85 m was subjected to the ambient temperature. The investigation has covered Re range from 300 to 1200, heat flux varied from 90 W/m^2 to 680 W/m^2 and annulus angle of inclination 0°(vertical), 30°, 45°, 60° , and 90° (horizontal). The results show that the heat transfer process improves as the angle of inclination deviates from the vertical to the horizontal position.

EXPERIMENTAL APPARATUS

An open air circuit was used which included a compressor (B) , orifice plate section (C), settling chamber (D), test section and a flexible hose (E). The air which is driven by compressor can be regulated accurately by using two control valves, as shown diagrammatically in **Fig. (1)**. The air induced by the compressor , enters the orifice pipe section (Standard British Unit) and then settling chamber through a flexible hose (E). The settling chamber was carefully designed to reduce the flow fluctuation and to get a uniform flow at the test section entrance by using flow straightener (G). The air then passed through 1.2 m long test section. A symmetric flow and a uniform velocity profile produced by a well design Teflon bell mouth (H) which is fitted at the annulus outer aluminum cylinder (I) and bolted inside the settling chamber (D). The inlet air temperature was measured by one thermocouple (J) located in the settling chamber (D) while the outlet bulk air temperature was measured by three thermocouples (Z) located in the test section exit. The local bulk air temperature was calculated by using a straight line interpolation between the measured inlet and outlet bulk air temperature.

The test section consisted of 4 mm wall thickness, 50 mm outside diameter and 1.2 m long aluminum cylinder (K) located centrally in 5 mm thickness , 90 mm inside diameter and 1.2 m long aluminum cylinder, by fitting it at the test section inlet with the 20 mm inside diameter , 50 mm outside diameter and 15 mm long Teflon tube (N) and at the test section exit with the teflon piece (M). A ring (P) is used to hold and support the aluminum cylinder (K) with the teflon piece (N) centrally inside the settling chamber by adjustable screws (Q). The teflon was chosen because of its low thermal conductivity in order to reduce the heat loss from the aluminum cylinder ends.

The inner cylinder was heated electrically using an electrical heater which consists of a nickel-chrome wire ®, wound as a coil spirals around solid teflon tube and is covered by a 2 mm thickness asbestos layer , and the space between the asbestos and the inner cylinder wall is fitted with a fine grade sand to avoid heat convection in it and to smooth out any irregularities in the heat flux. The hole apparatus is designed with a view to obtain a good concentricity of the core cylinder and the containing cylinder. The temperature of the outside surface of the inner cylinder was measured by seventeen asbestos sheath alumel-chromel (type K) thermocouples , arranged along the cylinder , the measuring heads of the thermocouples were made by fusing together the ends of two wires.

The thermocouples were fixed by drilling holes of 1.5 mm diameter in the cylinder wall and the ends of the holes chamfered by a 3 mm slug to locate the measuring junctions which were then fixed by a high temperature application Defcon adhesive . The excess adhesive was removed and the cylinder outer surface was cleaned carefully by fine grinding paper. All the thermocouples wires and heater terminals were taken out the test section through both teflon pieces (N,M) .

On the other hand , there were twelve thermocouples placed in three sections along the inner cylinder of the annulus (at z=1 cm, 53 cm, 108 cm) , four for each section arranged at angle ($\phi=0^\circ, 90^\circ, 180^\circ, 270^\circ$) around the inner cylinder. Other ten thermocouples were (type K) used to measure the inner surface temperature of the annulus outer cylinder (I). Thermocouples positions at the outer surface were located and then a 2 mm deep pits were drilled in which the thermocouples were fixed by Defcon adhesive. All thermocouples were used with leads , the thermocouple with lead and without lead were calibrated against the melting point of ice made from distilled water and the boiling points of several pure chemical substances. To determine the heat loss from the test section ends, two thermocouples were fixed in each teflon piece. The distance between these thermocouple was 12 mm. Knowing the thermal conductivity of the teflon , the ends condition could thus be calculated.

EXPERIMENTAL PROCEDURE

To carry out an experiment the following procedure was followed:

1- The inclination angle of the annulus was adjusted as required.
2- The compressor was then switched on to circulate the air , through the open loop. A regulating valves were used for adjusting the required mass flow rate.
3- The electrical heater was switched on and the heater input power then adjusted to give the required heat flux.
4- The apparatus was left at least three hours to establish steady state condition. The thermocouples readings were measured every half an hour by means of the digital electronic multimeter until the reading became constant , a final reading was recorded. The input power to the heater could be increased to cover another run in a shorter period of time and to obtain steady state conditions for next heat flux and same Reynolds number. Subsequent runs for other Reynolds number and annulus inclination angle ranges were performed in the same previous procedure.
5- During each test run , the following readings were recorded:

a- The angle of inclination of the annulus in degree.
b- The reading of the manometer (air flow rate) in mm H_2o.
c- The readings of the thermocouples in °C.
d- The heater current in amperes.

e- The heater voltage in volts.

DATA ANALYSIS

Simplified steps were used to analyze the heat transfer process for the air flow in an annulus where the inner cylinder was subjected to a uniform heat flux while the outer cylinder was subjected to the ambient temperature. The total input power supplied to the inner cylinder can be calculated:

$$Q_t = V'' \times I \qquad (1)$$

The convection and radiation heat transferred from the inner cylinder is :

$$Q_{cr} = Q_t - Q_{cond} \qquad (2)$$

where Q_{cond} is the conduction heat loss which was found experimentally equal to 3 % of the input power. The convection and radiation heat flux can be represented by:

$$q_{cr} = Q/A_1 \qquad (3)$$

where ($A_1 = 2\pi\, r_1\, L$)

The convection heat flux , which is used to calculate the local heat transfer coefficient is obtained after deduce the radiation heat flux from q_{cr} value. The local radiation heat flux can be calculated as follows:

$$q_r = F_{1-2}\, \varepsilon\, \sigma \left[\left((t_s)_z + 273 \right)^4 - \left(\overline{(t_{s2})_z} + 273 \right)^4 \right] \qquad (4)$$

where:

F_{1-2}= view factor between inner and outer cylinder ≈1

$(t_s)_z$ = local temperature of inner cylinder.

$\overline{(t_{s2})_z}$ = average temperature of outer cylinder.

ε = emissivity of the polished aluminum surface=0.09.

Hence the convection heat flux at any position is:

$$q = q_{cr} - q_r \qquad (5)$$

The local heat transfer coefficient can be obtained as:

$$h_z = \frac{q}{(t_s)_z - (t_b)_z} \qquad (6)$$

$(t_b)_z$ = Local bulk air temperature.

All the air properties were evaluated at the mean film air temperature (Keys 1966):

$$(t_f)_z = \frac{(t_s)_z + (t_b)_z}{2} \qquad (7)$$

t_f = Local mean film air temperature.

The local Nusselt number (Nu_z) then can be determine as:

$$Nu_z = \frac{h_z \quad D_h}{K} \tag{8}$$

The average values of Nusselt number Nu_m can be calculated based on calculation of average inner surface temperature and average bulk air temperature as follows:

$$\overline{t_s} = \frac{1}{L}\int_{z=0}^{z=L} (t_s)_z \quad dz \tag{9}$$

$$\overline{t_b} = \frac{1}{L}\int_{z=0}^{z=L} (t_b)_z \quad dz \tag{10}$$

$$\overline{t_f} = \frac{\overline{t_z} + \overline{t_b}}{2} \tag{11}$$

$$Nu_m = \frac{q \quad D_h}{k(\overline{t_z} - \overline{t_b})} \tag{12}$$

The average values of the other parameters can be calculated as:

$$Re_m = \frac{\rho \quad u_i \quad D_h}{\mu} \tag{13}$$

$$Gr_m = \frac{g \quad \beta \quad D_h^{\,3} \quad \left(\overline{t_z} - \overline{t_b}\right)}{\nu^2} \tag{14}$$

$$Pr_m = \frac{\mu \quad C_p}{k} \tag{15}$$

$$Ra_m = Gr_m \, . \, Pr_m \tag{16}$$

where:

$\beta = 1/\left(273 + \overline{t_f}\right)$

$u_i = \dot{m}/\rho A$

$A = \pi \quad \left(r_2^{\,2} - r_1^{\,2}\right)$

All the air physical properties ρ, μ, ν, and k were evaluated at the average mean film temperature ($\overline{t_f}$).

EXPERIMENTAL RESULTS

Range of Experiments

A total of 46 test runs carried out to cover annulus inclination angles, horizontal (α=0°), inclined (α=40° and 70°) and vertical (α=90°). The range of heat flux 96 W/m^2 to 860 W/m^2 and Reynolds number varied from 154 to 845.

Temperature Variation

The temperature variation in the horizontal position is plotted for selected runs in **Figs. (2)** and **Fig. (3)**. The variation of the surface temperature along inner cylinder for different heat flux and for approximately Re=218 is shown in **Fig. (2)**. It is obvious that the surface temperature increases at the stage of entrance and attains a maximum point after which the surface temperature begins to decrease at high heat flux and be almost constant for very small heat flux. The rate of surface temperature rises at early stage is directly proportional to the wall heat flux. The point of maximum temperature seems to move toward the annulus entrance as the heat flux increases. This can be attributed to the increasing of the thermal boundary layer faster due to buoyancy effect as the heat flux increases at the same Reynolds number.

Fig. (3) shows the effect of Reynolds number variation on the inner cylinder surface temperature for heat flux (q=682 W/m^2). It can be noticed that, the increasing of Reynolds number reduces the surface temperature as heat flux kept constant and the surface temperature values at entrance and at the same axial distance seem to be closer to each other then diverges downstream. This can be attributed to poverty of natural convection at annulus entrance and high mixing cup downstream.

The variations of surface temperature along the axis of vertical annulus for different Reynolds number and heat flux equals to 265 W/m^2 and for different heat flux and Reynolds number equals to 724 are shown in **Fig. (4)** & **Fig. (5)**, respectively. The effect of heat flux and Reynolds number on the inner cylinder temperature variation is the same as that obtained in the horizontal and inclined positions.

The extent of mixed convection depends on the relative magnitude of the heat flux and Reynolds number for the same angle of inclination. When heat flux and Reynolds number are kept constant, the extent of local mixing due to the buoyancy effect in a horizontal annulus is larger than other annulus angle of inclination. It can be expected that for the same condition of flow rate and input heat flux, the inner surface temperature variation along the annulus decreases as the angle of inclination changes from vertical to horizontal position.

Angle of Inclination Effect on the Temperature Distribution

The effect of inclination angle on the inner cylinder temperature variation for q=680 W/m^2 and Re=300 is shown in **Fig. (6)**. Figure shows a reduction in surface temperature as the annulus angle of inclination changes from vertical to horizontal position. This reduction slightly reverses downstream if the angle position changes from 0^o (horizontal) to 40^o and Reynolds number increases to 724 because of dominant forced convection in the heat transfer process as shown in **Fig. (7)**.

This behavior entirely reverses if the Reynolds number increases to 845 at the same heat flux as shown in **Fig. (8)**. The temperature variation along the surface at the same axial distance is approximately the same for α=70^o and 90^o (vertical), and slightly decreases upstream and reverses downstream as angle of inclination changes from 0^o (horizontal) to 40^o. The final behavior can be explained as follows: at annulus entrance, the effect of free convection is small and a predominant forced convection causes the surface temperature of the 70^o and 90^o (vertical) angle of inclination less than that of 0^o (horizontal) and 40^o angle of inclination, after a certain axial distance a significant reduction in the inner surface temperature as the inclination angle changes from 0^o to 40^o due to the free convection begins to dominant flow mixing which reduces the inner surface temperature. This behavior leads to the following conclusion that the heat transfer process improves as the angle of inclination varied from horizontal to vertical when Reynolds number is enough high because of the dominant forced convection in the heat transfer process and vice versa at low Reynolds number case. The increasing of heat flux decreases forced convection effect and the natural convection will be the dominant factor in the heat transfer process.

Local Nusselt Number (Nu_z)

The effect of heat flux on the Nu_z in the horizontal position for Re=218 is shown in **Fig. (9)**. It is clear that the results of higher heat flux for Nu_z were higher than that of lower heat flux. Figure shows also sharp decrease for the local Nusselt number values at the entrance of the annulus then become almost constant downstream for low heat flux (q=96 W/m^2) and increases as heat flux increases. This attributes to increase in both the thermal boundary layer thickness and the surface to bulk air temperature difference which accompany with an increase in the surface heat flux and that accelerate the development of secondary flow downstream.

The effects of Re on Nu_z variation with ZZ is shown in **Fig. (10)** for heat flux equal to 679 W/m^2 : respectively. For constant heat flux, results depicted that the deviation of Nu_z value moves towards the left and increases as the Reynolds number increases. This is obvious from inverse Graetz number (ZZ) which decreases as the Re increases. This situation reveals the domination of forced convection on the heat transfer process with a little effect of buoyancy force at high Re. As the Re reduces the buoyancy effect expected higher which improve the heat transfer process. The minimum value of the Nu_z increases as Re increases then the value of Nu_z increases further downstream for all curves due to strong natural convection in this region.

In horizontal annulus, the effect of the secondary flow is high, hence at low Reynolds number and high heat flux, situation makes the free convection predominant, since as the heat flux increases, the fluid near the heated wall becomes warmer and lighter than the bulk fluid in the annular gap core towards the outer wall. As a sequence, two upward currents for each side of the vertical plane flow along the heated side wall, and by continuity, the fluid near the outer wall of the annulus flow downward. This sets up two longitudinal vortices, which are symmetrical about a vertical plane .

As heat flux further increases the structure of the cellular motion changes from one-cell on each side of the annulus to two and gradually into a multi-cell structure. It is expected that the intensity of vortex increases downstream. The longitudinal vortex (or, in another express, the cellular motion) behaves so as to reduce the temperature difference between the heated inner cylinder surface and the air flow in which led to increasing the growth of the hydrodynamic and thermal boundary layer along the heated cylinder and causes an improvement in the heat transfer coefficient. At low heat flux and high Reynolds number the situation makes forced convection predominant and vortex strength decreases which decrease the temperature difference between the heated surface and the air, hence, the Nu_z values become close to the vertical cylinder values for the same conditions as be seen later.

The variation of the local Nusselt number with ZZ in the vertical position for Re=724 and various heat flux is shown in **Fig.(11)**. Curves depicted have the same general shape shown in **Fig. (9)**. The effect of Re on Nu_z for q=382 W/m^2 and the same position is shown in **Fig. (12)**. Results reveal that the effect of heat flux and Reynolds number on heat transfer coefficient in vertical position gives a similar trend as obtained for horizontal position.

Angle of Inclination Effect on Nu_z

Results for q=680 W/m^2 and Re=300, 724, and 845 are shown in **Fig. (13)**, **Fig. (14)**, and **Fig. (15)**; respectively. It is noticed from the first two figures that at the same axial distance the local Nusselt number value increases as the angle of inclination deviates from the vertical to the horizontal position. As explained before that with the free convection domination, for horizontal position creates upward airflow along the inner heated cylinder surface to form vortices having their center in the annulus upper part with the very complicated flow pattern and with the vortex intensity reduces as the angle of inclination change from horizontal to vertical position leading to increase the extent of the local mixing along the annulus due to high vortices intensity. As a result , the heat transfer process improves as angle of inclination deviates from vertical to horizontal position.

Other reverse situation will be obtained if the Reynolds number increases to 845 at the same heat flux as shown in **Fig. (15)**. For the same ZZ the Nu_z value increases gradually as the inclination

angle deviates from the horizontal to the vertical position. This behavior continues till a certain ZZ value (0.0105) where beyond it the Nu_z value becomes more closer to each other, and gives approximately equal value for each α=[0° (horizontal) and 40°] and α=[70° and 90° (vertical)].
In general, this situation relates to the small buoyancy effect at annulus entrance and a pure forced convection is dominant heat transfer process. Downstream, the secondary flow becomes more effective which improves the flow mixing and improves the heat transfer process which appears to be higher in the horizontal position and it's effect reduces as the annulus position deviates towards vertical position. As a result, the Nu_z value becomes closer to each other at this region at the same ZZ.
Fig. (16) and **Fig. (17)** show the effect of angle of inclination on the heat transfer processes for q=265 W/m^2, Re=154 and 378; respectively. **Fig. (17)** gives the same behavior that obtained in **Fig. (14)**, but the problem is in **Fig. (16)** which at the early sight may causes a distortion in a physics concepts that concluded from the previous figures of the local Nusselt number. Hence, if the light is perfectly focused on this natural behavior, the problem will be entirely understood. In this figure, in spite of low Reynolds number the local Nusselt number value at the entrance for the same ZZ increases gradually as the inclination angle deviates from the horizontal to the vertical position, then becomes closer to each other in the region bounded between semi-logarithmic value of ZZ=0.1 and 0.109, then a reverse situation occurs further downstream, and the Nu_z value becomes higher as the angle of inclination deviates from the vertical to the horizontal position.
This situation may be expected to occur due to a reverse flow existence at the entrance in α=40°, 70°, and 90° (vertical) due to high heat flux relative to Reynolds number creates a distortion in flow pattern and makes the air particals reverse near the heated wall due to very low density if comparison with these in the annular gap. The reverse flow enhance the heat transfer process and gives high Nu_z value. Further downstream the natural convection in horizontal and inclined positions will be stronger in that of vertical position leads to improve of heat transfer process in this positions greater than vertical position.

Correlation of Average Heat Transfer Data

The values of the Nu_m for horizontal (α=0°), inclined (α=40°, 70°), and vertical (α=90°) positions are plotted in **Figs. (18–21)** in the form of log(Nu_m) against log(Ra/Re) for the range of Re from 154 to 845, and Ra from 0.4767×10^5 to 1.3261×10^5. All the points as can be seen are represented by a straight lines of the following equations:

α=0° (horizontal) $$Nu_m=259.402\,(Ra/Re)^{-0.389} \quad (17)$$

α=40° $$Nu_m=265.199\,(Ra/Re)^{-0.40147} \quad (18)$$

α=70° $$Nu_m=326.960\,(Ra/Re)^{-0.413693} \quad (19)$$

α=90° (vertical) $$Nu_m=476.150\,(Ra/Re)^{-0.50374} \quad (20)$$

It was shown that the heat transfer equations for all the positions have the same following form:

$$Nu_m= a\,(Ra/Re)^{d} \quad (21)$$

Where a and d are given in **Table (1)**
The values of d which represent the slope of each curve decrease as the inclination angle deviates from horizontal to vertical position due to decreasing of the buoyancy effect.

The general equation that described the heat transfer process for a selected Re range from 154 to 845 and Ra range from 0.4767×10^5 to 1.3261×10^5 and inclination angle range from 40^o to 90^o (vertical) was derived in the following form:

$$(Nu_m)_{inc.} = 32.371\,(Ra)^{-0.389}.(Re)^{0.655}.[\sin(\alpha)]^{-2.70108} \qquad (22)$$

The values of measured Nu_m are compared with that of Nu_m calculated from eq.(22) as shown in Fig.22 which are represented by the solid line. The dashed upper and lower lines represent the maximum and minimum acceptable deviation between them which equal to ±15.3 %.

CONCLUSIONS

1- The variation of the surface temperature along the inner cylinder at all angles of inclinations is affected by the extent of the local mixing which increases as the heat flux increases, Re decreases and annulus orientation deviates from vertical to horizontal. The increase of local mixing causes an improvement in the local heat transfer process and reducing the heated surface temperature.

2- The variation of Nu_z with ZZ at any angle of inclination was affected by many variables summarized in the following points:

a- For the same Re and annulus orientation, the Nu_z increases with heat flux.

b- For the same heat flux and annulus orientation, the heat transfer process is dominated by:

i- Forced convection as Re increases and becomes relatively high if comparison with the applied heat flux.

ii- Natural convection as Re decreases and becomes low relatively if comparison with the applied heat flux.

c. For the same heat flux & Re , the Nu_z value decreases as cylinder position changes from horizontal towards vertical (i.e., the minimum value occurs in the vertical position and the maximum value occurs in the horizontal position).

3. The effect of buoyancy is small at the annulus entrance and increases in the flow direction.

REFERENCES

Ciampi, M., Faggiani, S., Grassai, W. and Incropera,F. P., (1986), Experimental study of mixed convection in horizontal annuli for low Reynolds numbers, Proceedings of the 8th Int. Heat Transfer Conference , München, Fed. Rep. of Germany Vol. 3 , pp. 1413-1418,.

Ciampi, M., Faggiani, S., Grassai,W. and Tuoni, G., (1987), Mixed convection heat transfer in horizontal, concentric annuli for transitional flow conditions, Int. J. Heat Mass Transfer, Vol. 30, No. 5, pp. 833-841,.

El-Shaarawi, M. A. I. and Sarhan , (1980), Combined free and forced convection laminar flow in a vertical concentric annuli, J. Heat Transfer , Vol. 102 , pp. 617-622,.

Falah, (1993), Combined free and forced convection in an inclination annulus, Thesis, University of Basra, College of Engineering, Mechanical Department,.

Grimson, J. , (1971), Advance fluid dynamics and heat transfer , Mc Graw-Hill , England ,.

Hanzawa, T. , Sako, A. , Endo, H. , Kagwa, M. , and Koto, K. , (1986), Combined free and forced laminar convective heat transfer from isothermally heated inner tube in vertical concentric annulus, J. Chemical Engineering of Japan ,Vol. 19 ,No. 1, pp. 78- 81 ,.

Hessami, M. A. , De Vahl Davis, G., Leonardi, E. and Reizes, J. A. , (1987), Mixed convection in vertical , cylindrical annuli , Int. J. Heat Mass Transfer , Vol.30, No.1 , pp. 151-164 , January ,.

Kays, W. M., (1966), Convective Heat transfer, Mc Graw-hill , New York,.

Lundberg, R. E. , Reynolds, W. C. and Mc Cuen, P. A. , (1962), Heat transfer in annular passages . General formulation of the problem for arbitrary wall temperature or heat fluxes, Int. J. Heat Mass transfer , Vol.6 , pp. 438-439 ,.

Milano, G. and Guglielmini, G. , (1988), Mixed convection of air in internally heated vertical concentric annuli, Proceedings of the 8^{th} Int. Heat Transfer Conference , München, Fed. Rep. of Germany, Vol.3 , pp. 1041-1056,.

NOMENCLATURE

A : annular gap area; m^2
A_1: inner cylinder surface area; m^2
D_h: hydraulic diameter=$2(r_2-r_1)$: m
I: current; Amp
κ : thermal conductivity; $W/m^2.°C$
L: annulus length; m
$\dot{m}$: volumetric flow rate; m^3/s
$(Nu_m)_{inc.}$: mean Nusselt number at any angle of inclination
Q: convection heat loss; W
Q_t: total heat given; W
Q_{cr}: convection- radiation heat loss; W
q_r: radiation heat flux; $W/m^2.°C$
q: convection heat flux; $W/m^2.°C$
r_1: outer radius of inner cylinder; m
r_2: inner radius of outer cylinder; m
V": voltage; volt

Table (1) Constants in Eq.(21) for Various Angles of Inclination.

α	a	d
0^o (horizontal)	259.402	–0.389
40^o	265.199	–0.40147
70^o	326.96	–0.413693
90^o (vertical)	476.15	–0.50374

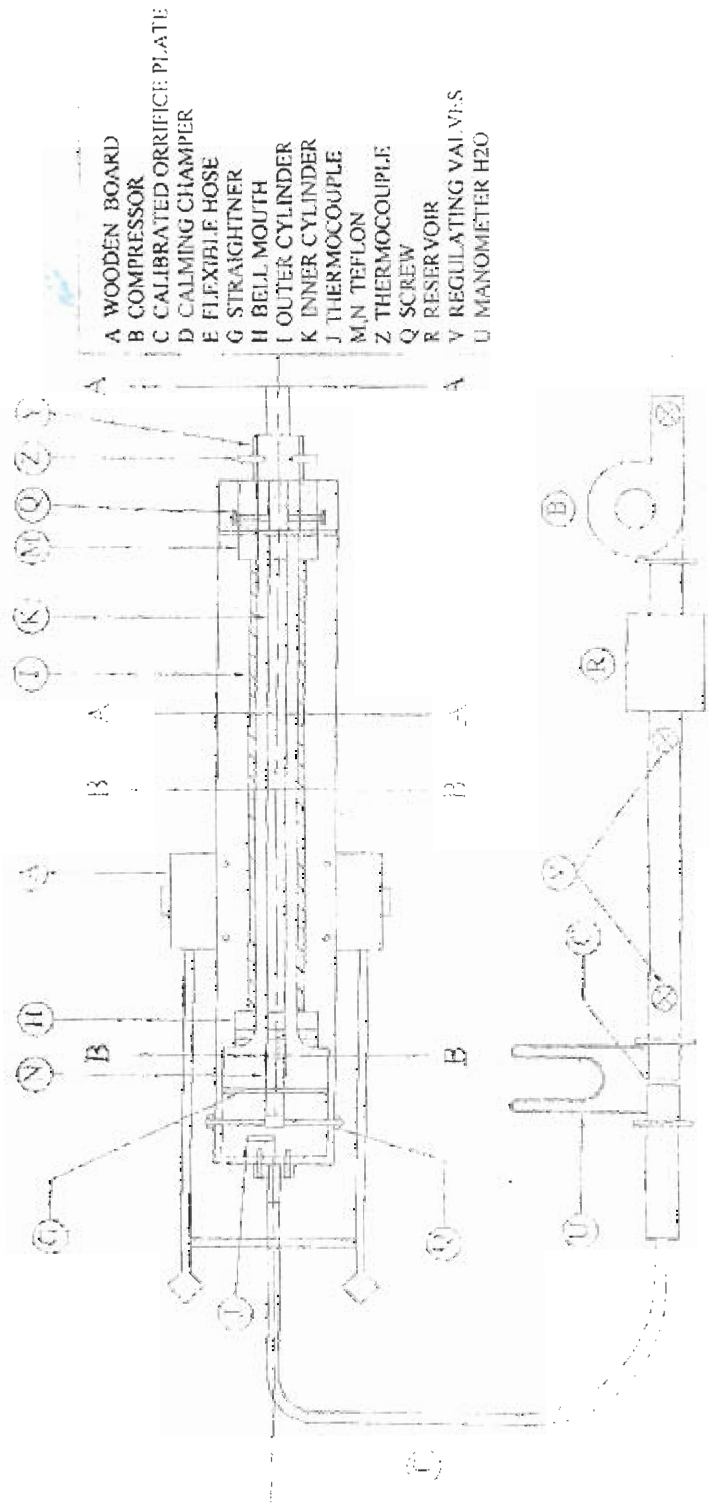

Fig.(1) Diagram of Experimental Apparatus.

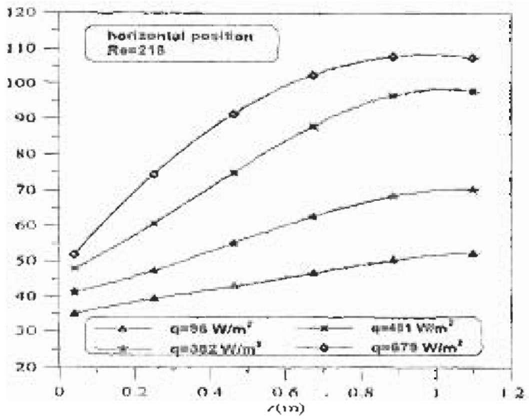

Fig.(2) Variation of the Surface Temperature with the Axial Distance,
Re=218, α =0° (Horizontal) .

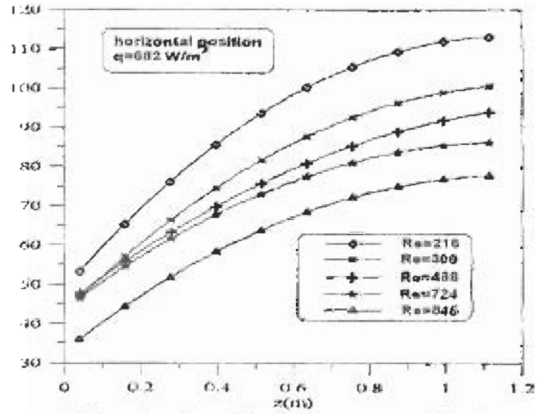

Fig.(3) Variation of the Surface Temperature with the Axial Distance,
q=682 W/m^2, α =0° (Horizontal).

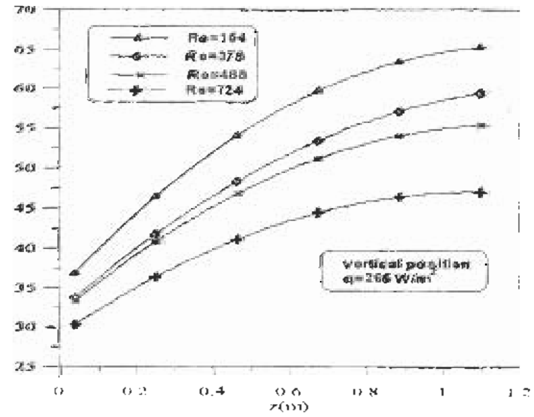

Fig.(4) Variation of the Surface Temperature with the Axial Distance,
q=265 W/m^2, α =90° (Vertical).

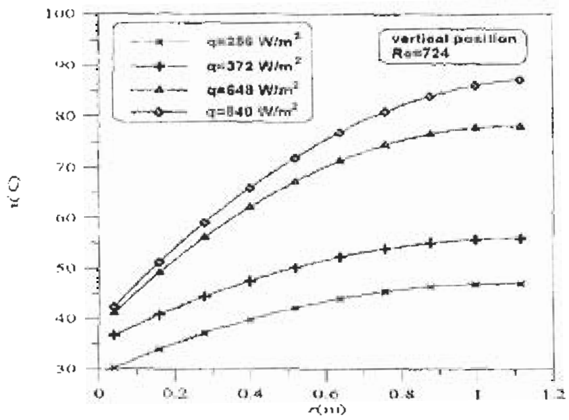

Fig.(5) Variation of the Surface Temperature with the Axial Distance,
Re=724, α =90° (Vertical).

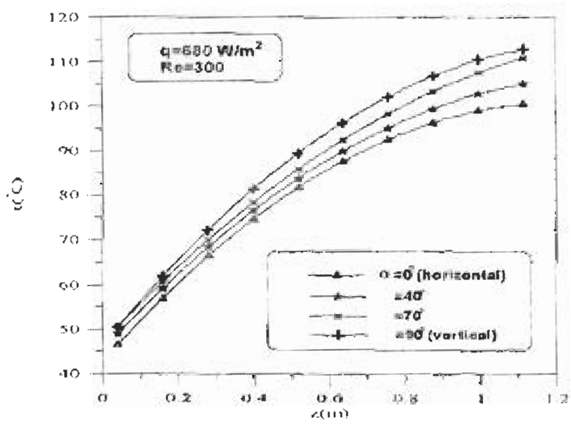

Fig.(6) Variation of the Surface Temperature with the Axial Distance for Various Angles, q=680 W/m^2, Re=300.

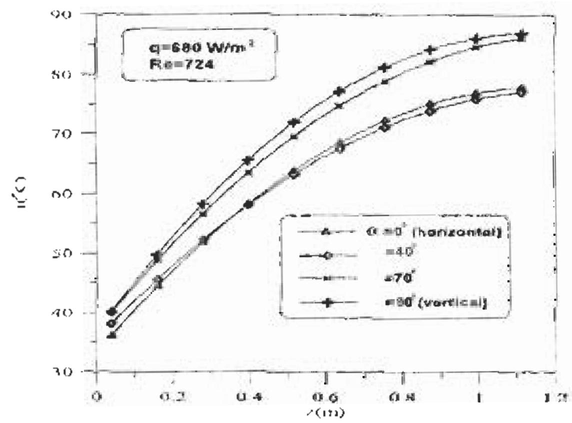

Fig.(7) Variation of the Surface Temperature with the Axial Distance for Various Angles,
q=680 W/m^2, Re=724.

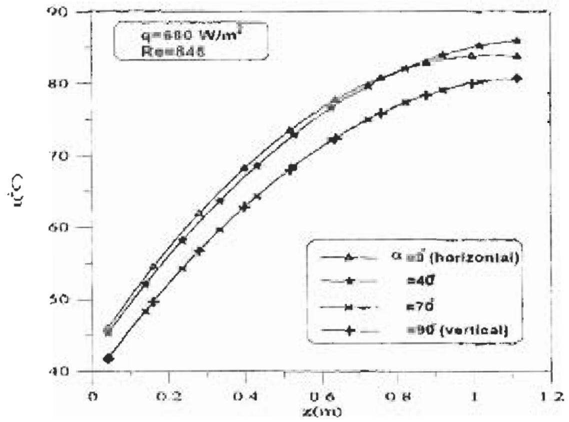

Fig.(8)Variation of the Surface Temperature with the Axial Distance for Various Angles, $q=680\ W/m^2$, Re=845.

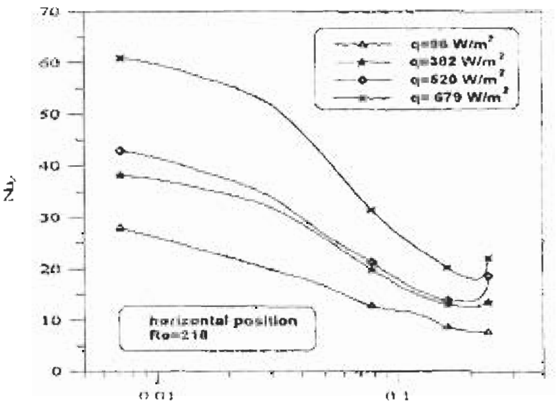

Fig.(9) Local Nusselt Number Versus Dimensionless Axial Distance, Re=218, $\alpha=0^{\circ}$ (Horizontal).

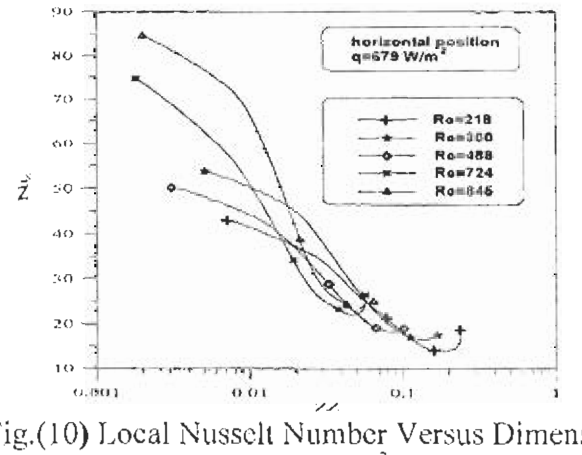

Fig.(10) Local Nusselt Number Versus Dimensionless Axial Distance, $q=679\ W/m^2$, $\alpha=0^{\circ}$ (Horizontal).

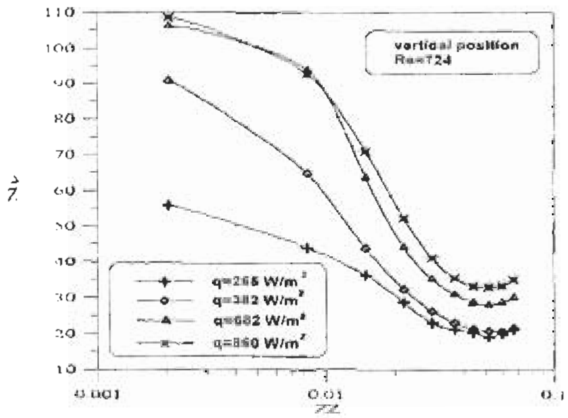

Fig.(11) Local Nusselt Number Versus Dimensionless Axial Distance, Re=724, α=90° (Vertical).

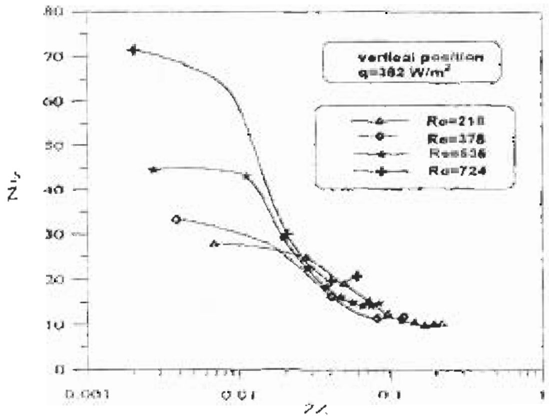

Fig.(12)Local Nusselt Number Versus Dimensionless Axial Distance, q=382 W/m^2, α=90° (Vertical).

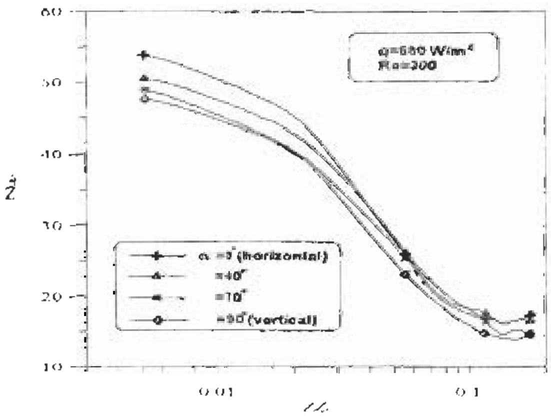

Fig.(13) Local Nusselt Number Versus Dimensionless Axial Distance for Various Angles, q=680 W/m^2, Re=300.

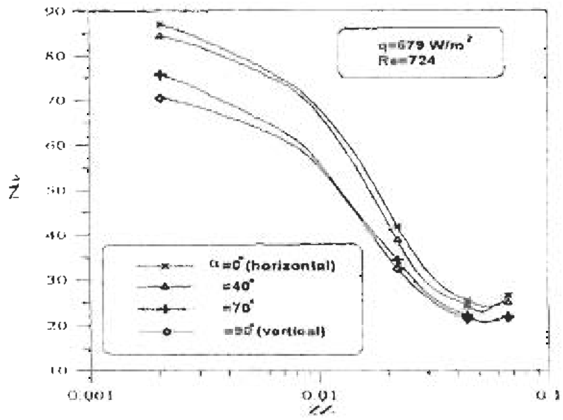

Fig.(14) Local Nusselt Number Versus Dimensionless Axial Distance for Various Angles, q=679 W/m^2, Re=724.

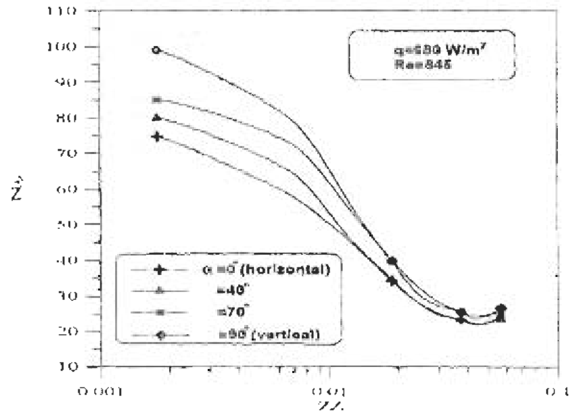

Fig.(15) Local Nusselt Number Versus Dimensionless Axial Distance for Various Angles, q=680 W/m^2, Re=845.

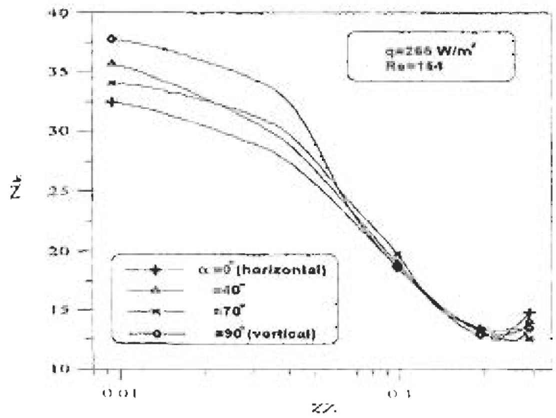

Fig.(16) Local Nusselt Number Versus Dimensionless Axial Distance for Various Angles, q=265 W/m^2, Re=154.

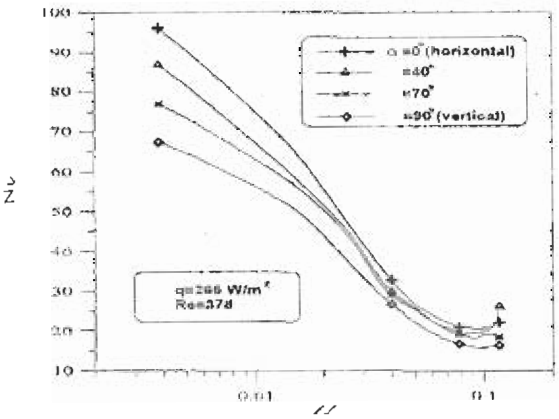

F ig.(17) Local Nusselt Number Versus Dimensionless Axial Distance for Various Angles, q=265 W/m^2, Re=378.

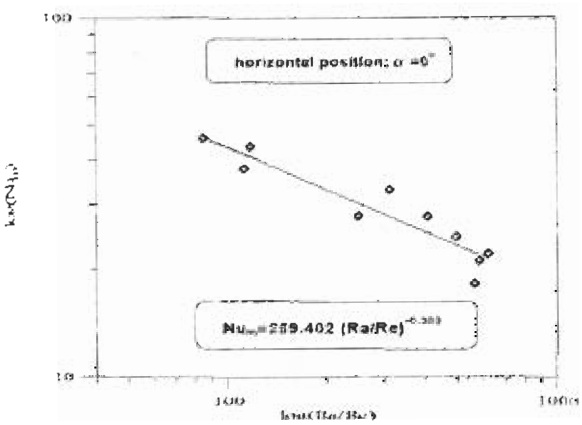

Fig.(18) Logarithm Average Nusselt Number Versus log(Ra/Re), α =0° (Horizontal).

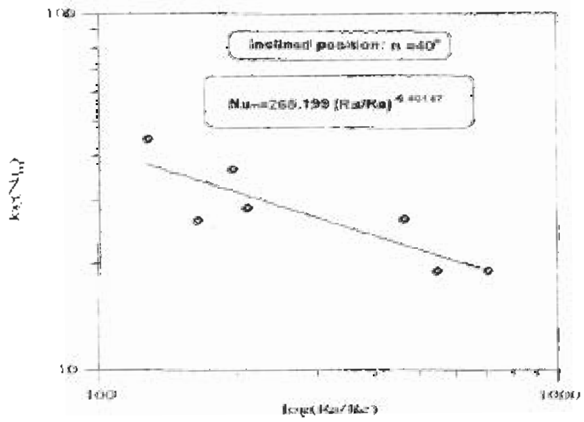

Fig.(19) Logarithm Average Nusselt Number Versus log(Ra/Re), α =40° .

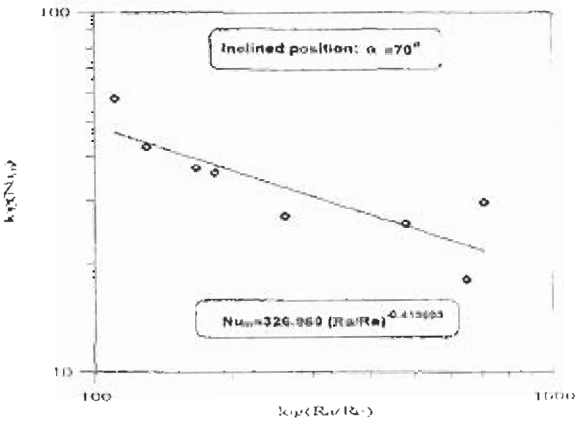

Fig.(20) Logarithm Average Nusselt Number Versus log(Ra/Re), $\alpha = 70^{\circ}$.

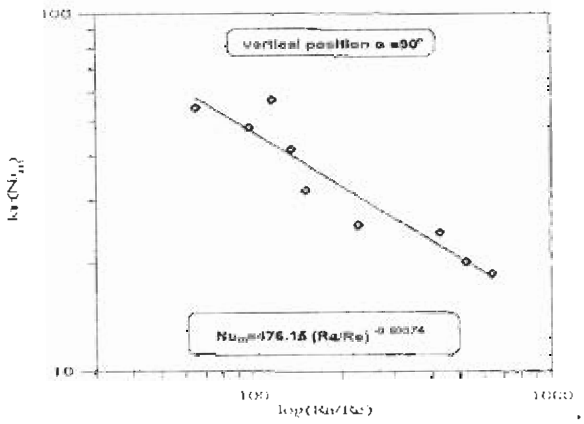

Fig.(21) Logarithm Average Nusselt Number Versus log(Ra/Re), $\alpha = 0^{\circ}$ (Vertical).

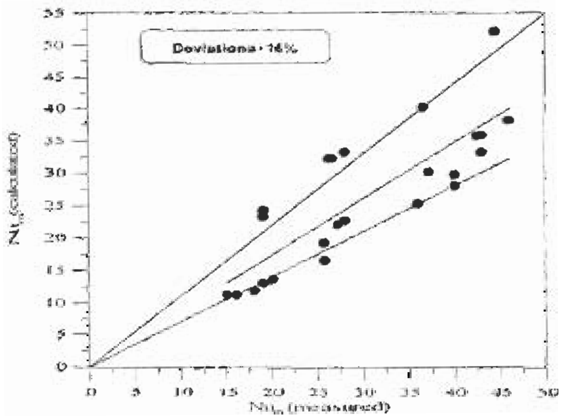

Fig.(24) Comparison Between Measured Nu_m and Nu_m Calculated from eq.(22).

A WAVELET NEURAL NETW0RK RAMWORK FOR SPEAKER IDNTIFCATION

Prof. Dr. W. A. Mahmoud **Dhiadeen.M.Salih** **Prof. Saleem M-R.Taha**
College of Engineering - University of Baghdad
Baghdad - Iraq

ABSTRACT
This paper introduces a new model-free identification methodology to detect and identify speakers and recognize them. The basic module of the methodology is a novel multi-dimensional wavelet neural network. The WNN approach include: a universal approximator; the time - frequency localization; property of wavelets leads to reduced networks at a given level of performance; The construct used as the feature mode classifier. Wavelet transform has been successfully applied to the processing of non - stationary speech signal and the feature vector that obtained becomes the input to the wavelet neural network which is trained off-line to map features to used for the classification procedure. An example is employed to illustrate the robustness and effectiveness of the proposed scheme.

الخلاصة
في هذا البحث تم اقتراح طريقة لنظام تمييز تعتمد على شبكة العصبية للتحويل المتموج ذات متعددة الأبعاد (wavelet neural network) حيث إن نظرية(WN) يتضمن التحديد الزمني والترددي والتابع للتحويل التموجي مساعدا بتقليل نسبة تعقيد الشبكة و على هذا الأساس استخدم هذه الشبكة كمصنف لخصائص لنماذج معينة من صوت كل متكلم حيث يستخلص بطريقة التحويل المتموج المتقطع (Discreet wavelet transform) لعدة مستويات بعد تقسيم كل صوت إلى عدد من مقاطع متساوية ومن ثم اخذ الطاقة المعدلة لكل مستوى حيث يتحصل بذلك على متجه ذات معاملات تدل لخصائص الكلمة للمتكلم وبعده يطبق جميع المتجهات المستحصلة لكل متكلم على شبكة التحويل المتموج (WN) وذلك لغرض تعليم الشبكة (Learning face) ومن ثم تطبيق صوت متكلم مجهول على الشبكة للتعرف عليه وقد أعطت هذه الطريقة عدد أوطئ من الحسابات وبذلك يزيد من كفاءة النظام ويقلل من وقت التنفيذ مقارنة لبقية الشبكات العصبية المستخدمة سابقا . هذه الطريقة تم تطبيقه على حاسبة سرعة معالجها (850 MHz Celeron) و(RAM 128 MB) ولغة برنامج هي MATLAB 6 . أما قاعدة البيانات فهي مكونة من خمسة و عشرين شخص (12 ذكور و 13 إناث) وقد كانت نسبة التمييز هي 82% مع زمن تعلم للشبكة لا يتجاوز 47 ثانية في حالة النص المستقل ونسبة 100% مع زمن تعلم للشبكة تصل إلى 55 ثانية في حالة النص المعتمد .

KEYWORDS
Speaker identification, speaker recognition, wavelet neural network wavelet transform, discrete wavelet transform, neural network, back – propagation algorithm.

INTRODUCTION
Recently, some strategic issues and approaches for speaker identification (SI) have been addressed by several investigators. The issue is the performance of SI so that recognition delays and false identify may be avoided .The complexity of the SI task lies in the fact that given utterance can be represented by an effectively infinite number of time - frequency pattern . typical classification problem, which generally include tow main modules: feature selection and classification where the second part i.e., classifier design have their own disadvantages due to the complex distribution of the feature vectors [Hex 2001]. Wavelet neural network (WNN) have recently attracted great interest ,because their advantages over radial base function network as thy are universal approximators but achieve faster convergence, Furthermore, WNNs possess a unique attribute: In addition to forming an orthogonal basis are also capable of explicitly representing the behavior of a function at various resolutions of input variables[George 2000].For instance, the task of pattern recognition is function mapping whose objective is to assign each pattern in a feature space to a specific label in a class space.

This paper is organized as follows the next section introduces some basic concepts in wavelets and wavelet neural networks; we describe next the general identification and classification architectures; focused attention is paid to the wavelet neural network; our example is used to illustrate the main features of the scheme; the paper concludes preprocess the speech signals (16 bit sampled in 8khz).then extract features vectors with discrete wavelet transform (DWT) to be trained off-line by WNN with different selection errors to get data base of speakers, then applied unknown speaker vector to the WNN to be classified and identify the speaker.

DISCRETE WAVELET TRANSFORM FOR REATURE EXTRACTING
The Discrete Wavelet Transform (DWT) is more popular in the field of signal digital processing. We thus introduce a simple feature extraction model based on the result of DWT. In order to parameterize the speech signal, we should first decompose the signal in the dyadic form using the Mallat's algorithm [Mallat 1989].

The ability ofDWT to extract features from the signal is dependent on the appropriate choice of the mother wavelet function [Burrus 1998]. Some of the popular families of wavelet bases functions are Harr, Daubechies, Coiflet, Symlet, Morlet, and Mexican Hat. The properties of the wavelet functions and the characteristics of the signal being analyzed need to be matched [Khalaf 2003] . The properties of wavelet function are tabulated in **Table (1).**

Table (1) Properties of Wavelet Functions

[illegible]	[illegible]	[illegible]
[illegible]	[illegible]	[illegible]
[illegible]	[illegible]	[illegible]
[illegible]	[illegible]	[illegible]
[illegible]	[illegible]	[illegible]
[illegible]	[illegible]	[illegible]
[illegible]	[illegible]	[illegible]

The objective of this module is to determine and extract appropriatpJeatures for the fault or defect classification task. An additional objective is to reduce the search space and to speed up the computation.. In preparation for feature extraction, a windowing operation is applied to the I-D signals in order to reduce the search space and facilitate the selection of appropriate features [Khalaf 2003].

WAVELET NEURAL NETWORKS

A neural network is composed of multiple layers of interconnected nodes with an activation function in each node and weights on the edges or arcs connecting the nodes of the network. The output of each node is a nonlinear function of all its inputs and the network represents an expansion of the unknown nonlinear relationship between inputs, x, and outputs, F (or y), into a space spanned by the functions represented by the activation functionsofthe network's nodes. Learning is viewed as synthesizing an approximation of a multidimensional function, over a space spanned by the activation functions $\Sigma\Phi(x), i = 1,2,...,m$, i.e.

[illegible]

where .Np is the number of wavelet nodes in the hidden layer and WI is the synaptic weight of WNN. The additional parameter c_i is introduce to help dealing with nonezero average .since wavelet If/"is zero mean. A WNN can be regarded as function aproximator ,which estimate an unknown function mapping [Q. Zhang 1992].This network structure is shown in **Fig .(1).**

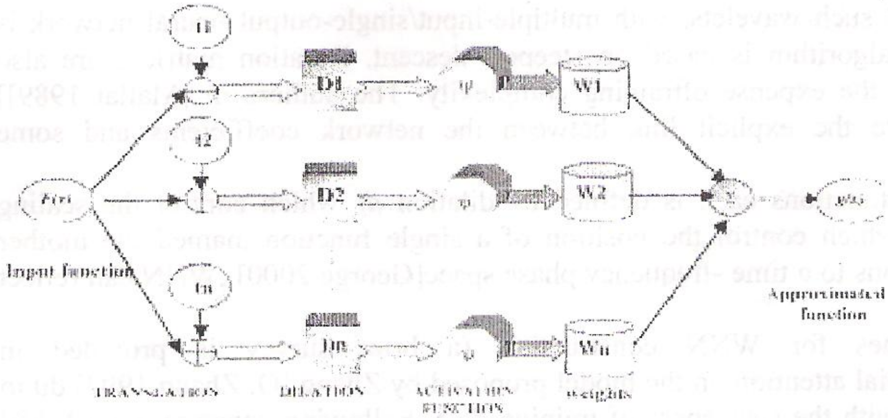

Fig (1) WNN Structure for approximation The combination of translation ,dilation ,and wavelet lying on the same line will be called a *wave/on* in the sequel.

The authors in [Oubez 1994], and independently, in [Bakshi 1992], arrive at very similar formulations of the wavelet network that are closer to the wavelet expansion than to neural networks. The wavelet
parameters are neither adapted as in [Q. Zhang 1992] .nor computed from prior Fourier data analysis as in [Pati 1993], but are taken incrementally from a predefined space-frequency grid of orthogonal wavelets.
This approach prescribes learning as a multiresolution, hierarchical procedure, and brings about the possibility of a type of network growth.

Wnn Initialization

The initialization of WNN consists in the evaluation of the param(;;cers f.J, *Wi* ,*ti* and *di* =1/sj for i =1,2 ...,*N*. To initialize f.J we need to estimate the mean of the function f(x) (from its available observation) and set f.J to the estimated mean. *WTS* are simply set to zero .the rest of problem is how to initialize *ti* 's and *s;* 's . The approximation error is minimized by adjusting the activation function and network parameters using empirical (experimental) data. Two types of activation functions are commonly used: global and local. Global activation functions are active over a large range of input values and provide a global approximation to the empirical data. Local activation functions are active only in the immediate vicinity of the given input value[Bakshi 1994].

It is well known that functions can be represented as a weighted sum of orthogonal basis functions. Such expansions can be easily represented as neural nets by having the selected basis functions as activation functions in each node, and the coefficients of the expansion as the weights on each output edge. Several classical orthogonal functions, such as sinusoids, Walsh functions, etc., but, unfortunately, most of them are global approximators and suffer, therefore, from the disadvantages of approximation using global functions. What is :needed is a set of basis functions which are local and orthogonal. A special class of functions, known as wavelets, possess good localization properties while they are simple orthonormal bases. Thus, they may be employed as the activation functions of a neural network known as the Wavelet Neural Network (WNN). WNNs possess a unique attribute: In addition to forming an orthogonal basis are also capable of explicitly representing the behavior of a function at various resolutions of input variables. The pivotal concept, in the formulation and design of neural networks with wavelets as basis functions, is the multiresolution representation of functions using wavelets. It provides the essential framework for the completely localized and hierarchical training afforded by Wavelet Neural Networks [George 2000]].

By linearly combining several such wavelets, with multiple-input/single-output neural network is obtained. The basic training algorithm is based on steepest descent. Rotation matrices are also incorporated for versatility at the expense oftraining complexity. The authors in [Mallat 1989]] demonstrate the way to have the explicit link between the network coefficients and some appropriate wavelet transform.

Wavelets occur in family of functions each is defined by dilation *dj* which control the scaling Parameter and translation *tj* which control the position of a single function ,named the mother wavelet *Ij/(x)*. Mapping functions to a time -frequency phase space[George 2000] .WNN can reflect properties more accurately.

There are several approaches for WNN construction (a brief survey is provided in [Q. Zhang 1992]),we pay special attention on the model proposed by Zhang [Q. Zhang 1992] du to its notable feature in dealing with the sparseness of training data. Following constructing a WNN involves tow stages: First, construct a wavelet library *W* of discretely dilated and translated version of wavelet mother function Ij/:

[illegible]

where Xk is the sampled input, and L is the number of wavelets in W, seconed select the best M wavelet based on the training data form wavelet library W, in ordex to build the regression Based on the previous discession we propose a network structure ,Given an n-element training set of the form:

[illegible]

To initialize t_j and Sj select a point p between interval of function a and b " $a < p < b$ The choice of this point will be detailed later. Then we set

Where $\zeta > 0$ is properly selected constant (the typical value of ζ is 0.5). the interval divided into two parts by p . in each sub interval we repeat the same procedure which will initialize t_2, S2and t_3 . s3 and so on , until all wavelet will initialize. \ This procedure applies in this form when a number of wavelons are used which is a power of 2. then we take the point p to be the center of gravity of $[a, b]$. There are several mother wavelets that could be useful in ore project .The continuos wavelet transform theory in the Morlet- Grossmann sense provides us with considerable flexibility in designing our networks **Ψ** = $x \exp(-1/2\, X^2)$ [Q. Zhang 1992] . shown in fig 2. There is Mexican - Hat. The mother wavelet Ψ= $(1 - X^2) \exp(-1/2\, X^2)$, shown in **Fig .(3)**.

This function, shown in **Fig. (4)**, consists of two cycles of the cosine function, windowed by a trapezoid that linearly tapers two thirds of the endpoints to zero[George 2000], these function will be used in training WNN.

Wavelet Neural Network Classifier

The MIMI WNN, depicted schematically in **Fig. (5)**, is used as the classifier. Potential dvantages of the WNN as a universal approximator and the time - frequency localization roperty of wavelets leads to reduced networks at a given level of performance ,so WNNs offer a ood compromise between robust implementations and efficient functional representations; the ulti-resolution organization of wavelets provides a heuristic *for* neural network growth.

Furthermore, WNNs may be optimized with respect to structure (nm-'berof nodes) and their arameters using a Genetic Algorithm as the optimization tool. The structure and the parameters f the network are determined iteratively until a performance metric is satisfied. The WNN onstruct suggests a means to parallel-process multiple signals in a multi-tasking environment, hus expediting considerably processing times. Finally, it offers an easy and user-friendly way to learn" new signal patterns, as long as training data is available.

This algorithm modifies the parameters vector *e* after each measurement *(Xk,Yk)* in the opposite irection of the gradient of the functional

[illegible] (4)

As is the case for backprobagation algorithm for neural network learning [Q. Zhang 1992] . The objective unction (4) is likely to be highly nonconvex ,so local minima are expected. To improve the ituation ,careful initialization of the algorithm is preformed and appropriate constraints ar-- set n the adjusted parameters.

- [illegible]
  [illegible]
- [illegible] (6)
  [illegible]
  [illegible]
  [illegible]
- [illegible] (7)
- [illegible] (8)
- [illegible] (9)
- [illegible] (10)
- [illegible]

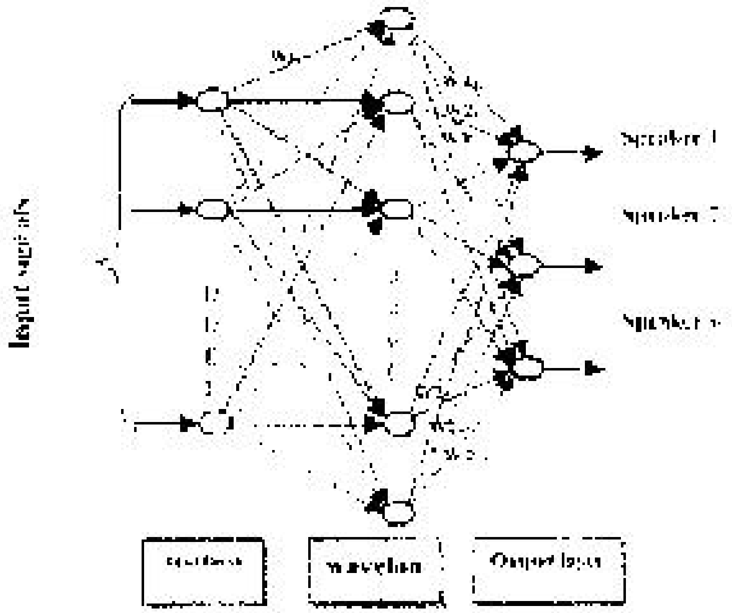

Figure [illegible] Complete Wavelet Neural Network.

Wavelet Neural Network Learning Algorithm:

The method of setting the values of weights (in training phase) is an important istinguishes characteristics of different neural networks. There are two common types of raining algorithms, supervised and unsupervised, sometimes there is a third method, i.e. elf-supervised or reinforcement training method [[Zhanshou 200].

The learning is based a Stochastic gradient type algorithm **Fig. (6)** which very imilar to the backprobagation algorithm for neural network ,first collect all the parameters *go,Wi,tidi* In a vector *e* and write *fa (-y)* to refer to the network defined by Eg.(3) whith the parameter vector *e* . The objective function to be minimized is

[illegible] 3

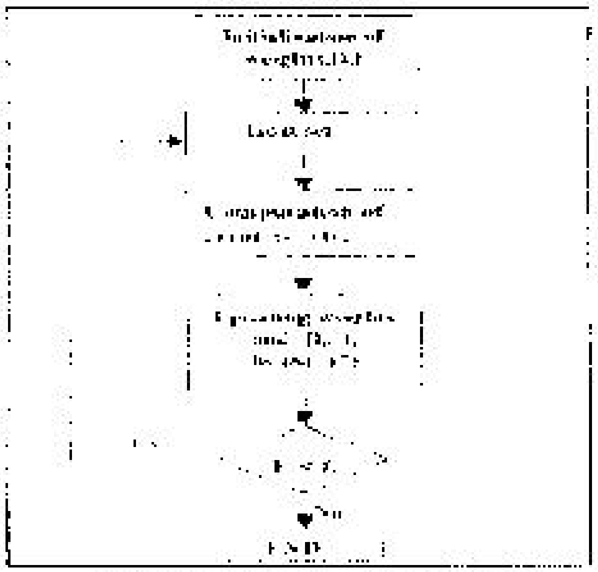

Fig (6) [illegible]

SPEAKER IDENTIFICATION AND CLASSIFICATION METHODOLOGY

Fig. (7) depicts the major modules of the identification and classification methodology. Sensor data are used first off-line to generate a feature base. From a feature library, those features are selected that provide a good match with the failure modes to be detected and identified. An incoming sensor signal is fed on-line in real-time to the feature extractor which attempts to extract a set of features. This feature vector is provided next as an input to the wavelet neural network; the latter is accompanied with an appropriate decision logic that decided upon the particular speaker class that the features (symptoms) belong to.

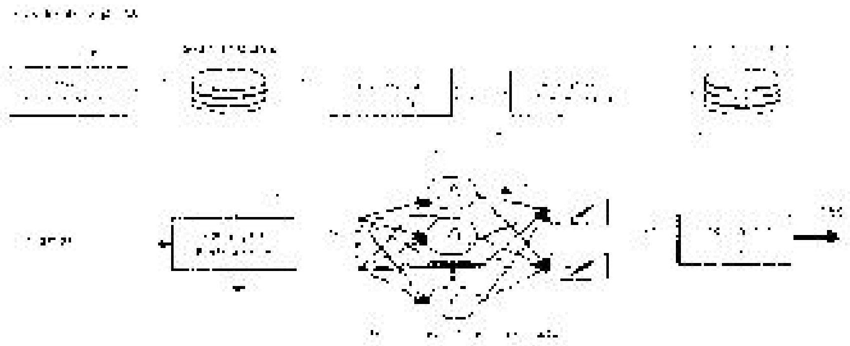

Fig. 7

EVALUATION TEST OF THE PROPOSED SPEAKER IDENTIFICATION SYSTEM

In this section the experimental result will be given.

[illegible]

The Preprocessing

- The speech signals used in this work are sampled with a sampling frequency of44.1 kHz.
- The speech signal is segmented into 256 samples per segment (frames), the overlapbetween frames is 128 samples per segment.

Feature Extraction

- Each frame of the spoken words is now expanded using the Discrete Wavelet Transform (DWT) up to 8 levels of decomposition.
- By computing the power in each segment in each level of the decomposition, a feature vectors 'Yill be obtained that describes the power distribution over the timefrequencyplane. IThis scale power density along every segment describes the power variation in each scale.
- The variance of the power overall the segments and for each of the 8 levels is computed, leading in a vector called (normalized power vector).

These steps will be shown in the **Fig (7).**

The proposed method is first studied with changing the wavelet functions and using different numbers of wavelones, because these two parameter influence directly on the speaker recognition accuracy. The Daubechies wavelet of order 4 (Db4) is chosen in the processing phases and. The Daubechies wavelets have some characteristics that are useful for speaker recognition

[Khalaf 2003]. **Table (2) and (3)** shows the percentage of correct classification for text - independent and text - dependent. respectively.

[illegible]

[illegible]	Accept	[illegible]
[illegible]	[illegible]	[illegible]
[illegible]	[illegible]	[illegible]
[illegible]	[illegible]	[illegible]

[illegible]

[illegible]	Accept	[illegible]
[illegible]	[illegible]	[illegible]
[illegible]	[illegible]	[illegible]
[illegible]	[illegible]	[illegible]

CONCLUSIONS

A model-free approach to the problem of speaker identification conditions hasbt-enpresented. The multi-dimensional WNN is an effective and efficient tool for classification. The computational to the feature extraction step where appropriate features must be computed from signal data that comprise eventually the input vector to the network. The WNN approach offers additional advantages in terms of learning and optimization functions that may be carried out offline or on-line. FUlibermore, the neural net topology suggests means for parallel processirig - useful in high frequency processes because of fast learning time. These shows promise as an effective model for the analysis of process data for many industrial and other engineered systems.

REFERENCES

He Xuming, Hu Guangrui and Tan Zhenghua (2001), Coevolutionary Approach To Speaker Identification Using Neural Networks" Proc. ICASSP 2001.

George Vachtsevanos, Peng Wang (2000), A WNN frame work for diagnostic complex engineered stems. Atlanta. GA 30332, USA.

Mallat, (1989). A Theory of Multi - Resolution Signal Decomposition, proceeding of IEEE .

Burrus C.S., Gopinath, R.A., and Gou, H., (1998), Introduction to Wavelet and Wavelet Transform.

prof. Dr. W. A. Mahmoud. R. F. Khalaf, Safiea K. Omran (2003). Speaker Identification Based On Wavelet And Neural Network, College Of Engineering - University of Baghdad ..

Q. Zhang and A. Benveniste, (1992), Wavelet networks, IEEE Transactions on Neural Networks, vol. 3, no. 6, pp. 889-898, Nov..

Pati and P.S. Krishnaprasad, (1993), Analysis and synthesis of feedforward neural networks using discrete affine wavelet transformations, IEEE Transactions on Neural Networks, vol. 4, no. 1, pp. 73-85, Jan..

Oubez and R.L. Peskin, (1994), Multiresolution neural networks, in SPIE.,vol. 242, pp. 649-659.

Bakshi and G. Stephanopoulos, (1992), Wavelets as basis functions for localized learning in a multi-resolution hierarchy, in Proc. IJCNN MD, , vol. 2, pp. 140-145.

Bakshi A.K. Koulouris, and G. Stephanopoulos, (1994), Wave-Nets: Novel learning techniques, and the induction of physically interpretable models." in SPIE., vol. 2242, pp. 637-648.

Zhanshou Y., (2000), Feed Forward Neural Networks And Their Applications In Forecasting, Msc. Thesis, Department of Computer Science, University of Housten, USA December